Waveguide-Based Photonic Sensors: From Devices to Robust Systems

Zur Erlangung des akademischen Grades eines

DOKTORS DER INGENIEURWISSENSCHAFTEN (Dr.-Ing.)

von der KIT-Fakultät für Elektrotechnik und Informationstechnik des
Karlsruher Instituts für Technologie (KIT)

genehmigte

DISSERTATION

von
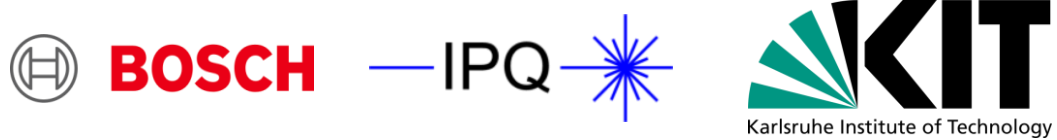
Johannes Milvich, M.Sc.

geboren in

Stuttgart, Deutschland

Tag der mündlichen Prüfung: 08.09.2020
Hauptreferent: Prof. Dr. Christian Koos
Korreferent: Prof. Dr. Dr. h.c. Wolfgang Freude
Korreferent: Prof. Dr. Joachim N. Burghartz

Table of contents

Abstract (German)

Integrierte photonische Sensorsysteme bestehen aus miniaturisierten, massen-produktionstauglichen Bauelementen, die sich einerseits die ausgereifte Halb-leitertechnologie zu Nutze machen, und die sich andererseits aus dem Baukas-ten vorhandener photonischer Komponenten bedienen, welche insbesondere für Telekommunikationsanwendungen entwickelt wurden. Integrierte photonische Sensorsysteme kombinieren einen integrierten photonischen Schaltkreis (pho-tonic integrated circuit, PIC), optoelektronische Lichtquellen und Photodetek-toren, sowie elektronische Komponenten für die Signalerzeugung und Signal-verarbeitung. Die optoelektronischen Komponenten sind entweder direkt auf dem PIC integriert oder sind externe Komponenten, in beiden Fällen wird das Licht in Wellenleiter auf dem PIC ein- und anschließend wieder ausgekoppelt. In solch einem System dient der PIC als Sensorelement, welches so entworfen wird, dass sich die optische Transmission mit hoher Sensitivität von den zu de-tektierenden Änderungen in seiner Umgebung beeinflusst wird. Ein wichtiges Beispiel ist ein biochemischer Sensor-PIC, welcher über Wellenleiter mit funk-tionalisierten Wellenleiteroberflächen die Adsorbtion von Molekülen detektie-ren kann. Eine Besonderheit ist, dass hierfür keine Markierung der zu detektie-renden Molekülgruppen wie z.B. Floureszenzfarbstoffe notwendig sind, weshalb solche Verfahren als „label-free" bezeichnet werden. Durch die Kom-paktheit der entsprechenden Sensorelemente können eine Vielzahl von Senso-ren parallel innerhalb eines einzelnen Chips auf einer Fläche im Bereich von nur einem Quadratmillimeter realisiert werden.

Gegenstand der vorliegenden Arbeit ist eine ganzheitliche Betrachtung von in-tegrierten photonischen Sensorsystemen auf mehreren Abstraktionsebenen. Die Betrachtung beinhaltet eine detaillierte Analyse des photonischen Wellenleiter-designs auf der untersten Abstraktionsebene, des photonischen Schaltungsde-signs und des Systemdesigns inklusive der Elektronik, der Lichtquellen und der Photodetektoren auf der mittleren Abstraktionsebene, sowie eine Analyse des Ansteuer- sowie Ausleseverfahrens um hochpräzise, eindeutige Messdaten zu generieren auf der obersten Abstraktionsebene. Ein besonderes Augenmerk

liegt hierbei auf der Optimierung der Leistungsfähigeit auf der Gesamtsysteme-bene, sowie auf der Kompensation von unvermeidbaren Variationen der Komponenteneigenschaften, welche unweigerlich mit einer Massenproduktion sowie mit einem energieeffizienten Sensorbetrieb unter realistischen Umgebungsbedingungen einhergehen.

Nach einem kurzen Überblick über wesentliche Ergebnisse dieser Arbeit folgt in den Kapiteln 1 bis 6 die eigentliche Abhandlung der Inhalte. Die darauffolgenden Anhänge beinhalten weiterführende konzeptionelle und mathematische Details sowie Verzeichnisse der Literaturangaben, der Akronyme, der verwendete mathematischen Symbole, der Figuren, der Tabellen und der Publikationen. Im Anschluss daran folgt eine Danksagung sowie ein Lebenslauf des Autors. Teile dieser Arbeit wurden bereits in Patenten [P1], [P2], internationalen Fachjournalen [J1], [J2], sowie in einem Konferenzbeitrag [C1] publiziert.

Die Hauptkapitel 1 bis 6 dieser Arbeit sind wie folgt strukturiert:

Kapitel 1 *gibt eine Einführung in das Gebiet der integrierten photonischen Sensorsysteme* und behandelt hierbei optische Sensoren, relevante Anwendungen und die Entstehung der integrierten photonischen Technologie aus der elektronischen Halbleiterindustrie. Weiterhin wird der Umfang der in dieser Arbeit durchgeführten Analyse aufgezeigt.

Kapitel 2 *stellt die mathematischen und konzeptionellen Grundlagen integrierter photonischer Sensorsysteme zusammen* und behandelt hierbei die Propagation von elektromagnetischen Wellen in photonischen Wellenleitern und den wellenleiterbasierten Sensormechanismus über den effektiven Brechungsindex einer optischen Mode. Weiterhin bietet es einen umfassenden Überblick über das komplette Sensorsystem ausgehend von phasensensitiven photonischen Schaltkreisen über die wichtigsten Systemkomponenten und deren technologischen Herausforderungen bis hin zu einer Gegenüberstellung der geläufigsten Systemkonfigurationen und Auslesekonzepte.

Kapitel 3 *analysiert das Design integrierter photonischer Wellenleiter für Sensoranwendungen.* Dieses Kapitel bietet physikalische Einsichten und umfängliche Designleitlinien, mit Hilfe derer für eine bestimmte Messaufgabe eine passende photonische Integrationsplattform, ein Wellenleitertypus, eine Modenfamilie sowie eine optimierte Wellenleitergeometrie ausgewählt werden können. Grundlage hierfür ist die Wechselwirkung einer geführten Wellenleitermode mit einer Änderung des Wellenleiterquerschnittes, die durch die zu bestimmende Messgröße hervorgerufen wird. Diese Wechselwirkung wird quantitativ durch den Feldinteraktionsfaktor beschrieben.

Kapitel 4 *analysiert die Leistungsfähigkeit und die Limitierungen des gesamten photonischen Systems* inklusive der phasensensitiven photonischen Schaltkreise, der Lichtquellen und Photodetektoren, sowie des elektrischen Ansteuer- sowie Ausleseverfahrens. Ein besonderes Augenmerk liegt hierbei auf Systemen, welche für eine kosteneffiziente Großserienproduktion ausgelegt wurden. Hierbei spielen insbesondere Variationen der Komponenteneigenschaften eine Rolle, welche unweigerlich mit einer Massenproduktion sowie einem energieeffizienten Sensorbetrieb unter realistischen Umgebungsbedingungen einhergehen.

Kapitel 5 *stellt ein besonders robustes photonisches Sensorsystem vor*, welches, basierend auf den Erkenntnissen aus den Kapiteln 3 und 4, für Sensoranwendungen außerhalb idealisierter Laborbedingungen und explizit für eine Großserienproduktion geeignet ist. Basierend auf einem integrierten Mach-Zehnder-Interferometer mit drei um 120° phasenverschobenen Ausgangssignalen wird ein spezielles Ansteuer- und Ausleseverfahren demonstriert, welches eine instantane Selbstkalibration und eine jederzeit eindeutige Phasenmessung ermöglicht.

Kapitel 6 *fasst die wesentlichen Ergebnisse und Schlussfolgerungen zusammen und identifiziert offene Herausforderungen* für eine erfolgreiche Kommerzialisierung integrierter photonischer Sensorsysteme.

Abstract

Integrated photonic sensor systems consist of miniaturized, mass-producible devices that leverage mature semiconductor fabrication technology as well as a well-established ecosystem of photonic components developed primarily for telecommunication applications. Integrated photonic sensor systems combine a photonic integrated circuit (PIC) that contains waveguide-based sensor components, opto-electronic light sources and detectors that can be integrated on the PIC or that can be coupled to the PIC from outside, and electronic components for signal generation and signal processing. Within this system, the PIC serves as the sensing element, designed to provide an optical transmission that sensitively depends on changes of the environmental parameter that have to be detected. A prominent example is a biochemical sensor PIC that exploits label-free detection of molecules binding specifically to a functionalized waveguide surface. Due to the compactness of the sensor PIC, it is rather straightforward to realize a multitude of parallel sensors on a single chip, with footprints of the order of a square millimeter.

This work aims at a holistic treatment of integrated photonic sensor systems over all levels of abstraction. It comprises a detailed analysis of photonic waveguide design on the lowest level, of the photonic circuit design to optimize the optical response and of the system design including electronics, light sources and detectors on an intermediate level, as well as of the readout design geared towards obtaining precise and unambiguous measurement results on the highest level of abstraction. A special emphasis is put on system-level performance optimization as well as on managing unavoidable variations of optical components that are inherently linked to mass production and energy-efficient system operation under realistic environmental conditions.

After a brief review of the major achievements in the introductory part of the thesis, Chapters 1-6 contain the main contents of this work. The subsequent appendices contain conceptual and mathematical details, lists of bibliographic references, acronyms, mathematical symbols, figures, tables and publications. The thesis concludes with acknowledgements and a curriculum vitae of the author.

Parts of this thesis have been published in patents [P1][P2], in international journals [J1][J2], and in a conference contribution [C1]. The main sections are structured as follows:

Chapter 1 *gives a general introduction to the field of integrated photonic sensor systems* by discussing the advantages of optical sensors, relevant applications, and the emergence of integrated photonic technologies from the electronic semiconductor industry, and by summarizing the scope of the analysis provided in this work.

Chapter 2 *provides the mathematical and conceptual fundamentals of integrated photonic sensor systems* by discussing propagation of electro-magnetic signals in photonic waveguides, the mechanism of waveguide-based effective refractive index sensing, and a sensor system overview reviewing phase-sensitive photonic circuits, core system components and associated technological challenges, as well as sensor system configurations and readout concepts.

Chapter 3 *analyzes the design of integrated photonic waveguides for sensing applications* and provides physical insights and comprehensive design guidelines for the selection of appropriate photonic integration platforms, waveguide types, mode families, and optimized waveguide geometries geared towards a specific measurement task. The analysis builds upon the interaction of a waveguide mode with a particular change of the waveguide properties, which is caused by the environmental parameter of interest. The strength of this interaction is quantified by the so-called field interaction factor.

Chapter 4 *analyzes the performance and limitations of the entire photonic sensor system*, including the phase-sensitive photonic circuits, light sources and detectors, as well as the electrical readout. A special focus is on systems that are geared towards cost-efficient mass-production and large-scale deployment and that are able to handle variations of components that are inherently linked to mass production and energy-efficient system operation under realistic conditions.

Chapter 5 *presents a particularly robust photonic sensor system* viable for large-scale sensor applications outside a controlled laboratory environment by aggregating the insights gained by the analyses in Chapters 3 and 4. Based on an integrated Mach-Zehnder interferometer with three 120°-phase-shifted output signals, a specific operation and readout concept is demonstrated that offers instantaneous self-calibration and unambiguous phase readout.

Chapter 6 *summarizes the work* with its key findings and conclusions and identifies remaining challenges for a successful commercialization of integrated photonic sensor systems.

Achievements

In this thesis, the role of photonic integrated circuits in fully integrated sensor systems is analyzed. The three main fields of research are **waveguide design for photonic sensors** [J1], **sensor-system analysis, performance estimation, and design** [J2], as well as **robust calibration and readout schemes using a 1×3 Mach-Zehnder Interferometer (MZI)** [C1][P2]. The following list briefly summarizes the main achievements in each research field.

Waveguide design for photonic sensors

Design guidelines: Based on a mathematical model of light propagation in sensor waveguides, comprehensive waveguide design guidelines for specific surface-sensing tasks are formulated. This represents the first broadly applicable analysis capable of covering different photonic integration platforms, different waveguide types, and different mode families [J1].

Explanation of waveguide sensitivity trends: The main dependencies of waveguide properties on geometrical and material parameters are identified and explained. It is shown that they result from the scaling laws of Maxwell's equations, from the effect of field enhancement, as well as from waveguide cladding asymmetry [J1].

Introduction of a broadly applicable surface sensitivity quality metric: With this metric, the influence of surface layers of different thicknesses and refractive indices on mode propagation can be evaluated [J1].

Computationally efficient recipe: For calculating the influence of surface layer variations on mode propagation in integrated waveguides, a numerically efficient technique is introduced that relies on field interaction integrals via a perturbation approach applied to a single numerical simulation [J1].

Sensor system analysis, limits and design guidelines

Holistic system model for waveguide-based photonic sensor systems: A comprehensive quantitative model of waveguide-based photonic sensor systems is formulated, which enables a consistent analysis and a broad benchmark of the performance of different sensor concepts and specific technical implementations [J2].

Analysis of the impact of laser frequency noise on sensors based on high-Q ring resonators and Mach-Zehnder interferometers: The system model also comprises the impact of laser frequency noise, which eventually limits the viability of high-Q ring resonators in sensing applications. MZI-based sensors with approximately balanced arm lengths are much more robust with respect to frequency noise of non-ideal laser sources. The importance of this aspect is demonstrated by using the frequency-noise spectrum of a vertical-cavity surface emitting laser (VCSEL) as a particularly efficient and low-cost light source for integrated sensor systems [J2].

Sensitivity and limit of detection benchmark: The model allows to benchmark the performance of ring resonators and Mach-Zehnder interferometers as the most common photonic sensor circuits when used within a fully integrated photonic sensor system under realistic operation conditions [J2].

Comprehensive sensor system design guidelines: Based on the findings, comprehensive guidelines for the selection of appropriate system components and sensor circuit design are formulated. Furthermore, sensitivity and noise trends are traced back to fundamental physical effects. The findings were summarized in an educational MATLAB application [J2].

Calibration and readout of a 1×3 Mach-Zehnder interferometer (MZI)

Mathematical description of a 1×3 MZI-based sensor system. A qualitative model of a 1×3 MZI-based sensor is formulated that accounts for component non-idealities and readout [C1]. This model builds the base for a patent application [P2].

Robust sensor calibration concept for 1×3 MZI-based sensor system. Based on the model, a strategy is formulated that enables an instantaneous self-calibration during sensor operation and that can hence eliminate impairments such as temperature drift, strain, pressure, humidity, or aging [C1][P2].

Robust sensor readout concept for 1×3 MZI-based sensor system. As an additional feature of the 1×3 MZI-based sensor system, a technique is introduced that allows for endless phase unwrapping and thereby provides absolute, unambiguous measurements. This technique is key to applications where the observed process is happening faster than the sampling frequency or where the device is turned off and on between several measurements [C1][P2].

1 Introduction

Sensors are devices that detect changes of an environment and convert them to an output signal, which is either visualized directly or processed further to control connected actuators. The steep rise of microelectronics and micromechanics in the last decades has led to improvements in size, affordability, and accuracy of such sensors. As a consequence, sensors have become ubiquitous devices that add intelligence to everyday objects such as cars, smartphones and homes, or that control complex processes in manufacturing, medicine, mobility, and robotics.

Light is the basis for a multitude of free-space and fiber-based **optical sensors** such as refractometers, media sensors, environmental sensors for temperature or humidity, mechanical sensors for strain or acoustics, as well as chemical or biological sensors. Optical sensors can passively probe analytes without the use of currents or direct physical contact. In addition, optical biological sensors can enable label-free detection of certain analytes without prior attachment of fluorescent markers or radioactive isotopes. However, at present, optical sensors still rely on highly versatile and sensitive optical systems that are typically built from macroscopic, discrete components, a fact which often results in rather bulky *bench-top* photonic sensor systems.

These limitations can be overcome by **integrated photonic sensor systems,** which harness the tremendous capabilities of highly advanced semiconductor fabrication technology. Integrated photonic sensor systems offer outstanding miniaturization, massive functional parallelization, and cost-efficient mass-production using ultra-robust processes along with co-integration and co-packaging with readily available (opto-)electronic components.

When it comes to large-scale deployment of efficient optical sensors, silicon-based photonic integration platforms are of particular interest, as they can exploit the enormous technology push of the mature complementary metal-oxide semiconductor (CMOS) fabrication processes. The advance of **integrated pho-**

tonics technology is driven mainly by an application pull from the ever-increasing bandwidth demands of the telecommunication industry. Tremendous effort is put into maturing silicon photonics by optimizing and expanding the photonic integrated circuit (PIC) component portfolio that so far comprises mainly passive waveguides, couplers, splitters, combiners, or electro-optic modulators. The high refractive index contrast of the silicon photonics platform enables small feature sizes and hence small device footprints, however, the indirect bandgap of silicon impedes monolithic integration of silicon-based light sources. As a consequence, the silicon-based PIC technology is often complemented by the integration of (or coupling to) light sources and detectors based on other materials. Today, integrated photonic technology is offered commercially via foundry services and associated photonic process design kits (PDK).

Within this work, the PIC technology will be used to realize **integrated photonic sensor systems**, with a special focus on waveguide-based sensors that rely on a change of the effective refractive index of a waveguide mode. This change of the effective refractive index leads to a phase shift, which is commonly translated into a measurable change of the optical output power via on-chip phase-sensitive photonic circuits such as resonators or interferometers. Other sensing principles such as absorption, Raman scattering, or surface plasmon resonance spectroscopy are not considered here. In the framework of our research, we model the entire integrated photonic sensor system including light sources and detectors, optical coupling interfaces, on-chip waveguides and phase-sensitive photonic circuits, analog-to-digital converters, as well as the sensor operation and signal read-out. A special emphasis is put on component and system performance optimization, as well as on managing unavoidable variations of different sensor components that are inherently linked to mass production and energy-efficient system operation under realistic environmental conditions.

The design of an entire integrated photonic sensor system requires a comprehensive understanding on three levels of abstraction, namely

i) **waveguide design**, which is key to select the appropriate waveguide for a given sensing task,

ii) **system design**, which is instrumental to lay out the system components for a given sensitivity and limit-of-detection target, and

iii) **readout design**, which allows the operator to obtain precise and unambiguous measurement data.

A visualization of an integrated photonic sensor system including the three focus areas of this work is shown in Fig. 1.1.
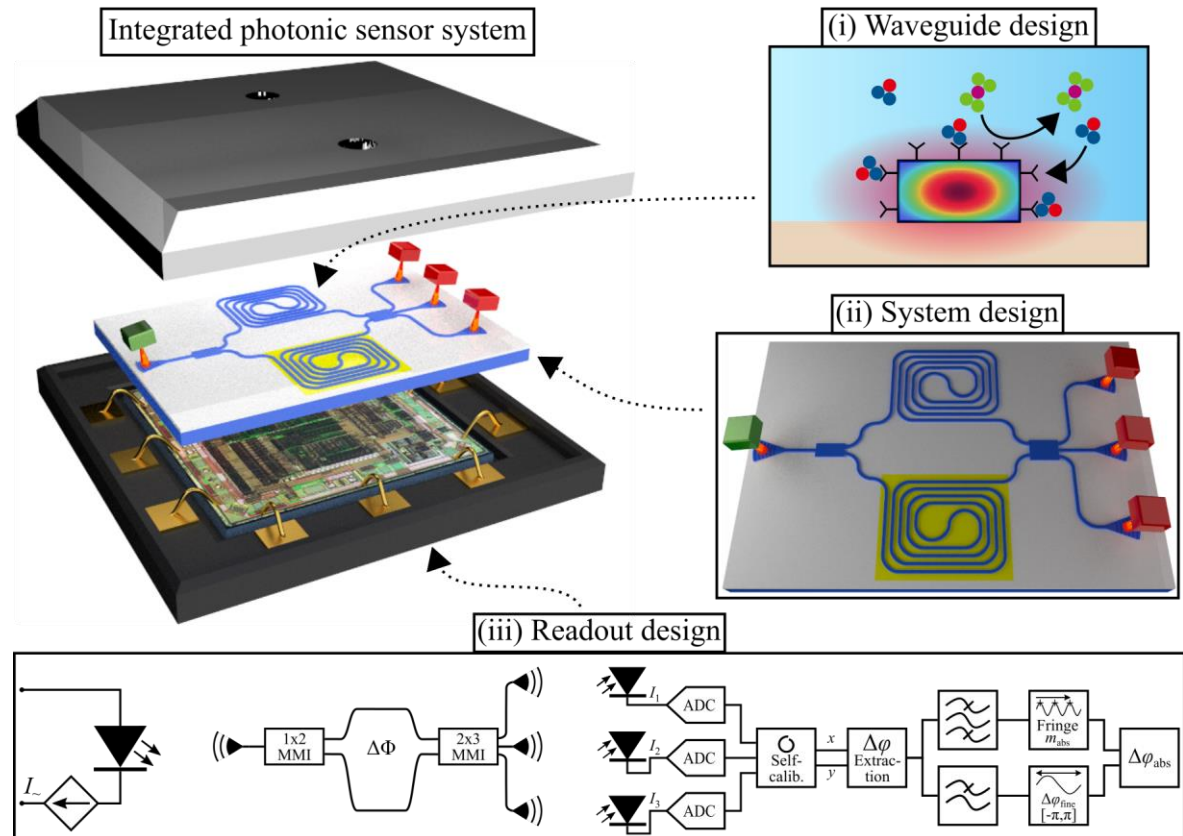
Fig. 1.1. Integrated photonic sensor system and focus areas of this thesis. The holistic design of an integrated photonic sensor system requires a comprehensive understanding on three levels of abstraction, namely (i) waveguide design, (ii) system design, and (iii) readout design, which are discussed extensively in Chapter 3, Chapter 4 and Chapter 5, respectively.

2 Fundamentals: Integrated photonic sensor systems

This chapter introduces the fundamentals of waveguide-based integrated photonic sensor systems. It starts with the mathematical description of electro-magnetic wave propagation in photonic waveguides in Section 2.1. The basic sensing principle via the effective refractive index of a propagating waveguide mode is introduced in Section 2.2, including a closer look at evanescent-field sensing. Section 2.3 gives a system-level overview of integrated photonic sensors. It introduces the two main phase-sensitive photonic circuit types, resonators and interferometers, followed by a discussion of core components and associated technological challenges. It continues with a comparison of attractive sensor system configurations focusing on the choice and the control of the optoelectronic light sources, detectors and sensor circuits, and concludes with a short overview of sensor readout concepts.

2.1 Electro-magnetic wave propagation in photonic waveguides

Waveguide-based integrated photonic sensor systems rely on electro-magnetic waves in the optical regime, typically in the visible (VIS), the near-infrared (NIR), or the mid-infrared spectrum (MIR). Different sensor applications benefit from different sections of the electro-magnetic spectrum, and hence require suitable material systems that are capable of efficiently guiding light in the respective wavelength range. This section describes the propagation of electro-magnetic waves in photonic waveguides including the key modal characteristics relevant for sensing.

2.1.1 Plane waves in homogeneous optical media

The general behavior of electro-magnetic fields is described by Maxwell's equations, which comprise the four coupled partial differential equations

$$\operatorname{curl}\mathbf{H}(\mathbf{r},t) = \mathbf{J}(\mathbf{r},t) + \frac{\partial \mathbf{D}(\mathbf{r},t)}{\partial t},$$

$$\operatorname{curl}\mathbf{E}(\mathbf{r},t) = -\frac{\partial \mathbf{B}(\mathbf{r},t)}{\partial t},$$

$$\operatorname{div}\mathbf{D}(\mathbf{r},t) = \rho(\mathbf{r},t),$$

$$\operatorname{div}\mathbf{B}(\mathbf{r},t) = 0. \tag{2.1}$$

In these equations, $\mathbf{E}$ and $\mathbf{H}$ are the vectorial electric and magnetic fields, $\mathbf{D}$ is the dielectric displacement, $\mathbf{B}$ the magnetic flux density, and $\mathbf{J}$ and ρ are the electric current and charge densities, respectively. In general, each quantity is a function of time t and space, described by the position vector $\mathbf{r} = (x, y, z)^{\mathrm{T}}$. In optics, we assume the absence of currents $(\mathbf{J} = 0)$ and free carriers $(\rho = 0)$, as well as non-magnetic materials $(\mu_{\mathrm{r}} = 1)$. The constitutive relations can be written with the help of the electric vacuum permittivity ε_0, the magnetic vacuum permeability μ_0 and the electric polarization $\mathbf{P}$ as

$$\mathbf{B}(\mathbf{r},t) = \mu_0 \mathbf{H}(\mathbf{r},t),$$

$$\mathbf{D}(\mathbf{r},t) = \epsilon_0 \mathbf{E}(\mathbf{r},t) + \mathbf{P}(\mathbf{r},t). \tag{2.2}$$

For now, we assume a linear, time-invariant system and time-harmonic solutions of the form $\mathbf{E}(\mathbf{r},t) = \underline{\mathbf{E}}(\omega,\mathbf{r})\exp(\mathrm{j}\omega t)$ and $\mathbf{H}(\mathbf{r},t) = \underline{\mathbf{H}}(\omega,\mathbf{r})\exp(\mathrm{j}\omega t)$ with complex vectorial electric and magnetic fields $\underline{\mathbf{E}}(\omega,\mathbf{r})$ and $\underline{\mathbf{H}}(\omega,\mathbf{r})$, where $\omega = 2\pi f$ is the angular frequency. We can then reformulate Eqs. (2.2) to

$$\underline{\mathbf{B}}(\mathbf{r},\omega) = \mu_0 \underline{\mathbf{H}}(\mathbf{r},\omega),$$

$$\underline{\mathbf{D}}(\mathbf{r},\omega) = \epsilon_0 \underline{\epsilon}_r(\mathbf{r},\omega)\underline{\mathbf{E}}(\mathbf{r},\omega). \tag{2.3}$$

Here, $\underline{\epsilon}_r(\mathbf{r},\omega)$ is the complex relative dielectric constant, which is linked to the complex refractive index $\underline{n}(\mathbf{r},\omega)$ via $\underline{n}^2(\mathbf{r},\omega) = \underline{\epsilon}_r(\mathbf{r},\omega)$. In isotropic, spatially homogeneous $(\nabla \underline{\epsilon}_{\mathrm{r}}(\mathbf{r},\omega) = 0)$ and lossless materials $(\underline{n} = n)$, Maxwell's equations can be written as

$$\text{curl}\,\underline{\mathbf{H}}(\mathbf{r},\omega) = j\omega\epsilon_0 n^2(\omega)\underline{\mathbf{E}}(\mathbf{r},\omega),$$
$$\text{curl}\,\underline{\mathbf{E}}(\mathbf{r},\omega) = -j\omega\mu_0\underline{\mathbf{H}}(\mathbf{r},\omega),$$
$$\text{div}\,\underline{\mathbf{E}}(\mathbf{r},\omega) = 0,$$
$$\text{div}\,\underline{\mathbf{H}}(\mathbf{r},\omega) = 0. \tag{2.4}$$

By taking the curl of the first two lines in Eq. (2.4), and with the help of the identity $\text{curl}\,\text{curl}\,\mathbf{X} = \text{grad}\,\text{div}\,\mathbf{X} - \text{div}\,\text{grad}\,\mathbf{X}$, the second-order linear partial differential wave equations can be derived. Using the vacuum propagation constant $k_0 = \omega/c$ where $c = 1/\sqrt{\epsilon_0\mu_0}$ is the speed of light, and with the scalar propagation constant $\beta(\omega) = k_0 n(\omega)$, the so-called Helmholtz Equations for the electric and magnetic fields can be written as

$$\text{div}\,\text{grad}\,\underline{\mathbf{E}}(\mathbf{r},\omega) + \beta^2(\omega)\underline{\mathbf{E}}(\mathbf{r},\omega) = 0,$$
$$\text{div}\,\text{grad}\,\underline{\mathbf{H}}(\mathbf{r},\omega) + \beta^2(\omega)\underline{\mathbf{H}}(\mathbf{r},\omega) = 0. \tag{2.5}$$

The general solutions to the Helmholtz Equations in (2.5) can be written as

$$\underline{\mathbf{E}}(\mathbf{r},\omega) = \underline{\mathbf{E}}_0(\mathbf{r},\omega)\exp(-j\boldsymbol{\beta}(\omega)\cdot\mathbf{r}),$$
$$\underline{\mathbf{H}}(\mathbf{r},\omega) = \underline{\mathbf{H}}_0(\mathbf{r},\omega)\exp(-j\boldsymbol{\beta}(\omega)\cdot\mathbf{r}). \tag{2.6}$$

Here, $\underline{\mathbf{E}}_0(\mathbf{r},\omega)$ and $\underline{\mathbf{H}}_0(\mathbf{r},\omega)$ are the electric and magnetic amplitudes of the fields at the angular frequency ω. The vectorial propagation constant $\boldsymbol{\beta}(\omega) = \beta(\omega)\hat{\mathbf{e}}$ points into the propagation direction of the wave, which is given by the unit vector $\hat{\mathbf{e}}$, see Fig. 2.1 for $\mathbf{e}_z = (0,0,1)^T$. Since $\text{div}\,\underline{\mathbf{E}}(\mathbf{r},\omega) = 0$ and $\text{div}\,\underline{\mathbf{H}}(\mathbf{r},\omega) = 0$, the direction of propagation defined by $\boldsymbol{\beta}(\omega)$ is perpendicular to the electric and magnetic field vectors $\underline{\mathbf{E}}_0(\mathbf{r},\omega)$ and $\underline{\mathbf{H}}_0(\mathbf{r},\omega)$. Solutions of this form are called plane waves, as the wavefronts are planes that are perpendicular to the direction of propagation.
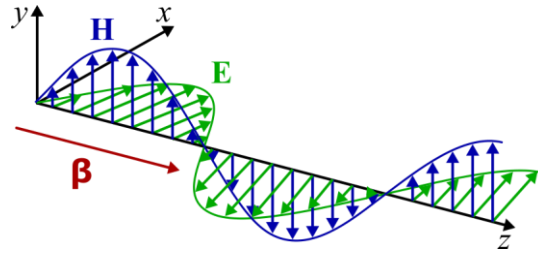
Fig. 2.1. Propagation of a plane electro-magnetic wave in an isotropic, homogeneous optical medium. The direction of propagation, here in z-direction, is dictated by the propagation vector **β**, and is perpendicular to the electric-field vector **E** as well as to the magnetic-field vector **H**. The vectors **E**, **H,** and **β** form a right-handed system.

Note that the time-averaged energy flow follows the same direction as $\boldsymbol{\beta}$, and can be calculated by taking the real part of the complex Poynting vector

$$\mathrm{Re}\big(\underline{\mathbf{S}}(\mathbf{r},\omega)\big) = \mathrm{Re}\left(\frac{1}{2}\big(\underline{\mathbf{E}}(\mathbf{r},\omega)\times\underline{\mathbf{H}}^{*}(\mathbf{r},\omega)\big)\right). \tag{2.7}$$

Lossy optical media can be approximated by a complex effective refractive index $\underline{n} = n - \mathrm{j}\kappa$. The real part of $\underline{n}$ corresponds to the regular refractive index n of the material. The negative imaginary part is the extinction coefficient $\kappa = \alpha/(2k_0)$, which is linked to the material loss coefficient α via the vacuum propagation constant k_0. The resulting non-zero imaginary part of the complex propagation constant $\underline{\beta} = \beta - \mathrm{j}\alpha/2$ leads to a decay term in the electro-magnetic fields and the optical power consequently decays exponentially with $P \propto \exp(-\alpha\,\hat{\mathbf{e}}\cdot\mathbf{r})$.

2.1.2 Waveguide modes

As opposed to free-space optics, integrated photonic waveguides are designed to confine the electro-magnetic waves within a certain waveguide cross section in order to couple, route, and read-out the optical signal in a defined space on a photonic integrated circuit (PIC). From a ray-optic perspective, the confinement of the electro-magnetic waves in the waveguide core is achieved by exploiting the effect of total internal reflection in an arrangement of materials with different refractive indices, just as in optical fibers. The simplest version is a so-called slab waveguide, which consists of stacks of thin layers of different materials,

(a) Material stack   (b) Total internal reflection   (c) Mode profiles
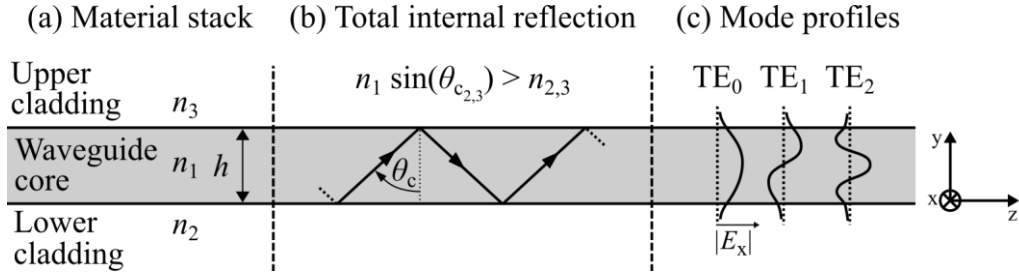
Fig. 2.2. Mode propagation in a slab waveguide.   **(a)** The material stack of a slab waveguide consists of a waveguide core with refractive index n_1 and height h, as well as a lower and an upper cladding with refractive indices n_2 and n_3, respectively. The refractive index profile is constant along the x- and z-direction.   **(b)** Due to the differences in refractive indices, total internal reflection occurs for rays in the waveguide core hitting the cladding interfaces at angles larger than the critical angle θ_c. The light is hence confined primarily to the waveguide core and effectively travels in z-direction.   **(c)** Depending on the angular frequency ω and the refractive index profile $n(\mathbf{r},\omega)$, a discrete number of guided eigenmodes can propagate in the waveguide. Shown here is the magnitude of the electric field component $|\underline{E}_x|$ of the first three transverse electric (TE) modes. Each guided mode comprises an evanescent portion within the waveguide cladding in the vicinity of the cladding interfaces.   The x- and y-directions are parallel and perpendicular to the substrate of the integrated photonic waveguide, respectively, and form a right-handed co-ordinate system.

effectively creating a lower and an upper cladding around the central waveguide core. Fig. 2.2(a) depicts such a slab waveguide with a refractive-index profile $n(\mathbf{r})$, which is uniform in x- and z-direction. Rays in the waveguide core hitting the cladding interfaces at angles larger than the critical angle $\theta_{c_{2,3}} = \arcsin\left(n_{2,3}/n_1\right)$ of total internal reflection will be confined to the core and hence effectively travel along the z-direction, see Fig. 2.2(b).

In contrast to the ideal optical media described in Eq. (2.4), Line 2, photonic waveguides are hence not spatially homogeneous, but are rather characterized by a distinct complex refractive index profile $\underline{n}(\mathbf{r},\omega)$. The two coupled differential Maxwell equations from Eq. (2.4) and the associated wave equations from Eq. (2.5) can hence be reformulated as

$$\operatorname{curl}\underline{\mathbf{H}}(\mathbf{r},\omega) = \mathrm{j}\omega\epsilon_0\underline{n}^2(\mathbf{r},\omega)\underline{\mathbf{E}}(\mathbf{r},\omega),$$
$$\operatorname{curl}\underline{\mathbf{E}}(\mathbf{r},\omega) = -\mathrm{j}\omega\mu_0\underline{\mathbf{H}}(\mathbf{r},\omega),$$

$$(2.8)$$

$$\left(\frac{1}{\underline{n}^2(\mathbf{r},\omega)}\operatorname{curl}\operatorname{curl}\right)\underline{\mathbf{E}}(\mathbf{r},\omega)=k_0^2\,\underline{\mathbf{E}}(\mathbf{r},\omega),$$

$$\left(\operatorname{curl}\frac{1}{\underline{n}^2(\mathbf{r},\omega)}\operatorname{curl}\right)\underline{\mathbf{H}}(\mathbf{r},\omega)=k_0^2\,\underline{\mathbf{H}}(\mathbf{r},\omega).$$

(2.9)

For integrated photonic waveguides with a refractive index profile $\underline{n}(\mathbf{r},\omega)$ that is invariant or periodic in z-direction, the wave equations (2.9), together with boundary conditions, define eigenvalue problems. We are looking for solutions where the eigenfunctions $\underline{\mathbf{E}}(\mathbf{r},\omega)$ and $\underline{\mathbf{H}}(\mathbf{r},\omega)$ exhibit modal field profiles that are confined in x- and y-direction, and where the propagation in z-direction is defined by the corresponding eigenvalue $\underline{\beta}(\omega)$. In standard slab, strip, or slot waveguides, the refractive index profile is invariant in z-direction. The associated modal field profiles $\underline{\mathbf{E}}_0(x,y,\omega)$ and $\underline{\mathbf{H}}_0(x,y,\omega)$ remain constant up to a phase shift. The eigenfunctions for a propagation in z-direction are hence of the form

$$\underline{\mathbf{E}}(\mathbf{r},\omega)=\underline{\mathbf{E}}_0(x,y,\omega)\exp\left(-\mathrm{j}\underline{\beta}(\omega)z\right),$$

$$\underline{\mathbf{H}}(\mathbf{r},\omega)=\underline{\mathbf{H}}_0(x,y,\omega)\exp\left(-\mathrm{j}\underline{\beta}(\omega)z\right).$$

(2.10)

Depending on the angular frequency ω and the refractive index profile $n(\mathbf{r},\omega)$ of the waveguide, a discrete number of guided modes can propagate in the waveguide. For typical planar waveguides on a PIC, these guided modes can be classified in two mode families:

Quasi-TE modes: (Quasi) transverse *electric* polarized, where the dominant component of the *electric* field is oriented parallel to the substrate (strong E_x and H_y, weak E_y and H_x, minor E_z and H_z); or

Quasi-TM modes (Quasi) transverse *magnetic* polarized, where the dominant component of the *magnetic* field is oriented parallel to the substrate (strong H_x and E_y, weak H_y and E_x, minor E_z and H_z).

Fig. 2.2(c) shows the magnitude of the E_x component of the first three TE modes throughout the slab waveguide. Each guided mode comprises an evanescent portion within the waveguide cladding, which decays exponentially for $|y|\to\infty$.

2.1.3 Modal effective refractive index, loss, and thermo-optic coefficient

For waveguides with core dimensions of the order of the wavelength in the core material, a non-negligible portion of the modal electric and magnetic fields of a guided mode is located outside of the waveguide core in the nearby cladding regions. This field portion is evanescent along y and x, i.e., it decays decay exponentially with increasing distance from the waveguide core. The share of the evanescent field within the total modal field increases with smaller waveguide core dimensions, and depends on the waveguide core and cladding refractive indices. The complex propagation factor $\underline{\beta}$ of such a waveguide mode is hence not only affected by the material properties of the waveguide core, but also by the material properties of the surrounding cladding regions. In contrast to plane waves in homogeneous media with a complex bulk refractive index $\underline{n}$ of a homogeneous material, a waveguide mode has a complex *effective* refractive index

$$\underline{n}_{e} = \underline{\beta}/k_0 = n_e - \mathrm{j}\kappa_e. \tag{2.11}$$

Here, the effective refractive index n_e and the effective extinction coefficient κ_e are determined by the material properties and the modal field distribution in the waveguide core as well as in the cladding regions. From now on, the effective loss originating from κ_e is denoted as the modal loss α, where the subscript "$_e$" is omitted. Furthermore, a guided mode exhibits a thermo-optic coefficient $\mathrm{TOC} = \mathrm{d}n/\mathrm{d}T$, which describes the dependency of the material refractive index n on temperature T, which is a function of both the core and cladding material properties. It is important to note that all three effective modal characteristics, n_e, α and TOC, differ for different modes in the same physical waveguide, which makes the selection of the right mode and polarization essential for designing an efficient sensor circuit.
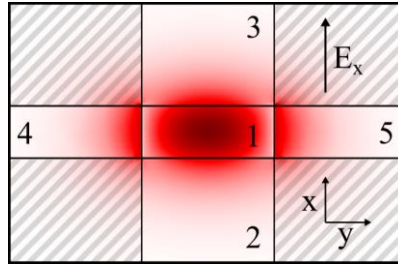
Fig. 2.3. Effective refractive index determination with Marcatili's method. The rectangular strip waveguide is sliced into five regions of interest, where the majority of the modal field is concentrated. The modal propagation is calculated based on the wavenumber k_1 in the core region (1), as well as the wavenumbers of two slab modes defined by infinitely extended refractive index profiles of the cross-sections 2-1-3 and 4-1-5, respectively.

The quantitative calculation of the effective refractive index of a waveguide mode is non-trivial. In rectangular strip waveguides, it can be approximated, e.g., by using Marcatili's method [1], see Fig. 2.3. Here, Maxwell's equations are solved serially, starting in the waveguide core (1) to obtain the wavenumber k_1, followed by solving them for two infinitely extended slab waveguides based on the refractive index profiles in x- and y-direction at the cross-sections (2-1-3), yielding $k_{2\text{-}1\text{-}3}$ and (4-1-5), yielding $k_{4\text{-}1\text{-}5}$. The modal fields in the hatched corner regions are ignored. The effective refractive index $n_e \approx \beta_M / k_0$ of the overall waveguide can then be calculated via Marcatili's approximation of the modal propagation constant as $\beta_M^2 = k_1^2 - k_{2\text{-}1\text{-}3}^2 - k_{4\text{-}1\text{-}5}^2$.

In practice, modern computer-based mode solvers such as Lumerical MODE [2] are used to calculate the effective refractive index of a waveguide mode far more accurately. As an example, Fig. 2.4 shows the calculated magnitude $|\underline{\mathbf{E}}|^2$ of the complex electric mode fields of the fundamental TE_0 and TM_0 modes of a rectangular strip waveguide. Typical sensing waveguide parameters were chosen, i.e., a wavelength of $\lambda = 1550$ nm, a width $w = 450$ nm, a height $h = 220$ nm, and a material stack consisting of a silicon (Si, $n_{Si} = 3.48$) waveguide core, supported by a silicon dioxide (SiO$_2$, $n_{SiO2} = 1.44$) buried oxide (BOX) bottom cladding, and a water (H$_2$O, $n_{H2O} = 1.31$) top cladding. It can be seen that for the TE_0 mode, a large portion of the field propagates inside the waveguide core, which has a much larger refractive index than the cladding. The field of the TM_0 mode extends further into the cladding, and the effective refractive index is hence influenced more by the refractive index of the cladding
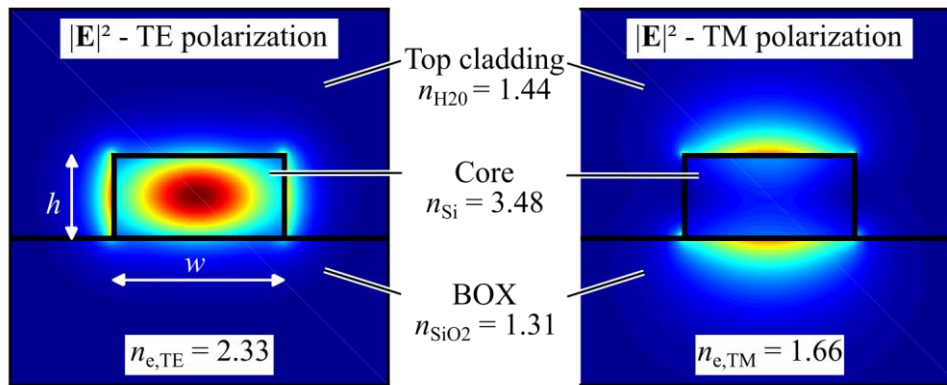
Fig. 2.4. Effective-refractive-index determination via numerical simulations. A typical rectangular silicon strip waveguide with dimensions $w \times h = 450 \times 220$ nm², featuring a buried silicon oxide (BOX) as the bottom cladding, and water as the top cladding. The fundamental modes in TE and TM polarization differ heavily in their electric field distributions $|\mathbf{E}|^2$, and consequently in their modal effective refractive index, as shown by these calculations from Lumerical MODE.
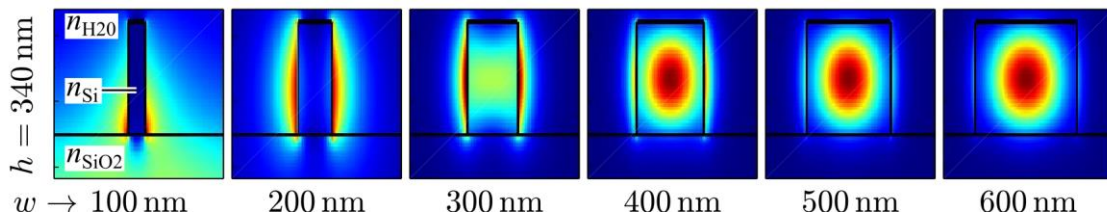
Fig. 2.5. Field distribution of a silicon strip waveguide for various widths. As an example, the fundamental quasi-TE mode is shown for a bottom SiO_2 cladding and a H_2O top cladding. Due to the asymmetric cladding refractive index, the fields get pushed into the lower cladding for ultra-narrow waveguides. The wider the waveguide, the more the fields are confined to the waveguide core.

materials. As a consequence $n_{e,TE} > n_{e,TM}$, which can be explained by a mix of the flat waveguide shape as well as the effect of field enhancement. For the TE polarization, an enhancement of the electric field E_x exists at the WG sidewalls because the normal component $D_x = \varepsilon_0 n^2(x) E_x(x)$ of the displacement must be continuous, while for TM polarization this field enhancement is to be seen at the top and at the bottom WG surfaces.

The impact of the waveguide dimensions on the modal fields is visualized in Fig. 2.5. For the same materials as in Fig. 2.4, the field distributions $|\mathbf{E}|^2$ for a waveguide height of 340 nm and for various waveguide widths w from 100…600 nm are plotted. It can be seen that for wide waveguide cores with

$w > 400$ nm, the TE$_0$ mode is strongly confined to the core. Narrower waveguide cores provide only weak guiding. If the core is too narrow, the mode cannot be guided. Higher-order modes can also be used for sensing applications, but the corresponding minimum waveguide dimensions and bend radii are larger, which reduces the achievable PIC density.

The field distribution of a waveguide mode is not only affected by the waveguide geometry as visualized in Fig. 2.5, but also by the frequency, see Appendix A.4 for details. As a consequence, the frequency-dependent refractive indices of the different materials are all incorporated in the dispersion relation $\underline{\beta}(\omega)$. The dispersion relation can be linearly approximated by expanding $\underline{\beta}(\omega)$ in a Taylor series around the central frequency of a narrow-band optical spectrum and taking only the first two terms. For homogeneous materials and for waveguide modes, the group refractive index n_g and the effective group refractive index n_{eg} can then by written as

$$
\begin{aligned}
n_g(\omega) &= \frac{c}{v_g} = n(\omega) + \omega \frac{\partial n(\omega)}{\partial \omega}, \\
n_{eg}(\omega) &= \frac{c}{v_{eg}} = n_e(\omega) + \omega \frac{\partial n_e(\omega)}{\partial \omega}.
\end{aligned}
\tag{2.12}
$$

These group refractive indices represent the ratio of the speed of light c and the (effective) group velocity $v_{(e)g}$, which describes the envelope velocity of a pulse propagating in the dispersive material (waveguide). The effective group refractive index n_{eg} of a waveguide mode is used to calculate spectral properties of photonic circuits such as the free spectral range of a resonator or an interferometer.

Fig. 2.6 depicts the important effective modal characteristics n_e, n_{eg}, a_{dB}/L and TOC, exemplarily for a silicon strip waveguide on a silicon dioxide BOX, operated at a wavelength of 1550 nm. Several common waveguide geometries are shown, each for the fundamental TE$_0$ as well as TM$_0$ mode. In a typical sensing application, a waveguide with a virtually lossless silicon dioxide top cladding is used for routing, while the oxide is removed in the sensor area and the sensor waveguide is exposed to a lossy water top cladding.

In Fig. 2.6(a), it can be seen that wider and higher waveguides have a larger field portion in the high-index waveguide core and hence a larger effective refractive index n_e. Moreover, modes in ultra-narrow waveguides are only weakly guided in the core, and the associated n_e approaches the bulk n of the respective cladding material. For sensor waveguides that aim at a large field overlap with the top cladding, different waveguide core aspect ratios are beneficial for the fundamental quasi-TM and quasi-TE modes.

In Fig. 2.6(b), the effective group refractive index n_{eg} is shown, which is affected both by waveguide dispersion as well as by material dispersion of the core and cladding materials. In Fig. 2.6(c), the modal power loss α of different waveguides is shown. Note that based on the modal power loss α, given in [1/m], we can calculate the field attenuation a^{dB} and hence the power attenuation $(a^2)^{dB}$ in decibels and its relation to the modal loss α as

$$\left(a^2\right)^{dB} = 10\log_{10}\exp\left(-\alpha L\right)$$

$$\left(a^2\right)^{dB}\Big/L = \alpha\,10\log_{10}\left(e\right) \approx 4.34\alpha$$

(2.13)

It can be seen that the absorption in bulk Si and SiO_2 at 1550 nm is close to zero. However, the effective modal loss of the fundamental TE and TM modes in a waveguide with a H_2O top cladding with $\alpha_{H_2O} \approx 990\,\mathrm{m}^{-1}$ can be substantial, and peaks at widths where a large portion of the mode field is located in the aqueous top cladding.

Furthermore, Fig. 2.6(d) shows that the TOC of the silicon waveguides with a SiO_2/H_2O cladding are rather similar. For the displayed waveguide modes, the lines are mostly overlaying and the difference is $\lesssim 10^{-5}\,\mathrm{K}^{-1}$. Athermal waveguides (or interferometers) can be designed by selecting a geometry where the effective TOC (and/or TOC difference in an interferometer) is zero.
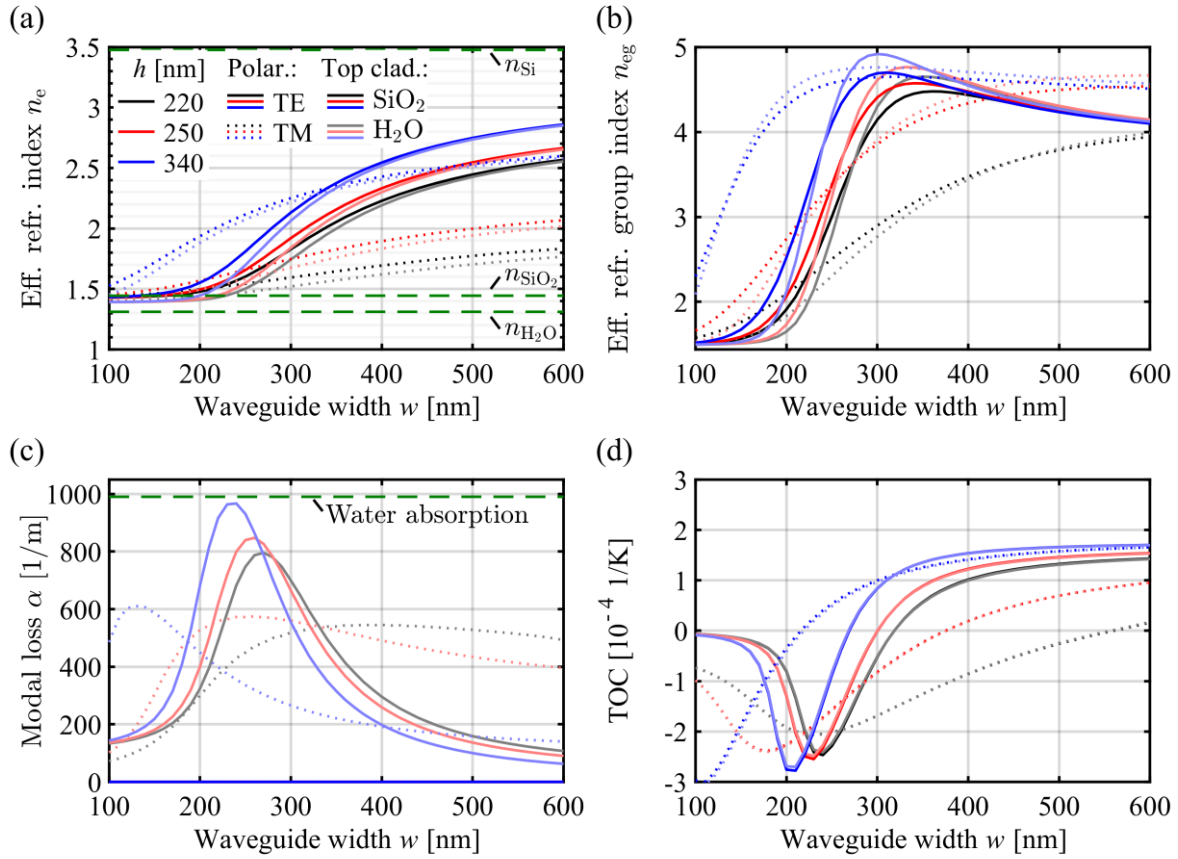
Fig. 2.6. Effective modal characteristics of a waveguide mode. Examples for a silicon strip waveguide on a silicon dioxide BOX operated at $\lambda = 1550$ nm, see Fig. 2.4. A silicon dioxide top cladding (SiO$_2$, non-transparent lines) is used for routing waveguides, whereas an aqueous top cladding (H$_2$O, semi-transparent lines) can be used in sensing sections. Results are plotted for the fundamental TE$_0$ (solid lines) and TM$_0$ (dotted lines) modes. **(a)** Effective refractive index n_e. Wider and higher waveguides have a larger field portion in the high-index waveguide core and hence a larger n_e. Modes in narrower waveguides are only weakly guided in the core, and the associated n_e approaches the bulk n of the respective cladding materials. The fundamental TM$_0$ and TE$_0$ modes benefit from different aspect ratios of the waveguide when it comes to maximizing the field overlap with the top cladding for sensing applications. **(b)** Effective group refractive index n_{eg}, affected by both waveguide dispersion as well as material dispersion of the core and cladding materials. **(c)** Modal loss α. Absorption in bulk Si and SiO$_2$ at 1550 nm is close to zero. However, the modal loss with an H$_2$O top cladding can be substantial and peaks at widths where a large portion of the mode field is found in the top cladding. **(d)** Thermo-optic coefficient TOC. The TOC of the waveguides with a SiO$_2$/H$_2$O cladding is similar, the plotted lines overlap for most of the displayed widths. Athermal waveguides can be designed by choosing a geometry where the effective TOC is zero. In an interferometer, the TOC of the sensor and reference arm can be matched to get a temperature-independent phase difference.

2.1.4 Bloch modes in periodic waveguides

Waveguides for sensing applications can benefit from structures with refractive index profiles that are not constant in the direction of propagation. A prominent example of such a waveguide is based on a sub-wavelength grating (SWG, [3,4,5,6,7,8]). Such a waveguide exhibits a periodic dielectric structure along the direction of propagating with period $\mathbf{a}$, i.e., $\epsilon_r(\mathbf{r}) = \epsilon_r(\mathbf{r}+\mathbf{a})$ and hence a periodic refractive index $n(\mathbf{r}) = n(\mathbf{r}+\mathbf{a})$, which is inserted into the wave equations (2.9). According to Bloch's theorem, the corresponding eigenfunctions $\underline{\mathbf{E}}(\mathbf{r},\omega)$ and $\underline{\mathbf{H}}(\mathbf{r},\omega)$ of such a structure exhibit a periodic part $\mathbf{u}(\mathbf{r},\omega)$ with underlying waveguide period $\mathbf{a}$ and can be written as

$$
\begin{aligned}
\underline{\mathbf{E}}(\mathbf{r},\omega) &= \mathbf{u}(\mathbf{r},\omega)\exp\left(-j\boldsymbol{\beta}_B(\omega)\cdot\mathbf{r}\right), \\
\underline{\mathbf{H}}(\mathbf{r},\omega) &= \mathbf{u}(\mathbf{r},\omega)\exp\left(-j\boldsymbol{\beta}_B(\omega)\cdot\mathbf{r}\right), \\
\mathbf{u}(\mathbf{r},\omega) &= \mathbf{u}(\mathbf{r}+\mathbf{a},\omega).
\end{aligned}
\tag{2.14}
$$

These eigenmodes of the periodic waveguide are called Bloch modes and exhibit a distinct Bloch propagation vector $\boldsymbol{\beta}_B(\omega)$ and an associated Bloch effective refractive index $n_{e,B}(\omega)$, which in combination with the period length $|\mathbf{a}|$ defines the operating mode of the waveguide. Periods that are much larger than the Bragg wavelength, i.e., $|\mathbf{a}| \gg \lambda/(2n_{e,B})$, will lead to a diffraction of light out of the waveguide, which is exploited, e.g., via diffraction grating couplers that are used to couple the light out of a photonic integrated circuit. For smaller periods around the Bragg wavelength, the waveguides act as Bragg gratings and hence reflect the light, which is used, e.g., in distributed Bragg reflectors. For periods even smaller than the Bragg wavelength, the waveguides are operated in the sub-wavelength regime. Here, the mode can propagate through the waveguide without diffraction and reflection. The period can then be used as an additional geometric parameter, e.g., to tailor the field distribution for specific sensing properties, which is analyzed in detail in Chapter 3.

2.2 Waveguide-based sensing

In Section 2.1, the fundamental properties of waveguide modes and important modal characteristics have been introduced. This section describes how a waveguide can be used as the core element of an integrated photonic sensor.

2.2.1 Principle of effective refractive index sensing

Equations (2.10) and (2.11) show that mode propagation in a waveguide is dictated by the (complex) propagation constant $\underline{\beta}$. Consequently, at a fixed angular frequency ω, any changes in the (complex) effective refractive index $\underline{n}_e = n_e - j\kappa_e$ and hence changes of either the effective refractive index n_e or the effective extinction coefficient κ_e will alter the mode propagation. As an example, the refractive index n of the waveguide core or cladding materials can change with stress or temperature. Furthermore, changes to the waveguide geometry, e.g., in the case of suspended, movable waveguides [9], will affect the field distribution and hence the effective refractive index n_e. One of the most common sensing applications with integrated photonic waveguides, however, leaves the waveguide core geometry as well as the waveguide and BOX materials unchanged, and instead relies on a changeable top cladding. A change in the top cladding modifies the effective modal characteristics n_e or κ_e due to the interaction with the evanescent portion of the guided mode fields. Such a changeable cladding can be realized, e.g., by exposing the waveguide core to an aqueous solution with a variable refractive index, or by supplying molecules in the solution that can adsorb to a functionalized surface on the waveguide core, as shown in Section 2.2.2 and discussed in detail in the analysis presented in Chapter 3.

The remainder of this work focuses on sensing applications, where changes in the effective refractive index n_e dominate over changes in the extinction coefficient κ_e. Sensors focusing on a variable loss such as absorption spectroscopy can also be realized in integrated waveguides, but will not be addressed in this work.

2.2.2 Evanescent-field homogeneous and surface sensing

A simple waveguide-based sensing application employs fully-cladded wave-guides with a stress or temperature-dependent effective refractive index. Beyond that, deliberately exposing a part of the waveguide to the environment enables a variety of additional attractive sensing applications that can probe the optical properties or contents of different media such as liquids or gases. These sensing variants make explicit use of the evanescent field of a waveguide mode and can be classified as either homogeneous sensing or surface sensing.

In the **homogeneous sensing** case, a plain waveguide core on a BOX is exposed to a homogeneous medium as the top cladding, see Fig. 2.7(a). Note that the waveguide core in a sensor waveguide can also be realized as a suspended waveguide to further increase the overlap of the evanescent field with the target medium. However, for simplicity, this work will always assume a waveguide core supported by a BOX. If the waveguide geometries are chosen such that a substantial portion of the evanescent field extends into the top cladding, changes Δn_M in the refractive index of the homogeneous medium will lead to a change
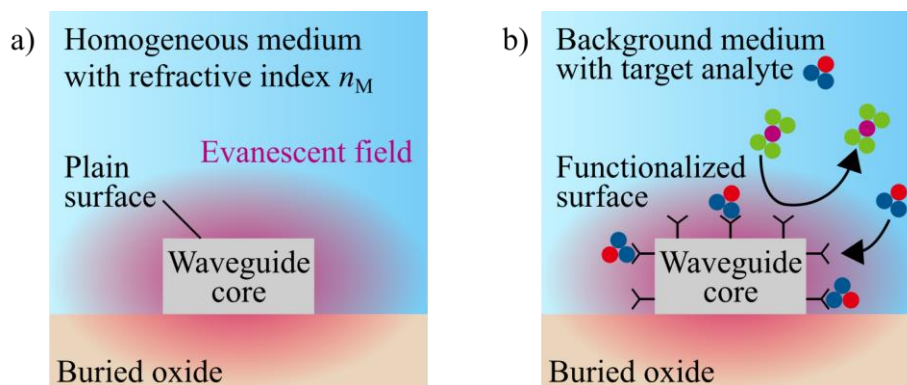
Fig. 2.7. Homogeneous sensing and surface sensing. **a)** For homogeneous sensing, the plain waveguide core is exposed to a homogeneous medium of refractive index n_M. Through the evanescent field of the waveguide mode, changes Δn_M in the refractive index of the homogeneous medium affect n_e. **b)** Surface sensing relies on target molecules that that are provided by a background medium and that are adsorbed on the waveguide core surface. By functionalizing the waveguide core surface with dedicated capture agents, the sensing process can be restricted to specific target analytes.

Δn_e of the effective refractive index of the waveguide mode accordingly. Homogeneous sensing is usually unspecific, i.e., the change cannot be traced back to a specific substance in the medium.

In the **surface sensing** case, the target analyte is not the homogeneous medium as such, but rather target molecules that are contained in the homogeneous medium, see Fig. 2.7(b). In this case, the waveguide core surface can be functionalized with dedicated binding agents such that only specific molecules of interest can attach. Again, if the waveguide geometry is chosen accordingly, the field overlap with the surface layer leads to a substantial change Δn_e if enough molecules adsorb on the surface.

Waveguides on PIC are usually passivated, to avoid environmental impact, typically via an all-around oxide cladding. Homogeneous and surface sensing hence typically requires dedicated sensitive waveguide regions, where the oxide cladding is locally removed. Any change Δn_e within such a sensitive waveguide region of length L will introduce an accumulated phase offset $\Delta\varphi = -k_0 L \Delta n_e$ to the propagating mode, see Fig. 2.8.
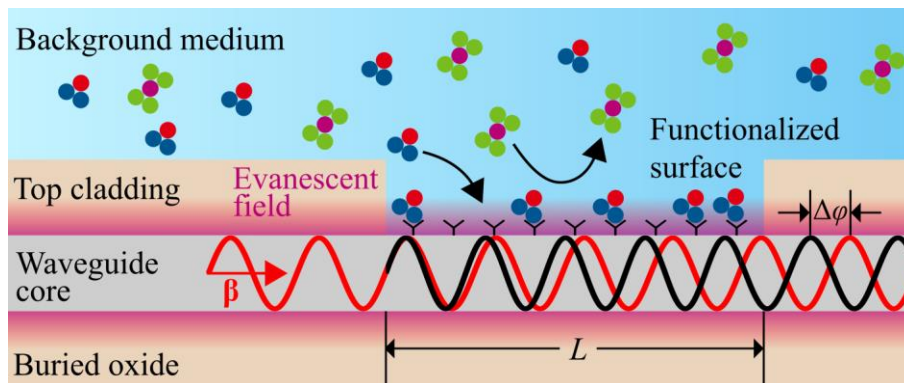
Fig. 2.8. Principle of waveguide-based refractive index sensing via the evanescent field. In a sensitive waveguide region, the passivating top cladding is removed to expose the waveguide core to the analyte. In the case of surface sensing, the waveguide core surface is functionalized such that specific molecules can be adsorbed. The target molecules are delivered by a background medium such as an aqueous solution. The evanescent field of the waveguide mode overlaps with the molecular layer on the core surface, thereby changing the modal effective refractive index. After a length L, this leads to an accumulated phase offset $\Delta\varphi = -k_0 \Delta n_e L$ that depends on the modal field overlap with as well as on the refractive index and thickness of the adsorbed molecular layer.

2.3   Sensor system overview

This section provides a system-level overview of integrated photonic sensors. To make use of sensor waveguides as introduced in Section 2.2, phase-sensitive photonic circuits such as resonators or interferometers are required that translate a phase shift into a measurable change of the optical output power, see Section 2.3.1. A fully integrated photonic sensor system comprises additional core components, which are discussed in Section 2.3.2 together with technological challenges associated with their implementation. Section 2.3.3 concludes the fundamentals section by discussing possible sensor operation and readout concepts based on different combinations of light sources, sensor circuits and photodetectors.

2.3.1   Phase-sensitive photonic circuits

Waveguide-based sensing via the effective refractive index n_e is not possible with a standalone waveguide connected to a light source and a photodetector, as the phase change $\Delta\varphi = -k_0 L \Delta n_\mathrm{e}$ caused by a change Δn_e of the modal effective refractive index cannot be measured directly. Instead, a phase-sensitive photonic circuit is required that translates $\Delta\varphi$ into measurable changes ΔP_o of the optical output power. The most prominent phase-sensitive circuits in integrated photonic sensor systems can be classified as resonators and interferometers. Two generic examples of these classes are depicted in Fig. 2.9, namely ring resonators (RR [10]) and Mach-Zehnder interferometers (MZI [11]).

In both examples, a laser provides an optical signal with frequency $k_0 = \omega/c$ and power P_i. For the resonator in Fig. 2.9(a), this signal is coupled into a waveguide resonator with a circumference L and a variable effective refractive index $n_\mathrm{e} + \Delta n_\mathrm{e}$. For the interferometer in Fig. 2.9(b), the signal is split by a multi-mode interference (MMI) coupler into a reference arm and a sensor arm. The two waveguide arms can exhibit an initial length offset ΔL, as well as an effective refractive index offset $\Delta n_{\mathrm{e},0}$, caused for example by different cladding materials. The sensor arm contains the targeted measurement quantity Δn_e. The two signals are combined in a second MMI, where they superimpose, such that an additional change Δn_e in the sensor arm leads to a measurable change of the output

power P_o. The (idealized) optical power transmissions $T = P_o/P_i$ are plotted within $[-\pi, \pi]$ of the respective operating points $\varphi_{OP,RR}$ and $\varphi_{OP,MZI}$.

For a ring resonator (RR) with a high quality factor Q, the transmission $T(\varphi_{RR})$ shows a Lorentzian resonance with depth $\hat{T}$ and full-width at half-maximum $\Delta\varphi_{FWHM,RR}$, while for a single-output Mach-Zehnder interferometer (MZI), the transmission $T(\varphi_{MZI})$ is sinusoidal with amplitude $\hat{T}/2$, i.e.,

$$
\left.
\begin{aligned}
T(\varphi_{RR}) &= 1 - \hat{T} \Big/ \left(1 + \left(2\varphi_{RR}/\Delta\varphi_{FWHM,RR}\right)^2\right), \\
\varphi_{RR} &= -k_0 L \Delta n_e + \varphi_{OP,RR}, \\
\varphi_{OP,RR} &= -k_0 L n_e,
\end{aligned}
\right\} \text{RR}
$$

$$
\left.
\begin{aligned}
T(\varphi_{MZI}) &= \hat{T}/2 \times \left(1 + \cos(\varphi_{MZI})\right), \\
\varphi_{MZI} &= -k_0 L \Delta n_e + \varphi_{OP,MZI}, \\
\varphi_{OP,MZI} &= -k_0 \left(L \Delta n_{e,0} - \Delta L n_e\right).
\end{aligned}
\right\} \text{MZI}
\tag{2.15}
$$
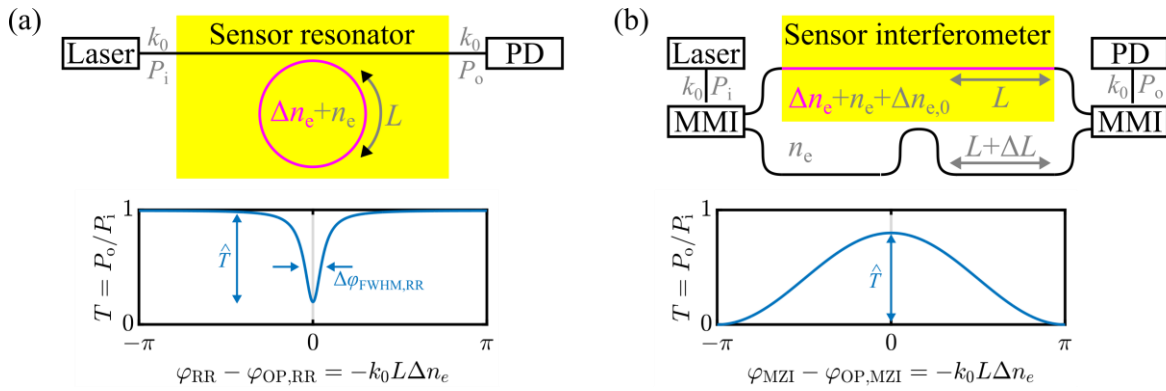
Fig. 2.9. Phase-sensitive photonic circuits. The most prominent phase-sensitive circuits in integrated photonic sensor systems can be classified into resonators and interferometers, which are drawn schematically including idealized optical transfer functions. **(a)** For ring resonators, light is coupled from a bus waveguide into a resonator waveguide with, which is subject to a refractive index change Δn_e that is to be detected. For high quality factors, the optical transmission $T(\varphi_{RR})$ exhibits a sharp Lorentzian resonance. By proper choice of the wavelength, the sensor operating point $\varphi_{OP,RR}$ can be adjusted to the vicinity of the resonance. **(b)** In Mach-Zehnder interferometers, the light is split into a reference arm and a sensor arm with variable Δn_e. After signal combination via interference, the optical transmission $T(\varphi_{MZI})$ follows a sinusoidal shape. Splitting and combining of light is accomplished by multi-mode interference (MMI) couplers.

Note that the operating point $\varphi_{\text{OP,MZI}}$ of the interferometer can be set to zero by matching the optical path lengths via $L\Delta n_{\text{e},0} = \Delta L n_{\text{e}}$, in which case the group delay $\tau_{\text{g,MZI}} = -\partial \varphi_{\text{MZI}}/\partial \omega = \left(\Delta n_{\text{eg}} L - n_{\text{eg}} \Delta L \right)/c \approx 0$ and hence the frequency dependency of the optical power transmission vanishes. In contrast, the operating point $\varphi_{\text{OP,RR}}$ and hence the group delay $\tau_{\text{g,RR}} = -\partial \varphi_{\text{RR}}/\partial \omega = n_{\text{eg}} L/c$ of the resonator is fixed, leading to an unavoidable frequency dependence. Chapter 4 extensively reviews integrated photonic phase-sensitive circuits.

2.3.2 Core components and technological challenges

This section discusses the core components and associated technological challenges in an integrated silicon photonic sensor system, as visualized in Fig. 2.10.
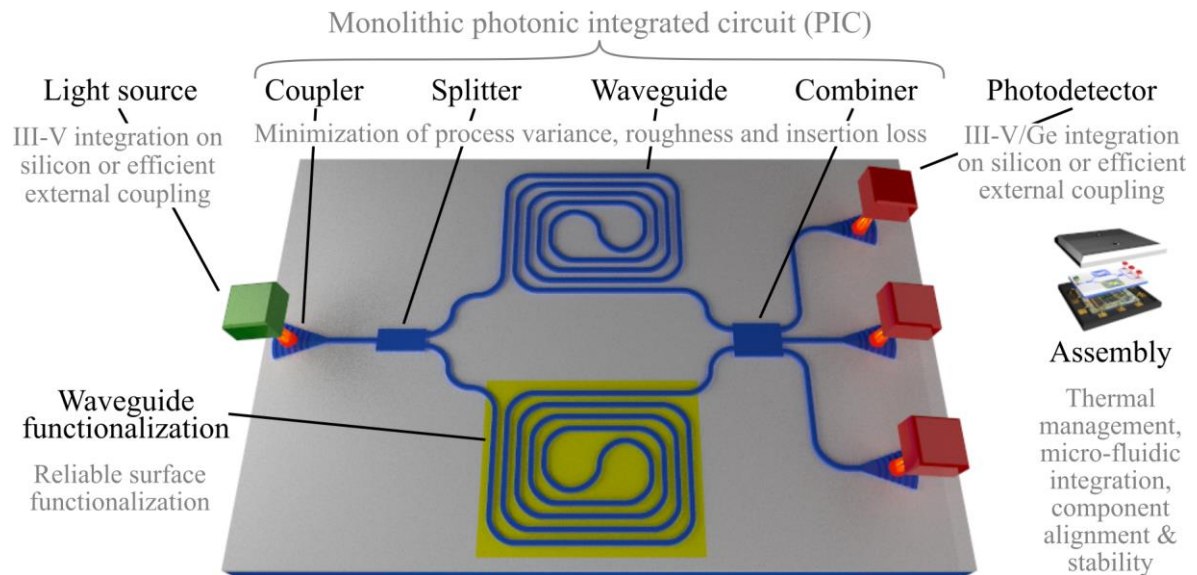
Fig. 2.10. Core components and associated technological challenges of a silicon photonic sensor system. The main subsystem in an integrated photonic sensor system is a PIC containing monolithically integrated structures (blue) such as passive couplers, splitters, waveguides, combiners, or active modulators (not shown). The associated technological challenges are denoted in grey. Light sources and photodetectors can either be monolithically integrated on the PIC or coupled to the PIC from outside. Within a sensitive region (yellow), the waveguide interacts with the environment. Depending on the sensing task, this can be accomplished, e.g., by locally removing the waveguide passivation cladding and by functionalizing the waveguide core surface to selectively interact with the target analyte. Special attention has to be paid to the assembly and packaging of the overall photonic sensor system, especially to the precise and stable alignment of external light sources and detectors, to the thermal management for avoiding interaction with the sensing process, as well as to a potential integration with micro-fluidic systems.

Light source   As of today, no efficient and mass-producible silicon-based light source is available for the silicon photonics integration platform due to silicon's indirect bandgap. Consequently, a light source such as a vertical-cavity surface-emitting laser (VCSEL) or distributed feedback (DFB) laser is typically coupled to the silicon PIC, which is fabricated on a more suitable photonic integration platform such as III-V-based photonics [12,13,14,15]. One possibility is to have the III-V chip completely separate from the silicon PIC while the optical connection is realized, e.g., via a free-space, optical fiber or photonic wire bond connection [16]. Another possibility is to attach the III-V light source directly to the silicon PIC via, e.g., flip-chip bonding [17], transfer printing [18] or a direct monolithic integration – in a hybrid approach, the silicon photonic circuit itself can be part of the laser [19,20]. These approaches differ in various aspects such as their possible output powers, their coupling efficiency, their cooling requirements, and the required alignment precision and manufacturing processes. Amon these, the use of an external VCSEL is a particularly energy-efficient and low-cost solution.

Monolithic PIC   Several photonic components can be monolithically integrated on a single PIC, see blue colored components in Fig. 2.10. This enables densely integrated and complex photonic circuits, comprising many sensor elements such as Mach-Zehnder interferometers, shown here, or ring resonators. The basic building blocks comprise passive components such as couplers, here drawn as grating couplers, waveguides for routing, as well as multi-mode interference (MMI) or directional couplers for signal splitting and combining. For these components, it is important to use highly mature fabrication processes providing minimal process variance, low surface roughness and few defects, in order to achieve low insertion losses and small back-reflections for each component, which ultimately improves the signal-to-noise ratio and hence the detection limit of the sensor system. Optionally, the PIC can be complemented by electrically controlled components, which are not drawn on the passive PIC in Fig. 2.10. Prominent examples are waveguide sections with a tunable effective refractive index known as phase modulators. Sensors with such modulators enable advanced signal processing methods, see Chapter 5.

Optional surface functionalization   A sensor PIC additionally requires a sensitive waveguide region, see yellow area, in which the waveguide interacts with the environment. Depending on the sensing task, this can be accomplished, e.g., by locally removing the passivation cladding, and by functionalizing the waveguide core surface to selectively interact with the target analyte. Technologically, it can be challenging to fabricate robust a surface functionalization that can withstand rough environmental conditions. Massively parallel sensor systems rely on fabrication processes that can provide a multitude of different surface functionalizations localized at the various sensitive regions on the PIC.

Photodetector   The optical output signals are coupled to monolithically integrated or external photodetectors, and the output signals are processed further in the electrical domain. For the silicon photonics integration platform, monolithically integrated detectors can be realized with state-of-the-art germanium detectors [21], or by coupling strategies of external detectors [12,13,15] as listed in the light source paragraph.

Assembly and packaging   Special attention has to be paid to the assembly and packaging of the overall photonic sensor system, especially to the precise and stable alignment of external light sources and detectors, to the thermal management to avoid interaction with the sensing process, and to the potential integration of micro-fluidic systems.

2.3.3   Sensor system configurations

This section discusses the most relevant sensor system configurations based on different light sources, sensor PIC, and light-detection mechanisms, as visualized in Fig. 2.11.

Light sources   The left-hand column of Fig. 2.11 shows three types of light sources with different optical power spectral densities $S_{P_i}(\omega)$: A broadband light source such as a light emitting diode (LED) or a superluminescent light emitting diode (SLED) with a wide frequency spectrum around its central frequency ω_0, a tunable laser with a narrow linewidth, but with a tunable central frequency ω_0, and a static laser, again featuring a narrow linewidth, but operated at a fixed frequency ω_0.
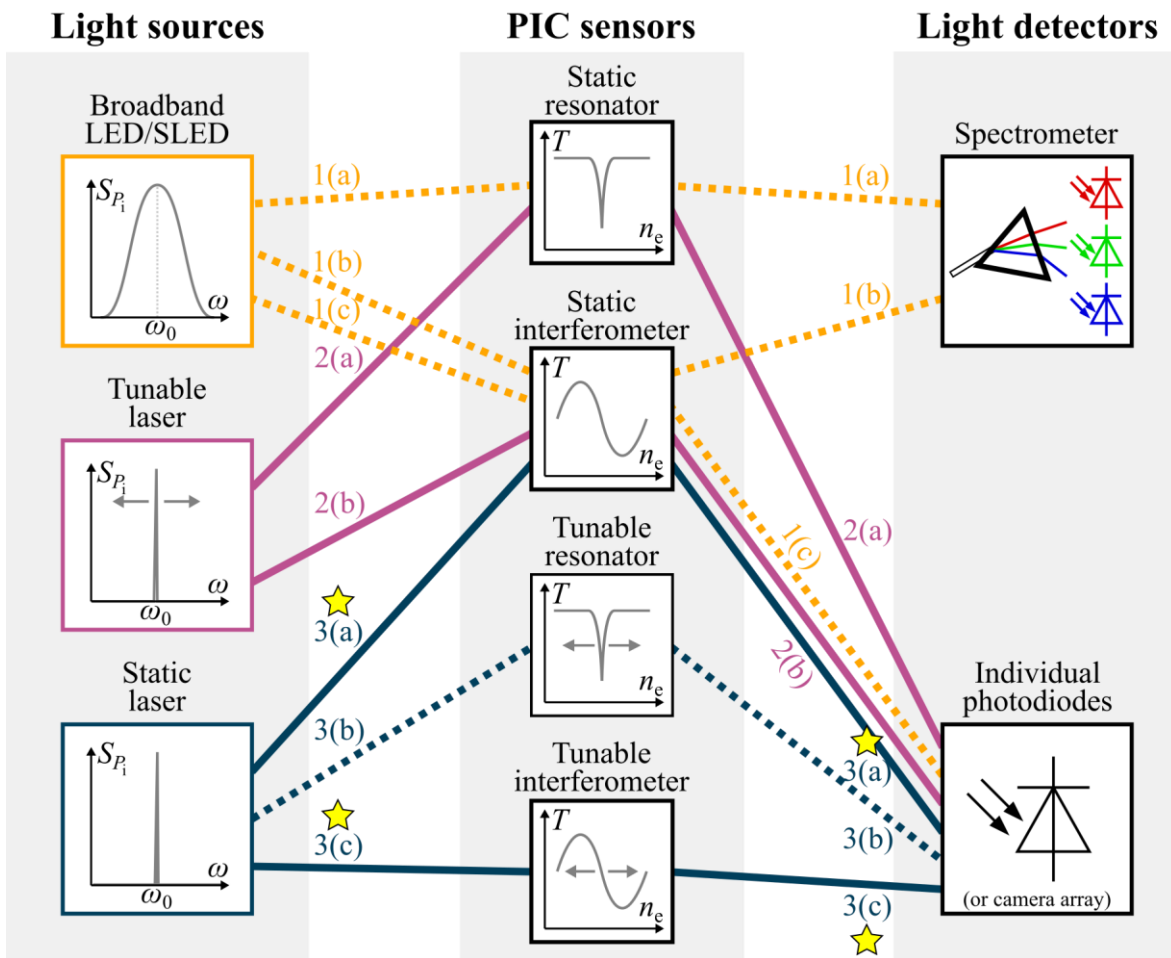
Fig. 2.11. Sketch of photonic sensor system configurations. The different configurations are based on different combinations of light sources, photonic sensor circuits on the PIC, and light detection mechanisms. Note that the dotted lines are of limited practical viability in integrated photonic sensor systems, while the stars mark the most promising configurations.

Note that by employing an on-chip tunable filter such as a tunable resonator in combination with a SLED, the rather broadband light source can effectively be converted into a tunable light source, at the cost of throwing away valuable power.

PIC sensors The central column of Fig. 2.11 shows resonant and interferometric sensors that are integrated on the PIC, with a typical Lorentzian and sinusoidal optical power transmission $T(n_e)$ based on the effective refractive index n_e, which can change during a measurement. In addition, tunable versions of both resonators and interferometers are included, which allow to modify the

operating point. Tunable PIC sensors use dedicated waveguide sections within the sensor circuit that, on top of the actual sensor operation, modify the effective refractive index profile and hence alter mode propagation. This refractive index profile modification can be achieved, e.g., thermally via heaters [22], electrically via free-carrier injection [23] or electro-optic materials [24], or mechanically by actuating suspended structures via electrostatics [9], which is well known from micro-electro-mechanical systems (MEMS). The non-tunable sensors are hence denoted as "static" to distinguish them from their "tunable" counterparts.

Light detectors The right-hand column of Fig. 2.11 shows two optical detection schemes based on a spectrometer and on individual photodiodes. Spectrometers split up the optical output signal into its spectral components and hence automatically deliver the optical output power spectral density $S_{P_o}(\omega) = S_{P_i}(\omega)T(\omega)$ depending on the measurand n_e. In contrast, individual photodiodes, or photodiode arrays in the form of image sensors or cameras as commonly used in laboratories, only record the time-dependent optical output power $P_o = \int S_{P_o}(\omega)\, d\omega$ integrated over the whole spectrum.

The colored lines, denoted as 1(a)-1(c) for broadband light sources, 2(a)-2(b) for tunable lasers, and 3(a)-3(c) for static, fixed-frequency lasers in Fig. 2.11, indicate possible photonic sensor system configurations. Note that the dotted lines are of limited practical viability in integrated photonic sensor systems, as described in the subsequent paragraphs.

Configuration 1(a) uses a broadband light source such as an LED, assumed to deliver constant input power spectral density $S_{P_i}(\omega) = S_{P_i}(\omega_0) = S_{P_{i0}}$ within the relevant spectral features of the static high-Q resonator used as the sensing element. For resonant sensors, the optical transmission also shows a Lorentzian spectral transmission $T(\omega)$, which shifts with n_e. By recording the spectral response and by tracking changes of the sensor resonance frequency $\omega_{\text{res}} \propto 1/n_e$ via Lorentzian fits, changes Δn_e of the effective refractive index in the sensor waveguide can be determined with good accuracy. The complete optical output spectral density $S_{P_o}(\omega) = S_{P_{i0}}T(\omega)$ is recorded by a spectrometer for each measurement point n_e. This readout concept is extremely popular for integrated photonic sensors in bench-top experiments due to the availability of precise and fast

spectrometers in optical laboratories. However, integrating a high-resolution spectrometer with a reasonably small footprint on a PIC is rather challenging.

Configuration 1(b) exchanges the resonator in 1(a) for an interferometer. For interferometric sensors, the spectral transmission $T(\omega) \propto 1 + \cos(\varphi_{\mathrm{MZI}})$ is sinusoidal and depends on the group delay difference $\tau_{\mathrm{g}} = -\partial \varphi_{\mathrm{MZI}} / \partial \omega$ between the interfering signals. As a consequence, to obtain useful data from a spectral readout of such an interferometer, a reasonably large group delay has to be ensured. As an example, the operating point $\varphi_{\mathrm{OP,MZI}}$ could be chosen so that at least one free spectral range $\mathrm{FSR} = 1/\tau_{\mathrm{g}}$ fits within the usable spectrum of the light source.

The use of a spectrometer at the sensor output to measure the spectrally resolved optical output power as detailed in Configurations 1(a) and 1(b) can be omitted and replaced by simpler photodiodes in three cases:

Frequency-tunable laser: The spectral response of the sensor can be obtained from sequential photodiode measurements during a frequency sweep of the laser, as described in Configurations 2(a) and 2(b).

Phase-tunable sensor: A tunable waveguide section is embedded within the sensor element. By deliberately tuning the sensor response, the transmission features and hence the measurand n_{e} can be traced with simple power measurements, see Configurations 3(b) and 3(c).

Completely static sensor operation: Active tuning can be omitted completely if the spectrum of the light source is narrow compared to the spectral features of the sensor. If a suitable operating point can be attained without such tuning, transmission changes originating from changes of the refractive index n_{e} can directly be measured by photodiodes. Note that MZI are more suitable for such a static operation in two ways. First, by adjusting the group delays of the interferometer arms, more broadband light sources can be used while keeping the sensitivity towards n_{e}. Second, the MZI readout can be designed to be operating-point independent, see Chapter 5. These non-tuned configurations based on simple photodiode measurements are described in Configurations 1(c) and 3(a).

Configuration 1(c) takes the opposite approach of Configuration 1(b), in that the interferometer is deliberately designed to be independent on frequency within the selected input bandwidth. This is achieved by eliminating the group delay difference τ_g between the interfering signals leading to $T(\omega) \propto T_0$. As the spectral information is irrelevant in this case, a simple measurement of the optical output power $P_\mathrm{o} = \int S_{P_\mathrm{o}}(\omega)\, d\omega$ via a photodiode suffices, and hence the spectrometer can be omitted. Under these assumptions, this configuration behaves similarly to Configuration 3(a), which uses a laser with a fixed center wavelength in combination with a static interferometer, as described in detail below.

Configuration 2(a) replaces the broadband light source in the resonator concept 1(a) with a tunable laser with center frequency ω_0 as the input light source. As a consequence, the spectrometer used to record the spectral characteristics of the resonator can be omitted and replaced by a simple photodiode. For the measurement, the output power P_o is recorded during a frequency sweep of the of the tunable laser, which allows to reconstruct the Lorentzian transmission spectrum of the ring resonator. It has to be noted that the frequency sweep has to happen much faster than the actual sensing process so that n_e is approximately constant within one sweep period and the reconstructed spectrum is not deformed. Alternatively, the need to record a full spectrum and fitting a Lorentzian can be bypassed by implementing a feedback loop to control the laser frequency, e.g., in a way that minimizes the optical output power. This operating point corresponds to the resonance condition of the resonator, i.e., the laser frequency is tracking the resonance shifts. Implementations based on this configuration are extensively reviewed within this thesis, see Chapters 4 and 5.

Configuration 2(b) replaces the static resonator from Configuration 2(a) with a static interferometer, but is otherwise identical insofar that the spectral information is obtained by a series of photodiode power measurements, which are linked to a frequency sweep of a tunable laser. Note that, as in Configuration 1(b), this concept can only provide additional information if the interferometer transmission exhibits a pronounced frequency-dependence within the tuning range of the laser, which requires a reasonably large group delay between the interfering signals. Although interferometric photonic sensor systems are rather

designed to suppress frequency noise by setting small group delays, the additional information provided by this concept can be used to vastly improve the robustness of the sensor readout by enabling instantaneous sensor calibration and endless phase unwrapping, as described in detail in Section 5.3.

Configuration 3(a) utilizes a static laser as the input light source that emits at a fixed frequency ω_0 in conjunction with a static interferometer as the sensing element and a simple photodiode for the recording of the output power. This is the simplest configuration from a hardware complexity perspective and hence represents a very attractive scenario for mass-deployable integrated photonic sensor systems. As a consequence, it is marked with a star in Fig. 2.11. This configuration is possible since interferometers deliver a well-known sinusoidal transmission $T(\Delta n_e)$ depending on the measurand Δn_e. Extracting the arbitrary output power amplitude A, e.g., from a reference channel measurement, is hence sufficient to reconstruct the effective index change via $\Delta n_e \propto \arcsin\left(\Delta P_o / A\right)$.

Note: On the contrary, the Lorentzian dependency of the optical transmission on $T(\Delta n_e)$ of a high-Q resonator is far more complex than the sinusoidal form in an interferometer. To reconstruct Δn_e in a resonator, information on the Q-factor, resonance frequency and insertion loss have to be known, which requires some sort of frequency or effective refractive index sweep. The reconstruction from a single power measurement is hence much less reliable. Furthermore, the Lorentzian resonance region represents only a small subset of the otherwise flat spectral response of high-Q resonators. For imperfect resonators and laser sources that cannot be spectrally matched by design, it is hence highly likely that the spectrum of the laser and resonator are not overlapping. The configuration of a static resonator driven by a static light source and read out with a single photodiode is hence not part of this comparison.

Configuration 3(b) combines the attractive sensing properties of a resonator, see Chapter 4, with a simple fixed-frequency light source. This is achieved by a tunable resonator that can be used to overlap the laser emission and the spectral features of the resonator, i.e., the resonator response is tuned towards the frequency ω_0 of the light source. From there, calibration routines enable the extraction of the spectral features of the Lorentzian resonance, which can subsequently be used to reconstruct the effective index change Δn_e from power

measurements using a simple photodiode. Alternatively, a feedback loop can be used to directly search for the resonance frequency by minimizing the optical output power, as described in Configuration 2(a). Technologically, however, fabricating a resonant sensor that is both tunable, e.g., via a thermal tuner, and simultaneously sensitive to the environment, e.g., via surface functionalization, without harmful interaction between these two mechanisms, poses additional fabrication and hardware complexity challenges.

Configuration 3(c)   uses a fixed-frequency light source in combination with a tunable interferometer and a simple photodiode power measurement. As in Configuration 2(b), the additional signal information gained from the tuning around the operating point can provide huge benefits by enabling instantaneous sensor calibration, as described in detail in Section 5.3. The difference to Configuration 2(b) is that the tunability is moved from the laser light source to the interferometer on the PIC. This has several distinct advantages. First, for a given photonic integration platform, the realization of an on-chip tuning mechanism can be much easier than integrating a reliable frequency-tunable laser. Second, the frequency of integrated lasers is often tuned via their current, leading to a parasitic power modulation that has to be accounted for in the signal processing. Third, when relying on tuning of the laser emission frequency, the interferometer has to include a large group delay difference between the interfering signals to provide sufficiently strong spectral features within the laser tuning range. This makes the circuit less robust to frequency noise, see Chapter 4. Fourth, due to the typical layout of on-chip interferometers such as Mach-Zehnder interferometer structures, the regions for sensing and tuning can be spatially separated on the PIC to avoid interference of the two physical mechanisms. This configuration offers an exceptionally good trade-off between design and readout simplicity and potent performance, and is hence marked with a star in Fig. 2.11.

2.3.4   Sensor readout concepts

This section highlights four generic sensor readout concepts that can be employed to determine the ring resonator phase $\varphi_{\mathrm{RR}} = -k_0 \Delta n_{\mathrm{e}} L + \varphi_{\mathrm{OP,RR}}$ or the MZI phase difference $\varphi_{\mathrm{MZI}} = -k_0 \Delta n_{\mathrm{e}} L + \varphi_{\mathrm{OP,MZI}}$ with one of the sensor system configurations introduced in Section 2.3.3. For RR, L represents the round-trip

length, while for MZI, L represents the arm lengths. The four sensor-readout concepts will be briefly discussed in the following paragraphs, an extensive analysis of the most attractive readout concepts is given in Chapters 4 and 5.

Readout concept 1 – Calibrated measurement   For this sensor readout concept, the optical output power spectrum $P_{\mathrm{o}}(\varphi_{\mathrm{RR}}) = P_{\mathrm{i}}T_{\mathrm{RR}}(\varphi_{\mathrm{RR}})$ of the ring resonator sensor or $P_{\mathrm{o}}(\varphi_{\mathrm{MZI}}) = P_{\mathrm{i}}T_{\mathrm{MZI}}(\varphi_{\mathrm{MZI}})$ of the Mach-Zehnder interferometer sensor is measured once before performing the actual measurement. The results can be used directly as a look-up table to map subsequent power measurements to the phase information. The spectrum is obtained by deliberately tuning the phase in the operating point $\varphi_{\mathrm{OP,RR}}$ or $\varphi_{\mathrm{OP,MZI}}$ by $\pm\pi$, e.g., by using dedicated waveguide sections that can modulate the phase. Alternatively, a suitable Lorentzian fit (for RR) or sinusoidal fit (for MZI) can be applied to obtain an idealized optical transmission function $T_{\mathrm{RR}}(\varphi_{\mathrm{RR}})$ or $T_{\mathrm{MZI}}(\varphi_{\mathrm{MZI}})$, respectively. With such a fit, measurements of P_{o} can be mapped to Δn_{e} via

$$\varphi_{\mathrm{RR}} = T_{\mathrm{RR}}^{-1}\left(\frac{P_{\mathrm{o}}}{P_{\mathrm{i}}}\right), \quad \varphi_{\mathrm{MZI}} = T_{\mathrm{MZI}}^{-1}\left(\frac{P_{\mathrm{o}}}{P_{\mathrm{i}}}\right). \tag{2.16}$$

Note that this readout concept is viable if a deliberate phase tuning is possible and if there is no drift expected that could corrupt the calibrated transmission throughout the duration of an experiment. The time-resolution of this readout concept is limited directly by the photodiode sampling frequency.

Readout concept 2 – Repeated spectral phase measurements   As for the calibrated measurement, this sensor readout concept also requires that the sensor phase can be tuned deliberately. However, in this concept, this phase tuning is performed repeatedly during the experiment. As a consequence, each measurement in fact consists of a whole phase spectrum instead of a single power measurement. By applying a subsequent fit to each measured spectrum, the phase information can be retrieved with larger precision compared to the extraction from a single data point. For example, the spectral fit can be used to determine a characteristic spectral feature such as a resonance condition at $\varphi_{\mathrm{RR}} = 2\pi m$ for integer $m = 1,2,3,\dots$ in a ring resonator, resulting in a minimized output power, or a constructive interference condition at $\varphi_{\mathrm{MZI}} = 2\pi m$ in a single-output Mach-Zehnder interferometer, resulting in a maximized output power.

Note that a finely resolved phase sweep improves precision and robustness, but the time-resolution of this readout concept is now limited by the sweep duration and requires additional signal processing.

Refractive index extraction from phase measurements: For systems operating with a fixed-frequency light source, a phase sweep can only be realized by tuning the initial effective refractive index $n_{e,0}$ in a tunable waveguide section. Performing such a phase sweep yields the optical transmission $T_{RR}(\varphi_{RR})$ or $T_{MZI}(\varphi_{MZI})$ that are required to extract the phases φ_{RR} or φ_{MZI} as in Eq. (2.16) . Two measured phase values $\varphi_{RR} - \varphi_{OP,RR}$ or $\varphi_{MZI} - \varphi_{OP,MZI}$ can directly be used to calculate the change Δn_e of the effective refractive index as

$$\Delta n_e = \begin{cases} -\dfrac{1}{k_0 L}\left(\varphi_{RR} - \varphi_{OP,RR}\left(n_{e,0}\right)\right) & \text{for RR,} \\[2ex] -\dfrac{1}{k_0 L}\left(\varphi_{MZI} - \varphi_{OP,MZI}\left(n_{e,0}\right)\right) & \text{for MZI.} \end{cases} \quad (2.17)$$

However, if the phase sweep is realized by tuning the angular frequency ω of the light source, the frequency dependency of the effective refractive index embodied in the dispersion relation $\beta(\omega)$ has to be taken into account. As shown in Eq. (2.12), the first two terms of a Taylor expansion of the dispersion relation $\beta(\omega)$ yield the effective group refractive index $n_{eg} = n_e + \omega\, \partial n_e / \partial \omega$. Because of the frequency tuning, Eq. (2.17) has to be rewritten and phase measurements derived from Eq. (2.16) yield the differences of the effective group refractive indices Δn_{eg} instead of Δn_e,

$$\Delta n_{eg} = \begin{cases} -\dfrac{1}{k_0 L}\left(\varphi_{RR} - \varphi_{OP,RR}\left(\omega\right)\right) & \text{for RR,} \\[2ex] -\dfrac{1}{k_0 L}\left(\varphi_{MZI} - \varphi_{OP,MZI}\left(\omega\right)\right) & \text{for MZI.} \end{cases} \quad (2.18)$$

Readout concept 3 – Continuous tracking of spectral features For this readout concept, the phase is initially tuned deliberately to a characteristic spectral feature, e.g., to a RR resonance at $\varphi_{RR} = 0$ in a ring resonator, resulting in the lowest possible output power, or to a MZI interference condition at $\varphi_{MZI} = 0$

in a single-output Mach-Zehnder interferometer, resulting in the highest possible output power. A feedback control is established that continuously tracks such a spectral feature by readjusting the active phase tuning as soon as the output power measurement changes in a certain direction. In this case, the feedback control signal is used to extract phase changes, which can then be processed to determine Δn_e (if the phase is tuned in the sensor itself at a constant frequency ω, see Eq. (2.17)) or Δn_{eg} (if the phase is tuned via the laser ω, see Eq. (2.18)).

In order to improve sensitivity, the sensor operating point should be located at a spectral feature that maximizes the output power change $\partial P_o / \partial \Delta n_e$ for a given change of the effective refractive index Δn_e. This is achieved by tuning the phase $\varphi_{OP,RR}$ or $\varphi_{OP,MZI}$ in the operating point to the inflection point of the Lorentzian or sinusoidal optical power transmission $T_{RR}(\varphi_{RR})$ or $T_{MZI}(\varphi_{MZI})$ of the ring resonators or Mach-Zehnder interferometers. In contrast to an operation at the extrema of the transmission, the operation in the inflection points maximizes $\partial P_o / \partial \Delta n_e$. In order to find this specific operating point, a small phase modulation can be applied in combination with another feedback control loop that continuously maximizes the amplitude of the corresponding output power modulation.

Readout concept 4 – Direct phase measurement Deliberate phase tuning or tracking of spectral features can be avoided in Mach-Zehnder interferometers, if the MZI is terminated, e.g., by a 3×3 multi-mode interference (MMI) coupler. Here, the sensor and the reference arm of the MZI are connected to the top and bottom input ports of the 3×3 MMI, leaving the central input port unconnected. The optical power $P_{o,v}$ in each of the three MMI coupler output ports v can be calculated by superimposing the complex electrical fields $\underline{E}_{o,s,v}$ and $\underline{E}_{o,r,v}$ v originating from the sensor and reference arm, respectively. Photodiodes with responsivity R translate these optical output powers into three output currents, which can be written as a column vector $\mathbf{I}_o = R \cdot \left(P_{o,1}, P_{o,2}, P_{o,3} \right)^T$. In the ideal case, the three currents are phase-shifted by 120° and have the same amplitude, as detailed in Chapter 5. Applying the 2×3 Clarke transformation matrix $\mathbf{M}_C$, known from the analysis of electrical three-phase circuits, onto the output currents $\mathbf{I}_o$, we obtain two 90° phase-shifted in-phase and quadrature signals

$\left(S_{\mathrm{I}}, S_{\mathrm{Q}}\right)^{\mathrm{T}} \propto \left(\cos\left(\varphi_{\mathrm{MZI}}\right), \sin\left(\varphi_{\mathrm{MZI}}\right)\right)^{\mathrm{T}}$. These signals can then be used directly to determine the actual phase difference φ_{MZI} by calculating the argument of the artificial signal $\underline{S} = S_{\mathrm{I}} + \mathrm{j}\, S_{\mathrm{Q}}$,

$$P_{\mathrm{o},\nu} = \left|\underline{E}_{\mathrm{o},\nu}\right|^{2} = \left(\underline{E}_{\mathrm{o,s},\nu} + \underline{E}_{\mathrm{o,r},\nu}\right)\left(\underline{E}_{\mathrm{o,s},\nu} + \underline{E}_{\mathrm{o,r},\nu}\right)^{*},$$

$$\mathbf{I}_{\mathrm{o}} = R \cdot \left(P_{\mathrm{o},1}, P_{\mathrm{o},2}, P_{\mathrm{o},3}\right)^{\mathrm{T}},$$

$$\begin{pmatrix} S_{\mathrm{I}} \\ S_{\mathrm{Q}} \end{pmatrix} = \mathbf{M}_{\mathrm{C}}\mathbf{I}_{\mathrm{o}} \propto \begin{pmatrix} -\dfrac{1}{2} & 1 & -\dfrac{1}{2} \\[2ex] -\dfrac{\sqrt{3}}{2} & 0 & \dfrac{\sqrt{3}}{2} \end{pmatrix} \begin{pmatrix} 1+\cos\!\left(\varphi_{\mathrm{MZI}} + \dfrac{2\pi}{3}\right) \\[2ex] 1+\cos\!\left(\varphi_{\mathrm{MZI}}\right) \\[2ex] 1+\cos\!\left(\varphi_{\mathrm{MZI}} - \dfrac{2\pi}{3}\right) \end{pmatrix}, \qquad (2.19)$$

$$\underline{S} = S_{\mathrm{I}} + \mathrm{j}\, S_{\mathrm{Q}} \propto \cos\left(\varphi_{\mathrm{MZI}}\right) + \mathrm{j}\sin\left(\varphi_{\mathrm{MZI}}\right) \propto \mathrm{e}^{\mathrm{j}\varphi_{\mathrm{MZI}}},$$

$$\varphi_{\mathrm{MZI}} = \arg\left(\underline{S}\right).$$

With this readout concept, phase-tuning mechanisms such as dedicated tunable waveguide sections or tunable lasers can be eliminated. In addition, it allows sensing independently of the operating point and hence provides uniform sensitivity and noise characteristics throughout the measurement range. Furthermore, it solves the issue of ambiguity within [-π,π] of simple transfer functions. The time-resolution is again limited only by the photodiode sampling frequency, and no feedback control mechanisms have to be employed. This readout concept can be extended to enable an instantaneous sensor calibration and an endless phase unwrapping to obtain unambiguous signals, which is discussed in detail in Chapter 5.

2.4   Summary: Fundamentals

This section introduced the basic concepts of integrated photonic systems. The analysis focused on integrated waveguide-based sensor elements. The mathematical foundation for photonic mode propagation in such waveguides was derived from Maxwell's equations with certain boundary conditions. Key modal characteristics such as the effective refractive index, the effective refractive group index, the loss, and the thermo-optic coefficient were introduced and visualized for typical sensing waveguides. The sensing principle based on changes of the effective refractive index of a photonic waveguide mode was reviewed. Surface sensing and homogeneous sensing were introduced, which both utilize the overlap of the evanescent field with a cladding medium of variable refractive index, and which represent two of the most prominent variants of integrated photonic sensors.

The photonic waveguide was subsequently introduced as the central sensing element within a fully integrated photonic sensor. Here, on the system level, the fundamental properties of phase-sensitive photonic circuits were discussed, which transduce changes of the effective refractive index into measureable changes of the optical output power. Furthermore, the core components and the associated technological challenges required in such a sensor system were reviewed. With the information on mode propagation, the sensing principle, and the system components at hand, a thorough discussion on benefits and drawbacks of a variety of sensor system configurations is performed. It is highlighted that the combination of a fixed-frequency laser, a (possibly tunable) Mach-Zehnder interferometer, and a simple photodiode output can be a particular attractive configuration due to the simplicity of the design, hardware implementation and signal processing. The chapter was concluded by briefly discussing sensor readout concepts that compare several spectral readout concepts. As a highly attractive option, we identify a direct readout concept that does not require any active tuning of operating point. This is achieved by employing a triple-output MZI in combination with a Clarke transformation that directly yields a signal with in-phase and quadrature signal components.

3 Sensor optimization by waveguide design

This chapter analyzes the design of integrated photonic waveguides for sensing applications. Based on the field-interaction factor of the waveguide mode with a particular region of the waveguide cross section, this chapter provides physical insights and comprehensive design guidelines for the selection of appropriate photonic integration platforms, waveguide types, mode families, and waveguide geometries targeting a given measurement task.

The following section is taken from the publication [J1]. In order to fit the structure and layout of this document, it was adapted accordingly. Appendices associated with this manuscript can be found in Appendix A.

Note that two authors contributed equally to this publication. The initial Ansatz and scope, as well as the concluding evaluation, interpretation and discussion were performed jointly. For the development of the methods and results, the focus of the author of this thesis was on the analytical mathematical model, while the focus of Daria Kohler was on the simulations.

[start of publication [J1]]

Surface sensing with integrated optical waveguides: a design guideline

Johannes Milvich,[1,2,3,6] Daria Kohler,[1,4,6] Wolfgang Freude[1] and Christian Koos[1,5]

[1] Institute of Photonics and Quantum Electronics (IPQ), Karlsruhe Institute of Technology (KIT), Engesserstr. 5, 76131 Karlsruhe, Germany

[2] Robert Bosch GmbH, Robert-Bosch-Campus 1, 71272 Renningen, Germany

[3] johannes.milvich@bosch.com

[4] daria.kohler@kit.edu

[5] christian.koos@kit.edu

[6] These authors contributed equally to this work

Abstract: Waveguide-based biochemical sensors exploit detection of target molecules that bind specifically to a functionalized waveguide surface. For optimum sensitivity, the waveguide should be designed to mediate maximum influence of the surface layer on the effective refractive index of the guided mode. In this chapter, we define a surface sensitivity metric which quantifies this impact and which allows to broadly compare different waveguide types and integration platforms. Focusing on silicon nitride and silicon-on-insulator (SOI) as the most common material systems, we systematically analyze and optimize a variety of waveguide types, comprising simple strips, slot and double slot structures, as well as sub-wavelength gratings (SWG). Comparing the highest achievable surface sensitivities, we provide universal design guidelines and physically interpret the observed trends and limitations. Our findings allow to select the appropriate WG platform and to optimize sensitivity for a given measurement task.

3.1   Introduction

Waveguide-based optical sensors are used in a variety of applications such as label-free detection of chemical or biological analytes that specifically bind to functionalized waveguide (WG) surfaces [4,5,25–32]. Such sensors exhibit large potential for miniaturization and cost-efficient mass production, utilizing established photonic integration platforms such as silicon or silicon nitride. Sensor schemes are most commonly based on interferometers, e.g., in Mach-Zehnder and Young configuration [26,28,29,32,33], or on resonant devices, such as ring, disk and Bragg resonators [4–6,25,26,29-32,34–38], which can be further enhanced by exploiting the Vernier effect [39]. Enabling large effective interaction lengths with the analyte, these sensor structures combine high sensitivity with small device footprint and lend themselves to high-density integration into massively parallel arrays.

The sensor principle relies on an optical WG that guides a mode which significantly extends into the cladding medium that surrounds the WG core. The interaction between the optical mode field and the varying surface layer properties alters the effective refractive index by Δn_{e} and thus the optical phase shift accumulated during propagation. The strength of this effect is expressed by the so-called surface sensitivity, which, in combination with the effective-index sensitivity from the phase measurement of the underlying resonator or interferometer, determines the overall sensitivity. Proper optimization of the WG towards high surface sensitivities is hence key for realizing high-performance sensors.

Over the last years, various approaches for optimizing special types of WG were published, both for surface sensing [5,7,29,32,36–40] and for detection of bulk refractive index changes in the WG cladding (homogeneous sensing) [4,5,7,25,26,30,31,36,37,39,40]. However, these investigations are often limited to specific WG types and geometries on certain material platforms, such as silicon [4,5,25,26,29–31,33-35,37,40,41], silicon nitride (Si_3N_4) [29,32,33,38,42] and polymers [33,40]. It is hence impossible to broadly compare the highest achievable surface sensitivities across different WG types and integration platforms. Moreover, most sensitivity analyses consider only a specific type of surface layer with prescribed refractive index.

In this chapter, we define a universal surface sensitivity that is broadly applicable to layers of different thicknesses and refractive indices. Focusing on Si_3N_4 and Si as the most common integration platforms, we systematically analyze a wide variety of WG types, comprising simple strip WG, slot and double slot WG, as well as sub-wavelength grating (SWG) WG. For each of these WG types, we identify the optimum geometry for both TE and TM polarization, and we compare the highest achievable surface sensitivities, taking into account implementation limitations that are associated with state-of-the art fabrication technologies. The focus of our analysis is on WG types that can be reliably mass-produced by optical lithography and single-etch structuring of WG on solid substrate layers. Note that even higher sensitivities can be achieved by more sophisticated WG concepts comprising ultra-small features [43] or suspended WG sections [9]. These schemes, however, require dedicated fabrication processes, which are not yet accessible through scalable foundry processes. Exploiting the scalability of Maxwell's equations with respect to refractive index and geometry, we derive and physically explain general trends and design rules to corroborate the numerical results. Our findings can be used as design guidelines to select the appropriate WG platform and to optimize sensitivity for a given measurement task.

3.2   Scope

3.2.1   Basic sensing principle: Wave propagation and effective refractive index

For illustrating the basic sensing principle, we regard homogeneous sensing with a waveguide core embedded in an infinitely extended cladding medium. First, we define a few quantities: The propagation of monochromatic plane waves with vacuum wavelength λ in a homogenous medium is determined by the propagation constant $\beta = nk_0$ (refractive index n, vacuum propagation constant $k_0 = 2\pi/\lambda$). Dielectric WG consist of a high-refractive index core (n_{core}) and a low-refractive index cladding medium (n_M). For integrated optical WG made from silicon or silicon nitride, the core is usually supported by a buried

oxide layer (BOX, bottom cladding) with refractive index n_{BOX}. The evanescent parts of the WG mode, which are essential for the sensing process, extend into the cladding region. The actual field distribution in the various materials determines the WG propagation constant β, which can be expressed by an effective refractive index $n_{\text{e}} = \beta/k_0$. If the refractive index of the WG cladding changes, β and hence n_{e} are modified, which impacts the phase shift $\varphi = -\beta L = -n_{\text{e}}k_0 L$ accumulated over a propagation length L. Due to the large optical frequencies, a change of n_{e} is measured with high accuracy. For a given WG length L, the measured phase shift can be referred to a change Δn_{e} of the effective index, which finally allows sensing a change of the cladding index. The larger Δn_{e} becomes for a certain cladding index change, the more sensitive the device becomes.

3.2.2 Parameters for WG-based sensing

Numerous parameters determine how sensitive Δn_{e} reacts on a cladding index change Δn_{M}. Fig. 3.1 summarizes the essential design elements for a WG: The material platform, the WG type, the polarization, and the WG geometry.

Platform Common integration platforms for optical sensors rely on a layer stack of a silicon (Si) or silicon nitride (Si_3N_4) device layer on a several micrometer thick BOX (SiO_2) as a bottom cladding, mechanically supported by a Si substrate. WG are structured in the device layer, and the BOX thickness is chosen to avoid leakage into the high-refractive index silicon substrate as well as to optimize grating coupler efficiency.

While Si WG are operated in the near infrared (NIR), Si_3N_4 WG are suitable for operation across the complete visible (VIS) and NIR spectrum. As the target media for biosensors are usually provided in the form of aqueous solutions, sensor operation at VIS wavelengths is much less impaired by water absorption than in the NIR. However, a large wavelength allows relaxed WG fabrication accuracies, and reduces scattering loss due to WG roughness. In this chapter, we thus consider Si WG operated at NIR telecom wavelengths around 1550 nm, where low-cost laser sources are readily available, as well as Si_3N_4 WG operated at 600 nm as an example of low-wavelength sensors, Fig. 3.1(a).
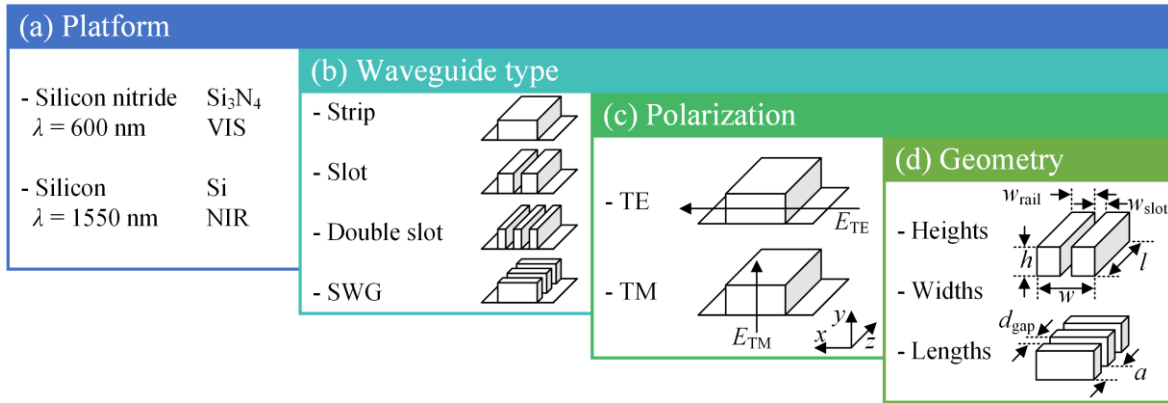
Fig. 3.1. Essential design elements for maximizing surface sensitivity. For each combination of **(a)** material platform, **(b)** WG type and **(c)** polarization, the optimum **(d)** geometry can be determined, observing reasonable technological constraints.

Waveguide type For both integration platforms, we study four typical WG types, denoted as strip, slot, double slot and subwavelength grating (SWG) WG, Fig. 3.1(b). The last three types require significantly smaller feature sizes than the strip WG and thus lead to more challenging fabrication processes. We concentrate on single-mode WG, combining stable operation with high surface sensitivity.

Polarization We study the fundamental mode of both (quasi-)TE and (quasi-)TM polarization, Fig. 3.1(c). The term (quasi-)TE refers to the case where the dominant transverse electric field component is oriented parallel to the substrate. Similarly, (quasi-)TM denotes a configuration in which the dominant transverse magnetic field component is parallel to the substrate. For the TE polarization, an enhancement of the electric field E_x exists at the WG sidewalls because the normal component $D_x = \varepsilon_0 n^2(x) E_x(x)$ of the displacement must be continuous, while for TM polarization this field enhancement is to be seen at the top and at the bottom WG surfaces.

Geometry For all combinations of platform, WG type and polarization, we study the impact of the WG geometry in terms of height, width, and length (SWG only) of WG features, Fig. 3.1(d). Three standard device layer heights h of 220 nm, 250 nm and 340 nm are considered for Si WG structured on silicon-on-insulator (SOI) wafers. Wafers for structuring Si_3N_4 WG are available with a maximum Si_3N_4 thickness of several hundred nanometers, if stoichiometric

growth is important, and we therefore consider typical WG heights h of 200 nm, 300 nm and 400 nm. For all WG types, we vary the overall width w in steps of 10 nm. For slot and double-slot WG, we additionally vary the slot width w_{slot} in four steps. For SWG WG, we vary the period a and the spacing d_{gap} between the WG elements, which can also be quantified by the fill factor $\mathrm{FF} = \left(a - d_{\mathrm{gap}} \right) / a$. We chose a minimum feature size of $80\,\mathrm{nm}$ to meet commercial technological conditions.

In the following, we define the surface sensitivity as a quantitative metric and maximize it by varying the various WG parameters. Given a certain sensor application, this data set allows to find the optimum design for a WG-based sensor.

3.3 Methods

3.3.1 Sensitivity of waveguide surfaces with respect to attached molecules

In WG-based sensing, two basic approaches are commonly used, which are compared in Fig. 3.2. For so-called homogeneous sensing, a bare WG core is exposed to a typically aqueous homogeneous target medium with refractive index n_{M}, Fig. 3.2(a). For surface sensing, a WG core is functionalized such that target molecules from an aqueous solution can bind to the core forming a surface layer with effective thickness t_{SL} and refractive index n_{SL}, Fig. 3.2(b).

For homogeneous sensing, a change in n_{M} causes a change Δn_{e} of the effective index. This change is the stronger the more the mode optical field extends into the target medium. Homogeneous sensing is usually unspecific, i.e., Δn_{e} cannot be traced back to a specific substance in the target medium if it is unknown which constituent is actually changing.

For surface sensing, the refractive index n_{M} of the aqueous solution remains essentially fixed, while the molecules, bound to the surface layer, influence the optical mode. By functionalizing the WG surface with dedicated capture agents, surface sensing can be used for specific detection of certain target analytes.
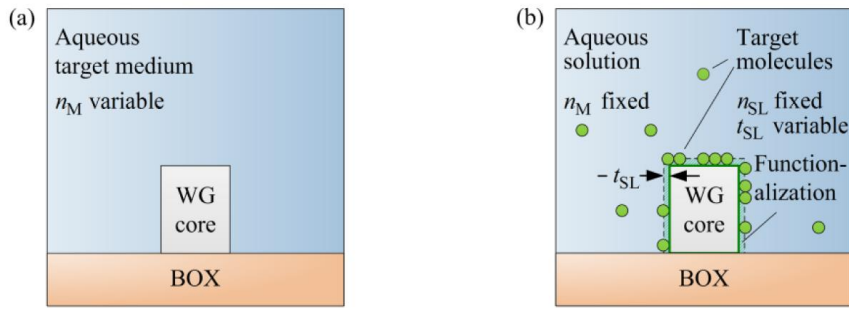
Fig. 3.2. Plain and functionalized strip WG on a buried silicon oxide (BOX) layer. **(a)** Homogeneous sensing. The aqueous target medium with refractive index n_M forms the homogeneous cladding of the WG core. A variation of n_M leads to a change in the effective refractive index of a guided mode. **(b)** Surface sensing. The refractive index n_M of the aqueous cladding solution remains constant. Target objects such as molecules, cells, vesicles or other corpuscles attach to the WG core, often mediated by a specific surface functionalization. The effect on the wave propagation is modelled with a surface layer (SL) having a refractive index n_{SL} and an effective layer thickness t_{SL}. The effective layer thickness takes into account the size of the target objects as well as the ratio of occupied binding sites.

The change Δn_e is the stronger, the more the optical field is concentrated within the surface layer. The definition of an effective layer thickness t_{SL} accounts for a possibly inhomogeneous distribution of target molecules within the surface layer. With biological samples, this effective thickness is in the nanometer range, and n_{SL} is typically around 1.5. For the remainder of this chapter, we concentrate on surface sensing, offering a wide variety of applications. We are hence interested in the detailed influence of the surface layer on the electric and magnetic field distribution.

Fig. 3.3 and Fig. 3.4 show the simulated electric field magnitudes of the fundamental quasi-TE mode of strip, slot and double slot WG, and for subwavelength grating WG, respectively. Details on the simulation parameters can be found in Appendix A.1. White contours mark the surface layer where molecules bind, leading to a change of the local refractive index. A higher field concentration in these regions increases the surface sensitivity. While in a typical strip WG, Fig. 3.3(a), a large portion of the power is located inside the WG core, slot and double slot WG concentrate the power between the rails, Fig. 3.3(b) and (c). This means that the surface layer experiences higher field strengths in slotted WG, leading to a larger Δn_e compared to a strip WG.
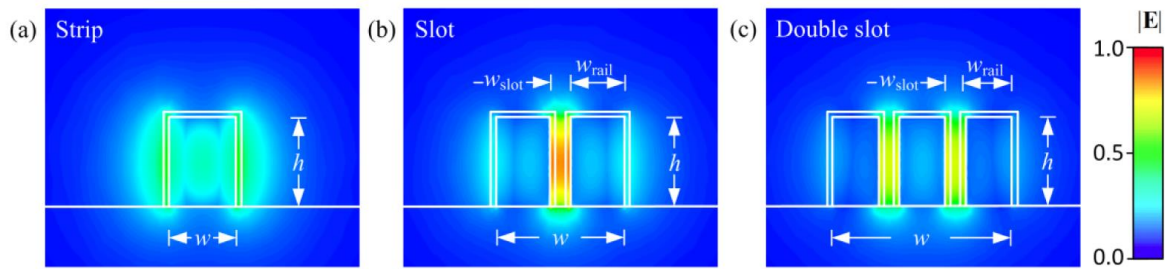
Fig. 3.3. Simulated electric field magnitudes of the fundamental quasi-TE mode in different WG geometries with height h and total width w. White contours mark the surface layer on the WG core. The larger the field strength in this region is, the larger the surface sensitivity becomes. The surface layer is disregarded for the field calculation.   **(a)** Strip WG. The surface layer experiences only moderate field strengths.   **(b)** Slot WG. A large field strength is located in the surface layers of the slot.   **(c)** Double slot WG. The field strength in each of the two slots is smaller than for a single slot, but the relevant surface layer area has doubled.
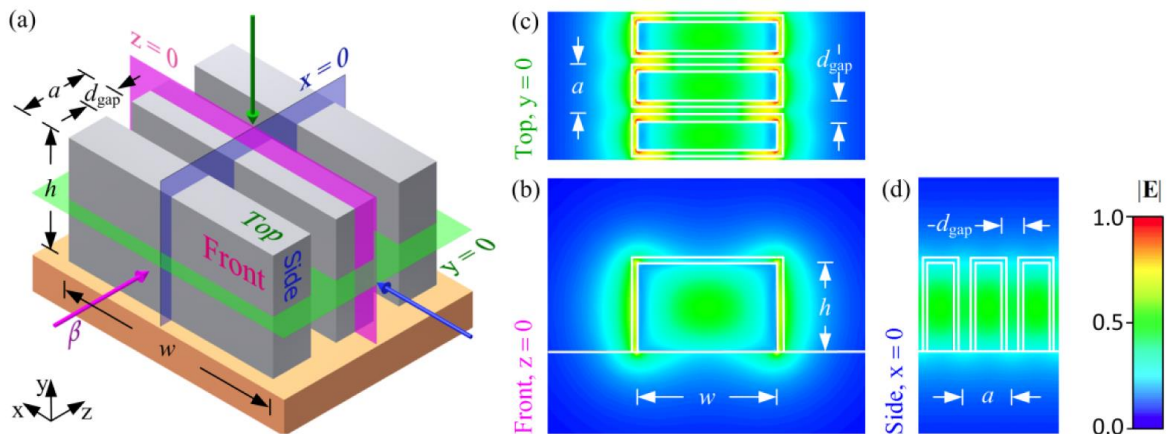
Fig. 3.4. Section of a subwavelength grating (SWG) WG and simulated electric field magnitudes of the fundamental quasi-TE mode. Compared to a strip WG, the surface layer area per unit length of the WG is increased.   **(a)** Schematic of a SWG WG with width w, height h, period a and gap size d_{gap}. The pink arrow marks the direction of propagation. Specific cross-sections $z = 0$, $y = 0$, $x = 0$ are indicated with colored planes. Front, Top and Side mark the associated views.   **(b)-(d)** Electric field magnitudes. White contours mark the surface layers on the WG core, which are disregarded for the field calculation. The larger the field strength in this region and the larger the surface, the bigger the surface sensitivity becomes.   **(b)** Front view at $z = 0$. The surface layer experiences only moderate field strengths.   **(c)** Top view at $y = 0$. Large field strengths (red areas) occur at the vertical edges of the blocks.   **(d)** Side view at $x = 0$. Moderate field strengths are found at surfaces $z = \text{const}$.

SWG WG are composed of a multitude of individual WG elements, thus increasing the surface layer area per unit length of the WG. Fig. 3.4(a) shows a section of a SWG WG with three periods along the propagation axis (pink arrow). For determining the surface sensitivity, a 3D elementary cell has to be simulated using periodic boundary conditions in the axial direction [44]. The three colored planes mark the cross sections where the field distributions of Fig. 3.4(b-d) are plotted. In Fig. 3.4(c), high field strengths (red regions) are located at the vertical edges of the blocks.

3.3.2 Surface sensitivity and field perturbation approach

In the following, we define the surface sensitivity $S^{(\text{surf})}$ as a quality metric for quantifying which WG design leads to the potentially highest overall sensor sensitivity. In order to obtain $S^{(\text{surf})}$ for a specific WG with a specific surface layer, a full simulation of the WG with and without the surface layer would be required. This would include various combinations of surface layer properties like layer refractive index n_{SL} and layer thickness t_{SL} and thus requires a multitude of high-resolution simulations to resolve the surface layer with a thickness in the range of a few nanometers. Exploring the whole parameter space as discussed in Section 3.2 and Fig. 3.2 would hence be a time-consuming and probably unrealistic endeavor.

To overcome this problem we use a perturbation approach. To this end, we perform a single finite-element method (FEM) simulation of a bare WG for each WG geometry, store the resulting fields and compute the influence of an additional surface layer using a field interaction factor. This technique is only valid for small perturbations, i.e., the modal field does not change significantly with the surface layer, and hence the effective refractive index n_{e} changes only slightly, too. In our case, binding events of molecules change the refractive index of a surface layer of thickness t_{SL} from n_{M} to n_{SL}, where n_{SL} is the refractive index of the attached molecules and n_{M} denotes the background refractive index of the solution. The conditions for the perturbation approach hold, if either the thickness is small – then the refractive index change $n_{\text{SL}} - n_{\text{M}}$ can be larger – or if $n_{\text{SL}} - n_{\text{M}}$ is small, in which case t_{SL} can be larger.

We will first consider the general case of a z-variant SWG WG. According to Eq. (A.10) and Eq. (A.11) in Appendix A.3, the local perturbation in the surface layer can be translated into a change $\Delta n_{\mathrm{e}}^{(\mathrm{surf})}$ of the effective refractive index via the field interaction factor $\Gamma_{\mathrm{SL}}(t_{\mathrm{SL}})$,

$$\Delta n_{\mathrm{e}}^{(\mathrm{surf})} = (n_{\mathrm{SL}} - n_{\mathrm{M}})\Gamma_{\mathrm{SL}},$$

$$\Gamma_{\mathrm{SL}}(t_{\mathrm{SL}}) = \frac{1}{Z_0} \frac{\dfrac{1}{a} n_{\mathrm{M}} \iiint\limits_{V_{\mathrm{SL}}} |\underline{\mathbf{E}}|^2 \, \mathrm{d}V}{\iint \mathrm{Re}\left(\underline{\mathbf{E}} \times \underline{\mathbf{H}}^*\right) \cdot \mathbf{e}_z \mathrm{d}A} = \frac{c}{n_{\mathrm{g,SL}}} \frac{W_{\mathrm{SL}}}{P}. \tag{3.1}$$

Note that the field interaction factor $\Gamma_{\mathrm{SL}}(t_{\mathrm{SL}})$ in Eq. (3.1) is different from the intensity-related field confinement factor $\Gamma_i^{(\mathrm{conf})} = W_{\mathrm{SL}}/W$, because it describes also slow-light propagation, see Eq. (A.6). For computing $\Gamma_{\mathrm{SL}}(t_{\mathrm{SL}})$, we simulate the fields of a unit cell for a bare SWG WG without surface layers, and integrate $|\underline{\mathbf{E}}|^2$ over the fictitious surface layer volume V_{SL} within that unit cell of length a. The result is proportional to the electric energy W_{SL} in the surface layer per unit cell, Eq. (A.3) and Eq. (A.6) for $i = \mathrm{SL}$, normalized to the cross-sectional power P of Eq. (A.1). The integral in the denominator extends over the entire (x,y)-plane.

For z-invariant WG such as strip, slot, or double slot structures, Eq. (3.1) can be simplified by exploiting the fact that the integral over $|\underline{\mathbf{E}}|^2$ is invariant along z. Simplifying the volume integral in the numerator, we obtain

$$\Gamma_{\mathrm{SL}}(t_{\mathrm{SL}}) = \frac{1}{Z_0} \frac{n_{\mathrm{M}} \iint\limits_{A_{\mathrm{SL}}} |\underline{\mathbf{E}}|^2 \mathrm{d}A}{\iint \mathrm{Re}\left(\underline{\mathbf{E}} \times \underline{\mathbf{H}}^*\right) \cdot \mathbf{e}_z \mathrm{d}A} \tag{3.2}$$

for the special case of z-invariant WG. We use Eq. (3.2) to analyze $\Gamma_{\mathrm{SL}}(t_{\mathrm{SL}})$ for a set of widely different silicon strip WG geometries, operated in quasi-TE polarization, see in Fig. 3.5(a) "Perturbation". As a comparison, we extract the numerically exact values $\Gamma_{\mathrm{SL}}^{(\mathrm{sim})}(t_{\mathrm{SL}}) = \Delta n_{\mathrm{e}}^{(\mathrm{surf, sim})}/(n_{\mathrm{SL}} - n_{\mathrm{M}})$ from $\Delta n_{\mathrm{e}}^{(\mathrm{surf, sim})}$ obtained by FEM simulations of quasi-TE fields that include the actual surface

layers, and plot them in Fig. 3.5(a) with a dashed line "Simulation". The agreement is very good except for large surface layer thicknesses t_{SL} on narrow and high WG. In this case, the majority of the field is contained within the surface layers, violating the assumption of a small field perturbation. The electric field outside the core decays approximately exponentially. For a penetration depth much larger than t_{SL}, the decay of the field magnitude and of the power within the surface layer can be approximated by a linear function. As a consequence, Γ_{SL} in Fig. 3.5(a) exhibits a region where it depends linearly on t_{SL}.

We now want to define a sensing sensitivity that is – in the framework of the perturbation approach – independent of the surface layer thickness. This can be achieved by looking at the derivative $\partial \left(\Delta n_e^{(surf)} \right) \big/ \partial t_{SL}$ at $t_{SL} = 0$. Because n_{SL} influences the result, we define the surface sensitivity as the derivative of the field interaction factor with respect to the surface layer thickness,

$$\Delta n_e^{(surf)} = \left(n_{SL} - n_M \right) S^{(surf)} \Delta t_{SL} = \left(n_{SL} - n_M \right) S^{(surf)} t_{SL},$$

$$S^{(surf)} = \frac{\partial \Gamma_{SL}}{\partial t_{SL}} \bigg|_{t_{SL}=0}. \tag{3.3}$$

Within the framework of the perturbation approach, the surface sensitivity $S^{(surf)}$ is independent of both the thickness and the refractive index of the surface layer, thus providing a universal guideline for a sensor design. To confirm this, we calculate the derivatives $\partial \Gamma_{SL} / \partial t_{SL}$ for the same WG types as used in Fig. 3.5(a), and plot them semi-logarithmically in Fig. 3.5(b) in a range $t_{SL} = (1 \ldots 350)\, \text{nm}$. We see that $\partial \Gamma_{SL} / \partial t_{SL}$ is constant for very small $\Delta \varepsilon(\mathbf{r}) = \varepsilon_0 \cdot \Delta \varepsilon_r(\mathbf{r})$, owing to the approximately linear dependence of Γ_{SL} on t_{SL} in this region. We extrapolate the curve to $t_{SL} = 0$, where the computation fails due to the finite spatial discretization. In Fig. 3.5(b) these extrapolated values are marked with filled circles and denoted by $S^{(surf)}$, see Eq. (3.2) and Eq. (3.3). Note that a WG design for best homogeneous sensitivity $S^{(hom)} = \Gamma_M \approx \lim_{t_{SL} \to \infty} \left(\Gamma_{SL} \right)$ is not necessarily optimum when it comes to surface sensing, see Eq. (A.12) in Appendix A.3 for rigorous definition of $S^{(hom)}$. This can be inferred by comparing $S^{(hom)}$ of the two top strip WG in Fig. 3.5(a) (blue and red arrows) to the corresponding $S^{(surf)}$ of the same WG in Fig. 3.5(b) (blue and red dots at $t_{SL} = 0$): A larger homogeneous sensitivity does not lead

to a difference in surface sensitivity. In sensing applications, the desired measurement quantity is the effective surface layer thickness t_{SL}.
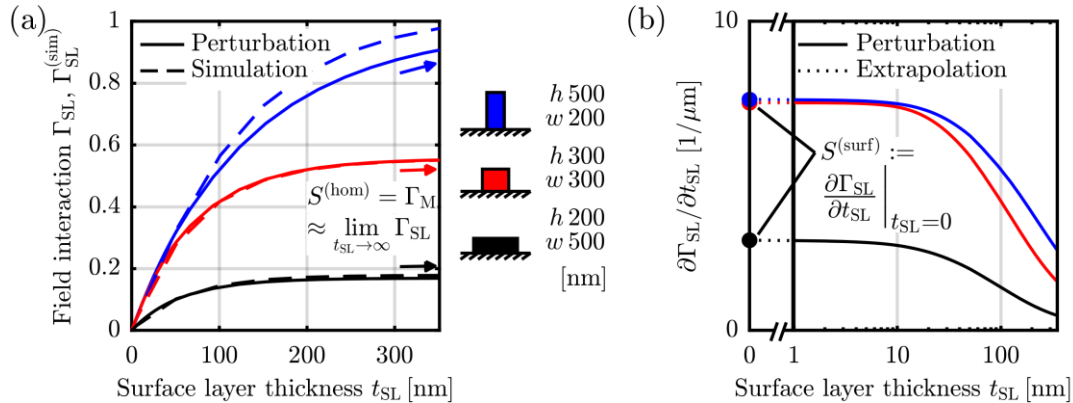
Fig. 3.5. Validation of perturbation model and definition of surface sensitivity $S^{(surf)}$ for a set of widely different silicon strip WG geometries propagating quasi-TE fields, see legend. **(a)** Field interaction factor Γ_{SL} in surface layer of thickness t_{SL}. For each geometry, we compare Γ_{SL} computed with a perturbation approach (based on a single FEM simulation without a surface layer) with $\Gamma_{SL}^{(sim)}$ obtained from numerically exact calculations (FEM simulations with different surface layers). For small t_{SL}, the agreement is very good. For large t_{SL} (marked by $\rightarrow$) and $n_{SL} \approx n_M$, the field interaction factor Γ_{SL} approaches Γ_M and thus the homogeneous sensitivity $S^{(hom)}$. **(b)** The surface sensitivity $S^{(surf)} = \partial\Gamma_{SL}/\partial t_{SL}\big|_{t_{SL}\to\infty}$ allows an easy comparison of different WG, irrespective of the actual surface layer properties.

From a measurement of Δn_e and for known bulk refractive indices n_{SL} and $\Delta n(\mathbf{r}) \ll n(\mathbf{r})$, t_{SL} can be inferred from (3.3). A proper choice of the WG then maximizes $S^{(surf)}$ and therefore the measurement sensitivity for t_{SL}.

3.4 Results

We extract the surface sensitivity $S^{(surf)}$ according to Section 3.3.2 for all kinds of WG outlined in Section 3.2.2. For each TE- or TM-operated WG core in Si_3N_4 or alternatively in Si, a few typical values of heights h, slot widths w_{slot}, periods a and fill factors FF are considered. For each combination of these parameters, the total WG width w (see Fig. 3.3) is then optimized to obtain optimum surface sensitivity $S_{opt}^{(surf)}$. To this end, the WG width is swept with a step size of 10 nm. The range of w was chosen to maintain single-mode operation and to avoid substrate leakage for a BOX thickness of $2\,\mu m$. The following

WG surface sensitivity analysis relates to Si_3N_4 cores operated in the VIS (Section 3.4.1) as well as to Si cores operated in the NIR (Section 3.4.2).

3.4.1   Silicon nitride with visible wavelengths

For Si_3N_4 strip WG operated at a vacuum wavelength of 600 nm, Fig. 3.6(a) displays the surface sensitivity $S^{(\mathrm{surf})}$ as a function of the WG width w for three different WG heights h and for both polarizations. Surface sensitivity generally benefits from large electric field strengths in the region of the surface layer as indicated in Fig. 3.3. Within their single-mode range, each WG shows a maximum $S_{\mathrm{opt}}^{(\mathrm{surf})}$ at a distinct width w_{opt}, marked by ● for TE and by ▲ for TM. Any deviation from this optimum width w_{opt} reduces the interaction factor of the mode field with the surface layers, e.g., by concentrating the modal field to the WG core in the case of large w, or by spreading the mode field over a wider cladding region for small w. In the second case, a large portion of the modal field propagates in the BOX, where it cannot contribute to sensing. In Fig. 3.6(b), the extracted w_{opt} (green, left vertical axis) and the corresponding $S_{\mathrm{opt}}^{(\mathrm{surf})}$ (magenta, right vertical axis) are plotted as a function of the WG height h. The largest $S_{\mathrm{opt}}^{(\mathrm{surf})}$ are found for large h and small w for both polarizations, with TE operation being more sensitive than TM operation. In the TE case, the two sides of the WG exploit the field enhancement, and only a small portion of the mode propagates in the BOX, see Section 3.5.2 for a detailed discussion.

We apply the same procedure to TE-operated Si_3N_4 slot and double slot WG and plot the results in Fig. 3.7. As for the strip WG, the sensitivity increases for higher WG. Decreasing WG width first leads to increasing sensitivity, which drops again as the width becomes too small and the mode extends far into the cladding, Fig. 3.7(a). Smaller slot widths increase the field strength in the slot, Fig. 3.7(b). This, together with the growth of the total core surface as compared to a strip WG, increases $S^{(\mathrm{surf})}$. The slot WG behaves as two strip WG if $w_{\mathrm{slot}} \gg w_{\mathrm{rail}}$. In this case, each of the strips carries half the power of the slot WG and both the optimum rail width and the optimum sensitivity converge to those of a single optimum strip WG, see top light green line (∞) and light magenta line (∞) in Fig. 3.7(b).The double slot WG behaves like three separate strip WG if $w_{\mathrm{slot}} \gg w_{\mathrm{rail}}$. In this case, each strip carries one third of the power

of the slot WG. As before, both the optimum rail width and the optimum sensitivity converge to those of a single optimum strip WG, see top light green line (∞) and light magenta line (∞) in Fig. 3.7(c) and in Fig. 3.7(d).
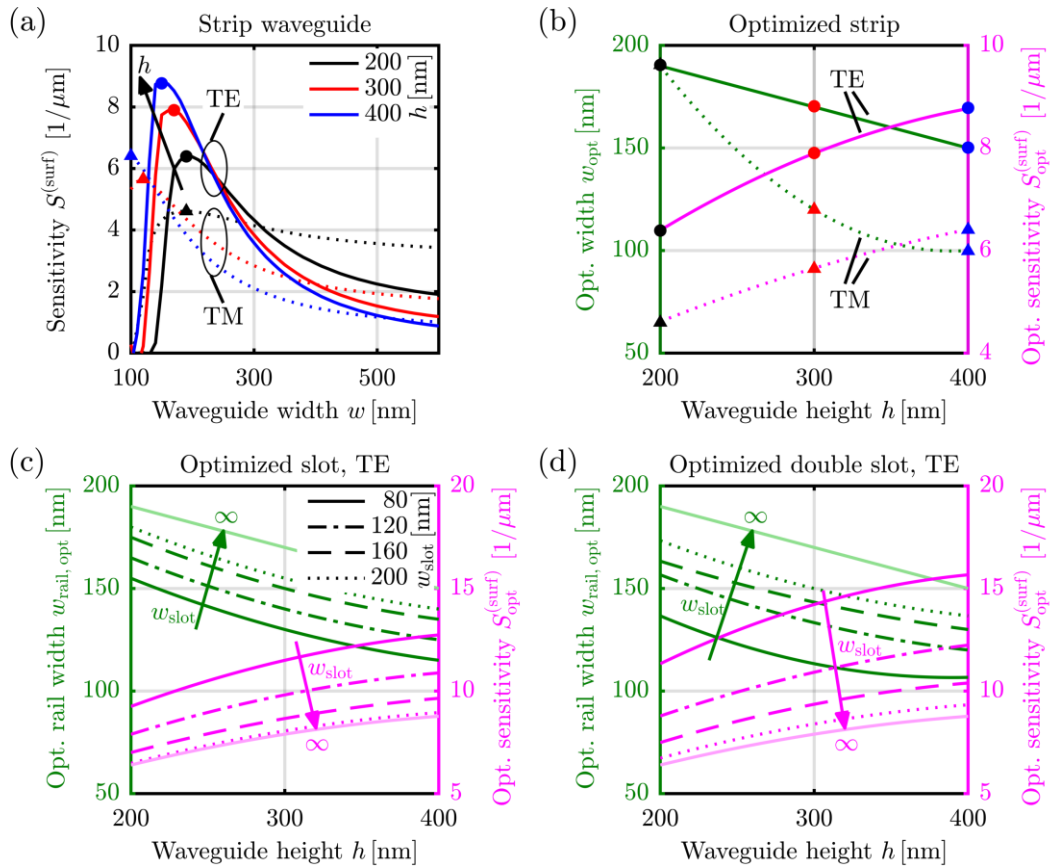
Fig. 3.6. Optimization of Si₃N₄ strip WG. **(a)** Surface layer sensitivity $S^{(\mathrm{surf})}$ of Si₃N₄ strip WG for three standard heights h as a function of WG width w in TE and TM operation. For decreasing WG width, the sensitivity first increases to its maximum value and then drops. The drop is caused by the fact that the mode extends far into the cladding or is even lost to the substrate for very small WG widths. The optimum sensitivities $S^{(\mathrm{surf})}_{\mathrm{opt}}$ at the corresponding optimum widths w_{opt} are marked by dots and triangles. **(b)** Comparison of optimum WG width (green, left axis) and optimized surface sensitivity (magenta, right axis) as a function of WG height. High and narrow WG (blue markers) are most sensitive.
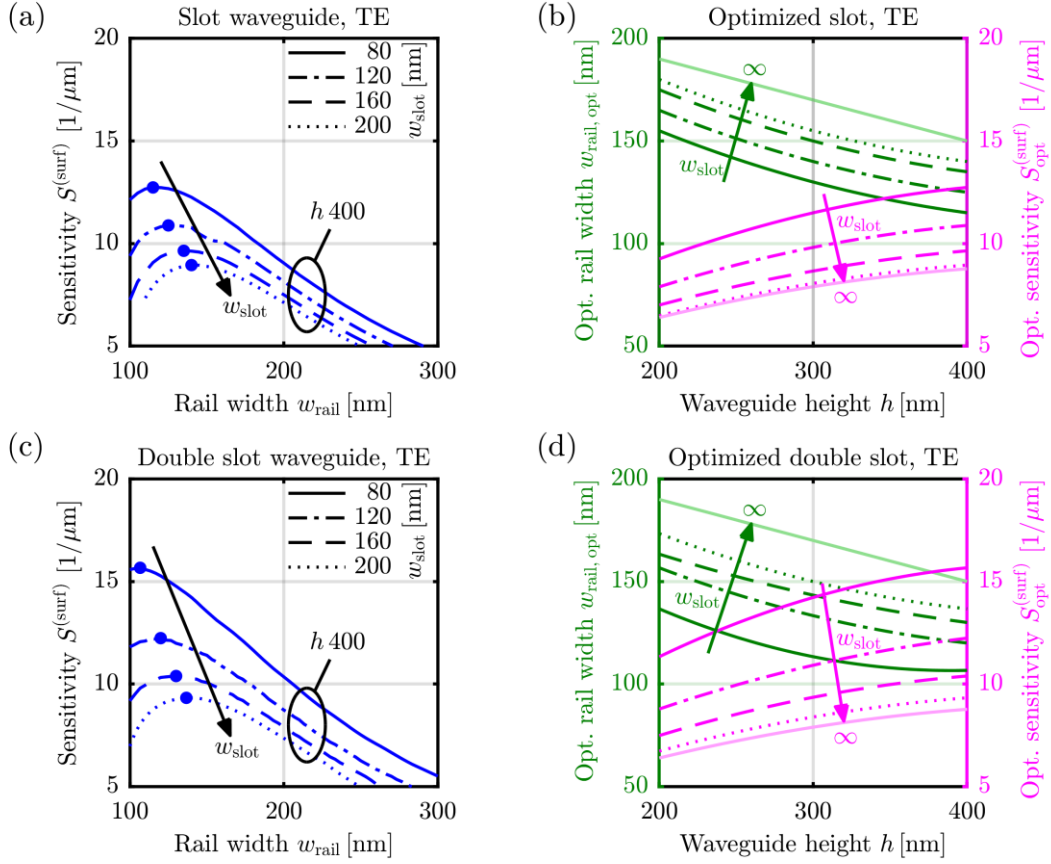
Fig. 3.7. Optimization of Si₃N₄ TE-operated slot and double slot WG. **(a,c)** Surface layer sensitivity $\mathbf{H}(t,\mathbf{r}) = \mathbf{H}(\mathbf{r})e^{j\omega t}$ of Si₃N₄ slot and double slot WG for a height of $h = 400$ nm as a function of rail width w for different slot widths. For decreasing rail width, the sensitivity first increases to its maximum value and then drops. The drop is caused by the fact that the mode extends far into the cladding or is even lost to the substrate for very small rail widths. The optimum sensitivities $S_{\mathrm{opt}}^{(\mathrm{surf})}$ at the corresponding optimum widths w_{opt} are marked by dots. **(b,d)** Optimized geometries for slot and double slot Si₃N₄ WG. Sensitivities are larger for small slot widths and higher WG, the fabrication of which is limited by technological constraints. The light solid lines indicate the limits for $w_{\mathrm{slot}} \to \infty$ (light green and light magenta).

3.4.2 Silicon with near-infrared wavelengths

For silicon WG operated in the NIR at $\lambda = 1550\,\mathrm{nm}$, we apply the same technique as described in Section 3.4.1 for extracting the optimized widths w_{opt} and sensitivities $S_{\mathrm{opt}}^{(\mathrm{surf})}$. In Fig. 3.8(a), we display the surface sensitivity $S^{(\mathrm{surf})}$ of a strip WG with different heights h and polarizations as a function of the strip width w. As for Si_3N_4 strip WG, Fig. 3.6(a), we see a sensitivity maximum within the range of single-mode operation. The TE sensitivity exhibits a pronounced maximum when varying the WG width, whereas the maximum of the TM sensitivity is much less pronounced, Fig. 3.8(a).

We extract the optimum sensitivity and find that, similar to Si_3N_4, the TE sensitivity can be optimized by choosing a high WG with a narrow width, while the optimum TM sensitivity depends only weakly on the WG height, Fig. 3.8(b). This is in contrast to the findings for the Si_3N_4 WG, Fig. 3.6(a) and Fig. 3.6(b). We attribute this to the fact that the refractive index of Si is significantly larger than that of Si_3N_4 and hence the asymmetry introduced by the underlying BOX is less significant for the case of Si WG. Consequently, for the WG heights h under consideration and for small w, the TM modal field does not extend into the BOX as strongly as for the Si_3N_4 WG. Regarding Si slot and double slot WG, Fig. 3.8(c) and Fig. 3.8(d), the trends for optimum WG parameters are similar to those of Si_3N_4 WG, Fig. 3.7, and thus the same conclusions as in Section 3.4.1 can be drawn.

For achieving better sensitivities, completely different WG structures in form of sub-wavelength gratings (SWG) were proposed [4,6,7], see Fig. 3.4. For a systematic comparison to strip and slot WG, we calculate and optimize the surface sensitivities of SWG WG, see Fig. 3.9. Fig. 3.9(a), left y-axis, shows the results obtained from two exemplary families of TE-operated SWG, which share the same period a, but differ in height h, and feature three different fill factors (50%, 60%, 70%, differing in opacity). For the smaller WG height ($h = 220\,\mathrm{nm}$, black lines) the sensitivity does not depend strongly on the WG width. Strip and slotted WG show a fast decrease of sensitivity for widths larger than w_{opt}, since the fields become smaller at the sensitive sidewalls and upper surfaces and are more confined to the core.
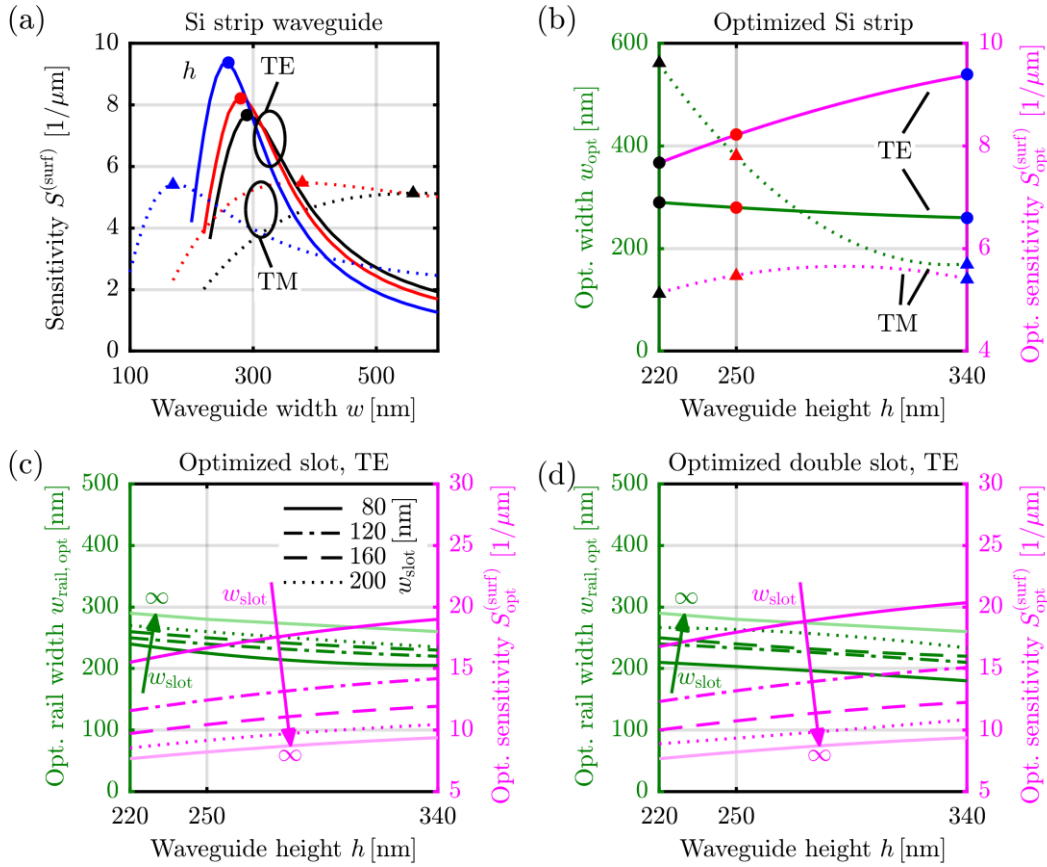
Fig. 3.8. Optimization of Si strip, slot and double slot WG. **(a),(b)** Surface layer sensitivity $S^{(\text{surf})}$ for Si strip WG with three standard heights h as a function of WG width w in TE and TM operation. For decreasing WG width, the sensitivity first increases to its maximum value and then drops. The drop is caused by the fact that the mode extends far into the cladding or is even lost to the substrate for very small WG widths. The optimum sensitivities $S^{(\text{surf})}_{\text{opt}}$ at the corresponding optimum widths w_{opt} are marked by dots and triangles in (a) and compared in (b). For TE polarization, high and narrow WG yield the best results. For TM, no pronounced sensitivity gain is observed for higher WG. **(c),(d)** Optimized geometries for slot and double slot Si WG. The sensitivity increases for smaller slot widths and higher WG, the fabrication of which is limited by technological constraints. The light solid lines indicate the limits for $w_{\text{slot}} \to \infty$ (light green and light magenta), which correspond to the case of individual strip WG as shown in (b). Compared to Si_3N_4, operated in the VIS, the Si rails, operated in the NIR, are typically 100 nm wider while the sensitivity is slightly larger.

This effect is less pronounced in the SWG WG, since the sensitive surface in between the individual blocks are still experiencing high field strengths. The maximum sensitivity shifts to smaller w, when the FF increases. This is to be expected: If the FF becomes larger, the effective refractive index increases and
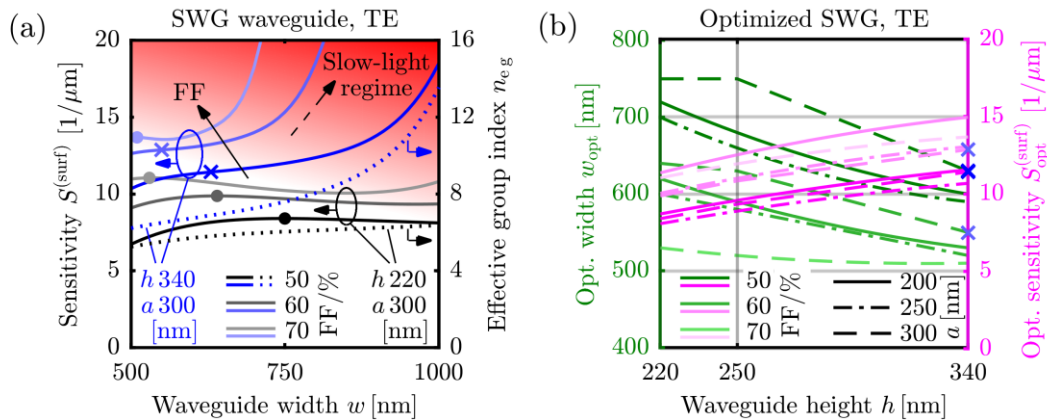
Fig. 3.9. Optimization of Si sub-wavelength grating (SWG) WG. **(a)** Sensitivity of two SWG WG families with different heights, but common period $a = 300\,\text{nm}$ as a function of WG width w for varying fill factors FF. Black lines with various shadings stand for a WG height of $h = 220\,\text{nm}$. In this case, the sensitivity does not change significantly with w. For higher SWG WG ($h = 300\,\text{nm}$, blue lines), the sensitivity traces do not exhibit an optimum before entering into the so-called slow-light regime, where the sensitivity is dominated by a largely increased effective group index n_{eg} (dotted lines for two different heights for FF = 50%). For these traces, we choose the inflection points (blue crosses) to define reasonable sensor designs that are not subject to the impairments associated with slow-light operation. Note that this does not represent an optimum in a strict mathematical sense. **(b)** Overview of optimized SWG WG sensitivities and geometries outside the slow-light regime for different heights, periods, and fill factors. As a trend, the sensitivity increases for high WG and small gap size $d_{\text{gap}} = a(1 - \text{FF})$. Sensitivities obtained from inflection points at the transition to slow-light operation are again marked by blue crosses. Note that the traces for FF = 70% and a = 200 nm or a = 250 nm do not appear in the plot since the associated gap sizes are below the minimum feature size of 80 nm.

the modal field is stronger confined to the SWG "core". For a sufficient influence of the analyte, the field must then extend into the SWG "cladding", which is achieved by decreasing the WG width.

Interestingly, for higher SWG WG ($h = 340\,\text{nm}$, blue lines), no optimum sensitivity within the observed range of w is found. Instead, the sensitivity increases strongly for larger FF and wider WG. This increase is caused by a decrease of the group velocity: Larger FF and increased w lead to an increase of the Bragg wavelength associated with the SWG structure. Once the Bragg wavelength comes close to the operation wavelength of the sensor, the device enters the so-called slow-light regime [8], which is characterized by a greatly reduced group velocity and a greatly increased effective group index n_{eg}.

This leads to strong interaction of the guided mode with the surface layer and hence to a sharp increase of the sensitivity even though the field confinement $\Gamma_i^{(\text{conf})}$ of the surface layer does not significantly increase, see Appendix A.3, Eq. (A.3). Note, however, that operation in the slow-light regime strongly increases the detrimental impact of environmental influences and fabrication tolerances [45] on mode propagation. Amongst others, the sensitivity and the optical propagation loss can vary significantly, such that reproducible device properties and hence a reliable sensor read-out are difficult to obtain in practice. This susceptibility to tiny changes can be seen exemplarily for the sensitivity of WG operating in the slow-light regime, Fig. 3.9(a), which is why we exclude them from the following discussion. For sensitivity traces entering into the slow-light regime without showing a pronounced maximum in Fig. 3.9(a), we choose the inflection points (blue crosses) to define reasonable sensor designs that are not subject to the impairments associated with slow-light operation without being optimum in a strict mathematical sense. Note that there is no distinct transition from "normal" SWG operation to the slow-light regime and that a strict classification is therefore difficult. The choice of the inflection point is motivated by the fact that it marks the width at which the influence of the increased effective group index n_{eg} starts dominating over the impact of the field confinement factor $\Gamma^{(\text{conf})}$, Eq. (A.6) in Appendix A.3, and dotted lines for two different heights for $\text{FF} = 50\%$, see Fig. 3.9(a).

The optimal sensitivities of the SWG WG and those obtained for the transition to the slow-light regime are summarized in Fig. 3.9(b), indicating again a general sensitivity increase with WG height. Sensitivities obtained from inflection points at the transition to slow-light operation are marked by blue crosses. As a trend, $\mathbf{E}(\mathbf{r})$ increases for small $d_{\text{gap}} = a(1 - \text{FF})$.

3.4.3 Comparison of optimized sensitivities

As a summary of the last two subsections, we compare the sensitivities for the Si_3N_4 platform in the VIS ($\lambda = 600\,\text{nm}$) and for the Si platform in the NIR ($\lambda = 1550\,\text{nm}$). In Fig. 3.10, we display the optimized surface layer sensitivities $S_{\text{opt}}^{(\text{surf})}$ of four WG types (strip, slot, double slot, SWG) with optimized widths w_{opt} and three different heights h for each platform. The left (right) panel

shows the results for TE (TM) polarization. Three SWG positions are empty because either the gap size is below the minimum feature size of 80 nm, or because the structures do not support a well-guided WG mode ("poor waveguiding").

Generally, WG operated in TE polarization tend to be more sensitive than their TM-operated counterparts are. Taking into account technological constraints such as a minimum feature size, the sensitivity of sophisticated WG designs can be increased by approximately a factor of two compared to a simple optimized strip WG. Moreover, slotted WG exhibit higher surface sensitivities than strip and SWG WG do. Generally, the silicon platform exhibits higher sensitivities than the silicon nitride platform, which can be attributed to the fact that a higher index contrast leads to a smaller penetration depth into the WG cladding and hence to a stronger interaction with a thin surface layer. Larger WG heights tend to be generally better. For the silicon photonic platform, a sensitivity improvement of a factor of four can be achieved by using optimum double slot WG operating in TE polarization instead of non-optimum standard strip WG featuring, e.g., WG dimensions of $w \times h = 450 \times 220\,\mathrm{nm}^2$ for TM operation. A detailed physical explanation of these trends is given in Section 3.5.2.

3.5 Discussion

For a better understanding of the trends summarized in Fig. 3.10, we first discuss in Section 3.5.1 the influence of the cladding asymmetry and we introduce universal scaling laws of Maxwell's equations that allow generalizing the findings to other wavelengths and material platforms. Subsequently, Section 3.5.2 explains in detail the trends when varying platform, operating wavelength, polarization, and WG geometry. Section 3.5.3 discusses our results in view of an overall sensor performance, including the impact of mode loss and analyte delivery as well as a practical instruction on finding global sensitivity optima.

3.5.1   Physical interpretation — Cladding asymmetry and scaling laws

Cladding asymmetry   We consider WG cores that are supported by a SiO_2 substrate (BOX) and are surrounded by an aqueous medium. Since the refractive index of SiO_2 is larger than that of water, the cladding of the WG is asymmetric. It is hence impossible to increase the interaction of the guided light with the functionalized surface of the WG core by indefinitely reducing the core dimensions. Any attempt to do so will predominantly increase the fraction of the mode fields in the BOX, which do not contribute to sensing, and therefore decrease the fraction in the surface layer, leading to a decrease of surface sensitivity.

Scaling laws   According to Appendix A.4, Table A.**1**, line (1), scaling the geometry of a WG by σ_g while simultaneously scaling the operating frequency by $\sigma_\omega = 1/\sigma_g$ leads to a simple geometrical scaling of the eigenfunctions of the electric and magnetic fields by a factor of σ_g. This effect has no impact on the homogeneous sensitivity, since the relative portion of the mode fields in the cladding medium remains the same. However, the surface sensitivity Eq. (3.3) as defined by a derivative with respect to the layer thickness t_{SL} scales by $1/\sigma_g$. *The optimum surface sensitivity of a WG with fixed RI profile hence scales proportionally to frequency and requires an inverse scaling of the geometry*.

Furthermore, scaling the refractive index profile of a WG by σ_n while simultaneously scaling the operating frequency by $\sigma_\omega = 1/\sigma_n$ does not change the distributions of the electric and the magnetic field. Note, however, that the ratio of the electric-field eigenfunction $\underline{\mathbf{E}}(\mathbf{r})$ and the magnetic field eigenfunction $\underline{\mathbf{H}}(\mathbf{r})$ must be scaled by a factor of $1/\sigma_n$, see Eq. (A.15) and the corresponding discussion. In total, this leaves the sensitivity unchanged, see Appendix A.4, Table A.**1**, line (2). *The optimum surface sensitivity of a WG with fixed geometry does not change for a scaling of the RI profile along with an inverse scaling of the frequency*.

3.5.2 Trends for increased surface sensitivity

High index-contrast platform   The surface sensitivity is maximized by an increased field concentration at the core surface that is in contact with the analyte-delivering aqueous medium. For a given wavelength, the surface sensitivity tends to increase if the refractive index ratio $n_{\text{core}}/n_{\text{M}}$ between core and cladding is increased. This is caused by the fact that the enhancement of surface-normal electric-field components is proportional to the square $\left(n_{\text{core}}/n_{\text{M}}\right)^2$ of the index ratio. Similarly, the surface sensitivity increases when the refractive index profile is scaled up by a factor of $\sigma_{\text{n}} > 1$ while the geometry is scaled down by $\sigma_{\text{g}} = 1/\sigma_{\text{n}}$ to maintain the same operating frequency, see Appendix A.4, Table A.**1**, line (4).

Short operating wavelength   For a given platform, higher surface sensitivities can be achieved with shorter wavelengths. The geometry of the WG has to be chosen guided by the scaling law in Appendix A.4, Table A.**1**, line (1). A Si_3N_4 WG operated in the VIS will achieve a higher optimized surface sensitivity than an up-scaled Si_3N_4 WG operated in the NIR.
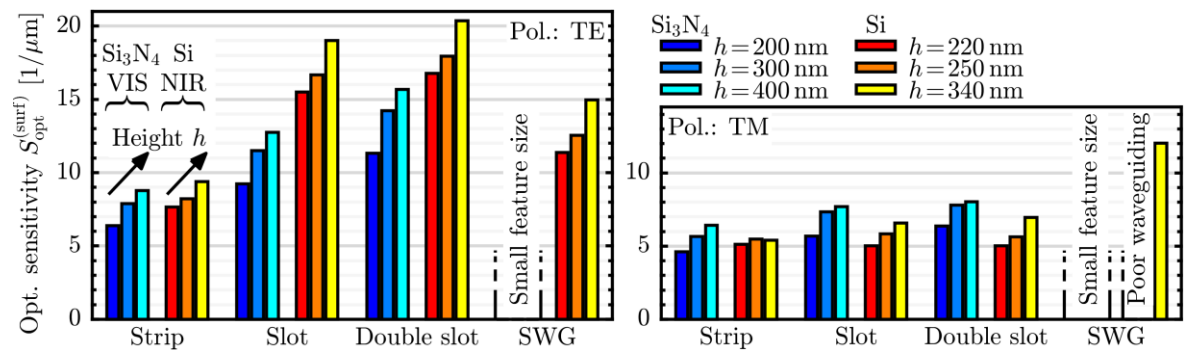
Fig. 3.10. Comparison of the optimized sensitivity for the Si_3N_4 platform in the VIS ($\lambda = 600$ nm) and for the Si platform in the NIR ($\lambda = 1550$ nm). We consider four WG types with three standard heights, operated in TE and TM polarization. Sensitivity can be increased by higher WG cores, by using Si rather than Si_3N_4, and by TE-operation instead of TM. The three more advanced WG types (slot, double slot and SWG) offer an enhancement of up to a factor of two compared to TE strip WG, coming at the cost of a more complex fabrication process. Some SWG WG are excluded either because the gap size is below 80 nm ("small feature size"), or because the structures do not support a well-guided WG mode ("poor waveguiding"). Typical slot, double slot and SWG WG do not benefit from TM operation.

When comparing optimized Si_3N_4 WG operated in the VIS with Si WG in the NIR, we see similar sensitivities, see Fig. 3.10. This is due to a combination of scaling the operating frequency along with WG geometry and an increase of the index contrast, which have contrary effects on the surface sensitivity that partially cancel each other. However, optimized WG in the high index-contrast Si platform will be as good as or better than those in the Si_3N_4 platform, as the limitation caused by the cladding asymmetry is more severe for lower core refractive indices.

TE polarization The TE-mode sensitivity generally outperforms that of the TM-mode. For high index-contrast WG as considered in this work, the surface sensitivity is dominated by regions exhibiting a large field enhancement due to field discontinuities at the core-cladding interface. In the case of strip WG and of vertical-slot WG, TE mode operation exploits more of these surfaces showing a field enhancement compared to TM mode operation, where the interface to the bottom oxide cladding (BOX) does not contribute to the sensitivity.

It has to be noted that in typical telecom applications, WG with large widths and small heights are used (e.g., $w \times h = 450 \times 220\,\mathrm{nm}^2$). These established WG geometries are often directly transferred to sensing applications. For these WG and for improper choices of WG widths exceeding 400 nm, the TM-polarized mode may exhibit higher sensitivity than the TE, see Fig. 3.8(a). However, under the assumption that the width w is chosen properly, TE-polarized modes exhibit optimized sensitivities. If an application demands Si WG operated with TM polarized light, SWG WG are best, see Fig. 3.10.

Enlarged surface Larger core surfaces can generally lead to higher sensitivities. This is exploited by slot, double slot and SWG WG, which introduce additional sensor surfaces compared to strip WG. For slot and double slot WG operated in TE polarization, these additional surfaces lead to an enhancement of the dominant transvers electric-field component and can hence further increase surface sensitivity, see Fig. 3.3. For SWG WG, the enhancement at the additional surfaces between the blocks affects the weaker longitudinal electric-field component, Fig. 3.4. The sensitivity gain of SWG WG is hence smaller than that of slot and double slot WG and depends only weakly on the polarization.

Narrow waveguides Optimized sensing WG have a narrower core than typical routing WG designed for low-loss light transport. Narrow WG increase the sensitivity for both TE and TM polarization. When narrowing the WG, the sensitive area of the surface layer remains essentially constant for TE polarization, but the surface field strength initially increases. For very small WG widths, the modal field expands into the cladding and the field interaction with the surface layer decreases, hence reducing surface sensitivity. For TM polarization, an additional effect comes into play: When reducing the WG width, the top surface, containing high field strengths due to the field discontinuity, becomes smaller, while the overall field strengths at the core surface become more dominant as the mode expands into the cladding. This interplay leads to a less pronounced optimum with respect to the WG width than for TE polarization, see Fig. 3.6 and Fig. 3.8.

High waveguides Higher WG cores outperform thinner WG cores. Higher WG cores reduce the relative portion of the fields located in the BOX (cladding asymmetry). Since this area does not contribute to sensing, less field strength in the BOX leads to larger sensitivities. In addition, and especially for the TE mode, higher WG cores enlarge the sensitive sidewall regions that are subject to field enhancement.

Small slot widths and gap sizes Smaller slot widths and gap sizes generally increase the sensitivity. For slot WG, the sensitivity gain for TE is more pronounced than for TM polarization.

3.5.3 Overall sensor system performance and the impact of mode loss

It is important to note that, when implementing these WG into functional sensors, the overall system performance will also depend on additional aspects that are outside the scope of our current analysis. One of the most important aspects is the propagation loss of the optical mode: Adsorption of target molecules to the WG surface is usually measured by recording the phase shift accumulated over a certain propagation length L. In technical implementations of sensors,

the phase measurement accuracy depends on the precision with which amplitudes can be measured in an interference setup. This precision and ultimately the detection limit of the sensor system decreases with increasing propagation losses, which, like the sensitivity, depends on WG platform, type, polarization and geometry. A rigorous system optimization would ideally have to take into account all these effects to account for mutual trade-offs and to find a global optimum of the WG design. This, however, would require a quantitative relationship between the WG geometry and the associated power propagation loss $\exp(\alpha L)$ characterized by the loss constant α, which is impossible to state in a general and reliable manner across different integration platforms.

For finding optima for the overall system sensitivity S_{sys} for a specific sensor implementation, we need to know three dependencies: The surface sensitivity $S^{(\mathrm{surf})}$ as a function of the WG geometry, provided in this chapter, the WG loss constant α as a function of the WG geometry, which must be experimentally determined for the specific WG type and technology, and the influence of this loss on the effective-index sensitivity $\underline{\mathbf{H}}\left(\mathbf{r}'/\sigma_{\mathrm{g}}\right), \underline{\mathbf{E}}\left(\mathbf{r}'/\sigma_{\mathrm{g}}\right)$, which translates $\Delta n_{\mathrm{e}}^{(\mathrm{surf})}$ into a measurable output signal, e.g., a current [10,25,28]. If the linewidth of the light source is neglected, the overall system sensitivity can be expressed by the product of the surface sensitivity and the effective-index sensitivity

$$S_{\mathrm{sys}} = S^{(\mathrm{surf})} S_{\mathrm{e}}(\alpha).$$
(3.4)

The results presented in this chapter can hence serve both as guidelines for identifying and selecting promising WG designs and as quantitative measures to determine the overall system sensitivity S_{sys} once the technology-dependent loss constant α and the architecture-specific relationship $S_{\mathrm{e}}(\alpha)$ are known.

Another aspect that may influence the overall performance of practical sensors is the analyte delivery to the sensor surface. In this context, narrow gaps or other high aspect-ratio voids tend to have less exchange with the surrounding liquid or might even not be accessible to large target objects such as cells or cellular vesicles. In these cases, simple strip WG geometries might exhibit advantages in comparison to more complex concepts featuring narrow strips and slots.

3.6   Summary: Photonic sensor waveguides

We have performed a comparative study of different WG types for application in label-free detection of chemical or biological analytes that specifically bind to functionalized WG surfaces. To this end, we have introduced the so-called surface sensitivity $S^{(\mathrm{surf})}$ as a general quality metric that is broadly applicable to surface layers of different thicknesses and refractive indices. This metric allows to optimize the WG design and to compare the fundamentally achievable sensor performances across different WG types and integration platforms. We specify optimized WG designs along with the corresponding surface sensitivities for the most common WG parameter combinations. We also introduce and explain a computationally efficient recipe for applying the methodology to additional WG types that are not covered by our current study.

The following key findings result from our study: First, sensitivity trends can be explained by the interplay of a cladding asymmetry, the scaling laws of Maxwell's equations and the effect of field enhancement. Second, WG with optimum surface sensitivities are typically high and narrow, are fabricated on high-index contrast platforms and operated in TE polarization. Third, the surface sensitivity of highly sophisticated WG such as slot, double slot or sub-wavelength grating exceeds that of optimized strip WG by a factor of two, and that of standard telecom strip WG by a factor of four if realistic feature size constraints are observed.

[end of publication [J1]]

4 Sensor optimization by system design

This chapter analyzes the performance and limitations of the entire photonic sensor system, including the phase-sensitive photonic circuits, light sources and detectors, as well as the electrical readout. A special focus is laid on systems that are geared towards cost-efficient production and large-scale deployment, including variation of component parameters that are inherently linked to mass production and energy-efficient system operation under realistic conditions.

The following sections are taken from the publication [J2]. In order to fit the structure and layout of this document, they were adapted accordingly. Appendices associated with this manuscript can be found in Appendix B.

[start of publication [J2]]

Integrated phase-sensitive photonic sensors: A system design tutorial

Johannes Milvich[1,2,*], Daria Kohler[1], Wolfgang Freude[1] and Christian Koos[1,3]

[1] Institute of Photonics and Quantum Electronics (IPQ), Karlsruhe Institute of Technology (KIT), Engesserstr. 5, 76131 Karlsruhe, Germany

[2] Robert Bosch GmbH, Robert-Bosch-Campus 1, 71272 Renningen, Germany

[3] e-mail: christian.koos@kit.edu

[*] Corresponding author: johannes.milvich@bosch.com

Abstract: Photonic integration has seen tremendous progress over the previous decade, and several integration platforms have reached industrial maturity. This evolution has prepared the ground for miniaturized photonic sensors that lend themselves to efficient analysis of gaseous and liquid media, exploiting large interactions lengths of guided light with surrounding analytes, possibly mediated by chemically functionalized waveguide surfaces. Among the various sensor concepts, phase-sensitive approaches are particularly attractive: Offering a flexible choice of the operation wavelength, these schemes are amenable to large-scale integration on mature technology platforms such as silicon photonics or silicon nitride (Si_3N_4) that have been developed in the context of tele- and data-communication applications. This paves the path towards miniaturized and robust sensor systems that offer outstanding scalability and that are perfectly suited for high-volume applications in life sciences, industrial process analytics, or consumer products. However, as the maturity of the underlying photonic integrated circuits (PIC) increases, system-level aspects of mass-deployable sensors gain importance. These aspects include, e.g., robust system concepts that can be operated outside controlled laboratory environments as well as readout

schemes that can be implemented based on low-cost light sources, without the need for benchtop-type tunable lasers as typically used in scientific demonstrations.

It is thus the goal of this tutorial to provide a holistic system model that allows to better understand and to quantitatively benchmark the viability and performance of different phase-sensitive photonic sensor concepts under the stringent limitations of mass-deployable miniaturized systems. Specifically, we explain and formulate a generally applicable theoretical framework that allows for a quantitatively reliable end-to-end analysis of the overall signal chain. Building upon this framework, we identify and explain the most important technical parameters of the system, comprising the photonic sensor circuit, the light source, the detector, as well as the readout and control scheme. We quantify and compare the achievable performance and the limitations that are associated with specific sensor structures based on Mach-Zehnder interferometers (MZI) or high-Q optical ring resonators (RR), and we condense our findings by formulating design guidelines both for sensor concepts. As a particularly attractive example, we discuss an MZI-based sensor implementation, relying on a vertical-cavity surface-emitting laser (VCSEL) as a power-efficient low-cost light source in combination with a simple and robust readout and control scheme. In contrast to RR-based sensor implementations, MZI can be resilient to laser frequency noise, at the cost of a slightly lower sensitivity and a moderately increased footprint. To facilitate the application of our model, we provide a Matlab-based application that visualizes the underlying physical principles and that can be readily used to estimate the achievable performance of a specific sensor system. The system-level design considerations are complemented by an overview of additional aspects that are important for successful sensor-system implementation such as the design of the underlying waveguides, photonic system assembly concepts, and schemes for analyte handling.

4.1 Introduction

Waveguide-based photonic sensors lend themselves to precise and highly sensitive analysis of a wide range of gaseous and liquid media [25–30], exploiting large interaction lengths of guided light with the surrounding analyte [46], possibly mediated by functionalized waveguide surfaces [47–49]. Utilizing established photonic integration platforms such as silicon photonics [50–53] or silicon nitride [54–57], photonic sensors are amenable to miniaturization and cost-efficient mass production and allow for massively parallel integration of multiplexed arrays on a single photonic chip [58]. Over the previous years, such devices have found their way into first commercial products [59–66], and this evolution will continue: Driven by the need for ubiquitous data acquisition in an increasingly connected world, often described by internet-of-things (IoT) scenarios, research efforts in the field of photonic sensors have intensified, and the application areas of such devices steadily expand. However, most of the associated proof-of-concept experiments are still performed in controlled laboratory environments, often relying on benchtop-type measurement equipment such as highly stable tunable lasers or high-resolution spectrometers for operation and readout. While these demonstration have shown impressive results [25,26,29,30,46–49], the question arises to which extent the associated performance can be transferred to highly integrated mass-deployable sensor systems that rely on, e.g., non-ideal light sources with limited emission power that suffer from environmental influences such as thermal drift, and that are subject to noise as well as limited resolution of analog-to-digital converters (ADC).

It is thus the goal of this tutorial to introduce and explain a comprehensive model for waveguide-based photonic sensor systems that allows to estimate the impact of the various non-idealities on the overall system performance and that can be used for comparing and designing sensor systems for operation under real-world constraints. Building upon the existing literature, we focus our analysis on phase-sensitive schemes, which are particularly attractive for highly scalable low-cost systems: In contrast to absorption-based spectroscopic sensors, where the operation wavelength is dictated by the spectral characteristics of the respective analytes, phase-sensitive concepts are much more flexible with respect to the readout wavelength. This allows to choose operating wavelengths

for best compatibility with highly mature integration platforms such as silicon-on-insulator or silicon nitride that have been developed in the context of data- and telecommunication applications. In our analysis, we investigate different implementations of ring resonators (RR) and Mach-Zehnder interferometers (MZI), which represent the most widely used concepts for phase-sensitive integrated photonic sensors. As a particularly attractive scenario, we consider the use of vertical-cavity surface-emitting lasers (VCSEL) as compact and efficient light sources, along with simple photodiodes for detection. We experimentally verify our theoretical models, provide design guidelines, and quantify achievable performance parameters of the various sensor concepts. We find that high-Q RR, while showing excellent performance in laboratory experiments, are particularly prone to laser frequency noise, which turns out to dictate the limit of detection (LoD) when using mass-producible semiconductor lasers with linewidths in the MHz range. In contrast to that, properly designed MZI-based sensors are much less sensitive to laser frequency noise while offering simple operation along with detection limits that can well compete with those of high-Q micro-resonators. Along with the paper, we provide a Matlab application that allows to estimate and compare the sensitivity and LoD of different sensor-system implementations based on noise parameters of the light source and the detection system.

This paper is structured as follows: Section 4.2 gives a brief overview of the state of the art of waveguide-based photonic sensors and the associated commercial products. Section 4.3 introduces a generic mathematical description of phase-sensitive sensor systems along with the model used for deriving the sensitivity and the associated LoD. Section 4.4 provides a quantitative analysis of the sensitivity and the LoD of typical RR- and MZI-based sensor implementations. In Section 4.5, we experimentally validate the model regarding the impact of laser frequency-noise on the LoD, using a low-cost 1550 nm VCSEL as a test device and a bench-top tunable light source (TLS) as a reference. Section 4.6 condenses the key findings of the analysis into a set of guidelines for sensor design. Section 4.7 provides an overview of additional aspects that are important for a successful implementation of integrated photonic sensor systems and that are covered in the broader literature. An overall summary is found in

Section 4.8. Details and mathematical descriptions of the signal and noise models are given in Appendices B.1…B.6.

4.2   Waveguide-based photonic sensors: State of the art and commercial products

This tutorial builds on the existing scientific literature and introduces a model that allows to estimate the performance of miniaturized phase-sensitive photonic sensor systems. As a starting point for this analysis, the following paragraphs provide an overview of the literature related to waveguide-based photonic sensors and of commercial products that rely on such devices.

On the scientific side, waveguide-based photonic sensors have been subject of intensive research activities over the previous decade, and the number of publications is steadily increasing. A comprehensive overview of the current state of the art can be found in several scientific review articles, e.g., by Luan *et al.* for silicon photonic biosensors using label-free detection techniques [67], by Zou *et al.* for mid-infrared silicon photonic waveguides and devices [68], by Makarona *et al.* for point-of-need bioanalytics based on planar optical interferometry [69], or by Gavela *et al.* for silicon photonic biosensors [70]. These review papers provide an overview of concepts and experimental demonstrations of integrated sensors along with a comparison of experimentally demonstrated performances in terms of sensitivity and LoD. Application demonstrations range from classical refractive-index (RI) sensors to biosensors that exploit chemically functionalized waveguide surfaces for label-free detection of cells, bacteria, viruses, or biomolecules such as proteins or nucleic acids.

Fostered by such research, waveguide-based sensors have found their way into first commercial products. Prominent examples are handheld trace-gas sensors based on absorption spectroscopy [59,60] or disposable sensor chips for bio-diagnostics that exploit resonance shifts in photonic crystals [61–64] or in highly multiplexed RR arrays [58,65,66]. This evolution will continue, and highly scalable miniaturized sensor systems will gain importance, building the base for ubiquitous data acquisition in an increasingly connected world. In this

context, rapid transition from proof-of-concept laboratory demonstrations to commercially viable sensor systems is key. In the following sections, we focus on integrated phase-sensitive photonic sensors, and we introduce a quantitatively reliable model that accounts for the constraints of highly scalable miniaturized systems operated under realistic field conditions. This model provides a fundamental understanding of concepts, design options and trade-offs for such systems and builds the base for important system-design decisions regarding the selection of the photonic circuits and the specifications of the corresponding optoelectronic components.

4.3 Sensor system model and performance parameters

In the following, we introduce a high-level description of the sensor-system model (Section 4.3.1), and subsequently evaluate the sensor performance to determine the sensor-system sensitivity (Section 4.3.2) as well as the sensor-system limit of detection (Section 4.3.3).

4.3.1 Sensor system description

The generic concept of an integrated phase-sensitive photonic sensor system is illustrated in Fig. 4.1(a). The system combines a photonic sensor chip with electronic control and readout circuits. In view of technically and commercially viable sensor systems, we focus our analysis on phase-sensitive concepts that rely on simple optical power measurements rather than on more demanding spectrally resolved detection techniques [71]. Note, however, that the fundamental concepts, performance trade-offs, and design choices outlined in this analysis can be transferred to spectrally resolved detection techniques as well, which ultimately also rely on power measurements. As a consequence, sensor concepts that are based on, e.g., tracking of spectral features such as resonances of ring resonators [72], Bragg gratings [73], or photonic crystals [63], are ultimately subject to detection limits that are similar to the ones estimated from our analysis.

(a)

Photonics

Laser   Sensor   Detector

PIC
ASIC

Electronics

Laser driver

ADC DSP

(b)

Δ_{env}

$S_{\mathrm{env}} = \Delta n_{\mathrm{e}} / \Delta_{\mathrm{env}}$

Δn_{e}

$S_{\mathrm{e}} = \Delta T / \Delta n_{\mathrm{e}}$

P_{i} $\Delta T = \Delta P_{\mathrm{o}} / P_{\mathrm{i}}$ P_{o}

L

(c)

| Laser driver | I_{i} | Laser | $\begin{array}{c}\Delta n_{\mathrm{e}}\\P_{\mathrm{i}}\\\omega\end{array}$ Sensor | P_{o} | Detector | I_{o} | ADC | I_{q} | DSP | $\Delta n_{\mathrm{e,r}}$ |

Noise ⇒ $I_{\mathrm{i,n}}$ $P_{\mathrm{i,n}}\ \omega_{\mathrm{n}}$ $P_{\mathrm{o,n}}$ $I_{\mathrm{o,n}}$ $I_{\mathrm{q,n}}$

$\mathrm{LoD} = 3\sigma_{\Delta n_{\mathrm{e,r}}}$
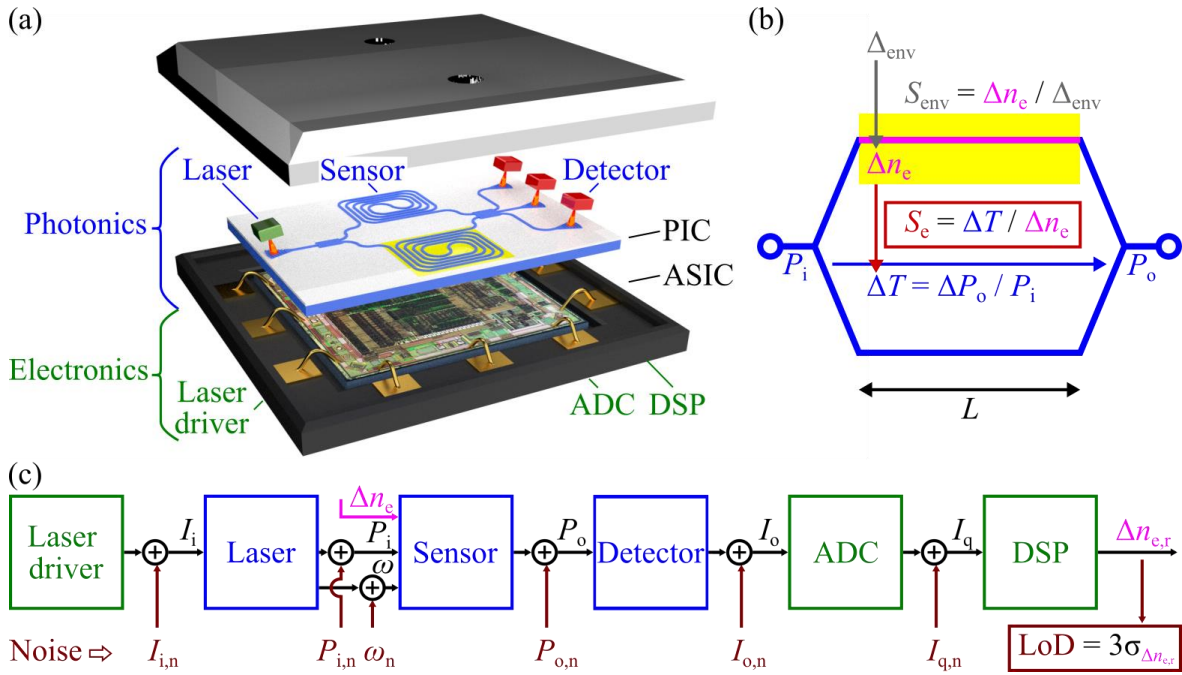
Fig. 4.1. Concept and model of an integrated phase-sensitive photonic sensor system. **(a)** Artist's view, comprising a photonic sensor chip with laser light sources and detectors ('Photonics'), along with electronic control and readout circuits ('Electronics'). **(b)** Principle of a photonic effective-index sensor. Within a sensitive waveguide region (magenta), an environmental change Δ_{env} (yellow) is converted into a change Δn_{e} of the effective modal refractive index via the waveguide sensitivity $S_{\mathrm{env}} = \Delta n_{\mathrm{e}}/\Delta_{\mathrm{env}}$, and this effective-index change leads to a phase shift $\Delta\varphi$ along the sensitive waveguide region. In a phase-sensitive photonic circuit such as a Mach-Zehnder interferometer (MZI), this phase shift leads to a change of the optical power transmission $T = P_{\mathrm{o}}/P_{\mathrm{i}}$, which is defined as the ratio of the optical output power Po and the effective input power P_{i}. The effective-index sensitivity $S_{\mathrm{e}} = \Delta T/\Delta n_{\mathrm{e}}$ is defined as the ratio of the power-transmission change ΔT and the effective-index change Δn_{e}. **(c)** Propagation of signal and noise quantities through the sensor system. All electronic and photonic stages add noise to the respective electrical currents I, optical powers P, or optical frequencies ω. The limit of detection (LoD) of the sensor system can be quantified by the 3σ-deviation of the reconstructed effective refractive index $\Delta n_{\mathrm{e,r}}$. All noise-related quantities are denoted by a subscript "n".

As an example for an integrated phase-sensitive photonic sensing element, the illustration in Fig. 4.1(a) shows an MZI with long waveguide spirals in each arm. The MZI is part of a photonic integrated circuit (PIC) that is connected to laser sources and detectors via grating couplers , see top level 'Photonics' of the stack in Fig. 4.1(a). Note that the MZI is just an example – the model developed

in the following can be generally applied to MZI and RR-based sensors. Similarly, the illustration in Fig. 4.1(a) shows a vertical-cavity surface-emitting laser (VCSEL) as a particularly simple light source that can be operated with small pump currents and that can be efficiently fabricated in large quantities [74]. On the bottom level 'Electronics', the system comprises laser drivers, photodetector readout electronics and analog-to-digital converters (ADC), as well as digital signal processing (DSP) circuits for electrical signal generation and evaluation. Depending on the integration level, the ADC and the DSP circuits may be realized from discrete components on a printed circuit board (PCB), as a monolithic field-programmable gate array (FPGA), or as an application-specific integrated circuit (ASIC, shown in Fig. 4.1(a)).

4.3.2 Sensor system sensitivity

A simplified schematic of the sensor PIC in the form of an MZI is illustrated in Fig. 4.1(b). A certain region of the PIC, indicated by a yellow area with a magenta waveguide section, is exposed to the environment to record a change Δ_{env} of an environmental parameter and to convert it into a change Δn_{e} of the effective modal index. We define this conversion as the waveguide sensitivity $S_{\mathrm{env}} = \Delta n_{\mathrm{e}} / \Delta_{\mathrm{env}}$. The effective-index change Δn_{e} is then translated into a phase shift in the corresponding MZI arm and thus leads to a change ΔT of the optical power transmission factor $T = P_{\mathrm{o}} / P_{\mathrm{i}}$ between the sensor input power P_{i} and the sensor output power P_{o} on the PIC. The magnitude of the transmission change ΔT for a given effective-index change Δn_{e} is quantified by the effective-index sensitivity $S_{\mathrm{e}} = \Delta T / \Delta n_{\mathrm{e}}$. The transmission change ΔT results in a measurable power change $\Delta P_{\mathrm{o}} = P_{\mathrm{i}} \Delta T$ at the output,

$$
\begin{aligned}
\Delta P_{\mathrm{o}} &= P_{\mathrm{i}} S_{\mathrm{e}} S_{\mathrm{env}} \Delta_{\mathrm{env}} = S_{\mathrm{sys}} \Delta_{\mathrm{env}} \,, \\
S_{\mathrm{sys}} &= P_{\mathrm{i}} S_{\mathrm{e}} S_{\mathrm{env}} = \Delta P_{\mathrm{o}} / \Delta_{\mathrm{env}} \,, \\
S_{\mathrm{e}} &= \Delta T / \Delta n_{\mathrm{e}} \,, \\
S_{\mathrm{env}} &= \Delta n_{\mathrm{e}} / \Delta_{\mathrm{env}} \,.
\end{aligned}
\tag{4.1}
$$

The system sensitivity S_{sys} is defined as the output power change ΔP_{o} with respect to environmental changes Δ_{env} and is governed by three main factors: The

effective optical input power P_i, the waveguide sensitivity S_{env}, and the effective-index sensitivity S_e. These quantities are described in more detail in the following paragraphs.

4.3.2.1 Effective optical input power P_i

The signal level is described by the effective optical input power P_i, which is obtained by multiplying the physical output power P_{LD} of the laser diode with the optical power transmission factors of the coupling interface between the laser and the sensor PIC, of the lossy on-chip circuits, as well as of the PIC-detector interface. In other words: The effective optical input power accounts for all optical excess losses that result from non-idealities of the various sensor components such as coupling losses in chip-chip interfaces or propagation losses in on-chip transport waveguides, but not the unavoidable loss that results, e.g., from destructive interference at the MZI output because this is accounted for by the power transmission factor $T = P_o/P_i$. We quantify all these excess losses by a single power transmission factor $\eta < 1$,

$$P_i = \eta P_{LD}. \tag{4.2}$$

The effective optical input power can hence be improved either by increasing the laser power or by decreasing the excess loss of the various components. This calls for advanced photonic assembly concepts and for efficient light-source integration, see Section 4.7 for further details.

4.3.2.2 Waveguide sensitivity S_{env}

The waveguide sensitivity S_{env} describes the dependence of the effective modal index change Δn_e on a change Δ_{env} of an environmental parameter, caused, e.g., by a change of the waveguide's surrounding medium, by adsorption of analyte molecules to the waveguide surface, or by a change of temperature or stress within the waveguide. For a given operating point, the waveguide sensitivity can be approximated by the associated derivative,

$$S_{env} = \frac{\partial n_e}{\partial \Delta_{env}}. \tag{4.3}$$

Note that the optimization of integrated waveguides with respect to the waveguide sensitivity S_{env} is a major subject in its own right [25,30,75,76]. A brief discussion of the various design options and of the associated state of the art can be found in Section 4.7.

For a refractive-index sensor, Δ_{env} is given by the refractive index n_{M} of the medium that surrounds the waveguide. In this case, the waveguide sensitivity S_{env} can directly be linked to the so-called bulk phase sensitivity $S_{\varphi} = \partial\varphi/\partial n_{\mathrm{M}}$, which is often given in radians per refractive index unit (RIU) [67]. This bulk sensitivity quantifies the phase shift $\Delta\varphi = -k_0 L \Delta n_{\mathrm{e}}$ accumulated in a sensor waveguide of length L upon a change Δn_{M} of the surrounding medium,

$$S_{\varphi} = \left| \frac{\partial\varphi}{\partial n_{\mathrm{M}}} \right| = k_0 L \frac{\partial n_{\mathrm{e}}}{\partial n_{\mathrm{M}}} = k_0 L S_{\mathrm{env}}. \tag{4.4}$$

In this relation, $k_0 = \omega/c$ is the vacuum propagation constant of the light, where ω denotes the angular frequency of the optical wave, and where the vacuum speed of light is denoted as c. For resonator-based refractive-index sensors, the bulk sensitivity can also be expressed by the shift $\Delta\lambda_{\mathrm{res}}$ of a resonance wavelength per refractive-change Δn_{M} of the surrounding medium,

$$S_{\lambda,\mathrm{RR}} = \frac{\partial\lambda_{\mathrm{res}}}{\partial n_{\mathrm{M}}} = \frac{\lambda}{n_{\mathrm{eg}}} S_{\mathrm{env}}. \tag{4.5}$$

Here, $n_{\mathrm{eg}} = n_{\mathrm{e}} - \lambda\,\partial n_{\mathrm{e}}/\partial\lambda$ is the effective group refractive index. Note that using wavelength-related bulk sensitivities for MZI is somewhat more intricate, since it is strongly dependent on the asymmetry of the interferometer arms, see Appendix B.1 for a more detailed discussion.

In the following analysis, we consider the waveguide design and hence the waveguide sensitivity S_{env} to be fixed. For a better comparability of the different sensor concepts, independently of the underlying waveguide design, we consider Δn_{e} as the physical quantity to be measured in the following sections, without further discussing its origin and its quantitative relationship to the actual change Δ_{env} of an environmental parameter. We are further only interested in refractive-index sensors in which Δ_{env} predominantly affects the real part of the

refractive index at the wavelength of interest while leaving the imaginary part, i.e., the waveguide loss, virtually unchanged. This is in contrast to absorption-based detection techniques, which rely on the molecular absorption properties at specific wavelengths and therefore often require light sources at dedicated wavelengths.

4.3.2.3 Effective-index sensitivity S_e

For a given set of laser, waveguide, photodetector, and assembly technologies, the effective optical input power P_i according to Eq. (4.2) and the waveguide sensitivity S_{env} in Eq. (4.3) are fixed. The remaining degree of freedom in Eq. (4.1) hence lies in the photonic sensor circuit design, which defines the effective-index sensitivity S_e, i.e., the ratio of the change of the power transmission T and the underlying change of the effective index,

$$S_e = \frac{\partial T}{\partial n_e} = \frac{\partial}{\partial n_e}\left(\frac{P_o}{P_i}\right).$$

(4.6)

To quantify S_e we need to consider the phase shift $\Delta\varphi = -k_0 L \Delta n_e$ that the optical signal accumulates during propagation through the sensitive waveguide of length L, see Fig. 4.1(b) for an exemplary illustration for an MZI-based sensor. Note that our model is based on wave propagation of the form $\exp\left(j\left(\omega t - \beta z\right)\right)$, where $\beta = n_e k_0$ is the propagation constant of the guided mode. The phase shift $\Delta\varphi$ is converted into a change of the sensor output power ΔP_o by either an interferometric or a resonant circuit – the corresponding relations depend on the underlying sensor concept and on the respective operating point, see Section 4.4 for a more detailed analysis. In general, the optical power transmission T of the integrated MZI or RR fundamentally depends on the modal power loss coefficient α and on the associated optical amplitude transmission factor $a = \exp\left(-\alpha L/2\right)$ of the sensitive waveguide section. Like S_{env}, the modal power loss coefficient α depends on the waveguide technology and geometry, and is hence regarded as a constant parameter for the optimization of the sensor system. This is a valid approach for all cases in which the sensor waveguide design is dictated by other constraints arising, e.g., from the underlying fabrication processes. In case the sensor waveguide design and hence α and S_{env} can be varied, a joint optimization of the system sensitivity $S_{sys} = P_i S_e S_{env}$ can be performed.

In this case, an adaptation of the waveguide design will simultaneously affect the environmental sensitivity S_{env} and the effective-index sensitivity S_{e} and may hence allow for an ideal trade-off that optimizes the overall system performance. This is, e.g., useful in applications where the evanescent field of the waveguide mode interacts with an absorbing analyte such that an increase of S_{env} is unavoidably accompanied by an increase of the absorption loss, which usually results in a decreased effective-index sensitivity S_{e} [30,75].

4.3.3 Sensor system limit of detection

The schematic signal propagation of the sensor system is depicted in Fig. 4.1(c) and comprises currents I_{i} and I_{o}, at the input of the drive laser and at the sensor output, as well as optical signals with angular frequency ω and powers P_{i} and P_{o} at the input and the output of the photonic section, see Table 4.1 for a summary of the symbols. The digitized signal of the ADC at the sensor output is described by a quantized photocurrent I_{q}. All signal quantities are random variables $x \in \left\{ I_{\mathrm{i}}, P_{\mathrm{i}}, \omega, P_{\mathrm{o}}, I_{\mathrm{o}}, I_{\mathrm{q}} \right\}$ with mean $\overline{x}$, fluctuation $\delta x = x - \overline{x}$ and variance $\sigma_{\tilde{x}}^2 = \overline{x^2}$. The output signal of the system is a reconstructed value $\Delta n_{\mathrm{e,r}}$ of the actual effective-refractive-index change Δn_{e}, which is distorted by the accumulated noise contributions.

The output signal of each stage contains noise that originates from previous stages, as well as uncorrelated random noise ζ_{n} with mean $\overline{\zeta_{\mathrm{n}}} = 0$ and variance $\sigma_{\zeta_{\mathrm{n}}}^2 = \overline{\zeta_{\mathrm{n}}^2}$ generated in the stage itself. The noise propagation through a specific stage can be described by a linearized transfer function in the respective operating point. As an example, the overall stochastic variance $\sigma_{P_{\mathrm{o}}}^2$ of the photonic sensor output power P_{o} can be approximated by

$$\sigma_{P_{\mathrm{o}}}^2 = \overline{\left| P_{\mathrm{o}} - \overline{P_{\mathrm{o}}} \right|^2} = \sigma_{P_{\mathrm{o,n}}}^2 + \left| \frac{\partial P_{\mathrm{o}}}{\partial P_{\mathrm{i}}} \right|^2 \sigma_{P_{\mathrm{i}}}^2 + \left| \frac{\partial P_{\mathrm{o}}}{\partial \omega} \right|^2 \sigma_{\omega}^2. \tag{4.7}$$

In these relations, the overbar $\overline{X}$ denotes the expectation value of the respective expression X, while $\partial P_{\mathrm{o}}/\partial P_{\mathrm{i}}$ and $\partial P_{\mathrm{o}}/\partial \omega$ represent the linearized transfer functions between the sensor input power P_{i} and frequency ω to the sensor output power P_{o} in its operating point. The total variance $\sigma_{P_{\mathrm{o}}}^2$ in Eq. (4.7) consists of a

sum of three uncorrelated noise terms, where $\sigma_{P_{o,n}}^2 = \overline{P_{o,n}^2}$ represents the additive noise originating from the sensor stage as such, while the other two terms describe the propagation of the noisy optical power and frequency with variances $\sigma_{P_i}^2$ and σ_ω^2 from the previous stage. Applying the same noise propagation scheme to all other stages in the system, we obtain an accumulated reconstruction variance $\sigma_{\Delta n_{e,r}}^2$ of the reconstructed effective refractive index $\Delta n_{e,r}$. This variance finally dictates the useful sensor resolution, and it defines the limit of detection LoD [25] as

$$\text{LoD} = 3\sigma_{\Delta n_{e,r}}. \tag{4.8}$$

A quantitative analysis of each noise source in Table 4.1, of the associated error propagation, and of the respective impact on the total LoD is given in Section 4.4.3.

Table 4.1: Description of signal variables and noise contributors in a highly integrated photonic sensor system. The cumulated noise in the reconstructed effective refractive index $\Delta n_{e,r}$ leads to a certain limit of detection.

Signals			Noise	
I_i	Laser input current	*(electrical)*	$I_{i,n}$	Laser driver current noise
P_i	Sensor input power	*(optical)*	$P_{i,n}$	Laser intensity noise
ω	Angular frequency	*(optical)*	ω_n	Laser frequency noise
P_o	Sensor output power	*(optical)*	$P_{o,n}$	Temperature-induced fluctuation of sensor output power
I_o	Photodetector output current	*(electrical)*	$I_{o,n}$	Photocurrent shot noise and additional detector noise
I_q	ADC output current	*(digital)*	$I_{q,n}$	ADC quantization noise
$\Delta n_{e,r}$	Reconstructed effective refractive index	*(digital)*	LoD	Limit of detection ($3\sigma_{\Delta n_{e,r}}$)

4.4 Quantitative analysis of integrated phase-sensitive photonic sensor systems based on ring resonators and Mach-Zehnder interferometers

With the overall sensor model described in Section 4.3 at hand, we can now perform a quantitative analysis of the performance of sensor systems based on different photonic circuits such as ring resonators and Mach-Zehnder interferometers. We first introduce the photonic sensor concepts and analytical models (Section 4.4.1), which allows us to determine the effective-index sensitivity S_e (Section 4.4.2). The corresponding mathematical relations are summarized in Table 4.2 and Table 4.3. Finally, we estimate and compare the limit of detection LoD (Section 4.5) for each RR- and MZI-based sensor implementation, which is summarized comprehensively in Table 4.4. Further mathematical details are provided in Table B.2 and Table B.3 in the Appendix.

4.4.1 Photonic sensor concepts and analytical models

In the following, we consider three different photonic sensor implementations of both ring resonators (RR, Section 4.4.1.1) as well as Mach-Zehnder interferometers (MZI, Section 4.4.1.2), as illustrated in Fig. 4.2. In each of these two sections, we introduce the sensor concepts, explain the sensing process, highlight key parameters, and derive the generic optical power transmission T, which is used as a basis for the subsequent sensitivity and LoD calculations.

4.4.1.1 Ring resonators

For RR-based sensor implementations, three different readout approaches are illustrated in Fig. 4.2(a). The first approach relies on a ring resonator in a so-called "all-pass configuration" [72], in which the ring is coupled to a single bus waveguide, which serves both as an input and an output port (RR_{AP}; associated elements indicated by solid lines). In the second implementation, another bus waveguide is coupled to the ring to tap a drop signal from the resonator that is detected by a single photodiode (add-drop ring resonator, RR_{AD}) – the additional elements to RR_{AP} are indicated by dotted lines.
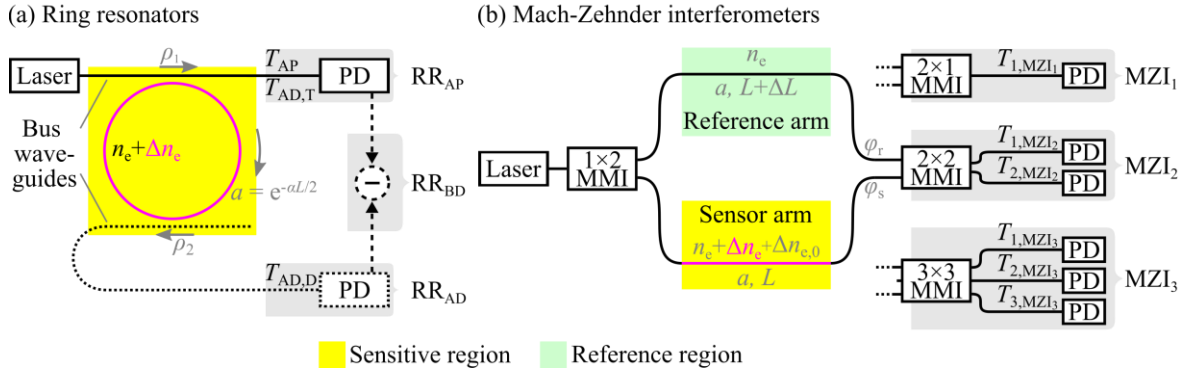
Fig. 4.2. Schematic of common phase-sensitive integrated photonic sensors. A laser launches an optical signal into a single-mode on-chip waveguide. All waveguide sections within a sensitive region (yellow) are subject to an effective-refractive-index change Δn_e resulting from a change Δ_{env} of an environmental parameter. The index change is translated into a measurable change of one or more optical output powers, which are recorded by photodiodes (PD). The corresponding change of the optical power transmission functions $T(\Delta n_e)$ depends on the specific implementation of the respective sensor circuit. Different implementations of photonic sensors are shaded in grey. **(a)** Sensor implementations based on ring resonators, comprising an all-pass ring resonator (RR_{AP}) with a single through port (solid lines), an add-drop ring resonator (RR_{AD}) having an additional drop-port bus waveguide (dotted lines), and a balanced-detection add-drop ring resonator (RR_{BD}) that relies on the difference signal between the through port and the drop port (dashed lines). The associated optical power transmission factors T_{AP}, $T_{AD,T}$, and $T_{AD,D}$ depend on the coupling to and from the resonator as given by the amplitude transmission ρ_1 and ρ_2 of the coupling sections, on the round-trip length L, and on the round-trip amplitude transmission factor a. Analytic expressions for the various power transmission factors are given in Eqs. (4.10) and (4.12), and in Appendix B.2. **(b)** Sensor implementations based on Mach-Zehnder interferometers: A 1×2 multimode interference (MMI) coupler splits the input signal into a reference and a sensor arm. Propagation through these arms leads to different phase shifts φ_r and φ_s at the input of the 2×1, 2×2, or 3×3 MMI coupler that is used to recombine the signals in the MZI with 1 (MZI_1), 2 (MZI_2) or 3 output ports (MZI_3), respectively. For the 3×3 MMI coupler, the signals are fed to the first and the last input port, whereas the second is left unconnected. In general, the optical power transmission factors depend on the arm lengths L and $L+\Delta L$ of the sensing and the reference arm, on the amplitude transmission factors a, which we assume to be identical for both arms, on the effective refractive index $n_e + \Delta n_e + \Delta n_{e,0}$ of the sensor arm, and on its counterpart n_e for the reference arm, see Eqs. (4.11) and (4.12).

The third implementation also comprises a drop waveguide but uses a pair of balanced detectors (BD) to extract the difference signal of optical powers at the through port and at the drop port (RR_{BD}) – the additional elements to RR_{AD} are indicated by dashed lines. All these implementations have specific advantages:

The RR$_{AP}$ concept is attractive due to its simple design and high resonator Q-factor, which leads to a high sensitivity, RR$_{AD}$ allow to multiplex several rings on a single bus waveguide, and RR$_{BD}$ simplify the feedback control to maintain the operating point of highest effective-index sensitivity, as detailed in Section 4.4.2.3.

Sensing in ring resonators relies on detecting a change Δn_e of the effective refractive index within the sensitive region, depicted in yellow in Fig. 4.2(a), which comprises the ring resonator. The corresponding phase shift $-k_0 L \Delta n_e$ in a resonator with round-trip length L causes a phase change with respect to the round-trip phase shift $\varphi_{OP,RR}$ in the operating point. This additional phase shift modifies the overall round-trip phase φ_{RR},

$$\varphi_{RR} = -k_0 L \Delta n_e + \varphi_{OP,RR},$$
$$\varphi_{OP,RR} = -k_0 L n_e, \tag{4.9}$$

which then leads to a change of the optical power transmission T, see Appendix B.2.

Key parameters are the operating point, characterized by the round-trip phase shift $\varphi_{OP,RR} = -k_0 L n_e$, the round-trip optical amplitude transmission $a = \exp(-\alpha L/2)$, as well as the amplitude transmission ρ_1 and ρ_2 and the corresponding cross-coupling amplitude transmission κ_1 and κ_2 at the coupling sections of the through and the drop port. The round-trip length L also dictates the free spectral range (FSR) $\Delta \omega_{FSR,RR}$ of the ring resonator, which corresponds to the frequency increment that increases the magnitude of the round-trip phase shift $k_0 L n_e$ by 2π and which is given by the reciprocal of the round-trip group delay $\tau_{g,RR} = -\partial \varphi_{OP,RR} / \partial \omega = n_{eg} L/c = 1/\Delta \omega_{FSR,RR}$.

In the following, we assume lossless coupling sections, $\kappa_1^2 + \rho_1^2 = \kappa_2^2 + \rho_2^2 = 1$, which are not affected by the change Δn_e of the effective index of the waveguide mode in the sensing region. Based on these parameters, we can calculate the optical power transmission as a function of the effective index change Δn_e and hence the ring resonator phase φ_{RR}, see also Section 4.4.2 and Appendix B.2 for further details,

$$T_{AP} = \frac{\rho_1^2 - 2\rho_1 a \cos(\varphi_{RR}) + a^2}{1 - 2\rho_1 a \cos(\varphi_{RR}) + (\rho_1 a)^2}$$

$$T_{ADT} = \frac{\rho_2^2 a^2 - 2\rho_1 \rho_2 a \cos(\varphi_{RR}) + \rho_1^2}{1 - 2\rho_1 \rho_2 a \cos(\varphi_{RR}) + (\rho_1 \rho_2 a)^2} \qquad (4.10)$$

$$T_{ADD} = \frac{(1 - \rho_1^2)(1 - \rho_2^2) a}{1 - 2\rho_1 \rho_2 a \cos(\varphi_{RR}) + (\rho_1 \rho_2 a)^2}$$

4.4.1.2 Mach-Zehnder interferometers

For MZI-based sensor implementations, we consider three typical two-arm implementations as illustrated in Fig. 4.2(b), featuring 1×2 multi-mode interference (MMI) coupler for splitting the input power in a sensor arm passing the sensitive region (depicted in yellow) and in a reference arm (depicted in green). For simplicity, we assume both arms to have the same power transmission, and we only consider the phase-shift difference in the following calculations.

The effective-refractive-index change Δn_e causes a phase shift $-k_0 L \Delta n_e$ in the sensor arm and modifies the phase difference $\varphi_{MZI} = \varphi_s - \varphi_r$ of the optical sensor and reference signals entering the 2×1 (MZI$_1$), 2×2 (MZI$_2$) or 3×3 MMI couplers (MZI$_3$). All MMI couplers are assumed to be lossless with ideal splitting ratios for equal output powers. In absence of an effective-refractive-index change in the sensitive region, $\Delta n_e = 0$, the optical signals in the reference and in the sensor arm experience a phase difference $\varphi_{OP,MZI}$, which determines the MZI operating point. The phase difference $\varphi_{OP,MZI}$ of the operating point may be caused either by a geometric length difference ΔL between the reference and the sensor arm or by a difference $\Delta n_{e,0}$ of the effective refractive index that occurs even in absence of an environmental change Δ_{env}. The overall phase difference at the output of the two arms may hence be written as

$$\varphi_{\mathrm{MZI}} = \varphi_{\mathrm{s}} - \varphi_{\mathrm{r}} = -k_0 L \Delta n_{\mathrm{e}} + \varphi_{\mathrm{OP,MZI}},$$

$$\varphi_{\mathrm{OP,MZI}} = -k_0 \left(L \Delta n_{\mathrm{e,0}} - \Delta L n_{\mathrm{e}} \right),$$

$$\varphi_{\mathrm{s}} = -k_0 L \left(n_{\mathrm{e}} + \Delta n_{\mathrm{e,0}} + \Delta n_{\mathrm{e}} \right),$$

$$\varphi_{\mathrm{r}} = -k_0 n_{\mathrm{e}} \left(L + \Delta L \right).$$

(4.11)

For the MZI, the free spectral range (FSR) $\Delta\omega_{\mathrm{FSR,MZI}}$ corresponds to the spectral period of the transmission fringes and is given by the reciprocal of the group delay difference $\tau_{\mathrm{g,MZI}} = -\partial\varphi_{\mathrm{OP,MZI}} / \partial\omega = \left(L \Delta n_{\mathrm{eg,0}} - \Delta L n_{\mathrm{eg}} \right) / c = 1 / \Delta\omega_{\mathrm{FSR,RR}}$. The phase difference $\varphi_{\mathrm{OP,MZI}}$ in the MZI operating point may be adjusted by design, e.g., via the geometric length difference ΔL of the two arm lengths, or by using different waveguide designs in the two arms that allow to adjust the effective refractive index offset $\Delta n_{\mathrm{e,0}}$. These methods may be combined with a dynamic operating-point adjustment, e.g., by implementing electronically or thermally controlled phase shifters in the MZI arms, or by tuning the laser frequency ω, see Section 4.4.2.3. Note that the operating point $\Delta\varphi_{\mathrm{OP,MZI}}$ of the interferometer can be set to zero independently of the operating wavelength by matching the optical path lengths via $L \Delta n_{\mathrm{e,0}} = \Delta L n_{\mathrm{e}}$. In this case, the group delay difference $\tau_{\mathrm{g,MZI}} \approx 0$ vanishes, thereby eliminating the frequency dependency of the optical power transmission.

The extra outputs of the MZI$_2$ and MZI$_3$ implementations help in data processing [77,78] at the cost of an increased readout complexity. Specifically, the three output currents of the MZI$_3$ can be processed by a Clarke transformation [79] to reduce the three output signals to a pair of signals that represent the in-phase and the quadrature-phase components of a complex signal with phase angle φ_{MZI}. This allows to make the sensor sensitivity independent of the operating point and further allows to eliminate directional signal ambiguity [80]. Note that, in principle, further output ports may added. This, however, only increases the complexity of the photonic circuit without improving the sensor performance any further. Three output ports may hence be considered an ideal trade-off between implementation complexity and functionality. A study on fundamental limits and design considerations for a coherent phase-readout of different kinds of MZI-based sensors can be found in [81].

Independent of the specific implementation, the change Δn_e of the effective refractive index leads to a change ΔT of the optical power transmission at the MZI outputs, which is finally evaluated. Key parameters are the phase difference $\varphi_{\mathrm{OP,MZI}}$ in the operating point, the length L of the sensitive waveguide section, and the amplitude transmission factors a of the MZI arms. For a two-arm MZI having a 1×2 multi-mode interference (MMI) coupler for splitting the power into the two arms and a lossless $\mu \times \mu$ MMI coupler ($\mu = 2, 3, \ldots$) with the first and the last input port connected to the MZI arms for recombining the signals, the general optical power transmission T for the vth output port ($v = 1 \ldots \mu$) can be written as

$$T_{v,\mathrm{MZI}_\mu} = \frac{a^2}{\mu}\left(1 + \sin\left(\varphi_{\mathrm{MZI}} + 2\pi\frac{v-1}{\mu} + \frac{\pi}{2}\mathrm{mod}\left(\mu,2\right)\right)\right),$$

$$\mu = 2,3,\ldots \ , \quad v = 1\ldots\mu. \tag{4.12}$$

In this relation, φ_{MZI} denotes the phase difference of the optical signals entering the two ports of the output MMI, see Eq. (4.11), a^2 is the power transmission factor of the MZI arms, and $\mathrm{mod}\left(\mu,2\right)$ refers to the remainder of the Euclidean division of μ by 2. The power transmission factor a^2 is assumed to be the same for both interferometer arms. Note that the overall power transmission T_{v,MZI_μ} of the different MZI output ports $v = 1\ldots\mu$ reveals a sinusoidal dependence on the phase difference φ_{MZI}. These sinusoidals are offset in phase by constant increments $2\pi/\mu$, which is a direct consequence of the distinct phase relations in $\mu \times \mu$ MMI couplers [82]. Note also that, for MZI_μ with $\mu > 1$, combination of the signals in the $\mu \times \mu$ MMI coupler does not introduce any additional power loss. This is different for an MZI terminated by a 2×1 MMI ($\mu = 1$), for which lossless combination of the signals is only possible for constructive interference at $\varphi_{\mathrm{MZI}} = 2\pi m$ ($m \in \mathbb{N}$). In this case, the optical power transmission can be written as

$$T_{v,\mathrm{MZI}_1} = \frac{a^2}{2}\left(1 + \cos\left(\varphi_{\mathrm{MZI}}\right)\right). \tag{4.13}$$

Note that in our further analysis, the power transmission factor a^2 is assumed to be the same for both interferometer arms.

4.4.2 Effective-index sensitivity

In this section, we analytically maximize the effective-index sensitivity of the RR- and MZI-based sensor implementations in Fig. 4.2 by optimizing the sensor operating point as well as the circuit design parameters, i.e., the round-trip length and coupling coefficients for RR, and the arm length for MZI. As a baseline, we use the generic optical power transmission T from Eq. (4.10) and Eq. (4.12) derived in the previous two sections, and we assume a set of technologically fixed parameters, namely the vacuum propagation constant k_0 of the light source as well as the effective index n_e and the modal power loss coefficient α of the sensor waveguide.

In order to quantify and to compare the effective-index sensitivity of all sensor implementations, we start by extending the optical power transmission T by defining an effective opto-electronic transmission τ and sensitivity $S_{e,\tau}$ (Section 4.4.2.1). This allows for a comparison with concepts that are relying on signals from multiple outputs (RR_{BD}, MZI_2, MZI_3) by including the combination of the digitized photodetector currents I_q. Based on τ, we quantify the optoelectronic effective-index sensitivity $S_{e,\tau}$ (Section 4.4.2.2), where we find general analytical expressions for both RR and MZI. With this sensitivity model at hand, we determine optimum operating points $\varphi_{OP,opt}$ (Section 4.4.2.3) of each sensor and derive the peak sensitivity $S_{e,\tau,peak}$ as a function of the remaining design parameters. We further provide details on the operating point control in fully integrated photonic sensor systems. We exploit $S_{e,\tau,peak}$ to analytically find optimum design parameters (Section 4.4.2.4), in particular for the MZI arm length and for the round-trip length and the amplitude transmission ρ_1, ρ_2 of the coupling sections in case of RR. We further formulate requirements regarding the laser diode linewidth $\Delta\omega_{FWHM,LD}$ that are associated with highly sensitive measurements in RR- and MZI-based sensor circuits. Finally, we perform a quantitative comparison of the optoelectronic effective-index sensitivity $S_{e,\tau,max}$ for each RR- and MZI-based sensor implementation (Section 4.4.2.5).

4.4.2.1 Optoelectronic transmission and optoelectronic effective-index sensitivity

In sensor systems relying on signals from multiple outputs (RR$_{BD}$, MZI$_2$, MZI$_3$), further processing steps such as additions or subtractions are required in the electronic or digital domain to obtain the output signal. To include these steps in our model, we extend the optical power transmission T of all sensor types by defining an effective optoelectronic transmission

$$\tau = f\left(T, \Re\right). \tag{4.14}$$

The effective optoelectronic transmission τ comprises the additional processing steps of the analog or digitized electric signals as well as the overall electric readout responsivity $\Re$, which accounts for the photodiode responsivity and for the gain of any electrical readout amplifiers. For simplicity, we assume the same frequency-independent electric readout responsivity $\Re$ for the various output ports of the photonic sensor circuits. In analogy to Eq. (4.6), we can then define an optoelectronic effective-index sensitivity

$$S_{e,\tau} = \frac{\partial \tau}{\partial n_e} \tag{4.15}$$

that refers to the optoelectronic transmission τ rather than to the optical transmission T. For sensor circuits with only one output (RR$_{AP}$, RR$_{AD}$, MZI$_1$), the optoelectronic transmission τ can be obtained from the optical transmission T by a simple multiplication with the electric readout responsivity $\Re$, $\tau = \Re T$, and Eq. (4.15) simplifies to $S_{e,\tau} = \Re S_e$. For sensor circuits with multiple outputs (RR$_{AP}$, RR$_{AD}$, MZI$_1$), further processing of the acquired and digitized photocurrents I_q is involved, leading to additions and subtractions of the respective optical power transmission factors. The effective optoelectronic transmission τ of the three RR and the three MZI circuits are shown in Column 2 of Table 4.2. For the case of MZI$_3$, the phase difference between the MZI arms can be extracted by merging the three readout signals into a complex-valued optoelectronic transmission function τ and by determining its argument, see last row of Table 4.2.

Table 4.2: Effective optoelectronic transmission τ of the different of RR-based and MZI-based sensor implementations as defined in Fig. 4.2. For each sensor implementation indicated in Column 1, Column 2 gives a general expression for the optoelectronic transmission τ, assuming the same electric readout responsivity $\mathfrak{R}$ for each output. The relations in Column 3 refer to the simplified τ for an effective-refractive-index change Δn_e, which are derived in Appendices B.2-B.3. These relations depend on the normalized output contrast $\hat{\tau}$ in Column 4 as a parameter. For the ring resonators, we assume that the device is operated at its optical resonance frequency, i.e., $\varphi_{\text{OP,RR}} = 2\pi m \ (m \in \mathbb{N})$, in the absence of an effective-index change ($\Delta n_\text{e} = 0$). Choosing am optimum operating point according to Section 4.4.2.3 corresponds to a simple shift of the effective optoelectronic transmission characteristics τ along Δn_e.

Sensor impl.	Effective optoelectronic transmission τ General	Simplified	Output contrast $\hat{\tau}/\mathfrak{R}$
RR_AP	$\tau_{\text{RR}_\text{AP}} = \mathfrak{R}T_\text{AP}$	$\begin{cases} 1- \\ \\ 0+ \\ \\ 1- \end{cases} \hat{\tau}\, \dfrac{1}{1+\left(\dfrac{2\Delta n_\text{e}}{n_\text{eg}/Q}\right)^2}$	$1-\dfrac{(a-\rho_1)^2}{(1-\rho_1 a)^2}$
RR_AD	$\tau_{\text{RR}_\text{AD}} = \mathfrak{R}T_\text{ADD}$		$\dfrac{\left(1-\rho_1^2\right)\left(1-\rho_2^2\right)a}{(1-\rho_1\rho_2 a)^2}$
RR_BD	$\tau_{\text{RR}_\text{BD}} = \mathfrak{R}(T_\text{AD}-T_\text{ADD})$		$\dfrac{(a+1)(\rho_1^2-1)(a\rho_2^2-1)}{(1-\rho_1\rho_2 a)^2}$
MZI_1	$\tau_{\text{MZI}_1} = \mathfrak{R}T_{1,\text{MZI}_1}$	$\hat{\tau}/2\times\left(1+\cos\left(\Delta n_\text{e}k_0 L+\varphi_{\text{OP,MZI}}\right)\right)$	a^2
MZI_2	$\tau_{\text{MZI}_2} = \mathfrak{R}\left(T_{2,\text{MZI}_2}-T_{1,\text{MZI}_2}\right)$	$\hat{\tau}/2\times\sin\left(\Delta n_\text{e}k_0 L+\varphi_{\text{OP,MZI}}\right)$	$2a^2$
MZI_3	$\tau_{\text{MZI}_3} = \mathfrak{R}\left(2T_{2,\text{MZI}_3}-T_{3,\text{MZI}_3}-T_{1,\text{MZI}_3}\right)$ $+\text{j}\mathfrak{R}\sqrt{3}\left(T_{3,\text{MZI}_3}-T_{1,\text{MZI}_3}\right)$	$\hat{\tau}/2\times\exp\left(-\text{j}\left(\Delta n_\text{e}k_0 L+\varphi_{\text{OP,MZI}}\right)\right)$	$2a^2$

4.4.2.2 Sensitivity analysis of RR- and MZI-based sensors

In the following, we develop quantitative models for the effective optoelectronic transmission and the optoelectronic effective-index sensitivity of RR- and MZI-based sensors. For the three RR-based implementations, we assume that the rings have identical round-trip lengths L, modal power loss coefficients α, and effective group refractive indices $n_\text{eg} = n_\text{e} + \omega\,\partial n_\text{e}/\partial\omega$ and thus identical intrinsic Q-factors Q_i, which are defined as the product of the cavity resonance frequency ω_res and the photon lifetime τ_c,

$$Q_\text{i} = \omega_\text{res}\tau_\text{c} = n_\text{eg}\frac{k_0}{\alpha}. \tag{4.16}$$

In the subsequent analysis, we consider different coupling strengths of the ring resonator to the single (RR_{AP}) or the pair (RR_{AD}, RR_{BD}) of bus waveguides, which we quantify by the quality ratio $c_Q = Q/Q_i$ of the loaded Q-factor Q and the intrinsic, unloaded Q-factor Q_i,

$$Q = c_Q Q_i, \quad c_Q \leq 1. \tag{4.17}$$

For loaded high-Q ring resonators, the power transmission characteristics can be approximated by a Lorentzian for the drop ports, and by its complement to unity transmission for the through ports. This is done by a Taylor approximation of the cosine term $\cos(\varphi_{RR}) \approx 1 - (\varphi_{RR} - \varphi_{res})^2 / 2$ in Eq. (4.10) for small offsets $\Delta\varphi_{RR} = \varphi_{RR} - \varphi_{res}$ of the round-trip phase from that the nearest resonance $\varphi_{res} = 2\pi m$ ($m \in \mathbb{N}$), i.e., for $|\Delta\varphi_{RR}| \ll 1$, see Appendix B.3 for details. For the remainder of this subsection, we assume for simplicity that the ring resonator is operated at its optical resonance frequency ω_{res} in the absence of an effective index change, i.e., for $\Delta n_e = 0$, and we consider the change of the effective optoelectronic transmission τ as a function of Δn_e. The dependence of the effective optoelectronic transmission τ on the effective index change Δn_e is then given by the simplified Lorentz-based optoelectronic transmission functions in the third column of Table 4.2 for the RR_{AP}, the RR_{AD}, and the RR_{BD} implementation. In Section 4.4.2.3, we will consider the choice of the optimum operating point given by a phase offset $\Delta\varphi_{OP,RR}$, which is adjusted by tuning the laser away from the resonance frequency of the ring. This simply corresponds to a horizontal shift of the effective optoelectronic transmission characteristics – the transmission characteristics for any other operating point $\varphi_{OP,RR}$ can be obtained by replacing Δn_e in Rows 2, 3, and 4 of Table 4.2 through $\Delta n_e - \varphi_{OP,RR}/(k_0 L)$. Note that, when using the Lorentzian approximation, the effective optoelectronic transmission characteristics of a ring-based sensor are fully defined by two simple parameters: The resonance depth or output contrast $\hat{\tau}$ and the resonance width $\Delta n_{eg,FWHM,RR} = n_{eg}/Q$ with respect to effective-index change Δn_e, see also Table B.3 in Appendix B.3.

Based on these models, Fig. 4.3(a) shows the effective optoelectronic transmission τ as a function of an effective index change Δn_e for the various RR-based sensor implementations. For the RR_{AP} and the RR_{AD}, we investigate the case of critical coupling (superscript "CC") as well as an under-coupled (superscript

"UC") implementation, for which the coupling to the through and drop port is chosen to maximize the sensitivity in the optimum operating point, see Section 4.4.2.4. The two black lines in Fig. 4.3(a) correspond to the critically coupled RR_{AP} (RR_{AP}^{CC}, solid black line, $c_Q = 1/2$) and to its under-coupled counterpart (RR_{AP}^{UC}, dashed black line, $c_Q = 2/3$). Similarly, the two red lines correspond to RR_{AD}, again critically coupled (RR_{AD}^{CC}, solid red line, $c_Q = 1/4$) and under-coupled (RR_{AD}^{UC}, dashed red line, $c_Q = 1/3$). For the RR_{BD}, we only consider an under-coupled implementation (RR_{BD}^{UC}, solid blue line, $c_Q = 1/3$), which simultaneously maximizes sensitivity and leads to perfect power transmission balancing of the two output ports in the optimum operating point.
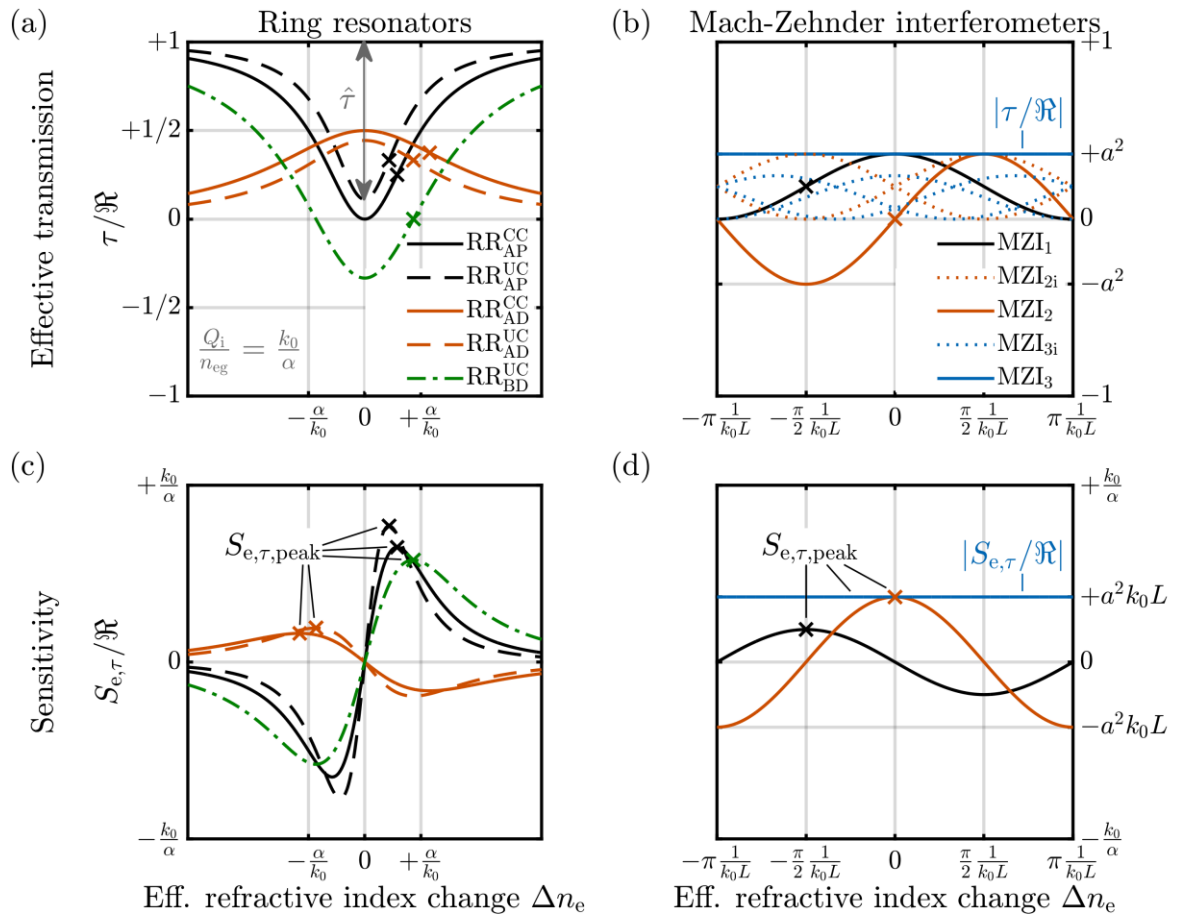

Fig. 4.3. Optoelectronic transmission τ and optoelectronic effective-index sensitivity $S_{e,\tau}$ of the different sensor implementations based on RR and MZI. **(a)** Effective optoelectronic transmission τ of RR-based implementations. *[Remaining figure caption on the following page]*

[Continuation of Fig. 4.3 caption]   For better comparability, all rings are assumed to have the same round-trip length L, the same modal power loss coefficient α, the same effective group refractive index n_{eg}, and thus the same intrinsic Q-factor Q_i. We plot the diagrams for a critically coupled all-pass ring resonator (RR_{AP}^{CC}, solid black line) and for its under-coupled counterpart (RR_{AP}^{UC}, dashed black line), for a critically coupled and for an under-coupled add-drop ring resonator each with a single photodetector (RR_{AD}^{CC}, solid red line, and RR_{AD}^{UC}, dashed red line), and for an under-coupled add-drop ring resonator with balanced detection at the output (RR_{BD}^{UC}, solid blue line), for which the photonic circuit is identical to that of RR_{AD}^{UC}. The results are normalized by the electric readout responsivity $\Re$, which is assumed to be the same for the various outputs. For single-output sensors, the quantity $\tau/\Re = T$ gives the optical transmission. Relevant transmission changes happen around the resonance for $\Delta n_e = \pm\alpha/k_0 = \pm n_{eg}/Q_i$. For simplicity, we assume that, in the absence of an effective-index change ($\Delta n_e = 0$), the devices are operated at an optical resonance frequency, i.e., $\varphi_{OP,RR} = 2\pi m \,(m \in \mathbb{N})$. The transmission characteristics for any other operating point defined by a non-zero phase offset $\Delta\varphi_{OP,RR}$ can be deduced from the plots by shifting the abscissa by $\Delta\varphi_{OP,RR}/(k_0 L)$.   **(b)** Effective optoelectronic transmission of single-, double-, and triple-output Mach-Zehnder interferometers (MZI$_1$, MZI$_2$, MZI$_3$; black, red and blue lines). Solid lines correspond to the individual outputs; dash-dotted lines show combined effective optoelectronic transmissions. The trace plotted for MZI$_3$ refers to the magnitude of the complex effective optoelectronic transmission obtained from the last row of Table 4.2. For simplicity, we assume identical arm lengths and that, in the absence of an effective-index change ($\Delta n_e = 0$), the phase shifts in the MZI two arms are identical or differ by an integer multiple of 2π, $\varphi_{OP,MZI} = 2\pi m \,(m \in \mathbb{Z})$. The transmission characteristics of any other operating point defined by a non-zero phase offset $\Delta\varphi_{OP,MZI}$ can be deduced from the plots by shifting the abscissa by $\Delta\varphi_{OP,MZI}/(k_0 L)$.   **(c, d)** Optoelectronic effective-index sensitivity $S_{e,\tau} = (1/\Re)(\partial\tau/\partial n_e)$ of RR and MZI, normalized by the electric readout responsivity $\Re$. For single-output sensors, $S_{e,\tau}/\Re = S_e$. Peak sensitivities $S_{e,\tau,peak}$ in the optimum operating point are marked with crosses in all subfigures. Quantitative values can be found in Table 4.3. The trace for MZI$_3$ again refers to the magnitude of the complex optoelectronic effective-index sensitivity obtained from the last row of Table 4.2. In this case, $S_{e,\tau}$ is independent of the operating point.

The sensitivity $S_{e,\tau}$, Fig. 4.3(c), is obtained by taking the derivative of the effective optoelectronic transmission τ with respect to the effective-index change Δn_e, see Eq. (4.15). Qualitatively, the effective optoelectronic transmissions of RR$_{AP}$ show steeper slopes with respect to Δn_e and thus a higher peak sensitivity $S_{e,\tau,peak}$ compared to those of RR$_{AD}$ and RR$_{BD}$. This can be understood from the fact that both RR$_{AD}$ and RR$_{BD}$ require a second waveguide to be coupled to the ring, which decreases the loaded Q-factor and hence reduces the slope of the Lorentzian that approximates the resonance. Furthermore, slightly under-coupled resonators outperform critically-coupled ring resonators.

We also formulate simplified expressions for the optoelectronic transmission τ of the various MZI-based sensor implementations, see third column of Table 4.2, which have been derived from Eqs. (4.11), (4.12) and (4.13). It can be seen that the output contrast of the MZI_1 is only half of all other MZI_μ versions, see Column 4 of Table 4.2. Fig. 4.3(b) shows the corresponding effective optoelectronic transmission τ as a function of the effective index change Δn_e. We limit our consideration to the range $\Delta n_e \in [-\pi; +\pi]/(k_0 L)$, exploiting the fact that the transmission characteristics are periodic with respect to Δn_e, where the period is given by the effective-index increment that increases the MZI phase difference φ_{MZI} by 2π. For the case of MZI_2 (MZI_3), we additionally indicate the individual contributions MZI_{2i} (MZI_{3i}) of the various MMI coupler outputs $\nu = 1, 2$ ($\nu = 1, 2, 3$) in dashed lines. This leads to a pair of sinusoidals that are phase-shifted by π in case of MZI_2 and to three sinusoidals that are phase-shifted by $2\pi/3$ for MZI_3. Note that for MZI_3, the optoelectronic transmission is a complex number, see Column 3, last row in Table 4.2, for which we plot the magnitude only. The MZI sensitivity shown Fig. 4.3(d) is again obtained by taking the derivative of the effective optoelectronic transmission τ with respect to the effective-index change Δn_e. Note that for the plots in Fig. 4.3(b) and (d), we assume operating points for which the phase difference of the two arms corresponds to an integer multiple of 2π, $\varphi_{OP,MZI} = 2\pi m$ $(m \in \mathbb{Z})$. The transmission characteristics of any other operating points defined by a non-zero phase offset $\Delta \varphi_{OP,MZI}$ can be deduced from the plots by shifting the abscissa by $\Delta \varphi_{OP,MZI}/(k_0 L)$.

4.4.2.3 Optimum operating points and peak sensitivity

For ring resonators, the optimum operating points offering the peak sensitivity $S_{e,\tau,peak}$ can be found at the inflection points of the Lorentzian that approximates the optical power transmission in the vicinity of the resonance frequency ω_{res}. Using the relations summarized in Appendix B.3, Table B.3, we can calculate the phase offset in the optimum operating point of a ring resonator as

$$\Delta \varphi_{OP,RR,opt} = \pm \frac{1}{2\sqrt{3}} \frac{\alpha L}{c_Q}. \qquad (4.18)$$

In a typical experiment, a resonance is found by either tuning the input laser frequency or the effective refractive index of the waveguide in the resonator until minimum (RR_{AP}) or maximum (RR_{AD}) power transmission is achieved. From this resonance condition, the optimum operating point can be reached either through a frequency offset $\Delta\omega_{\text{OP,RR,opt}} = \omega_{\text{res}} / \left(2\sqrt{3}Q\right)$ or through a refractive index offset $\Delta n_{\text{e,OP,RR,opt}} = n_{\text{eg}} / \left(2\sqrt{3}Q\right)$, see Table B.3 in Appendix B.3.

For MZI_1 and MZI_2, the operating points for peak sensitivity $S_{\text{e},\tau,\text{peak}}$ can be found accordingly, leading to phase offsets

$$\Delta\varphi_{\text{OP,MZI,opt}} = \pm\frac{\pi}{2} + \begin{cases} 0 & \text{for } \text{MZI}_1, \\ \dfrac{\pi}{2} & \text{for } \text{MZI}_2. \end{cases} \tag{4.19}$$

The effective optoelectronic transmissions of MZI_1, MZI_2 and MZI_3 are drawn in solid lines. For MZI_3, the sensitivity is again a complex number for which we only plot the magnitude. Due to the advantageous signal combination, the magnitude of the sensitivity does not depend on the operating point for MZI_3.

With the optimum operating points at hand, we can now formulate relations for the associated peak sensitivity. To this end, we first express the peak sensitivities of RR- and MZI-based sensor implementations in terms of the output contrast $\hat{\tau}$ between minimum and maximum transmission of the respective device, as specified in the last column of Table 4.2,

$$S_{\text{e},\tau,\text{peak}} = \begin{cases} \dfrac{3}{8}2\sqrt{3}\dfrac{Q}{n_{\text{eg}}}\hat{\tau} = \dfrac{3}{8}2\sqrt{3}\dfrac{k_0}{\alpha}c_{\text{Q}}\hat{\tau} & \text{for RR}, \\[2ex] \dfrac{\hat{\tau}}{2}k_0 L & \text{for MZI}. \end{cases} \tag{4.20}$$

To derive these relationships, we assumed again that the power transmission of the ring resonators can be approximated by a Lorentzian for the drop ports, and by its complement to unity transmission for the through ports, see Eq. (B.3) and (B.4) as well as Table B.3 of Appendix B.3. For RR, the output contrast $\hat{\tau}$ represents the amplitude of this Lorentzian, which is equivalent to the resonance

depth, and $c_Q = Q/Q_i$ refers to the ratio of the loaded Q-factor Q and the intrinsic, unloaded Q-factor Q_i, see Eq. (4.17). For MZI$_1$ and MZI$_2$, $\hat{\tau}$ is given by the peak-to-peak swing of the effective transmission τ when tuning the MZI phase difference φ_{MZI} over 2π. For MZI$_3$, $\hat{\tau}$ is calculated by summing over the output contrasts of the individual output ports.

Note that maintaining the optimum operating point of sensors based on RR, MZI$_1$, or MZI$_2$ is not a trivial task. In many cases of practical interest, the fabrication process of the sensor PIC is imperfect, such that it is impossible to reliably set the optimum operation point by design. In this case, a method to actively tune the system to $\Delta\varphi_{OP,RR,opt}$ or $\Delta\varphi_{OP,MZI,opt}$ is required. Furthermore, the operating points are affected by long-term drifts, caused for example by temperature or degradation effects. As a consequence of these drifts, measurement of absolute quantities over extended periods of time is usually much harder than detecting abrupt changes. As an example, relative measurements are usually sufficient for biosensors that detect binding events of target analytes to functionalized waveguide surfaces, which typically occur over time scales of a few minutes [66]. In contrast to that, long-term monitoring of absolute gas concentrations crucially relies not only on robust sensor calibration, but also on effective elimination of drift phenomena. To this end, it is necessary to equip the sensor system with appropriate stabilization mechanisms and/or feedback loops that can dynamically adjust tuning parameters to maintain the optimum operating point. This tuning can rely on, e.g., waveguide sections with thermal or free-carrier-injection phase shifters, a technique which is applicable to both MZI and RR. For RR and asymmetric MZI with non-zero group delay difference $\tau_{g,MZI} = \left(L\Delta n_{eg,0} - \Delta L n_{eg} \right)/c$, the operating point may also be set by tuning the laser frequency. This is not an option in the case of symmetric MZI with zero or very small group-delay differences, which lead to an FSR $\Delta\omega_{FSR,MZI} = 1/\tau_{g,MZI}$ that exceeds the tuning range of the underlying light source. On the other hand, sensor systems based on symmetric MZI are less sensitive to laser frequency noise, see Section 4.4.3 for details.

For the balanced detection schemes such as in the RR$_{BD}$ and MZI$_2$ sensor implementations, the associated feedback loop to control these tuning elements is simple, as the effective optoelectronic transmission τ in the optimum operating

point is always exactly zero. The feedback control loop just has to minimize τ, and hence does not require any reference bias. It can be designed without knowledge of the expected signal levels, which may even vary over time.

For MZI_1, RR_{AP} and RR_{AD}, a more sophisticated feedback loop is required to tune to the optimum operating point. As an example, a small phase modulation can be employed that can easily be extracted at the sensor output. In the optimum operating point, the modulation amplitude at the senor output reaches a maximum, since the phase sensitivity is maximized along with the optoelectronic effective-index sensitivity. The feedback control loop has then to maintain the maximum modulation amplitude at the output.

For the MZI_3-based implementation, the sensitivity is independent of the operating point, which renders active feedback control unnecessary and thus vastly reduces system complexity. Moreover, a large dynamic range at constant sensitivity can be obtained by unwrapping the measured phases, provided that the acquisition bandwidth at the sensor output is fast enough to continuously track the phase change. Combining an unbalanced MZI_3 with a sufficiently large modulation of the operation wavelength allows for endless phase unwrapping even if the signal is not tracked continuously [80].

4.4.2.4 Optimum design parameters for overall maximum sensitivity

In the preceding sections, we have calculated the transmission functions and the extended effective optoelectronic transmission functions that define the effective-index sensitivities for a set of selected sensor implementation examples. We found that each sensor can be tuned to an optimum operating point that offers highest sensitivity towards changes of the effective refractive index in the sensitive regions, see Eq. (4.20). We will now expand our consideration and globally optimize the sensor design to identify the fundamental sensitivity limit that can be achieved for a given technology-specific modal power loss coefficient α and a given operating wavelength $\lambda = 2\pi/k_0$. In this consideration, the only remaining design parameters are the arm length L for the MZI and the round-trip length L along with the amplitude transmission ρ_1, ρ_2 of the coupling sections for the RR. In the following, we analytically optimize these parameters based on Eq. (4.20) to obtain a maximum sensitivity, where, for the

case of ring resonators, ρ and L are also encoded in c_Q and $\hat{\tau}$. We only discuss
the results in the subsequent paragraphs – the mathematical details of this opti-
mization are given in Appendix B.4.

Ring resonator coupling coefficients   The top panel of Fig. 4.4(a) shows the
peak optoelectronic effective-index sensitivity $S_{e,\tau,\text{peak}}$ of an all-pass ring reso-
nator (RR_{AP}) tuned to the optimum operating point relative to the maximum
achievable peak optoelectronic effective-index sensitivity $S_{e,\tau,\text{max}}$ as a function
of the amplitude transmission ρ_1 of the coupling section between the ring and
the bus waveguide. Notably, $S_{e,\tau,\text{max}}$ is achieved for an under-coupled ring res-
onator ($\rho_1 = \sqrt{a}$) and not for critical coupling ($\rho_1 = a$). For the add-drop con-
figuration (RR_{AD}), $S_{e,\tau,\text{peak}}$ depends on the amplitude transmission ρ_1 and ρ_2
of the through port and drop port coupling sections and is plotted as a colored
contour map in the bottom panel of Fig. 4.4(a). Also here, $S_{e,\tau,\text{max}}$ is found in a
slightly under-coupled (UC) regime ($\rho_1 = \rho_2 = a$), yielding a roughly 20%
higher peak sensitivity compared to the critically coupled (CC) case ($\rho_1 = \rho_2 a$).
The characteristics for the add-drop configuration with balanced detection
(RR_{BD}) are the same as for RR_{AD}.

Device length   Fig. 4.4(b) shows the peak sensitivities of different RR- and
MZI-based sensor implementations as a function of the attenuation αL. For
MZI, an optimum arm length of $L_{\text{opt}} = 1/\alpha$ can be found. This optimum results
from the fact that large arm lengths increase the accumulated phase shift but
decrease the optical power transmission and hence the output contrast. Exploit-
ing the full potential of low-loss waveguide technologies through MZI-based
sensors hence requires large device footprints. For RR, we consider different
implementations based on all-pass (RR_{AP}), add-drop (RR_{AD}), and balanced-de-
tection (RR_{BD}) schemes. We consider both critically coupled (CC) and under-
coupled (UC) implementations, see Table 4.3 for the exact choice of the ampli-
tude transmission ρ_1 and ρ_2 of the coupling sections. Irrespective of the exact
RR-based sensor implementation, the sensitivity is essentially length-independ-
ent for $\alpha L \ll 1$, provided that the coupling coefficients are adapted to the re-
spective value of $a = \exp(-\alpha L/2)$ as indicated in Fig. 4.4(a). Note that $\alpha L \ll 1$
is typically the case for ring resonators with radii on the order of tens of mi-
crometers realized on state-of-the-art integration platforms.
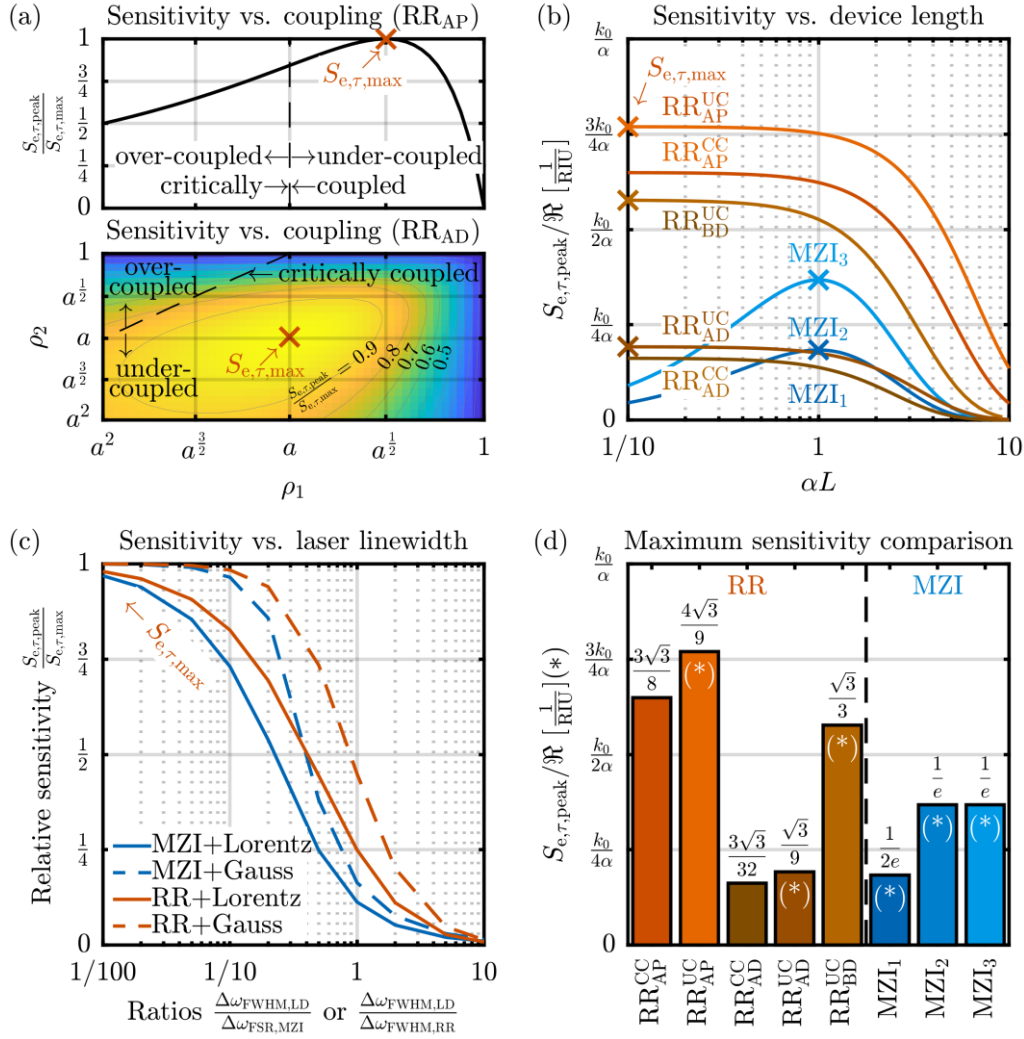
Fig. 4.4. Design optimization for maximum peak optoelectronic effective-index sensitivity and comparison of sensor implementations. **(a)** Influence of the amplitude transmission ρ_1 and ρ_2 of the through-port and drop-port coupling sections on the peak optoelectronic effective-index sensitivity $S_{\mathrm{e},\tau,\mathrm{peak}}$ of all-pass (RR$_{\mathrm{AP}}$, top panel) and add-drop (RR$_{\mathrm{AD}}$, bottom panel) RR with indications of over-coupled (OC), under-coupled (UC), and critically-coupled (CC) regimes. $S_{\mathrm{e},\tau,\mathrm{peak}}$ is normalized to its maximum peak value $S_{\mathrm{e},\tau,\mathrm{max}}$ for the respective configuration. The characteristics for the add-drop configuration with balanced detection (RR$_{\mathrm{BD}}$) are that same as for RR$_{\mathrm{AD}}$. For the RR$_{\mathrm{AP}}$ configuration, critical coupling is achieved for $\rho_1 = a$. For the RR$_{\mathrm{AD}}$ and RR$_{\mathrm{BD}}$ configuration, critical coupling requires $\rho_1 = a\rho_2$, indicated by a dashed line in the lower panel. **(b)** Influence of RR round-trip length (red) and MZI arm length (blue) on the peak effective-index sensitivity $S_{\mathrm{e},\tau,\mathrm{peak}}$, normalized by the electric readout responsivity $\Re$. Optimum device lengths are marked with crosses. Note that for the case of RR in a certain coupling state, the effective-index sensitivity is essentially independent of the round-trip length L as long as the round-trip attenuation is small, $\alpha L \ll 1$. For MZI, an optimum arm length of $L_{\mathrm{opt}} = 1/\alpha$ can be found. *[Remaining figure caption on the following page]*

[Continuation of Fig. 4.4 caption] **(c)** Sensitivity fading caused by frequency noise of the drive laser, quantified by a finite linewidth. We consider Lorentzian as well as Gaussian emission spectra, which are characterized by their full widths at half maximum $\Delta\omega_{\mathrm{FWHM,LD}}$. For RR, $\Delta\omega_{\mathrm{FWHM,LD}}$ imposes a lower practical limit on the spectral width $\Delta\omega_{\mathrm{FWHM,RR}}$ of the resonance and hence leads to an upper limit of the usable Q-factor for a given laser source. Note that these limitations do not apply to MZI, since $\Delta\omega_{\mathrm{FSR,MZI}}$ can always be made arbitrarily large by matching the group delay in the two arms. **(d)** Comparison of the peak effective-index sensitivity $S_{\mathrm{e},\tau,\mathrm{peak}}$ and the fundamentally achievable maximum peak effective-index sensitivity $S_{\mathrm{e},\tau,\mathrm{max}}$ for the various sensor concepts. All sensitivities are given as fractions of k_0/α and are ultimately limited the modal power loss coefficient α. Note that higher wavenumbers k_0 do generally not increase the optoelectronic effective-index sensitivity $S_{\mathrm{e},\tau}$: For a given quantum efficiency of the photodetector, the electric readout responsivity $\Re$ is inversely proportional to the photon energy and hence to the vacuum wavenumber $k_0 = \omega/c$, which exactly cancels the influence of k_0 on $S_{\mathrm{e},\tau}$. For a given waveguide technology, MZI can ultimately perform almost as well as RR while being insensitive to the laser linewidth. For MZI as well as under-coupled (UC) ring resonators, the graph indicates the maximum peak effective-index sensitivities $S_{\mathrm{e},\tau,\mathrm{max}}$ that can be achieved. These implementations are marked with a white asterisk (∗).

Note that our considerations did so far not take into account any non-idealities of the drive laser such as frequency noise, quantified by a non-zero linewidth, which can lead to a fading of the sensitivity. In the following, we consider laser sources with non-zero linewidths. To cover the range of practically relevant line shapes, we perform the analysis for both Lorentzian and Gaussian line shapes, see Appendix B.4 for details. The results are shown in Fig. 4.4(c). We can observe a fading of the optoelectronic effective-index sensitivity if the laser linewidth $\Delta\omega_{\mathrm{FWHM,LD}}$ approaches the full width at half maximum $\Delta\omega_{\mathrm{FWHM,RR}}$ of the ring resonance or the MZI free spectral range $\Delta\omega_{\mathrm{FSR,MZI}}$. As a rule of thumb, the laser linewidth should be kept two orders of magnitude smaller than the spectral features of the sensor transmission characteristics. Specifically, for high-Q RR, the laser linewidth becomes a particularly crucial parameter and may set an upper limit for usable ring resonator Q-factors for a laser with a given linewidth. Note that, besides the decreased optoelectronic effective-index sensitivity, laser frequency noise can also add to the overall noise of the readout signal, thereby impairing the limit of detection – see Section 4.4.3.4 for a more detailed discussion. Note also that MZI are not subject to any fundamental limitations related to the laser linewidth: By matching the group delays in the two

arms, the MZI FSR $\Delta\omega_{\text{FSR,MZI}}$ can always be made much larger than any practically relevant laser linewidth.

4.4.2.5   Sensitivity comparison of optimized sensor implementations

Assuming optimum device lengths L_{opt} and amplitude transmission factors $\rho_{1,\text{opt}}$ and $\rho_{2,\text{opt}}$ of the RR coupling sections, and neglecting detrimental effects that result from non-zero laser linewidths, we can calculate the peak optoelectronic effective-index sensitivity $S_{\text{e},\tau,\text{peak}}$ and the fundamentally achievable maximum peak optoelectronic effective-index sensitivity $S_{\text{e},\tau,\text{max}}$ of the various sensor concepts, see Appendix B.4 for details. The results are indicated in Fig. 4.4(d), and the corresponding sensor parameters are summarized in Table 4.3. The right-hand part of Fig. 4.4(d) shows the maximum peak effective-index sensitivity $S_{\text{e},\tau,\text{max}}$ of MZI with optimized arm lengths in different output configurations. The more complex implementations MZI$_2$ and MZI$_3$ allow to enhance $S_{\text{e},\tau,\text{max}}$ by using appropriate combinations of the output signals. Specifically, MZI$_2$ use a balanced detection of two complementary photodiode currents, which allows to double $S_{\text{e},\tau,\text{max}}$ compared to MZI$_1$. Moreover, balanced detection leads to zero effective transmission τ_{OP} in the optimum operating point and thereby simplifies feedback control for operating point stabilization. MZI$_3$ provide the same sensitivity as MZI$_2$ and are additionally insensitive with respect to the operating point [78,80], eliminating the need of a feedback control for operating-point stabilization. The left-hand part of Fig. 4.4(d) shows $S_{\text{e},\tau,\text{peak}}$ of typical RR-based sensor implementations.

For the same ring cavity, the RR$_{\text{AP}}$ implementation generally outperforms the corresponding RR$_{\text{AD}}$ concept by a factor of 4 due to the increased power loss introduced by the additional waveguide that is coupled to the RR$_{\text{AD}}$ resonator. For both implementations, optimized under-coupled (UC) operation leads to the maximum peak effective-index sensitivity $S_{\text{e},\tau,\text{max}}$, which outperforms the best $S_{\text{e},\tau,\text{max}}$ of critically coupled (CC) operation by roughly 20%. For RR$_{\text{AD}}$, the optimized under-coupled sensors are furthermore easier to reliably fabricate due to symmetric coupling gaps of the two tapping bus waveguides. The RR$_{\text{BD}}$ exploits both the drop- and through-ports and increases $S_{\text{e},\tau,\text{max}}$ by a factor of 3 compared to only using the drop-port.

Table 4.3: Peak optoelectronic effective-index sensitivity $S_{e,\tau,peak}$ and maximum peak optoelectronic effective-index sensitivity $S_{e,\tau,max}$ along with corresponding optimized design parameters for the various RR- and MZI-based sensor implementations. For the ring resonators (RR), we assume a given vacuum wavenumber k_0 and modal power loss coefficient α and calculate the peak optoelectronic effective-index sensitivity $S_{e,\tau,peak}$ in the optimum operating point for different implementations based on all-pass (RR$_{AP}$), add-drop (RR$_{AD}$), and balanced-detection (RR$_{BP}$) schemes as defined in Fig. 4.2. The quantity $a = \exp(-\alpha L/2)$ denotes the round-trip amplitude transmission factor. The maximum peak optoelectronic effective-index sensitivity $S_{e,\tau,max}$ is obtained for the under-coupled (UC) implementations, indicated by an asterisk ($*$) in the last column. For the critically-coupled (CC) implementations of RR$_{AP}$ and RR$_{AD}$, the peak sensitivity $S_{e,\tau,peak}$ is smaller than for the UC implementation. The parameters a, ρ_1 and ρ_2 fully define the quality ratio $c_Q = Q/Q_i$ of the RR, see Eq. (4.17), as well as the effective output contrast $\hat{\tau}$ and the effective optoelectronic transmission τ_{OP} for RR and MZI in the respective optimum operating point. For the MZI, we choose the optimum arm length $L = 1/\alpha$.

	L_{opt}	$\rho_{1,opt}$	$\rho_{2,opt}$	c_Q	$\dfrac{\hat{\tau}}{\mathfrak{R}}$	$\dfrac{\tau_{OP}}{\mathfrak{R}}$	$\dfrac{S_{e,\tau,peak}}{\mathfrak{R}}$ $\left(\dfrac{S_{e,\tau,max}}{\mathfrak{R}}$ if $(*)\right)$
RR$_{AP}^{CC}$	$< \dfrac{1}{\alpha}$	a	-	$\dfrac{1}{2}$	1	$\dfrac{1}{4}$	$\dfrac{3\sqrt{3}}{8}\times\dfrac{k_0}{\alpha}$
RR$_{AP}^{UC}$	$< \dfrac{1}{\alpha}$	$\sqrt{a}$	-	$\dfrac{2}{3}$	$\dfrac{8}{9}$	$\dfrac{1}{3}$	$\dfrac{4\sqrt{3}}{9}\times\dfrac{k_0}{\alpha}$ $(*)$
RR$_{AD}^{CC}$	$< \dfrac{1}{\alpha}$	a^2	a	$\dfrac{1}{4}$	$\dfrac{1}{2}$	$\dfrac{3}{8}$	$\dfrac{3\sqrt{3}}{32}\times\dfrac{k_0}{\alpha}$
RR$_{AD}^{UC}$	$< \dfrac{1}{\alpha}$	a	a	$\dfrac{1}{3}$	$\dfrac{4}{9}$	$\dfrac{1}{3}$	$\dfrac{\sqrt{3}}{9}\times\dfrac{k_0}{\alpha}$ $(*)$
RR$_{BD}^{UC}$	$< \dfrac{1}{\alpha}$	a	a	$\dfrac{1}{3}$	$\dfrac{4}{3}$	0	$\dfrac{\sqrt{3}}{3}\times\dfrac{k_0}{\alpha}$ $(*)$
MZI$_1$	$\dfrac{1}{\alpha}$	-	-	-	$\dfrac{1}{e}$	$\dfrac{1}{2e}$	$\dfrac{1}{2e}\times\dfrac{k_0}{\alpha}$ $(*)$
MZI$_2$	$\dfrac{1}{\alpha}$	-	-	-	$\dfrac{2}{e}$	0	$\dfrac{1}{e}\times\dfrac{k_0}{\alpha}$ $(*)$
MZI$_3$	$\dfrac{1}{\alpha}$	-	-	-	$\dfrac{2}{e}$	$\dfrac{1}{e}$ [a]	$\dfrac{1}{e}\times\dfrac{k_0}{\alpha}$ $(*)$

[a] Note that due to the complex-valued transmission τ of MZI$_3$, we specify $|\tau_{OP}|/\mathfrak{R}$.

Moreover, RR$_{BD}^{UC}$ implementations allow to push the effective transmission τ_{OP} in the optimum operating point to zero, which simplifies feedback control for

operating-point stabilization. Note that the optoelectronic effective-index sensitivity $S_{e,\tau}$ of an integrated phase-sensitive sensor can generally not be increased by using shorter operation wavelengths and hence larger wavenumbers $k_0 = \omega/c$, even though the normalization of the vertical axis by k_0/α might suggest this: For a given quantum efficiency of the photodetector, the electric readout responsivity $\mathfrak{R}$ is inversely proportional to the photon energy and hence to the vacuum wavenumber, which exactly cancels the effect that the phase change is proportional to k_0.

Comparing broadly the various RR- or MZI-based sensor implementations, we find that the maximum peak effective-index sensitivity $S_{e,\tau,\max} \propto \alpha^{-1}$ is ultimately dictated by the modal power loss coefficient α. This can be intuitively understood: In RR, the ratio k_0/α is directly linked to the Q-factor since $k_0/\alpha = Q_i/n_{eg}$, see Eq. (4.16), and hence the slope of the Lorentzian resonance, see Eq. (4.20). In MZI, k_0/α is related to the fundamental design trade-off between phase sensitivity and output contrast. The fundamental dependency of $S_{e,\tau,\max}$ on k_0 is eliminated due to the electric readout responsivity $\mathfrak{R}$, which accounts for the photodiode responsivity for the gain of any electrical readout amplifier, as well as for processing steps of the analog or digitized electric signals.

4.4.3 Limit of detection

In Section 4.4.2, we have compared the different RR- and MZI-based sensor implementations in terms of their sensitivity towards a change Δn_e of the effective refractive index in the sensitive waveguide region. We will now quantify and compare the limit of detection LoD, i.e., the smallest refractive-index change Δn_e that can be detected by the various sensors. To this end, we assume that all deterministic influences can be eliminated by proper technology control, device design, and calibration, and we thus disregard fabrication errors and the corresponding waveguide/component errors or splitter/coupler/detector imbalances as well as absolute sensor temperature or stress. Note that controlling the impact of these deterministic errors is a complex task in its own right, and a wide range of approaches has been explored in the literature. Apart from im-

proved fabrication processes [83,84] and error prediction [85], photonic components can be designed specifically for increased tolerance with respect to fabrication errors [86]. Moreover, waveguides or waveguide pairs in interferometer arms can be designed to minimize temperature effects [86–89], and on-chip as well as off-chip reference structures can be employed to compensate for environmental drift [66,90]. Factory calibration mechanisms can account for variations in the fabrication process [91], and advanced readout concepts and signal processing can dynamically recalibrate the sensor system at runtime [80]. Consequently, the remaining unavoidable measurement uncertainty and the associated LoD of the photonic sensor system is associated only with stochastic noise sources, which we analyze in the following paragraphs.

The noise-propagation model is illustrated in Fig. 4.5. As noise sources ζ_n, we consider laser frequency and intensity (power) noise ω_n and $P_{i,n}$ with variances $\sigma_{\omega_n}^2 = \overline{\omega_n^2}$ and $\sigma_{P_{i,n}}^2 = \overline{P_{i,n}^2}$, which partially result from noise $I_{i,n}$ of the laser drive current, see Fig. 4.1(c). Note that our model treats the laser frequency and intensity (power) noise ω_n and $P_{i,n}$ as statistically independent random variables and does not account for the exact dependence of these quantities on the drive-current noise $I_{i,n}$. This is illustrated by dashed lines in Fig. 4.5. We further include temperature fluctuations ϑ_n between the sensor and the co-integrated reference structure on the photonic chip, which are characterized by a variance $\sigma_{\vartheta_n}^2$. In the model shown in Fig. 4.1(c), these temperature fluctuations are accounted for via a temperature-induced fluctuation $P_{o,n}$ with variance $\sigma_{P_{o,n}}^2 = \overline{P_{o,n}^2}$ of the optical sensor output power P_o. At the detector side, we consider the photocurrent shot noise $I_{s,n}$ with variance $\sigma_{I_{s,n}}^2 = \overline{I_{s,n}^2}$ as well as additional photodetector noise $I_{NEP,n}$ with variance $\sigma_{I_{NEP,n}}^2 = \overline{I_{NEP,n}^2}$, quantified by the so-called noise-equivalent power (NEP). Both of these noise currents contribute towards the total output-photocurrent noise $I_{o,n}$ with variance $\sigma_{I_{o,n}}^2 = \overline{I_{o,n}^2}$, see Fig. 4.1(c) and in Fig. 4.5. We further account for quantization noise introduced by analog-to-digital conversion of the photocurrent, described by a quantization-noise current $I_{q,n}$ with variance $\sigma_{I_{q,n}}^2 = \overline{I_{q,n}^2}$. All these noise sources $\zeta_n \in \left\{ \vartheta_n; \omega_n; P_{i,n}; I_{s,n}; I_{NEP,n}; I_{q,n} \right\}$ are treated as random variables with zero mean $\overline{\zeta_n} = 0$ that have associated variances $\sigma_{\zeta_n}^2 = \overline{\zeta_n^2}$. Note that the subscript "n" in these quantities refers to newly added noise in a certain stage of the sensor signal chain, in contrast to the noise that was accumulated from previous stages

and that is denoted by symbols without subscript "n", see Eq. (4.7). In the following, we assume for simplicity a unity propagation factor through the ADC, $\left|\partial I_q / \partial I_o\right|^2 = 1$, and add all three detection-related current noise variances to obtain the variance $\sigma_{I_q}^2 = \sigma_{I_{s,n}}^2 + \sigma_{I_{NEP,n}}^2 + \sigma_{I_{q,n}}^2$ of the quantized output current I_q.

The propagation of these noise quantities and of the associated noise variances $\sigma_{\zeta_n}^2$ through the system is illustrated in Fig. 4.5. Each noise variance $\sigma_{\zeta_n}^2$ is associated with a noise propagation factor W_ζ that describes the propagation of $\sigma_{\zeta_n}^2$ through the sensor system to the overall variance $\sigma_{\Delta n_{e,r}}^2$ of the reconstructed effective-refractive-index change $\Delta n_{e,r}$. In the illustration of Fig. 4.5, each noise propagation W_ζ is associated with a solid trace of the respective color that connects the variance of the respective noise source (colored ellipse) to the overall variance $\sigma_{\Delta n_{e,r}}^2$ (green ellipse).
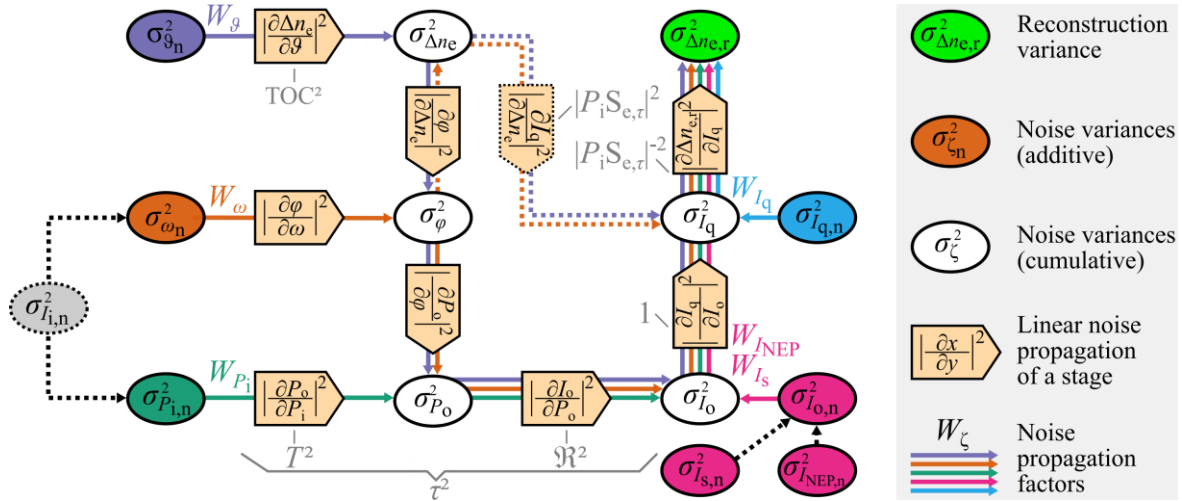
Fig. 4.5. Illustration of the noise propagation. The individual noise quantities $\zeta_n \in \left\{ \vartheta_n ; \omega_n ; P_{i,n} ; I_{s,n} ; I_{NEP,n} ; I_{q,n} \right\}$ with associated additive noise variances $\sigma_{\zeta_n}^2$, indicated by filled colored ellipses, propagate through different stages of the sensor system and contribute to cumulative noise variances of the intermediate quantities $\sigma_{\Delta n_e}^2$, σ_φ^2, $\sigma_{P_o}^2$, $\sigma_{I_o}^2$ and $\sigma_{I_q}^2$, all indicated by white ellipses. For simplicity, we assume all noise quantities to be uncorrelated, such that the variances of the respective contributions towards the overall reconstruction variance $\sigma_{\Delta n_{e,r}}^2$ may simply be added, see Eq. (4.21). We consider laser frequency noise ω_n (brown) and intensity (power) noise $P_{i,n}$ (dark green) with variances $\sigma_{\omega_n}^2 = \overline{\omega_n^2}$ and $\sigma_{P_{i,n}}^2 = \overline{P_{i,n}^2}$, neglecting a potential correlation of these quantities, which might result from their joint dependence on laser drive current noise $I_{i,n}$ with variance $\sigma_{I_{i,n}}^2 = \overline{I_{i,n}^2}$. We further consider temperature fluctuations ϑ_n (purple) between the sensor and the co-integrated reference structure on the photonic chip, which feature a variance $\sigma_{\vartheta_n}^2$. *[Remaining figure caption on the following page]*

[Continuation of Fig. 4.5 caption] At the detector side, our model includes the photocurrent shot noise $I_{\text{s,n}}$ with variance $\sigma_{I_{\text{s,n}}}^2 = \overline{I_{\text{s,n}}^2}$ as well as additional photodetector noise $I_{\text{NEP,n}}$ with variance $\sigma_{I_{\text{NEP,n}}}^2 = \overline{I_{\text{NEP,n}}^2}$, quantified by the so-called noise-equivalent power (NEP), both contributing towards the total photocurrent noise $I_{\text{o,n}}$ at the sensor output with variance $\sigma_{I_{\text{o,n}}}^2 = \overline{I_{\text{o,n}}^2}$ (magenta). We further account for quantization noise introduced by the digital-to-analog conversion of the photocurrent I_{o}, described by the quantization noise current $I_{\text{q,n}}$ with variance $\sigma_{I_{\text{q,n}}}^2 = \overline{I_{\text{q,n}}^2}$ (blue). The noise propagation factors W_ζ from each noise variance σ_ζ^2 to the reconstruction variance $\sigma_{\Delta n_{\text{e,r}}}^2$ (light green) of the effective refractive index $\Delta n_{\text{e,r}}$ are depicted by solid traces of the color associated with the respective noise source. The various noise propagation factors W_ζ are obtained by multiplying the linearized small-signal power transmission factors of the stages along the respective noise path. These small-signal power transmission factors of the various stages are indicated in arrow-shaped ochre fields, with simplified expressions in grey next to the respective field. The calculation of the noise propagation factors W_ω and W_ϑ can be simplified by skipping the explicit calculation of the error propagation via the intermediate quantities σ_φ^2, $\sigma_{P_{\text{o}}}^2$, $\sigma_{I_{\text{o}}}^2$ and $\sigma_{I_{\text{q}}}^2$, but instead taking the detour indicated by the dotted lines. To this end, we first translate the temperature fluctuations ϑ_{n} or the frequency noise fluctuations ω_{n} into equivalent fluctuations of the effective refractive index n_{e}, which are then propagated to the cumulative variance $\sigma_{I_{\text{q}}}^2$ of the quantized output current by re-using the results from the sensitivity calculations of Section 4.4.2, $\left| \partial I_{\text{q}} / \partial \Delta n_{\text{e}} \right|^2 = \left| P_{\text{i}} S_{\text{e},\tau} \right|^2$. As this term cancels with the term $\left| P_{\text{i}} S_{\text{e},\tau} \right|^{-2}$ associated with the reconstruction of the effective-index change $\Delta n_{\text{e,r}}$ from the quantized output current I_{q}, we obtain simple expressions for the impact of these two noise sources on the associated reconstruction variance, $\sigma_{\Delta n_{\text{e}},\vartheta}^2 = \text{TOC}^2 \sigma_{\vartheta_{\text{n}}}^2$ and $\sigma_{\Delta n_{\text{e}},\omega}^2 = (n_{\text{eg}}/\omega)^2 \sigma_{\omega_{\text{n}}}^2$ (RR), and $\sigma_{\Delta n_{\text{e}},\omega}^2 = 0$ (MZI with group-delay-matched arms).

Assuming that the various noise sources are statistically independent, the overall variance $\sigma_{\Delta n_{\text{e,r}}}^2$ can thus be expressed as a sum of the variances $\sigma_{\zeta_{\text{n}}}^2$ weighted with the corresponding noise propagation factors W_ζ,

$$\sigma_{\Delta n_{\text{e,r}}}^2 = \sum_\zeta W_\zeta \sigma_{\zeta_{\text{n}}}^2, \quad W_\zeta = \left| \frac{\partial \Delta n_{\text{e,r}}}{\partial \zeta_{\text{n}}} \right|^2, \quad \zeta_{\text{n}} \in \left\{ \vartheta_{\text{n}}; \omega_{\text{n}}; P_{\text{i,n}}; I_{\text{s,n}}; I_{\text{NEP,n}}; I_{\text{q,n}} \right\},$$

$$\sigma_{\Delta n_{\text{e,r}}}^2 = \underbrace{W_\vartheta \sigma_{\vartheta_{\text{n}}}^2}_{\sigma_{\Delta n_{\text{e,r}},\vartheta}^2} + \underbrace{W_\omega \sigma_{\omega_{\text{n}}}^2}_{\sigma_{\Delta n_{\text{e,r}},\omega}^2} + \underbrace{W_{P_{\text{i}}} \sigma_{P_{\text{i,n}}}^2}_{\sigma_{\Delta n_{\text{e,r}},P_{\text{i}}}^2} + \underbrace{W_{I_{\text{s}}} \sigma_{I_{\text{s,n}}}^2}_{\sigma_{\Delta n_{\text{e,r}},I_{\text{s}}}^2} + \underbrace{W_{I_{\text{NEP}}} \sigma_{I_{\text{NEP,n}}}^2}_{\sigma_{\Delta n_{\text{e,r}},I_{\text{NEP}}}^2} + \underbrace{W_{I_{\text{q}}} \sigma_{I_{\text{q,n}}}^2}_{\sigma_{\Delta n_{\text{e,r}},I_{\text{q}}}^2}.$$

$$(4.21)$$

In this relation, the contribution of an individual noise source ζ_{n} to the uncertainty of the reconstructed effective refractive index $\Delta n_{\text{e,r}}$ is quantified by the associated reconstruction variances $\sigma_{\Delta n_{\text{e,r}},\zeta}^2 = W_\zeta \sigma_{\zeta_{\text{n}}}^2$.

Table 4.4: Quantification of various noise sources along with the corresponding noise propagation factors as defined in Eq. (4.21) and Fig. 4.5. The columns refer to different noise sources ζ_n within the sensor system, which contribute to the total limit of detection (LoD). The second and the third row relate to analytic descriptions of the individual noise variances $\sigma_{\zeta_n}^2$ at their origin and to the corresponding noise propagation factors W_ζ through the sensor system to the reconstructed value of the effective-index change. The subsequent rows describe the associated reconstruction variances $\sigma_{\Delta n_{e,r},\zeta}^2$ that contribute to the uncertainty of $\Delta n_{e,r}$ and that thus quantify the minimum detectable refractive-index change. Note that these reconstruction variances are split up into base expressions for each noise source, which are identical for all sensor implementations, fourth line, as well as into implementation-dependent multiplication factors, which show the implementation-specific impairments for the operating points according to Table 4.3. For RR, impairments by laser frequency noise are unavoidable. In case of MZI, the impact of laser frequency noise can be diminished by using symmetric devices with matched group delays in the two interferometer arms, leading to a zero multiplication factor, indicated by an asterisk (*).

		Tempera-ture $\zeta_n = T_n$	Laser frequency $\zeta_n = \omega_n$	Laser intensity $\zeta_n = P_{i,n}$	PD shot noise $\zeta_n = I_{s,n}$	PD NEP $\zeta_n = I_{NEP,n}$	Quantization $\zeta_n = I_{q,n}$
Noise variances	$\sigma_{\zeta_n}^2$	$\sigma_{T_n}^2$	$4\pi^2 \int_0^{\Delta f} S_F(f)\,df$	$P_i^2 \int_0^{\Delta f} S_{RIN}(f)\,df$ $\cong P_i^2 RIN \Delta f$	$2q_e I_o \Delta f$	$\mathfrak{R}^2 NEP^2 \Delta f$	$\dfrac{LSB^2}{12} = \dfrac{I_{o,max}^{-2N}}{12}$
Noise propagation factors	W_ζ	TOC^2	$\left(\dfrac{\partial \varphi_{OP}}{\partial \omega}\right)^2 \left(\dfrac{1}{k_0 L}\right)^2$	$\left(\dfrac{1}{P_i}\right)^2 \left(\dfrac{|\tau|}{S_{e,\tau}}\right)^2$	$\left(\dfrac{1}{P_i}\right)^2 \left(\dfrac{1}{S_{e,\tau}}\right)^2$	$\left(\dfrac{1}{P_i}\right)^2 \left(\dfrac{1}{S_{e,\tau}}\right)^2$	$\left(\dfrac{1}{P_i}\right)^2 \left(\dfrac{1}{S_{e,\tau}}\right)^2$
Reconstruction variances	$\sigma_{\Delta n_{e,r},\zeta}^2$	$TOC^2 \sigma_{T_n}^2$	$\left(\dfrac{\sigma_{\omega_n}}{\omega}\right)^2$	$\left(\dfrac{\alpha}{k_0}\right)^2 RIN \Delta f$	$\left(\dfrac{\alpha}{k_0}\right)^2 \dfrac{q_e \Delta f}{\mathfrak{R} P_i}$	$\left(\dfrac{\alpha}{k_0}\right)^2 \dfrac{NEP^2 \Delta f}{P_i^2}$	$\left(\dfrac{\alpha}{k_0}\right)^2 \dfrac{2^{-2N}}{12}$
RR_{AP}^{CC}				$\times 4/27$	$\times 32/27$	$\times 64/27$	$\times 64/27$
RR_{AP}^{UC}				$\times 9/48$	$\times 54/48$	$\times 27/16$	$\times 4/3$
RR_{AD}^{CC}		$\times 1$	$\times n_{eg}^2$	$\times 16/3$	$\times 256/9$	$\times 1024/27$	$\times 256/27$
RR_{AD}^{UC}				$\times 3$	$\times 18$	$\times 27$	$\times 16/3$
RR_{BD}^{UC}				$\times 0$	$\times 2$	$\times 6$	$\times 16/3$
MZI_1			$\times \underbrace{\left(\Delta n_{eg,0} - n_{eg}\dfrac{\Delta L}{L}\right)}_{=0\ (*)}$	$\times 1$	$\times 4e$	$\times 4e$	$\times 4$
MZI_2		$\times 1$		$\times 0$	$\times 2e$	$\times 2e$	$\times 4$
MZI_3				$\times 0$	$\times 2e$	$\times 6e$	$\times 8/3$

(Relative implementation impairments)

In order to quantify the total LoD according to Eq. (4.8), we calculate the 3σ-deviation of the reconstructed effective refractive index $\Delta n_{\mathrm{e,r}}$ that results from the various noise contributions according to Eq. (4.21).The following sections are dedicated to the detailed quantification of all discussed noise-related terms, i.e., the noise variances $\sigma^2_{\zeta_{\mathrm{n}}}$ (Section 4.4.3.1), the corresponding noise propagation factors W_{ζ} (Section 4.4.3.2), as well as the associated reconstruction variances $\sigma^2_{\Delta n_{\mathrm{e,r}},\zeta}$ (Section 4.4.3.3). This allows us to perform a quantification and comparison of the limit of detection LoD (Section 4.4.3.4) for each RR- and MZI-based sensor implementation. The mathematical details on the noise variances, noise propagation factors and reconstruction variances are summarized in Table 4.4.

4.4.3.1 Noise variances

Regarding temperature variations, we assume that the absolute temperature of the sensor can be accounted for by proper stabilization, calibration and referencing [88], and that the sensor and the reference structures are based on waveguides with negligible differences in thermo-optic coefficients (TOC) [89]. Note that, in general, on-chip temperature variations do not affect MZI and RR alike. For MZI, the temperature-dependent behavior of the power splitter at the input and the power combiner at the output, typically realized as multimode interference (MMI) or directional couplers, as well as of the waveguides in the sensor and reference arms have to be taken into account. For the couplers, careful design can at least reduce the impact of temperature fluctuations, whereas temperature-induced shifts of the phase difference between sensor and reference arms can be largely suppressed by balancing arm lengths and waveguide TOC. In case of a balanced MZI with athermal couplers, the output signal is not distorted by absolute temperature drifts that affect both arms alike, as the MZI reference arm inherently acts as a temperature reference. For RR, the temperature-dependent properties of the coupling section as well as of the sensor waveguide within the resonator have to be taken into account, which can again both be reduced via athermal designs. However, in contrast to MZI, there is no configuration that inherently compensates the temperature dependence of the phase shift in the RR waveguide, and a dedicated reference RR has to be added for independent measurement of the temperature-dependent behavior. The data

measurement from the reference structure can then be used for compensating the temperature dependence, e.g., by suitable feedback control or signal processing techniques. In general, sensor and reference waveguides should be routed in close proximity and with good thermal coupling to one another, ideally using interleaved circuit layouts that eliminate the impact of on-chip temperature gradients [92]. In addition, further temperature-reference structures can be included on a chip or package level to eliminate the impact of global temperature offsets by appropriate signal processing techniques.

As a consequence, stochastic on-chip temperature fluctuations remain as the only noise contribution. These fluctuations are quantified by the variance $\sigma_{\vartheta_n}^2$ of the temperature difference between the photonic sensor and the corresponding reference structure, which contribute to output-power fluctuations $P_{o,n}$ of the sensor. For MZI, $\sigma_{\vartheta_n}^2$ relates to the variance of the temperature difference between the two interferometer arms, whereas for RR, $\sigma_{\vartheta_n}^2$ represents the variance of the temperature difference between the sensor ring and the corresponding reference ring.

Regarding laser frequency fluctuations, it is not possible to state a universal analytical expression for $\sigma_{\omega_n}^2$ since frequency-noise spectra of integrated lasers differ strongly. In theory, the variance $\sigma_{\omega_n}^2$ of the laser frequency fluctuation can be obtained by integrating the one-sided laser frequency noise spectrum $S_F(f)$ over the relevant frequency interval $\left[1/T_{obs}, \Delta f\right]$, where T_{obs} denotes the overall observation during a complete set of measurements while Δf denotes the electronic acquisition bandwidth of the sensor system, see also Eq. (B.16) in Appendix B.5. In practice, however, this approach is hard to apply, since the laser frequency noise spectrum $S_F(f)$ usually increases strongly towards small Fourier frequencies $f \to 0$ such that the integral diverges for $T_{obs} \to \infty$. Specifically, real lasers without frequency stabilization are typically subject to slow frequency drift, which leads to an additional $1/f^{\gamma}$-part in the frequency noise spectrum, where γ typically lies between 0 and 2 [93]. For most sensor systems with typical acquisition bandwidths Δf in the kHz or the lower MHz range, the contribution of this $1/f^{\gamma}$-part dominates the variance $\sigma_{\omega_n}^2$ of the frequency fluctuations, while the spectrally white frequency-noise background can be neglected. As a consequence, the intrinsic linewidth of the laser source, which is

given by the spectrally white component of the frequency-noise, is often not a relevant metric for laser sources in integrated phase-sensitive photonic sensors. For a given laser source, the frequency fluctuations usually have to be measured individually using, e.g., a heterodyne technique, see Appendix B.5 for details.

The variance of the laser output power fluctuation is denoted as $\sigma_{P_{i,n}}^2$ and can be calculated from the relative intensity noise (RIN) spectrum $S_{\mathrm{RIN}}(f)$, which is often expressed in dB Hz^{-1} [94]. Note that for the typically small electronic acquisition bandwidths Δf employed in sensing applications, the RIN spectrum is mostly flat. The input power variance can hence be approximated as $\sigma_{P_{i,n}}^2 = P_i^2 \mathrm{RIN} \Delta f$, where the quantity RIN refers to the constant, one-sided spectral density $S_{\mathrm{RIN}}(f)$ in the limit of low frequencies and is a commonly used performance metric for lasers. Note that both $\sigma_{P_{i,n}}^2$ and $\sigma_{\omega_n}^2$ may sensitively depend on the fluctuations of the laser drive current as well as on temperature fluctuations of the laser, in which case the respective variances may be correlated. For simplicity, we neglect this effect in our analysis.

The variance $\sigma_{I_{o,n}}^2$ of the photodetector output current fluctuations comprises both the photocurrent shot noise as well as additional noise contributions of the detector circuit such as thermal noise and dark-current shot noise, which, for a given device, are often quantified by the noise-equivalent power (NEP). For a given internal noise level, the NEP specifies the optical input power of the photodetector that leads to a signal-to-noise ratio of one at the output. Photocurrent shot noise is characterized by the variance $\sigma_{I_{s,n}}^2 = 2 q_e I_o \Delta f$, here expressed as a function of the average output current I_o in the operating point, the acquisition bandwidth Δf and the elementary charge q_e [95]. In contrast to that, the NEP-related current noise is independent of the actual signal level and features a variance $\sigma_{I_{\mathrm{NEP,n}}}^2 = \Re^2 \mathrm{NEP}^2 \Delta f$ [96]. In this relation, $\Re$ denotes the electric readout responsivity that accounts for the responsivity of the photodetector and for any optional subsequent amplifiers, see Section 4.4.2.1. Furthermore, Δf is the electronic acquisition bandwidth, and the NEP level, specified in $\mathrm{W}/\sqrt{\mathrm{Hz}}$, is assumed to be constant within $0 < f < \Delta f$.

Finally, we consider quantization noise originating from a finite ADC resolution of N bits, which does not depend on the acquisition bandwidth Δf. The quanti-

zation process introduces an erroneous current $I_{q,n}$ characterized by the associated variance $\sigma_{I_{q,n}}^2 = \mathrm{LSB}^2 / 12$ [97], where LSB is the quantization step corresponding to the least significant bit as defined by the ADC range as well as resolution N. Since we need to tune the sensors to the optimum operating point, and since we assume that we cannot reliably set the initial operating point by design, the ADC has to cover the whole range from zero output current to maximum output current $I_{o,max}$ at each output port, and thus $\mathrm{LSB} = I_{o,max} 2^{-N}$.

The equations required to calculate the noise variances $\sigma_{\zeta_n}^2$ for all noise sources ζ_n are listed in Row 2 of Table 4.4. The noise variance models above show that the acquisition bandwidth Δf is a major factor for the noise analysis. The measurement bandwidth is connected to the integration time T_{int} and to the minimum required sampling frequency f_s by $T_{int} = 1/f_s = 1/(2\Delta f)$. Except for quantization noise, choosing an appropriate integration time is hence crucial for the sensor performance. The relations shown in Row 2 of Table 4.4 indicate that the noise variances $\sigma_{P_{i,n}}^2$, $\sigma_{I_{s,n}}^2$ and $\sigma_{I_{NEP,n}}^2$ of the laser RIN as well as of the photodetector shot noise and NEP decrease for smaller acquisition bandwidths Δf or longer integration times T_{int}, i.e., longer averaging pays off and can eventually render the impact of these noise sources insignificant. In contrast to this, the stochastic processes describing temperature and laser frequency noise are not mean free, thus leading to reconstruction variances that eventually grow with longer integration times. This can be quantified by the respective Allan variances [98], which exhibit typical bathtub-like characteristics when plotted as a function of integration time. To obtain reliable results for measurements with long observation times T_{obs}, the non-stationary portions of these noise sources have to be eliminated by suitable stabilization or referencing systems. A detailed discussion with respect to laser frequency noise can be found in Appendix B.6.

4.4.3.2 Noise propagation factors

The noise propagation factors W_ζ for each noise source ζ_n can be obtained following the concept of the noise propagation model described in Fig. 4.5, where we again use linear approximations for all transmission functions in the respective operating point. The resulting noise propagation factors are specified in Table 4.4, Row 3.

To explain these relations, let us first consider the propagation factor W_{I_s} related to photodetector shot noise with variance $\sigma^2_{I_{s,n}}$, see Column 5 in Row 3 of Table 4.4, which translates into an equivalent reconstruction variance $\sigma^2_{\Delta n_{e,r}, I_s} = W_{I_s} \sigma^2_{I_{s,n}}$ of the reconstructed effective-refractive-index change $\Delta n_{e,r}$, see also Fig. 4.5. For calculating the noise-propagation factor W_{I_s}, we exploit the fact that changes of the effective index are related to changes of the output current via the optoelectronic effective-index sensitivity $\partial I_o / \partial n_e = P_i S_{e,\tau}$, see last column of Table 4.3 for the corresponding expressions of the various sensor implementations. The reconstruction algorithm of a properly calibrated sensor exactly inverts this relationship such that the contribution $\sigma^2_{\Delta n_{e,r}, I_s}$ of the shot noise to the variance of the reconstructed effective-index change $\Delta n_{e,r}$ can be expressed as $\sigma^2_{\Delta n_{e,r}, I_s} = \sigma^2_{I_{s,n}} / \left| P_i S_{e,\tau} \right|^2$. The overall noise propagation factor can thus be written as $W_{I_s} = \left| P_i S_{e,\tau} \right|^{-2}$. This noise propagation factor does not only apply to shot noise, but can generally be used to calculate the contribution of any current noise to the uncertainty of the reconstructed effective refractive index $\Delta n_{e,r}$, $W_{I_s} = W_{I_q} = W_{I_{NEP}}$, see Columns 6 and 7 in Row 3 of Table 4.4. In the case of laser RIN, the associated noise propagation factor $W_{RIN} = \left| \tau \right|^2 W_{I_o} = \left| \tau \right|^2 \left| P_i S_{e,\tau} \right|^{-2}$ additionally contains the squared magnitude of the effective optoelectronic transmission $\left| \tau \right|^2$, which describes the translation of the input-power variance $\sigma^2_{P_i}$ to a contribution towards the variance $\sigma^2_{I_o}$ of the sensor output current I_o, see Column 4 in Row 3 of Table 4.4. Hence, all four noise sources considered so far, i.e., laser intensity noise, photodiode shot noise, photodiode NEP noise, as well as quantization noise, have a noise propagation factor that is proportional to $\left| P_i S_{e,\tau} \right|^{-2}$. For these noise contributions, a large sensitivity always helps to reduce the associated LoD.

The remaining noise sources are on-chip temperature fluctuations ϑ_n and laser frequency noise ω_n, see Columns 2 and 3 in Row 3 of Table 4.4. Both effects have direct impact on the phases φ_{RR} and φ_{MZI} according to Eqs. (4.9) and (4.11). For these noise sources, the noise propagation factors W_ϑ and W_ω are finally independent of the sensitivity-related term $\left| P_i S_{e,\tau} \right|^2$.

In the case of temperature fluctuations, the noise propagation factor W_ϑ can be obtained by calculating the relationship between a temperature-difference fluctuation ϑ_n and the corresponding fluctuation $\Delta n_{e,\vartheta} = \text{TOC}\,\vartheta_n$ of the effective-

index difference between the sensor and the reference waveguide. The propagation of this effective-index perturbation $\Delta n_{e,\vartheta}$ to the output current I_o and the subsequent propagation through the reconstruction algorithm are given by $\left| P_i S_{e,\tau} \right|^2$ and $\left| P_i S_{e,\tau} \right|^{-2}$, respectively, such that the net effect cancels. This leads to a noise propagation factor $W_\vartheta = \text{TOC}^2 \left| P_i S_{e,\tau} \right|^2 \left| P_i S_{e,\tau} \right|^{-2} = \text{TOC}^2$ as indicated in Row 3, Column 2 of Table 4.4. In the graphical illustration of the noise-propagation model in Fig. 4.5, this corresponds to a detour in the noise-propagation path as illustrated by the purple dashed line, which directly connects the variance $\sigma^2_{\Delta n_e}$ of the refractive-index difference with the variance $\sigma^2_{I_q}$ of the quantized output current. The propagation factor W_ω for laser frequency noise can be obtained in a similar way by considering the associated shift of the sensor operating point φ_{OP}. To this end, we again calculate the equivalent effective-refractive-index change $\Delta n_{e,\omega}$ that would lead to the same operating-point phase shift $\Delta\varphi_{OP}$ as a laser frequency shift ω_n. The two quantities are related by $\Delta n_{e,\omega} = \left(\partial\varphi_{OP}/\partial\Delta n_e\right)^{-1}\left(\partial\varphi_{OP}/\partial\omega\right)\omega_n = \left(-1/k_0 L\right)\left(\partial\varphi_{OP}/\partial\omega\right)\omega_n$. The propagation of the effective-index perturbation $\Delta n_{e,\omega}$ to the output current I_o and the subsequent propagation through the reconstruction algorithm does again not have any overall effect, thus leading to a noise propagation factor $W_\omega = \left(1/k_0 L\right)^2\left(\partial\varphi_{OP}/\partial\omega\right)^2$, see Column 3 in Row 3 of Table 4.4 as well as brown dashed signal propagation in Fig. 4.5. For RR, this simplifies to $W_\omega = \left(n_{eg}/\omega\right)^2$, where $n_{eg} = n_e + \omega\left(\mathrm{d}n_e/\mathrm{d}\omega\right)$ denotes the group refractive index of the waveguide mode that is subject to the frequency fluctuation. In the case of MZI, the frequency dependence $\partial\varphi_{OP,MZI}/\partial\omega$ of the phase difference in the operating point can be approximated by $\partial\varphi_{OP,MZI}/\partial\omega \approx \left(\varphi_{OP,MZI}/\omega\right)\times\left(n_{eg}/n_e\right)$, see Eq. (B.11) in Appendix B.6.

4.4.3.3 Reconstruction variances

With the help of the noise variances $\sigma^2_{\zeta_n}$ and the noise propagation factors W_ζ explained in the previous two paragraphs, we now calculate the individual contributions $\sigma^2_{\Delta n_{e,r},\zeta} = W_\zeta \sigma^2_{\zeta_n}$ of each noise source ζ_n to the overall reconstruction variance $\sigma^2_{\Delta n_{e,r}}$ of the reconstructed effective refractive index in the sensitive region. For better comparison, we split up the results into noise-type-specific base expressions, which are identical for all sensor implementations, fourth row

of Table 4.4, as well as into sensor-implementation-dependent multiplication factors, subsequent rows of Table 4.4.

It is important to note that the reconstruction variances $\sigma^2_{\Delta n_{\mathrm{e,r}},\zeta}$ depend on the operating point and that the implementation-dependent factors shown in Table 4.4 are only valid in the optimum operating points, as defined in Eq. (4.18) for RR and Eq. (4.19) for MZI. In these operating points, we can use specific values for the optoelectronic transmission $\tau = \tau_{\mathrm{OP}}$ and the optoelectronic effective-index sensitivity $S_{\mathrm{e},\tau} = S_{\mathrm{e},\tau,\mathrm{peak}}$ or $S_{\mathrm{e},\tau} = S_{\mathrm{e},\tau,\mathrm{max}}$, see Table 4.3. Outside the optimum operating point, the reconstruction variances $\sigma^2_{\Delta n_{\mathrm{e,r}},\zeta}$ can be obtained by calculating τ and $S_{\mathrm{e},\tau}$ from the generic transmission according to Eqs. (4.10) and (4.12) along with the relations of τ according to Table 4.2, Column 2. Note that in the case of multi-output implementations such as the MZI$_2$, MZI$_3$ and RR$_{\mathrm{BD}}$, the implementation-dependent factors of the reconstruction variances $\sigma^2_{\Delta n_{\mathrm{e,r}},\zeta}$ can include covariance terms that result from correlations of the noise in the different output signals. As an example, the current fluctuations of the different output signals caused by laser RIN are correlated, while the current fluctuations originating from the NEP or the shot noise of the various photodetectors are not.

Regarding laser frequency noise, impairments are unavoidable for RR-based sensor implementations. In contrast to this, the impact of laser frequency noise in MZI-based schemes can be diminished by using symmetric devices with matched group delays in the two interferometer arms, leading to a zero multiplication factor as indicated by an asterisk in Table 4.4.

4.4.3.4 LoD comparison of optimized sensor implementations

With a fully quantified noise analysis according to Table 4.4 at hand, we now compare the different sensor implementations and discuss the impact of each noise source on the associated LoD. The results of this analysis are visualized in Fig. 4.6. In a first step, we analyze the contributions of the different noise sources to the LoD – the results are plotted in the first row and denoted as Fig. 4.6(a). We then compare how the individual sensor and readout implementations are affected by each noise source – this is shown in the second row and denoted as Fig. 4.6(b). Finally, we quantitatively estimate typical contributions

of the various noise sources to the LoD and identify dominating effects for each sensor implementation, see Fig. 4.6(c).

LoD as a function of noise-source parameters   The individual contributions $\sigma^2_{\Delta n_{\mathrm{e,r}},\zeta}$ of the various noise source ζ_{n} to the overall variance $\sigma^2_{\Delta n_{\mathrm{e,r}}}$ of the reconstructed effective-index difference $\Delta n_{\mathrm{e,r}}$ can be used to calculate the associated individual LoD contributions $\mathrm{LoD}_\zeta = 3\sigma_{\Delta n_{\mathrm{e,r}},\zeta}$, each of which corresponds to the sensors' total LoD in case all other noise sources are negligible. If several noise sources are relevant, the overall LoD can be calculated as the square root of the sum of squares of the individual LoD, where we assume for simplicity that the various noise sources are statistically independent,

$$\mathrm{LoD}=\sqrt{\sum\nolimits_\zeta \mathrm{LoD}_\zeta^2} \ . \tag{4.22}$$
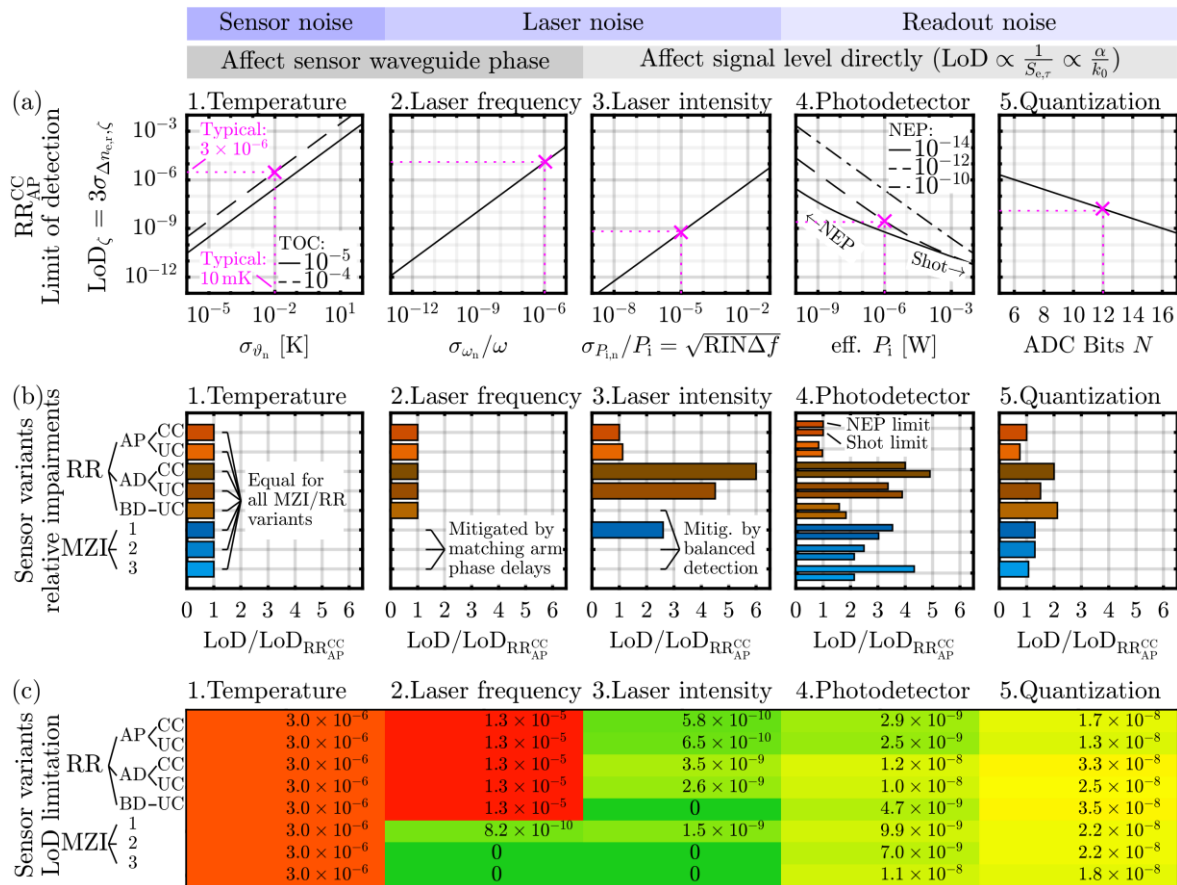

Fig. 4.6. Limit of detection (LoD) for measured effective-refractive-index changes in various RR- and MZI-based sensor implementations.   *[Remaining figure caption on the following page]*

[Continuation of Fig. 4.6 caption] The individual contributions LoD_ζ of the various noise sources ζ_n are calculated using the equations in Table 4.4 and are plotted in Columns 1…5. Assuming for simplicity that the noise sources ζ_n are statistically independent, the overall LoD can be calculated as the square root of the sum of squares of the individual LoD_ζ, see Eq. (4.22) . The LoD_ζ, resulting from noise sources that directly affect the signal level are proportional to α/k_0, which is set to $\alpha/k_0 = 5 \times 10^{-5}$ in this plot. For LoD_ω originating from laser frequency noise, we assume $n_\text{eg} = 4$ to quantify the impact on RR-based sensor implementations. The choice for α/k_0 and n_eg reflect the situation for typical silicon photonic waveguides. For LoD_{I_s} originating from photodetector shot noise, we assume perfect photodiodes with $\Re = q_\text{e}/(\hbar\omega)$, and we assume an acquisition bandwidth of $\Delta f = 100\,\text{Hz}$. **(a)** Individual LoD_ζ contributions of the various noise sources ζ_n plotted for the $\text{RR}_\text{AP}^\text{CC}$ sensor implementation as a reference. Dotted magenta lines indicate typical cases found in integrated sensors. The impact of temperature fluctuations between sensor and reference structures is plotted for two different thermo-optic coefficients (TOC), see Column 1. The impact of photodetector shot noise and noise-equivalent power are plotted as a function of the effective optical input power P_i defined in Eq. (4.2) for three different noise-equivalent power (NEP) levels, see Column (4). Depending on P_i and NEP, the device is either shot-noise-limited or NEP-limited. **(b)** LoD impairments of various sensor implementations with respect to the $\text{RR}_\text{AP}^\text{CC}$ considered as a reference case in Subfigure (a). The LoD impairments of these implementations differ from that of the $\text{RR}_\text{AP}^\text{CC}$ by constant factors, which are indicated by colored bars. A missing bar indicates that the respective sensor implementation is not prone to this specific noise source. Temperature fluctuations have the same impact on all sensor implementations. Laser frequency noise is a problem only for RR-based sensors. For MZI, the impact on the LoD can be mitigated by matching the group delay of the sensor and reference arm, which effectively decouples the effective-index sensitivity from a sensitivity towards frequency noise. Laser intensity noise can be mitigated by sensor implementations using multiple output ports that measure power differences rather than absolute levels. For the photodetector noise sources, we consider the two extreme cases of shot-noise limitation (lower bar) and NEP limitation (upper bar). For quantization noise, the ADC ranges are scaled to capture the full contrast of the respective current. **(c)** LoD bottlenecks of the various sensor implementations compared on a logarithmic color scale for the typical noise parameters marked by dashed magenta lines in Subfigure (a). For these parameters, noise sources affecting the sensor waveguide phase, i.e., sensor temperature variations and, in case of RR-based implementations, laser frequency fluctuations, have the largest impact on the LoD, whereas the impact of intensity, photodetector and quantization noise is manageable.

The individual LoD_ζ are plotted for all noise sources in Fig. 4.6(a), each as a function of typical underlying noise variances and/or other key parameters of the associated noise source. According to Table 4.4, the LoD_ζ of all noise sources which directly affect the signal level, i.e., the laser intensity noise

($\zeta_n = P_{i,n}$), the PD shot noise ($\zeta_n = I_{s,n}$) and NEP ($\zeta_n = I_{NEP,n}$), and the quantization noise ($\zeta_n = I_{q,n}$), are all proportional to α/k_0. For the plots in Fig. 4.6(a), we assume a rather large $\alpha/k_0 = 5 \times 10^{-5}$, which corresponds to a silicon waveguide with 10 dB/cm at $\lambda = 1.55$ µm. As a comparison, a silicon nitride waveguide with 2.3 dB/cm at $\lambda = 0.6$ µm yields $\alpha/k_0 = 5 \times 10^{-6}$ and thus reduces the contributions of these four noise sources by an order of magnitude. We assume an effective group refractive index of $n_{eg} = 4$ for the sensor waveguides, which is a typical number in silicon photonics and which is only relevant for the frequency-noise-related LoD_ω, see third column of Table 4.4. We further assume an acquisition bandwidth of $\Delta f = 100$ Hz, which generally impacts all but the quantization-noise-related LoD_{I_q}. Note that the contribution LoD_g of temperature fluctuations also depends on the acquisition bandwidth, even if we do not account for a quantitative relationship in our model. Furthermore, we assume perfect photodiodes with a quantum efficiency of one, which are only affected by photodetector shot noise. Regarding the effective optical input power P_i, we do not make any assumption in the context of Fig. 4.5(a) but treat it as a variable parameter that can change over many orders of magnitude, see Fig. 4.5(a), Column 4. The effective input power P_i is only relevant for the contributions LoD_{I_s} and $\text{LoD}_{I_{NEP}}$ from photodetector shot noise and NEP noise, while the LoD contributions of all other noise sources are independent of P_i. For the sake of visual clarity, we restrict our analysis of the various LoD_ζ in Fig. 4.6(a) to only one sensor implementation, namely a critically coupled all-pass ring resonator (RR_{AP}^{CC}), which serves as a reference for the subsequent discussion. For all other sensor implementations, the LoD_ζ are either zero or they follow the same trends and lie within the same order of magnitude, such that they can be quantified by a simple multiplier, see discussion of Fig. 4.6(b) below. The five plots in Fig. 4.6(a) allow to quickly estimate the LoD contributions LoD_ζ of the various noise sources and to formulate requirements for individual sensor system components if a certain target LoD has to be achieved. Dotted magenta lines and crosses indicate noise-source parameters and the corresponding LoD_ζ found in typical integrated sensors and serve as reference for a specific case study, see discussion of Fig. 4.6(c) below.

In Fig. 4.6(a), Column 1, the LoD impact of temperature fluctuations between sensor and reference structures is plotted for two different thermo-optic coefficients, $\text{TOC} = 10^{-4}$ K^{-1} [99] and $\text{TOC} = 10^{-5}$ K^{-1} [100], which are typical magnitudes for silicon and silicon nitride waveguides, respectively. Note that the TOC is not just the thermo-optic coefficient of the core material but refers to the effective thermo-optic coefficient of the overall waveguide, i.e., the ratio of an effective-index change and the associated temperature change. The corresponding LoD contribution scales as $\text{LoD}_{\vartheta} \propto \text{TOC} \times \sigma_{\vartheta_n}$. Column 2 and Column 3 of Fig. 4.6(a) show the LoD contribution of the laser frequency and intensity noise, which scale as $\text{LoD}_{\omega} \propto \sigma_{\omega_n}/\omega$ and $\text{LoD}_{P_i} \propto \sigma_{P_{i,n}}/P_i \approx \sqrt{\text{RIN}\Delta f}$, respectively. The combined impact of photodetector shot noise and various levels of photodetector noise-equivalent power (NEP) are plotted in Column 4 of Fig. 4.6(a) as a function of the effective input power P_i. Note that the effective optical input power P_i does not directly correspond to the power of the underlying laser diode, but additionally accounts for all optical excess losses that result from non-idealities of the various sensor components such as coupling losses in chip-chip interfaces or propagation losses in on-chip transport waveguides, see Section 4.3.2 and Eq. (4.2). The device is either shot-noise-limited for large P_i or small NEP with a $\text{LoD}_{I_s} \propto \sqrt{\Delta f/P_i}$, or it is NEP-limited for small P_i or large NEP with a $\text{LoD}_{\text{NEP}} \propto \sqrt{\Delta f}/P_i$. The critical input power P_i that marks the crossover between the shot-noise-limited and NEP-limited regime depends on the NEP level. In most sensor realizations, either one or the other can be neglected. Column (5) of Fig. 4.6(a) shows the LoD contribution of quantization noise as a function of the number of ADC bits N, which scales with $\text{LoD}_{I_q} \propto 2^{-N}$.

LoD comparison of the different sensor implementations In Fig. 4.6(a), we have analyzed the LoD contributions for the $\text{RR}_{\text{AP}}^{\text{CC}}$ reference sensor implementation. Fig. 4.6(b) shows how the various other sensors types perform in relation to this reference. The relative impact of the various noise sources is described by colored bars, where a bar length of 1 corresponds to the LoD of the $\text{RR}_{\text{AP}}^{\text{CC}}$ reference, and where a missing bar indicates that this sensor implementation is not prone to this specific noise source. As an example, the identical bar lengths in Column 1 of Fig. 4.6(b) indicate that the relative temperature differences be-

tween sensor and reference structures have the same impact on all sensor implementations. This is a consequence of the fact that temperature-induced fluctuations of the effective-index difference between sensor and reference structure cannot be separated from the sensor signal itself, irrespective of the underlying sensor implementation. Column 2 of Fig. 4.6(b) compares the impairments with respect to laser frequency noise. Here, we observe a distinct advantage of the MZI-based sensor implementations compared to their RR-based counterparts. In MZI, the group delay of the two arms can be matched such that the optical phase at the output of the arms is always perfectly correlated, since the corresponding signals were emitted by the same light source at the same instant of time. When bringing these signals to interference, any phase or frequency noise of the light source cancels. Note that this phenomenon is independent of the absolute group delay in each arm. It is hence possible to simultaneously maximize the optoelectronic effective-index sensitivity $S_{e,\tau}$ by selecting the optimum sensor arm length $L_{opt} = 1/\alpha$, and mitigating the effects of laser frequency fluctuations by adapting the group delay of the reference arm to that of the measurement arm. For all MZI-based sensors, LoD_{ω} is hence zero, see lower part of Fig. 4.6(b), Column 5. This decoupling of optoelectronic effective-index sensitivity $S_{e,\tau}$ and sensitivity towards frequency noise is not possible in RR, which rely on interference of portions of incoming light with portions of light of previous round-trips, all of which were emitted by the light source at different instants of time and hence feature uncorrelated phases. Tailoring the optoelectronic effective-index sensitivity $S_{e,\tau}$ by appropriate choice of the round-trip length thus unavoidably affects the impact of frequency noise. As consequence, the LoD_{ω} increases in proportion to the optoelectronic effective-index sensitivity $S_{e,\tau}$. This effect is independent of the detection scheme and the Q-factor of the coupled cavity, i.e., all RR-based sensor implementations are equally impaired by laser frequency noise, see upper part of Column 5 of Fig. 4.6(b). Note that, while the sensitivity of a RR-based sensor implementation can always be increased by a higher Q-factor, the LoD is eventually limited by the frequency noise of the laser source. Increasing the resonator Q-factor hence becomes ineffective once LoD_{ω} dominates the overall LoD. The comparison of the sensor implementations with respect to laser RIN is shown in Column 3 of Fig. 4.6(b). It turns out that sensors that use multiple output ports and thus measure power

differences rather than absolute levels can mitigate the impact of RIN if the operating point is chosen correctly. Furthermore, we find that the RR_AP implementations outperform their respective RR_AD counterparts, mainly due to the higher optoelectronic effective-index sensitivity. For the photodetector noise sources shown in Column (4) of Fig. 4.6(b), relative impairments for the two extreme scenarios, i.e., the shot-noise-limited regime as well the NEP-limited regime are shown by a pair of narrower bars for each sensor type. The relative impairments attributed to these two cases of photodetector noise differ slightly for the sensor implementations, e.g., due to the different implementation-dependent sensitivities, the different number of photodetectors, and the different average power levels on each photodetector. Due to its superior sensitivity, the RR_AP again features a comparatively low LoD contribution. The effect of quantization noise on the sensor implementations is shown in Column (5) of Fig. 4.6(b) and is almost identical for all sensor implementations. The slight differences here are caused again by the implementation-dependent sensitivity differences, combined with a scaled ADC range that matches the implementation-specific maximum output current $I_\text{o,max} = P_\text{i} \Re \hat{T}$ of each detector, where $\hat{T}$ is the optical output contrast of each individual output port which can be calculated from Eq. (4.10) and Eq. (4.12), see for example Table B.2 in Appendix B.2 for ring resonators.

Identification of typical LoD limitations In order to identify the noise source that dominates the total LoD, we indicate in Fig. 4.6(c) the magnitude of the individual LoD_ζ for typical noise parameters. These noise parameters and their impact on the various LoD_ζ of the $\text{RR}_\text{AP}^\text{CC}$ are indicated by dashed magenta lines in Fig. 4.6(a). The colors in Fig. 4.6(c) indicate the order of magnitude of the respective LoD contribution.

It can be seen in Column 1 of Fig. 4.6(c) that fluctuations of the temperature difference between sensor and reference structures may have substantial impact on the LoD, both for MZI and RR. The displayed $\text{LoD}_\vartheta \approx 3 \times 10^{-6}$ is obtained for $\sigma_{\vartheta_\text{n}} = 10\ \text{mK}$, which assumes a typical distance between sensor and reference structures of $100\ \mu\text{m}$ along with random temperature gradients with a standard deviation of the order of $1\ \text{K/cm}$ and TOC of the order of $10^{-4}\ \text{K}^{-1}$, roughly corresponding to the TOC of a silicon waveguide [99]. The detrimental

117

effects of temperature differences between on-chip sensor and reference structures can be mitigated by different measures. First, sensor and reference structures should be positioned as close to each other as possible, for example by designing the MZI arms as interleaved spiral waveguides [101], or by using similar techniques for nesting ring resonators with non-circular shapes. Second, the exposure of the sensing and reference structures to potential temperature changes should be matched. For example, a microfluidic channel that might transport a fluid with a different temperature as the PIC itself, and that is flowing over the sensitive waveguide area, should also flow over the reference waveguide area, and the reference waveguide should not be shielded from these temperature effects by isolating claddings. Third, the geometry and/or materials of the sensor and reference waveguides can be adjusted to lower the effective thermo-optic coefficient [102,103].

The effect of laser frequency fluctuations as the second noise source that directly affects the phase shift in the sensor waveguide is shown in Column 2 of Fig. 4.6(c). We find that frequency fluctuations cause a large $\mathrm{LoD}_\omega \approx 10^{-5}$ in RR-based sensor implementations. For our estimation, we assume a typical value of $\sigma_{\omega_n} / \omega \cong 10^{-6}$, which roughly corresponds to a laser operating at 1.55 µm with a long-term standard deviation of the emission frequency of $\sigma_{\omega_n} = 2\pi \times 100\ \mathrm{MHz}$, see Appendix B.6. Note that these rather large fluctuations are usually dominated by the low-frequency part of the laser's frequency noise spectrum and may hence be much larger than its intrinsic linewidth, which is given by the spectrally white component of the frequency noise spectrum, see Section 4.4.3.1 and Appendix B.5 for details. As mentioned above, the impact of laser frequency noise on MZI-based sensor implementations can be mitigated completely by matching the group delays of the two interferometer arms, which allows to decouple the effective index sensitivity from the sensitivity towards frequency fluctuations. For the typical noise levels considered in our analysis, laser frequency fluctuations are the most prominent limitation for the LoD of RR-based sensor implementations, emphasizing the importance of stable laser drive currents and temperature control. It might additionally be necessary to include a frequency stabilization mechanism that can at least compensate for the slow frequency drift. However, implementing such a mechanism into a

highly integrated sensor system requires additional technical effort and might represent a challenge for low-cost solutions.

Columns 4 and 5 of Fig. 4.6(c) indicate that the intensity noise of typical lasers as well as the typical photodetector noise levels only play a minor role for the chosen example of an integrated photonic sensor with $\alpha/k_0 = 5 \times 10^{-5}$. This is mainly due to the fact that the respective LoD scale with the square root of the acquisition bandwidth, and typical acquisition bandwidths are rather small in sensing applications as compared to those used in telecommunication applications. In our example, we use a laser with a rather large RIN of -120 dB/Hz and an acquisition bandwidth of $\Delta f = 100\,\mathrm{Hz}$, which corresponds to $\sigma_{P_{i,n}} / P_i = \sqrt{\mathrm{RIN}\Delta f} \cong 10^{-5}$ and an associated low $\mathrm{LoD}_{P_i} \approx 10^{-9}$. At the same acquisition bandwidth, a typical photodetector with $\mathrm{NEP} = 10^{-12}\,\mathrm{W}/\sqrt{\mathrm{Hz}}$ that receives roughly 1 μW (-30 dBm) of optical power would still allow the system to achieve a low $\sqrt{\mathrm{LoD}_{I_{\mathrm{NEP}}}^2 + \mathrm{LoD}_{I_S}^2} \approx 10^{-8}$. When it comes to the selection of an appropriate ADC, the required analog operating range plays a crucial role. In our calculations, we assume that the ADC have to be capable of covering the whole output contrast range of the sensor to allow for reliably tuning to the desired operating point. If the fabrication tolerances allow setting the operating point reliably by design and if tuning is always possible, the analog operating range of the ADC can be reduced, and the impact of quantization noise on the LoD can be reduced further. In our example shown in Column (5) of Fig. 4.6(c), a 12-bit ADC that covers the whole output current range leads roughly to $\mathrm{LoD}_{I_q} \approx 3 \times 10^{-8}$.

4.5 Experimental validation of the impact of laser frequency noise

In Section 4.4, we identified laser frequency noise as the dominant LoD contribution of typical RR-based sensor implementations using non-ideal light sources. This aspect and the associated quantitative model are verified experimentally in this section. To this end, we use the measurement setup depicted in Fig. 4.7(a). We use an external laser (LAS) at a wavelength of around 1.54 μm to drive an under-coupled add-drop ring resonator sensor ($\mathrm{RR}_{\mathrm{AD}}$), realized as a

silicon photonic integrated circuit (PIC). To investigate the influence of laser frequency noise, we first perform the experiment with a benchtop-type, highly stable tunable light source (TLS). We then compare the results obtained with the TLS to those obtained with a pigtailed VCSEL as an example for a particularly simple light source type that may be used in low-cost integrated sensors. In both cases, the lasers and the PIC are temperature-stabilized to remove the impact of thermal drift. Light is coupled to and from the PIC via optical fibers and an on-chip grating couplers (GC). At the output of the PIC, light is send to an external photodetector (PD). We use an oscilloscope (OSC) to record and digitize the resulting photocurrent and store it for offline analysis of the signal and the noise contributions. Note that an erbium-doped fiber amplifier (EDFA, not shown in Fig. 4.7(a)) was used after the sensor PIC to compensate for the rather high grating coupler losses and to ensure a sufficiently high power level at the input of the high-speed photodiode (Finisar XPDV120R) that was used in this experiment. We verified that the EDFA, which was followed by a bandpass filter with a 2-nm passband to suppress amplified spontaneous emission (ASE) noise, did not have any impact on the investigation towards frequency-noise sensitivity of this sensor.

In our experiments, we first capture the light at the drop port of the add-drop ring resonator and measure the associated photocurrent for different operating point offsets $\Delta\varphi_{OP,RR}$ in the vicinity of a ring resonance at $\varphi_{res} = 2\pi m \ \left(m \in \mathbb{N}\right)$ by adjusting the laser frequency. In the case of the VCSEL, the emission frequency was tuned via the injection current. In each operating point, we record the time-dependent output current and extract the mean photocurrent I_q, blue crosses in Fig. 4.7(b) and (c), as well as its standard deviation σ_{I_q}, red crosses. In our measurements, we use an acquisition bandwidth of $\Delta f = 500$ kHz and an observation time of $T_{obs} \approx 1$ ms. We verified that, for the investigated operating points, the ASE of the EDFA did not impact the photocurrent noise to a relevant degree. We then fit a Lorentzian resonance model of an RR_{AD}, see Table B.3 in Appendix B.3, to the measured mean photocurrents I_q, see solid blue line in Fig. 4.7(b) and (c). In these fits, we use the peak transmission, the Q-factor, and the resonance frequency ω_{res} as fit parameters, while the effective group refractive index n_{eg} is obtained from an inde-

pendent transmission measurement of the resonator. Both the mean photocurrent I_q and its standard deviation σ_{I_q} are normalized to the maximum current measured in resonance, which is given by $\hat{I}_q = P_i\hat{\tau}$, where P_i denotes the effective optical input power and where $\hat{\tau}$ refers to the optoelectronic transmission on resonance.
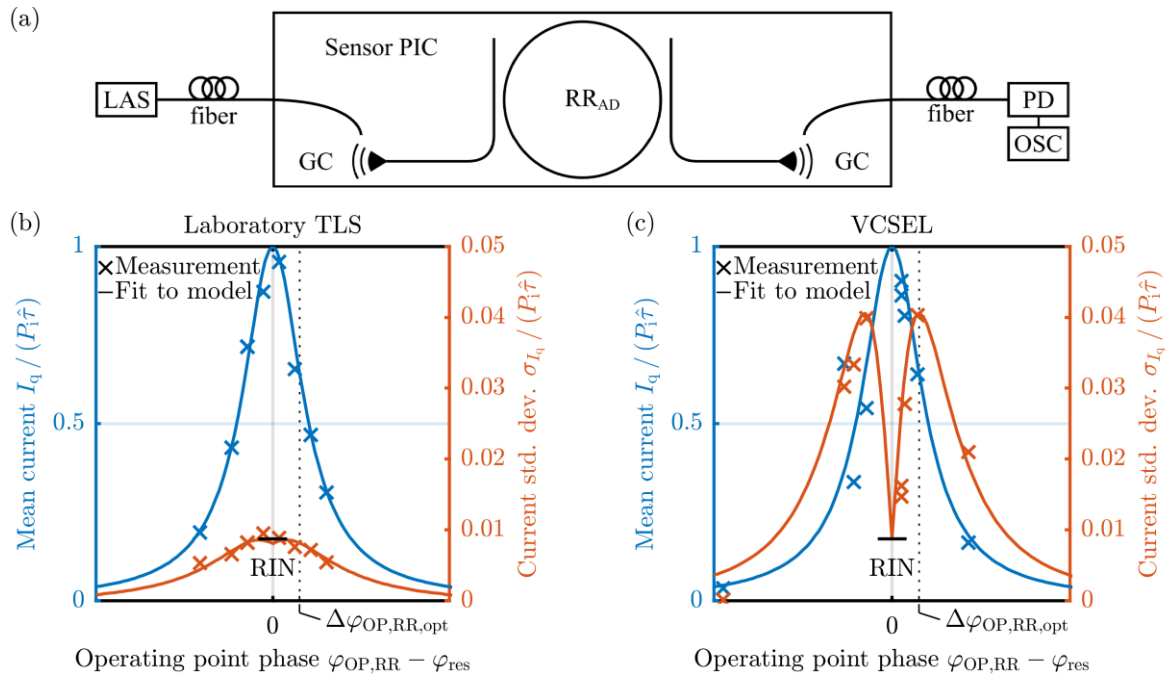

Fig. 4.7. Experimental validation of the model for laser frequency noise and relative intensity noise (RIN). **(a)** Measurement setup consisting of a tunable laser (LAS), a sensor PIC containing an under-coupled add-drop ring resonator (RR_{AD}), an external photodetector (PD), and an oscilloscope (OSC). The optical connections from and to the silicon PIC are realized with optical fibers and grating couplers (GC) designed for 1550 nm. The overall insertion loss of the PIC amounts to 15.5 dB, including fiber-chip coupling losses of 6 dB per GC. An erbium-doped fiber amplifier (EDFA, not shown) is used after the sensor PIC to compensate for these losses and to ensure a sufficiently high power level at the input of the high-speed PD (Finisar XPDV120R) **(b, c)** Normalized mean output current $I_q/(P_i\hat{\tau})$ (left axes, blue) and normalized output-current standard deviation $\sigma_{I_q}/(P_i\hat{\tau})$ (right axes, red) of the RR_{AD}^{UC} drop port, shown at different operating point offsets $\Delta\varphi_{OP,RR}$ in the vicinity of a resonance at $\varphi_{res} = 2\pi m$. The experiment is performed twice – once with a TLS (b) and once with a VCSEL (c), which differ with respect to their frequency stability. The crosses denote measured data points, which were obtained by recording the output currents, whereas the solid blue lines are Lorentzian resonance fits and the solid red lines are fits to the transmission and noise-propagation models derived in Section 4.4. *[Remaining figure caption on the following page]*

121

[Continuation of Fig. 4.7 caption] The optimum operating point $\Delta\varphi_{\mathrm{OP,RR,opt}}$ of highest optoe-lectronic effective-index sensitivity is marked with dotted lines. For operation with a TLS, the output current noise follows the optoelectronic transmission τ. In contrast to this, the output current noise of the VCSEL-operated $\mathrm{RR}_{\mathrm{AD}}^{\mathrm{UC}}$ follows the shape of the optoelectronic effective-index sensitivity $\left|S_{\mathrm{e},\tau}\right|$. This indicates that, in the given measurement setup, the TLS-driven sensor is mainly impaired by relative intensity noise (RIN) of the optical power coupled to the device. Note that, for our experiment, this RIN is not dominated by the laser source, but by temporal fluctuations of the power coupling efficiency at the PIC input, which amounts to approximately 1 % in both experiments. In contrast to this, laser frequency fluctuations are found to be the dominant noise source for the VCSEL-driven sensor. The frequency fluctuations extracted from these experiments amount to 435 MHz for the VCSEL and to 10 MHz for the TLS and are in fair agreement with independent measurements of the frequency noise characteristics, see Appendix B.5.

In a next step, we analyze the operating-point-dependent current deviations, where significant differences between the VCSEL and the TLS-based measurement can be seen. The most prominent difference is that in the case of the VCSEL-based experiment, the current noise is much larger and follows the characteristic shape of the optoelectronic effective-index sensitivity $\left|S_{\mathrm{e},\tau}\right|$, which corresponds to the magnitude of the slope of the frequency-dependent optical transmission, see Fig. 4.3(c). In contrast to that, the current noise measured in the TLS-based experiment rather seems to follow the shape of the optoelectronic transmission τ, see Fig. 4.3(b). Note that in both cases, the current deviation strongly depends on the operating point, and we may hence assume that the photodetector NEP as well as quantization noise can be neglected – both effects would lead to a constant noise background which is independent of the operating point. Moreover, we neglect shot noise, which is irrelevant at the power levels of typically $P_{\mathrm{i}} = 1\,\mu\mathrm{W}$ measured in our experiment, and we exclude sensor thermal noise due to the temperature stabilization of the sensor PIC. The only remaining noise sources are hence intensity noise of the optical signal coupled to the PIC and laser frequency noise. According to Fig. 4.5 and Table 4.4, in the case of an $\mathrm{RR}_{\mathrm{AD}}$, only intensity noise at the sensor input is translated to the output current via the optoelectronic transmission $\tau = \Re T$, while frequency noise is translated to the output current via $\left|S_{\mathrm{e},\tau}\right| = \Re\left|S_{\mathrm{e}}\right|$. The output current deviations can hence be modeled by the square root of the sum of the respective variances,

$$\sigma_{I_q} \approx \sqrt{\left(\tau\sigma_{P_{i,n}}\right)^2 + \left(\frac{n_{eg}P_i}{\omega}\left|S_{e,\tau}\right|\sigma_{\omega_n}\right)^2} ;$$

$$\frac{\sigma_{I_q}}{P_i\hat{\tau}} \approx \frac{1}{\hat{\tau}}\sqrt{\left(\tau\sqrt{\text{RIN}\Delta f}\right)^2 + \left(\frac{n_{eg}}{\omega}\left|S_{e,\tau}\right|\sigma_{\omega_n}\right)^2} .$$

(4.23)

For fitting the measured operating-point-dependent current deviations σ_{I_q} to Eq. (4.23), we re-use the values of the optoelectronic transmission τ and its peak $\hat{\tau}$, the corresponding Q-factor, the optoelectronic effective-index sensitivity $S_{e,\tau}$, the resonance frequency ω_{res}, and the effective group refractive index n_{eg} , which are obtained from the fit of the measured mean photocurrents I_q, as well as from the independent transmission measurement, and only vary the relative-intensity-noise level RIN and the laser frequency deviations σ_{ω} as free parameters. For the TLS experiment, see solid red line in Fig. 4.7(b), we find a rather small TLS frequency fluctuation of $\sigma_{\omega_n} = 2\pi \times 10$ MHz, which is in fair agreement with the directly measured value of $\sigma_{\omega_n} = 2\pi \times 23$ MHz, see Appendix B.5. The output current noise is hence dominated by RIN. Using an acquisition bandwidth of $\Delta f = 500$ kHz, we find a relative intensity noise level of $\text{RIN} = 2 \times 10^{-10}$ Hz^{-1} (- 97 dB Hz^{-1}) for the optical power coupled to the PIC, which equals $\sigma_{P_{i,n}} / P_i = \sqrt{\text{RIN}\Delta f} = 1\%$. This value is clearly higher than the typical RIN levels expected from benchtop-type TLS, and we therefore attribute the optical power fluctuations to the measurement setup, in particular to mechanical vibrations affecting the coupling from the fibers to the PIC. This is confirmed by repeating the coupling experiments with different lasers and by observing that the RIN level of the optical signal at the PIC output does not depend on the laser source. In the VCSEL-based experiment, we fit the same noise model of Eq. (4.23) based on Table 4.4 to the measured current deviations, see solid red line in Fig. 4.7(c). We use the same RIN level of 2×10^{-10} Hz^{-1} (- 97 dB Hz^{-1}) as in the TLS experiment, which leaves only the laser frequency fluctuation σ_{ω} as a free parameter. An optimum fit is obtained for of $\sigma_{\omega_n} = 2\pi \times 435$ MHz, which is again in fair agreement with the directly measured value of $\sigma_{\omega_n} = 2\pi \times 175$ MHz, see Appendix B.5. Note that even though the optimum operating point $\Delta\varphi_{OP,RR,opt}$ exhibits the highest current noise, it does not yield the worst LoD: Since both the current fluctuations caused

by laser frequency noise and the sensitivity increase in proportion to $\left|S_{\mathrm{e},\tau}\right|$, the LoD is independent on the operating point as long as laser frequency noise is the dominant impairment.

4.6 Guidelines for sensor design

Based on the sensitivity and noise analysis detailed in the preceding sections, we formulate guidelines for designing integrated phase-sensitive photonic sensor systems that combine high sensitivity and low limit of detection with manageable technical complexity. All guidelines are summarized in a practical example of a favorable sensor design that relies on readily available optic and electronic components.

4.6.1 Sensitivity

The effective-index sensitivity $S_{\mathrm{e}} = \partial/\partial n_{\mathrm{e}}\left(T\right) = \partial/\partial n_{\mathrm{e}}\left(P_{\mathrm{o}}/P_{\mathrm{i}}\right)$ of all discussed sensor implementations is proportional to k_0/α, see Table 4.3, and can hence be increased by operation at high wavenumbers $k_0 = \omega/c$ and by decreasing the modal power loss coefficient α. In contrast to this, the optoelectronic effective-index sensitivity $S_{\mathrm{e},\tau} = \Re S_{\mathrm{e}}$ can generally not be increased by using shorter larger wavenumbers $k_0 = \omega/c$ since, for a given quantum efficiency of the photodetector, the electric readout responsivity $\Re$ is inversely proportional to the photon energy and hence to the vacuum wavenumber, see Section 4.4.2.5. Still, for sensing of analytes in aqueous solutions, short wavelengths in the visible range offer the advantage that absorption loss occurring in the evanescent portion of the guided field is less of a problem than for near-infrared (NIR) wavelengths. When it comes to blood analysis, photonic sensors largely rely on the so-called therapeutic window between 600 nm and 1100 nm, which offers a good compromise between pronounced hemoglobin absorption at shorter wavelengths and strong water absorption at longer wavelengths [104]. Once the wavelength is fixed, the appropriate implementation of the sensor concept should be chosen. Amongst the various sensor implementations discussed in this paper, simple all-pass ring resonators with a single bus waveguide in a slightly under-coupled operation $(\mathrm{RR}_{\mathrm{AP}}^{\mathrm{UC}})$ exhibit the highest sensitivity, see

Fig. 4.4, but may be prone to laser frequency noise, see also subsequent paragraph. In contrast to this, rather simple Mach-Zehnder interferometers provide comparable sensitivity if their arm length is adapted to the modal loss, i.e., $L = 1/\alpha$, see Fig. 4.4 and do not suffer from laser frequency noise. This comes at the cost of an increased footprint, which can be reduced by using interleaved spirals in the interferometer arms, thereby also minimizing temperature differences between the sensor and the reference arms. Note that, in practical implementations of sensor systems, the package size and cost are usually not dominated by the sensor waveguide structures themselves but rather by peripheral components such as electronic readout circuits and by the assembly processes. The footprint of MZI-based sensor structures should hence not play an important role unless massively parallel sensor arrays are required.

4.6.2 Limit of detection

The limit of detection offered by integrated sensor systems that are built from standard components and that are subject to typical environmental conditions is dominated by the two noise sources that directly induce a phase shift in the sensor waveguide: On-chip temperature fluctuations and laser frequency noise. Stochastic on-chip temperature differences between sensor and reference waveguides lead to impairments in ring resonators and Mach-Zehnder interferometers alike. These impairments can be reduced by proper waveguide design and routing, sensor layout, and temperature control. Laser frequency noise is mainly a problem for ring resonators and can be mitigated completely in Mach-Zehnder interferometers by design. In fact, for RR-based sensor implementations operated by a light source with a given linewidth, there is an upper limit of the Q-factor, beyond which the LoD will not improve further with higher Q. MZI hence allow to build high-sensitivity sensors with low-cost light sources and without complex frequency stabilization schemes. Compared to on-chip temperature fluctuations and laser frequency noise, the impact of noise sources that directly affect the signal level at the sensor output is usually less problematic, see Fig. 4.6(a). This applies, e.g., to laser relative intensity noise, to photodetector shot noise and to additional photodetector noise quantified by the NEP, as well as to quantization noise. Note that the LoD contribution of these four noise sources is automatically reduced by the optoelectronic effective-index

sensitivity, see Section 4.4.3.2. The LoD contribution of the photodetector shot noise, the additional photodetector noise quantified by the NEP, and the quantization noise sources are reduced by increasing the effective input power P_i.

4.6.3 Readout

We find that balanced detection schemes allow to eliminate the impact of RIN on the LoD, see Fig. 4.6(b), and to simplify the feedback control that stabilizes the operating point, both for MZI and RR-based sensor implementations. For MZI, balanced detection additionally allows to exploit the full optical power that is available at the device output and therefore doubles the sensitivity compared to single-output implementation, see Fig. 4.4(d). In contrast to that, balanced detection in RR-based sensor implementations necessarily requires a second output port, which reduces the Q-factor of the ring. This has a detrimental effect on the sensitivity, which is only partially compensated for by the fact that the full output power is used, see Fig. 4.4(d). Regarding MZI, using a triple-output configuration does not increase the sensitivity compared to its dual-output counterpart, Fig. 4.4(d). However, in combination with a detection scheme based on a Clarke transformation, triple-output MZI allow to directly extract the phase difference of the two interferometer arms independently of the operating point and thereby eliminate the need for operating-point stabilization, thus vastly reducing the system complexity. Regarding the LoD contribution of the photodetectors, the triple-output MZI provides the same performance as its double-output counterpart provided that all detectors are operated at the shot-noise limit, Fig. 4.6(b). For NEP-limited operation, the photodetector-related LoD contribution of the triple-output MZI is increased by a factor of $\sqrt{3}$ relative to the double-output scheme due to the noise in the additional detector. Note that using an optical hybrid with four detectors at the MZI output does not bring any additional benefit but further increases the complexity of the sensor PIC. Specifically, a quadruple-output MZI provides the same overall performance as a triple-output device in case of shot-noise limited operation and increases the photodetector-related LoD contribution by an additional factor of $\sqrt{4/3}$ for NEP-limited operation. We hence identify a triple-output MZI as an ideal trade-off between the complexity of the optical chip, the complexity of the electronic control and readout circuits, and the LoD performance.

4.6.4 Favorable sensor implementation

With these findings, we now propose a favorable sensor design that combines a triple-output MZI with readily available optical and electronic components. The system is illustrated in Fig. 4.8(a). We consider a laser operating in the visible regime at 600 nm (green box) and an effective input power P_i including all coupling losses of 10 μW, which can be easily achieved with low-cost VCSEL and state-of-the-art optical coupling approaches. The laser has a RIN of -120 dB/Hz and a frequency noise standard deviation of $\sigma_{\omega_n} = 2\pi \times 20 \text{ MHz}$. The waveguides are based on silicon nitride and exhibit a low propagation loss of 3 dB/cm along with a TOC of approximately 10^{-5} K^{-1}. The MZI arms are length-optimized, $L = 1/\alpha \approx 15 \text{ mm}$, and matched with respect to the optical group delay such that the frequency noise of the laser does not play a role. The waveguides are routed as two interleaving spirals, marked in blue/yellow in Fig. 4.8, which ensures small temperature differences between the arms. For a waveguide spacing of 5 μm and an on-chip temperature gradient of 1 K/cm, we estimate typical values of $\sigma_{\vartheta_n} = 0.5 \text{ mK}$ for the mean temperature differences between the reference and the measurement arm. The sensor PIC footprint fits into an on-chip area of 400×400 μm². The three photodetectors, illustrated as red boxes, have a responsivity of 0.4 A/W and a NEP of $10^{-10} \text{ W}/\sqrt{\text{Hz}}$. The corresponding output currents are digitized with 10-bit ADC at an acquisition bandwidth of 100 Hz, and the phase shifts can be extracted by a Clarke transformation, see Table 4.2, which is performed in an ASIC shown below the PIC. With these assumptions, which are summarized on the right-hand side of Fig. 4.8(b), the sensor can achieve a limit of detection of LoD = 10^{-6} for the effective-index fluctuations. This LoD is dictated by the NEP of the photodetectors, which leaves room for further improvement. We also provide a MATLAB application [105] that allows to estimate the performance for other sensor concepts and device specifications.

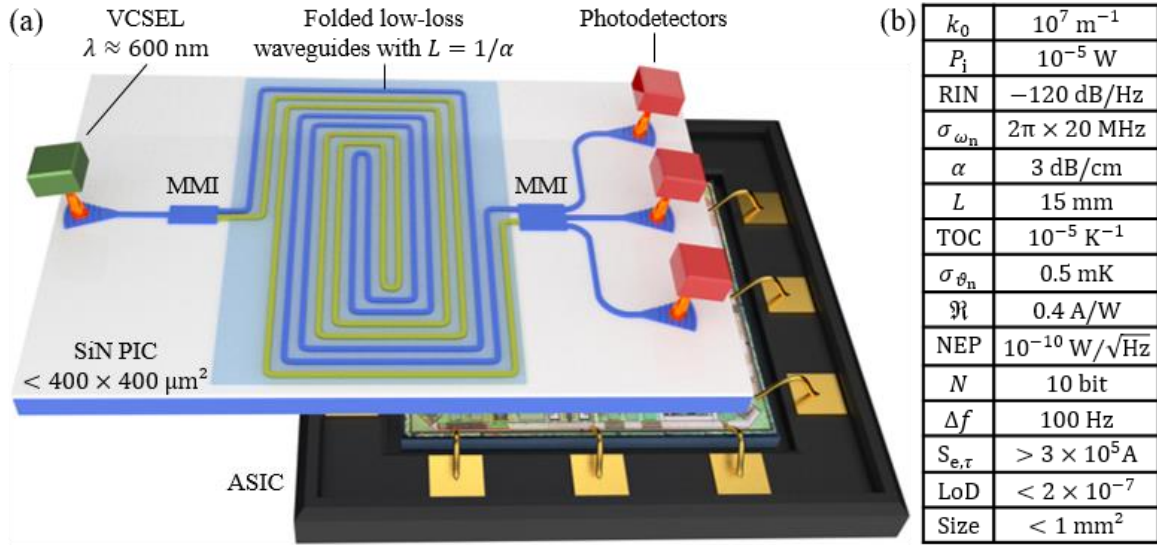| (b)	
k_0	$10^7 \, \text{m}^{-1}$
P_i	$10^{-5} \, \text{W}$
RIN	$-120 \, \text{dB/Hz}$
σ_{ω_n}	$2\pi \times 20 \, \text{MHz}$
α	$3 \, \text{dB/cm}$
L	$15 \, \text{mm}$
TOC	$10^{-5} \, \text{K}^{-1}$
σ_{ϑ_n}	$0.5 \, \text{mK}$
$\Re$	$0.4 \, \text{A/W}$
NEP	$10^{-10} \, \text{W}/\sqrt{\text{Hz}}$
N	$10 \, \text{bit}$
Δf	$100 \, \text{Hz}$
$S_{e,\tau}$	$> 3 \times 10^5 \, \text{A}$
LoD	$< 2 \times 10^{-7}$
Size	$< 1 \, \text{mm}^2$

Fig. 4.8 Analysis of a favorable implementation of a highly integrated photonic sensor, based on readily available optical and electronic components. (a) Graphical illustration of the sensor concept, relying on a SiN-based triple-output MZI (MZI$_3$) with optimally balanced arms that are folded into each other, fed by a power-efficient low-cost VCSEL at a wavelength of 600 nm. The scheme is insensitive to laser frequency and intensity noise and minimizes the impact of temperature fluctuations, does not require any operating-point stabilization or tuning and thus lends itself to highly scalable, technically robust sensor systems. (b) Specifications of the various sensor components used for the performance estimation. Other sensor concepts and device specifications can be analyzed by a MATLAB application that is based on the model described in this paper and that can be accessed in [105].

4.7 Further design aspects: Waveguide design, assembly, and analyte handling

Besides the system-level design aspects explained in the previous sections, successful implementation of an integrated photonic sensor device requires consideration of additional aspects. This includes, e.g., the design of the underlying waveguides for maximum sensitivity S_{env} with respect to environmental parameters, photonic system assembly concepts that allow to efficiently complement the sensor PIC with light sources and detectors, and schemes for handling of liquid or gaseous analytes relying, e.g., based on co-integration of micro-fluidic systems. In the following sections, we provide a brief overview of these aspects that have been intensely discussed in the in the literature over the previous years.

4.7.1 Waveguide design and surface functionalization

Optimization of integrated waveguides with respect to the waveguide sensitivity S_{env}, see Eq. (4.3) , is an important subject in its own right. In general, the waveguide sensitivity S_{env} can be maximized by proper choice of waveguide type, material, and geometry, thereby enhancing the interaction of the guided optical mode with the medium that is subject to the change Δ_{env} of the environmental parameter of interest. In most cases, this parameter is either the refractive index of a homogeneous medium that surrounds the waveguide core or the thickness, possibly in combination with the refractive index, of a thin layer of analyte molecules that specifically bind to a functionalized surface of the waveguide core. Such surface sensing applications allow for highly multiplexed detection of analytes in massively parallel sensor arrays [65,66], but crucially rely on robust processes that permit to selectively functionalize individual sensor elements without any degradation of or cross-reaction with differently functionalized sensor areas [106-110].

Waveguides with high sensitivity S_{env} can be realized on different material platforms such as silicon-on-insulator [50–53] or silicon nitride [54–57], where both quasi-TE or quasi-TM waveguide modes are exploited, possibly along with slot-waveguide concepts [48] or sub-wavelength grating (SWG) structures [111,112], see Refs. [25,30,75] for an overview. A particularly comprehensive overview of sensor waveguide designs covering different waveguide types, polarizations and wavelengths can be found in the reviews [25,30]. A detailed discussion of the benefits of slot and sub-wavelength grating waveguides compared to strip waveguides can be found in [75]. Reference [75] provides detailed geometrical design guidelines along with a comparative study of a variety of silicon-on-insulator and silicon-nitride waveguide types that are specifically geared towards detection of target molecules bound to a functionalized waveguide surface.

4.7.2 Photonic system assembly and light-source integration

Photonic sensor systems crucially rely on techniques that allow to efficiently combine sensor PIC, typically made from of indirect-bandgap silicon-on-insulator or silicon-nitride waveguides, with light sources based on direct-bandgap III-V compound semiconductors. Importantly, these techniques should offer a path towards compact and reliable assemblies that are amenable to industrial mass production. One option is to use monolithically co-integrated laser sources, realized, e.g., through heterogeneous integration of III-V epitaxial layers that are transferred to pre-structured silicon-based PIC [12–15,113–115] and that are then collectively processed on a wafer level. While this approach stands out due to good scalability, it requires highly developed front-end fabrication processes, and is thus mainly suited for high-volume applications. Alternatively, readily processed VCSEL or DFB lasers may be transferred to passive PIC by micro transfer printing [116] or by conventional flip-chip bonding [117]. These concepts offer higher flexibility with respect to the underlying light sources and sensor PIC, but often rely on high-precision assembly techniques with limited throughput. When it comes to efficient co-integration on a package level, 3D-printed micro-lenses [118] or so-called photonic wire bonds [119,120] may open a path towards fully automated assembly of compact multi-chip systems with outstanding flexibility and performance. Similarly, options for efficiently implementing photodetectors on sensor PIC range from monolithic integration of germanium detectors on silicon photonic waveguides [21] to heterogeneous integration of III-V layers [15] and to transfer-printed III-V photodetectors [121]. The decision of the optimal light-source integration and system assembly concept heavily depends on the desired applications and in particular on the expected production volumes.

4.7.3 Analyte handling and microfluidics

Besides the opto-electronic system concept and the associated technological implementation, the delivery of the gaseous or liquid analytes to the sensing area is a key aspect in case of chemical sensors. In many cases, this calls for efficient

co-integration with advanced micro-fluidic systems [122–124]. A comprehensive review of optofluidic integration can be found in [67], which discusses several microfluidic systems that are co-integrated with PIC-based sensors and that rely on the two primarily used materials, namely polydimethylsiloxane (PDMS) and on the negative-tone photoresist SU-8. In general, the PIC can be co-integrated with standalone pre-processed microfluidic chips [125], or the microfluidic structures can be processed on a wafer scale directly on the PIC [126]. In addition, digital microfluidics [127], a platform for manipulation of microdroplets based on the electrowetting effect, can be co-integrated with PIC [128–131]. Digital microfluidic systems allow for a precise spatial and temporal control over microdroplets, offering transporting, mixing and splitting functions for lab-on-chip applications.

4.8   Summary: Photonic sensor systems

We have developed a holistic model for integrated phase-sensitive photonic sensors that allows to consistently analyze and to broadly benchmark the performance of different sensor concepts and technical implementations. Our model covers the entire signal chain from the light source through the sensor PIC and the photodetectors to the analog-to-digital converters (ADC) while accounting for the non-idealities of each component. We perform an in-depth performance analysis of different sensor systems with respect to their sensitivity and their limit of detection (LoD), considering in particular the limitations of highly integrated, mass-deployable sensor systems that rely on non-ideal components and that are operated outside a controlled laboratory environment. We examine the potential and the limitations of different sensor implementations based on ring resonators and Mach-Zehnder interferometers, and we extract globally optimized design parameters and optimum operating points for each implementation. We find that resonator-based sensors are particularly prone to laser frequency noise and validate the underlying theoretical model by experimentally investigating impact of frequency noise on a ring-resonator-based sensor. Based on our analysis, we formulate design guidelines and estimate the achievable performance for different sensor implementations. The key insights are merged into a specific proposal for a particularly attractive sensor design that relies on

a triple-output Mach-Zehnder interferometer in combination with readily available low-cost light sources and photodetectors. We further provide a MATLAB-based tool that incorporates the full model developed here that can be readily used to estimate the achievable performance of a specific sensor system based on ring resonators or Mach-Zehnder interferometers.

Funding

Acknowledgements

Johannes Milvich received the B.Sc. and the M.Sc. degrees in Electrical Engineering in 2011 and 2014 from University of Stuttgart. Between 2014 and 2017 he pursued his Ph.D in Electrical Engineering in a collaboration between the Corporate Research department of Robert Bosch GmbH and the Institute of Photonics and Quantum Electronics (IPQ) at Karlsruhe Institute of Technology (KIT). Since 2017, he is with the Automotive Electronics division of Robert Bosch GmbH. His research interests include integrated photonics and semiconductor image sensors.

Daria Kohler received her Dipl.-Phys. (M.Sc.) degree in physics from the Karlsruhe Institute of Technology (KIT), Germany, in 2013. Between 2014 and 2020, she worked as a PhD candidate at the Institute of Photonics and Quantum Electronics (IPQ). Since 2020, she has been employed as a research associate and technical project manager at Carl Zeiss Semiconductor Manufacturing Technology (SMT) GmbH, Germany. Her research interests are integrated photonics and biosensors as well as extreme-ultraviolet optics and lithography.

Wolfgang Freude received the Dipl.Ing. (M.S.E.E.) and the Dr.Ing. (Ph.D.E.E.) degrees in Electrical Engineering in 1969 and 1975 from the University of Karlsruhe. He is Professor at the Institute of Photonics and Quantum Electronics and a Distinguished Senior Fellow, both at Karlsruhe Institute of Technology (KIT). His research activities are in the area of optical and wireless high-data rate transmission, and in the field of highdensity integrated-optics with a focus on silicon photonics. He has authored and co-authored more than 320 publications as well as a book and seven book chapters. Wolfgang Freude is an Honorary Doctor of the Kharkov National University of Radioelectronics, Ukraine. He serves as a programme chair for the OSA Advanced Photonics Congress committee "Photonic Networks and Devices", and as an editorial board member for the Springer Nature journal "Light: Science & Applications".

Christian Koos is a full professor at Karlsruhe Institute of Technology (KIT), Institute of Photonics and Quantum Electronics (IPQ) since 2010. He received the Dipl.-Ing. (M.Sc.) and Dr.-Ing. (Ph.D.) degrees in electrical engineering from the University of Karlsruhe in 2002 and 2007, respectively. From 2007 to 2008, he worked as a postdoctoral researcher at the Institute of Photonics and Quantum Electronics (IPQ). From 2008 to 2010, he was with the Corporate Research and Technology Department, Carl Zeiss AG, Germany, where he led the technology forecast in area of nanotechnology and optical metrology. His research activities comprise photonic integration, nonlinear optics, optical communications and signal processing, as well as optical metrology and sensing.

[end of publication [J2]]

5 Towards robust sensor systems: The fault-tolerant 1×3 Mach-Zehnder interferometer

Chapters 3 and 4 describe the process of finding suitable waveguide and sensor system designs based on the most viable options of state-of-the-art photonic technology. In the sensitivity and noise analysis in Chapter 4, Mach-Zehnder interferometers were identified as versatile and robust sensor variants, especially when used in mass-deployable integrated photonic sensor systems using readily available sensor components and fabrication technologies. This chapter explores in detail the specific sensor implementation of a 1×3 Mach-Zehnder interferometer with a single optical input and three optical output ports, see [132,133]. The analysis provides a detailed model of the complete sensor and focuses on adequate signal generation and processing strategies, which aim at overcoming drawbacks of simple single-output MZI sensors and hence at delivering the most accurate and reliable sensor signal based on imperfect systems.
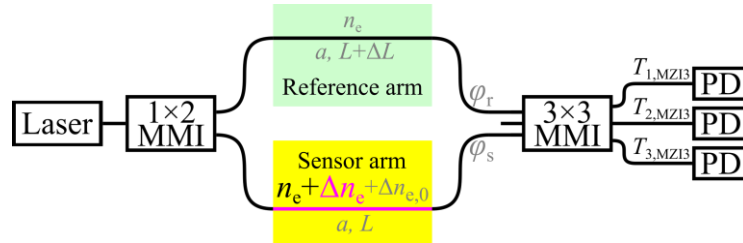

Fig. 5.1. Schematic of the 1×3 MZI integrated photonic sensor. A laser launches an optical signal into a single-mode waveguide. A 1×2 multimode interference (MMI) coupler splits the signal into a reference and a sensor arm. All waveguide sections within a sensitive region (yellow) are subject to an effective-refractive-index change Δn_e as a consequence of an environmental change Δ_{env}. This causes different phase shifts φ_r and φ_s at the end of the arms, where the two signals are combined by a 3×3 MMI coupler where two input and three output ports are connected. The index change Δn_e is hence translated into a measurable change of the three optical output powers, which is recorded by three photodiodes (PD). In general, the frequency-dependent optical power transmission factors $T_{v,MZI3}$ ($v \in \{1,2,3\}$) depend on the arm lengths L and $L+\Delta L$, on the amplitude transmission factors a (here identical), and on the effective refractive indices $n_e + \Delta n_e + \Delta n_{e,0}$ of the sensor and n_e of the reference arm.

5.1 Drawbacks of a single-output Mach-Zehnder interferometer sensor

Although Mach-Zehnder interferometers with a single output port are widely used to measure phase differences in integrated photonic sensors, they exhibit several severe drawbacks, which are illustrated in Fig. 5.2 and described in detail in this section.

Fringe-order ambiguity   Due to the periodic nature of the optical transmission function T with respect to the absolute MZI phase difference $\varphi_{\text{MZI}} = \varphi_{\text{r}} - \varphi_{\text{s}}$, different fringe orders cannot be distinguished by simply measuring the transmission at any given time. As a consequence, the phase difference cannot be determined on an absolute scale, but only within an unambiguity period of 2π. In addition, proper tracing of changes of the phase difference is only possible if it is assured that the phase difference cannot change by more than π between any subsequent measurements, see Fig. 5.3.
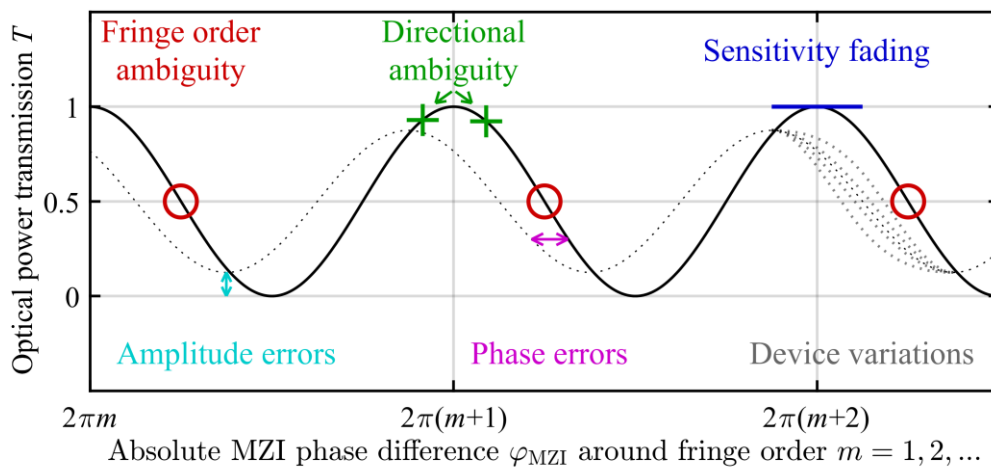
Fig. 5.2. Drawbacks of a conventional single-output MZI₁. The optical transmission varies sinusoidally with respect to the phase difference $\varphi_{\text{MZI}} = \varphi_{\text{r}} - \varphi_{\text{s}}$ between the two MZI arms. The signal is hence ambiguous for different fringe orders at integer multiples m of 2π, as well as directionally ambiguous within a single 2π-period. The sensitivity towards phase changes is furthermore fading at multiples of π. The actual amplitude and phase transmission properties can have static errors, e.g., due to fabrication inaccuracies, and dynamic errors, e.g., due to temperature-dependent properties. Furthermore, tolerances in the fabrication process can cause device-to-device variations, requiring additional calibration.

Fig. 5.3. Fringe-order ambiguity between subsequent sampling times. The phase difference φ_{MZI} is measured with the sampling frequency f_{s}. If the time difference $t_{\mathrm{s}} = 1/f_{\mathrm{s}}$ between two measurement samples (hatched areas) is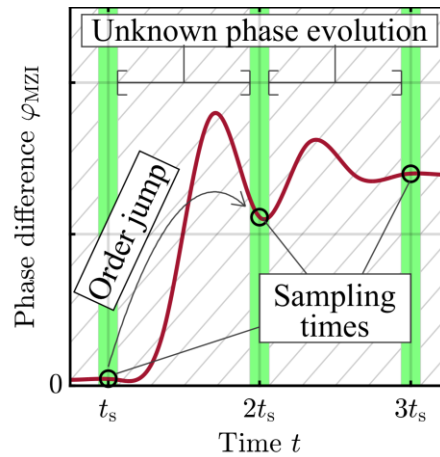 large compared to the rate of the phase difference evolution within the experiment, jumps in the fringe order cannot be tracked, and a proper phase unwrapping is impossible. This is especially relevant if one wants to compare independent measurements taken at different times, e.g., after turning the sensor off and on again, or if the change within a single measurement occurs at a rate that exceeds the bandwidth of the acquisition electronics.

This is especially relevant if one wants to compare independent measurements taken at different times, e.g., after turning the sensor off and on again, or if the change within a single experiment happens at a rate that exceeds the bandwidth of the measurement setup.

Directional ambiguity For single-output MZI, the optical transmission is even ambiguous within a single fringe order, reducing the unambiguity range to π. For example, when starting a measurement without a phase difference between the MZI arms, the constructive interference will lead to a peak optical output power. Changes of the optical transmission from that starting point do not indicate the direction of the underlying phase change.

Sensitivity fading For phase differences that are multiples of π, i.e., at the extrema of the optical transmission, changes in the phase differences do not lead to a measureable change in the optical transmission to a first-order approximation. The sensitivity is hence a function of the operating point. As a consequence, additional signal processing or an active operating point regulation is required to maintain a constant sensitivity.
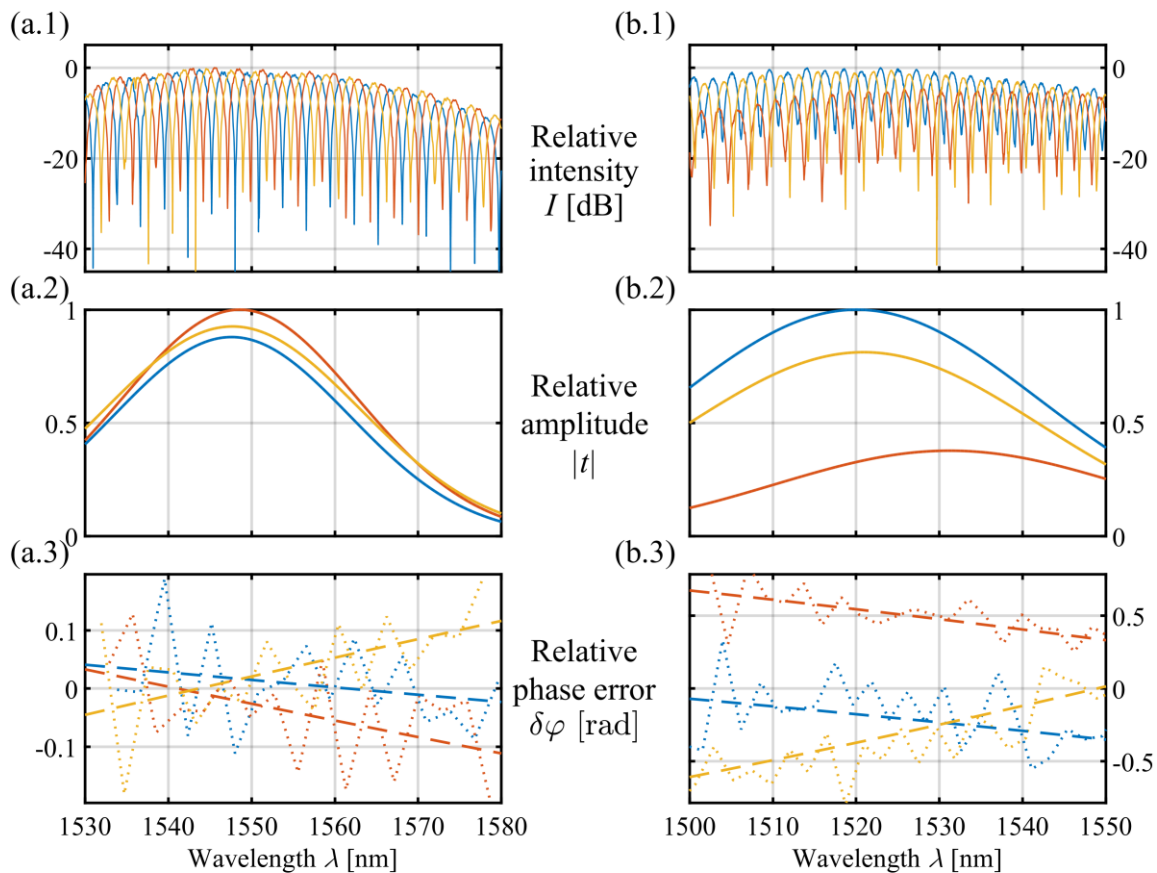
Fig. 5.4. Measured amplitude and phase errors of the outputs of 1×3 MZI. (a) MZI$_3$ containing a 3×3 MMI with relatively low amplitude and phase errors. (b) MZI$_3$ containing a 3×3 MMI with high amplitude and phase errors. (1) The envelope of the transmission spectra of the three output ports of Device (a) peak at the design wavelength of 1550 nm, whereas the envelopes of the spectra of Device (b) show different peaks (2) Uniform power splitting can be observed around the design wavelength for Device (a), while the ouput ports of Device (b) exhibit vastly different transmission levels. (3) Device (a) shows phase errors of several mrad compared to the ideal phase shifts around the design wavelength, while Device (b) exhibits massive distortions.

Amplitude and phase errors and device variations Due to imperfect fabrication or environmental effects such as thermal drift, the MZI response can exhibit static or dynamic amplitude or phase errors. In addition, different sensors, even if fabricated on the same chip, can vary from device to device, which makes a direct comparison of measurements even more complicated. As an example, Fig. 5.4 shows the measured characterization of two 1×3 MZI terminated by 3×3 MMI couplers. The top row shows intensity spectra over a range

of 50 nm for two clearly imperfect MZI. The relative amplitudes as well as phase errors shown in the second and third row can be significant, especially far away from the design wavelength. As a consequence, sophisticated calibration processes have to be established to extract reliable information from the measured signals.

Note that the use of a dual-output $\mathrm{MZI_2}$ employing a 2×2 MMI coupler increases the sensitivity as shown in Chapter 4, but does not solve the fundamental drawbacks of a single-output MZI.

5.2 Enhanced triple-output Mach-Zehnder interferometer sensor model

The following sections analyzes in detail a 1×3 MZI sensor designed and operated with strategies that combat all drawbacks depicted in Section 5.1. This is mainly achieved by using the information contained in the three output signals to construct a complex artificial signal $\underline{S}$, which contains the full phase information. This allows for an exact reconstruction of the measurement signal φ_{MZI}, which is independent of the actual operating point. To this end, the complex signal $\underline{S}$ has to be constructed in a way so that the measurement data is retrieved in the shape of Euler's formula as

$$\underline{S} = S_{\mathrm{I}} + \mathrm{j}\, S_{\mathrm{Q}} \propto \cos\left(\varphi_{\mathrm{MZI}}\right) + \mathrm{j}\sin\left(\varphi_{\mathrm{MZI}}\right) \propto \mathrm{e}^{\mathrm{j}\varphi_{\mathrm{MZI}}}. \tag{5.1}$$

Obtaining this phase information is not possible with single-output or dual-output MMI couplers, as the respective output powers are proportional to $1 + \cos\left(\varphi_{\mathrm{MZI}}\right)$ and $\pm\sin\left(\varphi_{\mathrm{MZI}}\right)$. On the other hand, four or more output ports are also widely used [134] to obtain the phase information as shown in Eq. (5.1) . However, no additional information as in the case of the triple-output MZI is obtained, making the 1×3 MZI sensor concept the simplest and smallest device that allows for a full phase reconstruction.

This Section is structured as follows: A key component for this 1×3 MZI sensor concept is a 3×3 multimode interference (MMI) coupler with three input and output ports, which is placed at the output of the MZI sensor and reference arms,

see Section 5.2.1. Section 5.2.2 describes the complete mathematical model of the 1×3 MZI sensor concept in matrix notation. Based on such a device, the three optical output ports are read out by photodiodes, digitized, and processed further via a Clarke transformation, see Section 5.2.3. With this readout concept, the phase difference measurement is enhanced substantially, and drawbacks of directional ambiguity as well as sensitivity fading are eliminated. In Section 5.2.4, it is shown that the output of this sensor can be used to calibrate the response and hence eliminate the impact of amplitude errors, phase errors, as well as device-to-device variations.

5.2.1   Model of a 3×3 multi-mode interference coupler

The key to obtaining the full phase-difference information between the sensor and reference arm of the MZI is the use of a 3×3 MMI coupler, see Fig. 5.5(a).

The single-mode waveguides of the two interferometer arms are connected to the top (In1) and the bottom (In3) input port of the 3×3 MMI coupler, where they expand into a multi-mode region. Details on MMI coupler design can be found in [135,136]. For a 3×3 MMI coupler, the centers of the three input and output ports are located at $\left[-W_{\mathrm{MMI},3\times3}/3, 0, W_{\mathrm{MMI},3\times3}/3 \right]$ for a total width $W_{\mathrm{MMI},3\times3}$, although they can be positioned a little further out to account for an effective width [135]. The single-mode waveguides can be tapered towards the MMI coupler to improve operation, see Fig. 5.5(b). The width $W_{\mathrm{MMI},3\times3}$ is chosen as small as possible to minimize device footprint, but large enough to accommodate enough guided modes in the multi-mode region, and large enough to account for the minimum feature sizes of the fabrication technology, especially at the regions between the waveguide ports. Based on the selected width, the length of the multi-mode region is chosen so that the three output ports lie on the self-imaging plane, i.e., $L_{\mathrm{MMI},3\times3} = 3L_\pi / N_{\mathrm{out}} = L_\pi$. To obtain $L_\pi = \pi/(\beta_0 - \beta_1)$, the propagation constants β_0, β_1 of the two lowest-order quasi-TE or quasi-TM modes in the multi-mode region have to be calculated, e.g., via a numerical simulation. Note that the wider the MMI coupler, the longer L_π – for a compact device footprint, finding the smallest $W_{\mathrm{MMI},3\times3}$ is essential.
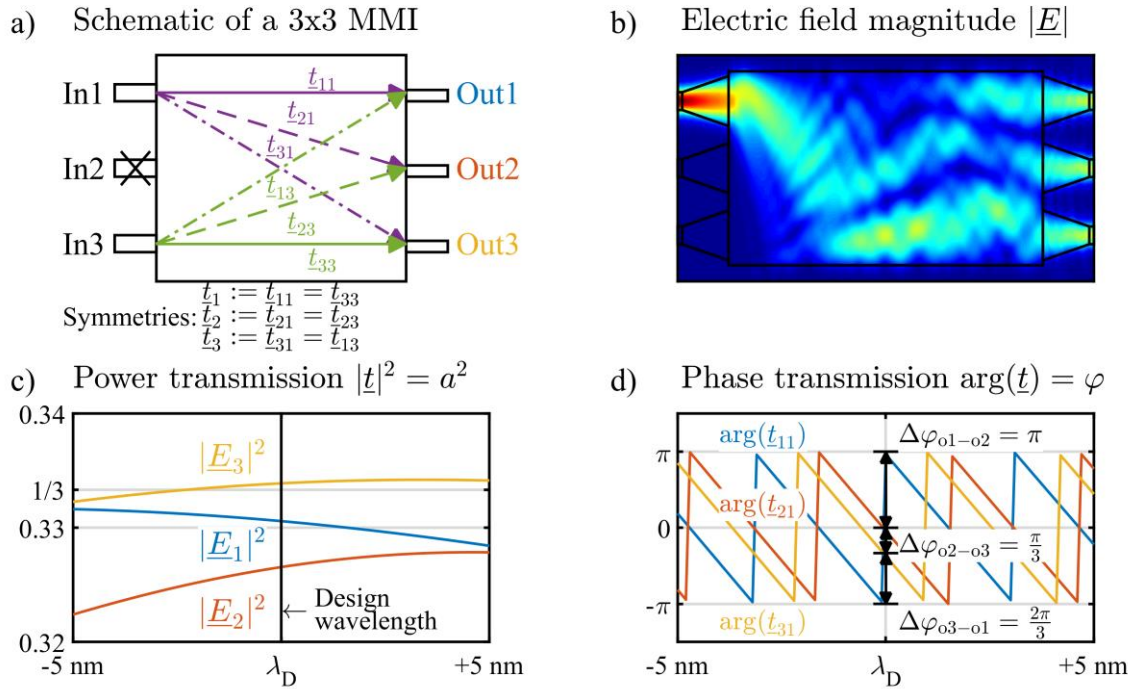
a) Schematic of a 3x3 MMI

b) Electric field magnitude $|\underline{E}|$

c) Power transmission $|\underline{t}|^2 = a^2$

d) Phase transmission $\arg(\underline{t}) = \varphi$

Fig. 5.5. Properties of a 3×3 Multi-Mode Interferometer. **(a)** Schematic of the 6-port device with complex transmission coefficients $\underline{t}_{mn}$ leading from the input n to the output m. The central input port is not connected in the two-arm MZI. In symmetric devices, the t-parameters for the straight, center and cross transmission can be grouped as $\underline{t}_1$, $\underline{t}_2$ and $\underline{t}_3$. **(b)** Simulation of the electric field magnitude in the MMI when an electric field is launched into a single input port shows the multi-mode self-interference pattern that leads to an equal power transmission into each output port. **(c)** The magnitude of the simulated t-parameters slightly differs from the ideal case of $1/\sqrt{3}$ around the design wavelength λ_D. **(d)** The phase transmission simulation shows the phases of the electric field at the three output channels. Around the design wavelength, the relative phase differences between the channels come close to the ideal values of $\Delta\varphi_{o1\text{-}o2} = \pi$, $\Delta\varphi_{o2\text{-}o3} = \pi/3$ and $\Delta\varphi_{o3\text{-}o1} = 2\pi/3$.

After the multi-mode region at L_π, the three output ports channel the electromagnetic waves back into three single-mode waveguides, which are subsequently routed to photodiodes and digitized in ADC for further signal processing.

The transmission from an input port n to an output port m can be described by complex t-parameters $\underline{t}_{mn} = a_{mn}e^{j\varphi_{mn}}$ with electric field amplitude coefficients a_{mn} as well as a phase coefficients φ_{mn}. In symmetric devices, the t-parameters for the straight, center and cross transmission can be clustered as $\underline{t}_1$, $\underline{t}_2$ and $\underline{t}_3$. For visualization, Fig. 5.5(b) shows the self-interference pattern in the multi-

mode region when only one input is active, which leads to an equal power splitting in the three output ports if the MMI is designed correctly. As a result, Fig. 5.5(c) and Fig. 5.5(d) show simulation results of the amplitude and phase transmission of the three output ports around a certain design wavelength λ_D using a 2.5D simulation with the software Lumerical. The amplitudes differ only slightly from the ideal $1/\sqrt{3}$ splitting ratio as long as the operating wavelength is sufficiently close to the targeted design wavelength λ_D. When an electric field is launched into a top input port of the 3×3 MMI coupler, the phase differences of the electro-magnetic fields between the three output ports are $\Delta\varphi_{o1\text{-}o2} = \varphi_{11} - \varphi_{21} = \pi$, $\Delta\varphi_{o2\text{-}o3} = \varphi_{21} - \varphi_{31} = \pi/3$ and $\Delta\varphi_{o3\text{-}o1} = \varphi_{31} - \varphi_{11} = 2\pi/3$ in the ideal case. Real devices are subject to phase errors.

In a t-parameter transfer matrix notation, the complex electric field transmission matrix $\underline{\mathbf{t}}_{\mathrm{MMI,o}}$ of the 3×3 MMI coupler at the output can be written as an element-wise Hadamard product (denoted by "∘" as opposed to the scalar product "·") of an amplitude matrix $\mathbf{a}_{\mathrm{MMI,o}}$ (containing a_{mn}) and a complex phase matrix $\underline{\boldsymbol{\varphi}}_{\mathrm{MMI,o}}$ (containing $e^{j\varphi_{mn}}$) as

$$\underline{\mathbf{t}}_{\mathrm{MMI,o}} = \begin{pmatrix} \underline{t}_{11} & \underline{t}_{12} & \underline{t}_{13} \\ \underline{t}_{21} & \underline{t}_{22} & \underline{t}_{23} \\ \underline{t}_{31} & \underline{t}_{32} & \underline{t}_{33} \end{pmatrix} = \begin{pmatrix} a_{11}e^{j\varphi_{11}} & a_{12}e^{j\varphi_{12}} & a_{13}e^{j\varphi_{13}} \\ a_{21}e^{j\varphi_{21}} & a_{22}e^{j\varphi_{22}} & a_{23}e^{j\varphi_{23}} \\ a_{31}e^{j\varphi_{31}} & a_{32}e^{j\varphi_{32}} & a_{33}e^{j\varphi_{33}} \end{pmatrix} = \mathbf{a}_{\mathrm{MMI,o}} \circ \underline{\boldsymbol{\varphi}}_{\mathrm{MMI,o}}.$$

$$(5.2)$$

Note that contrary to the optical *power* transmission T in the previous sections, these complex transmission factors $\underline{t}_{mn}$ as well as the corresponding complex transmission matrix $\underline{\mathbf{t}}$ concern the electrical *field* amplitude and phase.

Further information is added to the electric field transmission matrix by splitting the coefficients into an ideal part, denoted with the superscripts [id], and error contributions, denoted with the superscripts [err], which are again connected via the Hadamard product "∘" as

$$\underline{\mathbf{t}}_{\text{MMI,o}} = \underbrace{\underbrace{\frac{1}{\sqrt{3}} \underbrace{\begin{pmatrix} 1\,1\,1 \\ 1\,1\,1 \\ 1\,1\,1 \end{pmatrix}}_{\mathbf{a}_{\text{MMI,o}}^{\text{id}}} \circ \underbrace{\begin{pmatrix} e^{\text{j}0} & e^{-\text{j}\pi} & e^{\text{j}2\pi/3} \\ e^{-\text{j}\pi} & e^{\text{j}0} & e^{-\text{j}\pi} \\ e^{\text{j}2\pi/3} & e^{-\text{j}\pi} & e^{\text{j}0} \end{pmatrix}}_{\underline{\boldsymbol{\varphi}}_{\text{MMI,o}}^{\text{id}}}}_{\underline{\mathbf{t}}_{\text{MMI,o}}^{\text{id}}} \circ \underbrace{\underbrace{\begin{pmatrix} \gamma_{a_{11}} & \gamma_{a_{12}} & \gamma_{a_{13}} \\ \gamma_{a_{21}} & \gamma_{a_{22}} & \gamma_{a_{23}} \\ \gamma_{a_{31}} & \gamma_{a_{32}} & \gamma_{a_{33}} \end{pmatrix}}_{\mathbf{a}_{\text{MMI,o}}^{\text{err}}} \circ \underbrace{\begin{pmatrix} e^{\text{j}\delta\varphi_{11}} & e^{\text{j}\delta\varphi_{12}} & e^{\text{j}\delta\varphi_{13}} \\ e^{\text{j}\delta\varphi_{21}} & e^{\text{j}\delta\varphi_{22}} & e^{\text{j}\delta\varphi_{23}} \\ e^{\text{j}\delta\varphi_{31}} & e^{\text{j}\delta\varphi_{32}} & e^{\text{j}\delta\varphi_{33}} \end{pmatrix}}_{\underline{\boldsymbol{\varphi}}_{\text{MMI,o}}^{\text{err}}}}_{\underline{\mathbf{t}}_{\text{MMI,o}}^{\text{err}}}.$$

$$(5.3)$$

The product of the first two matrices represents the ideal transmission $\underline{\mathbf{t}}_{\text{MMI,o}}^{\text{id}}$ and consist of the ideal amplitude transmission matrix $\mathbf{a}_{\text{MMI,o}}^{\text{id}}$ with $a_{mn}^{\text{id}} = a_{\text{MMI,o}}^{\text{id}} = 1/\sqrt{3} \quad \forall n,m$, and the ideal phase matrix $\underline{\boldsymbol{\varphi}}_{\text{MMI,o}}^{\text{id}}$ with phase shifts of 0, $-\pi$ and $2\pi/3$ on the main diagonal, the ± 1 diagonal and the ± 2 diagonal, respectively. The last two matrices contain non-ideal error terms, in the absence of errors both simplify to matrices of ones. The amplitude error matrix $\mathbf{a}_{\text{MMI,o}}^{\text{err}}$, consists of the coefficients $\gamma_{a_{mn}}$, while the phase error matrix $\underline{\boldsymbol{\varphi}}_{\text{MMI,o}}^{\text{err}}$ consists of the coefficients $e^{\text{j}\delta\varphi_{11}}$, where $\delta\varphi_{mn}$ is the phase error term. These error matrices are especially important for the calibration part in Section 5.2.4. A transmission matrix can hence be expressed either by a Hadamard product of the ideal and the error matrices, or by a Hadamard product of the amplitude and phase matrices, i.e.,

$$\underset{\substack{\mathbf{a}^{\text{id}}\circ\underline{\boldsymbol{\varphi}}^{\text{id}} \quad \mathbf{a}^{\text{err}}\circ\underline{\boldsymbol{\varphi}}^{\text{err}} \quad \mathbf{a}^{\text{id}}\circ\mathbf{a}^{\text{err}} \quad \underline{\boldsymbol{\varphi}}^{\text{id}}\circ\underline{\boldsymbol{\varphi}}^{\text{err}}}}{\underline{\mathbf{t}} = \quad \underline{\mathbf{t}}^{\text{id}} \quad \circ \quad \underline{\mathbf{t}}^{\text{err}} \quad = \quad \mathbf{a} \quad \circ \quad \underline{\boldsymbol{\varphi}}} \qquad (5.4)$$

In the case of a two-arm MZI, the central input port of the 3×3 MMI is unused, and hence the central column of these matrices can be omitted, which leads to a simplified 2×3 matrix

$$\underline{\mathbf{t}}_{\text{MMI,o}} = \underbrace{\underbrace{\frac{1}{\sqrt{3}} \underbrace{\begin{pmatrix} 1 & 1 \\ 1 & 1 \\ 1 & 1 \end{pmatrix}}_{\mathbf{a}_{\text{MMI,o}}^{\text{id}}} \circ \underbrace{\begin{pmatrix} e^{\text{j}0} & e^{\text{j}2\pi/3} \\ e^{-\text{j}\pi} & e^{-\text{j}\pi} \\ e^{\text{j}2\pi/3} & e^{\text{j}0} \end{pmatrix}}_{\underline{\boldsymbol{\varphi}}_{\text{MMI,o}}^{\text{id}}}}_{\underline{\mathbf{t}}_{\text{MMI,o}}^{\text{id}}} \circ \underbrace{\underbrace{\begin{pmatrix} \gamma_{a_{11}} & \gamma_{a_{13}} \\ \gamma_{a_{21}} & \gamma_{a_{23}} \\ \gamma_{a_{31}} & \gamma_{a_{33}} \end{pmatrix}}_{\mathbf{a}_{\text{MMI,o}}^{\text{err}}} \circ \underbrace{\begin{pmatrix} e^{\text{j}\delta\varphi_{11}} & e^{\text{j}\delta\varphi_{13}} \\ e^{\text{j}\delta\varphi_{21}} & e^{\text{j}\delta\varphi_{23}} \\ e^{\text{j}\delta\varphi_{31}} & e^{\text{j}\delta\varphi_{33}} \end{pmatrix}}_{\underline{\boldsymbol{\varphi}}_{\text{MMI,o}}^{\text{err}}}}_{\underline{\mathbf{t}}_{\text{MMI,o}}^{\text{err}}} \quad (5.5)$$

Note that for an ideal MMI coupler without amplitude errors, i.e., $\delta a_{mn} = 1$, and without phase errors, i.e., $\delta \varphi_{mn} = 0$, the error terms can be omitted since both $\mathbf{a}_{\mathrm{MMI,o}}^{\mathrm{err}}$ and $\underline{\boldsymbol{\varphi}}_{\mathrm{MMI,o}}^{\mathrm{err}}$ are matrices of ones.

5.2.2   Model of a 1×3 Mach-Zehnder interferometer

The PIC model of the 1×3 MZI starts with a single-mode waveguide connected to a 1×2 MMI coupler with transmission $\underline{\mathbf{t}}_{\mathrm{MMI,i}}$ at the MZI input. Here, the signals are split into a sensor and a reference arm, the respective transmission can be described by a 2×2 matrix $\underline{\mathbf{t}}_{\mathrm{Arms}}$. The sensor and reference signals are subsequently connected to the top and bottom input ports of a symmetric 3×3 MMI coupler, where they superimpose each other. The transmission to the three output ports can hence be described by the simplified $\underline{\mathbf{t}}_{\mathrm{MMI,o}}$ from Eq. (5.5). Subsequently, the three optical signals are routed via single-mode waveguides to individual photodetectors. The electrical field transmission $\underline{\mathbf{t}}_{\mathrm{MZI_3}}$ from the complex electrical field amplitude at the input $\underline{E}_{\mathrm{i}}$ to the three complex electrical field amplitudes at the output $\underline{\mathbf{E}}_{\mathrm{o}}$ is sketched in Fig. 5.6. It can be written in general form as a matrix multiplication via

$$\underline{\mathbf{t}}_{\mathrm{MZI_3}} = \underline{\mathbf{E}}_{\mathrm{o}} / \underline{E}_{\mathrm{i}} = \underline{\mathbf{t}}_{\mathrm{MMI,o}} \underline{\mathbf{t}}_{\mathrm{Arms}} \underline{\mathbf{t}}_{\mathrm{MMI,i}} \tag{5.6}$$

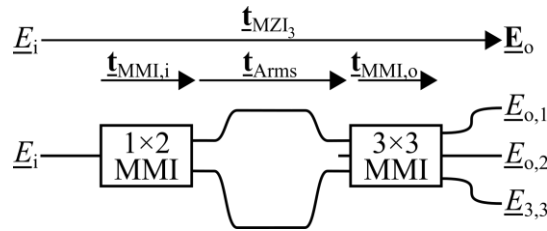**Fig. 5.6. Schematic model of a 1×3 Mach-Zehnder interferometer.**   The complex electrical field amplitude at the input $\underline{E}_{\mathrm{i}}$ carried by a single-mode waveguide is split into a sensor arm and a reference arm by a 1×2 multi-mode interference (MMI) coupler with electric field transmission $\underline{\mathbf{t}}_{\mathrm{MMI,i}}$. The sensing operation modifies the transmission $\underline{\mathbf{t}}_{\mathrm{Arms}}$ in the MZI arms. The two signals are combined in a 3×3 MMI, where the central input port remains unused. The transmission matrix to the three single-mode output waveguides can hence be simplified to 3×2 transmission matrix $\underline{\mathbf{t}}_{\mathrm{MMI,o}}$. The total transmission from the complex electrical field amplitude at the input $\underline{E}_{\mathrm{i}}$ to the three complex electrical field amplitudes at the output represented by the 3×1 matrix $\underline{\mathbf{E}}_{\mathrm{o}}$ is denoted as $\underline{\mathbf{t}}_{\mathrm{MZI_3}}$.

The derivation of the general optical transfer function of the 1×3 MZI can be found in Appendix C.1. In the ideal case without any MMI amplitude or phase errors, and for identical power loss in the two MZI arms, i.e., $a_s = a_r = a$, each output channel $v = 1, 2, 3$ contains the superposition of the electrical fields from the sensor and the reference arms, $\left| \underline{E}_{o,s,v}^{id} \right| = \left| \underline{E}_{o,r,v}^{id} \right| = \left| \underline{E}_i \right| a / \sqrt{6}$, as derived from Eq. (C.5) in Appendix C.1. As a result, in the ideal case, the corresponding optical output powers $P_{o,v}^{id} = \frac{1}{2} \left| \underline{E}_{o,v}^{id} \right|^2 = \frac{1}{2} \left(\underline{E}_{o,s,v}^{id} + \underline{E}_{o,r,v}^{id} \right) \left(\underline{E}_{o,s,v}^{id} + \underline{E}_{o,r,v}^{id} \right)^*$ of the three output channels can be expressed by the 3×1 matrix $\mathbf{P}_o^{id}$ as

$$\mathbf{P}_o^{id} = \frac{P_i}{3} a^2 \begin{pmatrix} 1 + \cos\left(\varphi_{MZI} + \dfrac{2\pi}{3} \right) \\ 1 + \cos\left(\varphi_{MZI} \right) \\ 1 + \cos\left(\varphi_{MZI} - \dfrac{2\pi}{3} \right) \end{pmatrix}. \tag{5.7}$$

It can be seen that the cosinusoidal dependence of the three ideal optical output powers $\mathbf{P}_o^{id}$ on the phase difference φ_{MZI} are phase-shifted by $2\pi/3$ or $120°$ with a maximum output power of $(2/3) P_i a^2$ in each channel.

5.2.3 Signal processing via a Clarke Transformation to eliminate directional ambiguity and sensitivity fading

From the output ports of the 3×3 MMI coupler, the three optical signals are routed to three photodiodes with responsivities $\mathbf{R} = \left(R_1, R_2, R_3 \right)^T$. Here, the optical fields are converted into electrical output currents, i.e., $\mathbf{I}_o = \mathbf{R} \circ \mathbf{P}_o = \mathbf{R} \circ \left| \underline{\mathbf{E}}_o \right|^2$. For the remainder of this work, identical responsivities $R_1 = R_2 = R_3 \equiv R$ are assumed, however, non-idealities can of course be included in the calculation. The three output currents $\mathbf{I}_o = \left(I_1, I_2, I_3 \right)^T$ are shown in Fig. 5.7(a) for an ideal system without amplitude and phase errors, and in Fig. 5.7(d) for exaggerated amplitude and phase errors in the individual components.
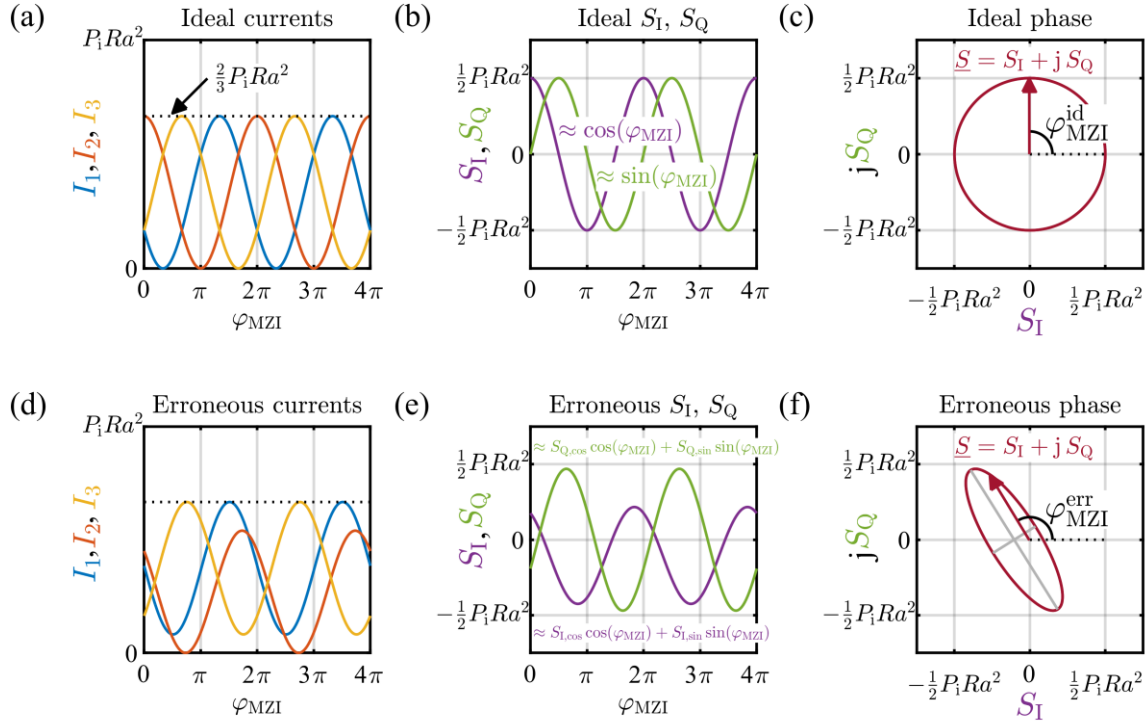
Fig. 5.7. Clarke transformation for complex phase extraction in 1×3 MZI. **(a)** Ideal 120°-phase-shifted output currents $\mathbf{I}_\mathrm{o} = (I_1, I_2, I_3)^\mathrm{T}$ in an amplitude- and phase-error-free MZI. **(b)** A Clarke transformation of the three output currents yields the two signals $(S_\mathrm{I}, S_\mathrm{Q})^\mathrm{T} = \mathbf{M}_\mathrm{C}\mathbf{I}_\mathrm{o} \propto (\cos(\varphi_\mathrm{MZI}), \sin(\varphi_\mathrm{MZI}))^\mathrm{T}$. **(c)** These signals are used in the artificial signal $\underline{S} = S_\mathrm{I} + \mathrm{j}S_\mathrm{Q} \propto \exp(\mathrm{j}\varphi_\mathrm{MZI})$. The phase difference φ_MZI is extracted via $\varphi_\mathrm{MZI} = \arg(\underline{S})$. **(d)-(f)** Identical signal processing for an MZI with amplitude and phase errors yields erroneous signals. The extracted phase difference $\varphi_\mathrm{MZI}^\mathrm{err}$ will contain significant errors unless the system is properly calibrated.

The advantage of the 1×3 MZI is the possibility to directly measure a complex phasor, from which the desired phase can be extracted. To this end, signals containing the in-phase component $\cos(\varphi_\mathrm{MZI})$ and the quadrature component $\sin(\varphi_\mathrm{MZI})$ of the MZI phase difference φ_MZI need to be available simultaneously, see Eq. (5.1). It can be shown that the three cosine terms contained in the ideal optical output powers $\mathbf{P}_\mathrm{o}^\mathrm{id}$ in Eq. (5.7) can be rewritten as a function of $(\cos(\varphi_\mathrm{MZI}), \sin(\varphi_\mathrm{MZI}))^\mathrm{T}$ and a corresponding 3×2 transformation matrix, which is from now on denoted as $\mathbf{M}_\mathrm{C}^{\mathrm{T}\lozenge}$:

$$\begin{pmatrix} \cos\left(\varphi_{\mathrm{MZI}} + \dfrac{2\pi}{3} + \delta\varphi_{13} - \delta\varphi_{11} \right) \\[2mm] \cos\left(\varphi_{\mathrm{MZI}} + 0 + \delta\varphi_{23} - \delta\varphi_{21} \right) \\[2mm] \cos\left(\varphi_{\mathrm{MZI}} - \dfrac{2\pi}{3} + \delta\varphi_{33} - \delta\varphi_{31} \right) \end{pmatrix} = \mathbf{M}_{\mathrm{C}}^{\mathrm{T}\Diamond} \begin{pmatrix} \cos\left(\varphi_{\mathrm{MZI}} \right) \\[2mm] \sin\left(\varphi_{\mathrm{MZI}} \right) \end{pmatrix}, \quad \text{where}$$

$$\mathbf{M}_{\mathrm{C}}^{\mathrm{T}\Diamond} = \begin{pmatrix} \cos\left(-\dfrac{2\pi}{3} - \delta\varphi_{13} + \delta\varphi_{11} \right) & \sin\left(-\dfrac{2\pi}{3} - \delta\varphi_{13} + \delta\varphi_{11} \right) \\[3mm] \cos\left(-0 - \delta\varphi_{23} + \delta\varphi_{21} \right) & \sin\left(-0 - \delta\varphi_{23} + \delta\varphi_{21} \right) \\[3mm] \cos\left(+\dfrac{2\pi}{3} - \delta\varphi_{33} + \delta\varphi_{31} \right) & \sin\left(+\dfrac{2\pi}{3} - \delta\varphi_{33} + \delta\varphi_{31} \right) \end{pmatrix};$$

$$(5.8)$$

$$\cos(a+b) = \cos(a)\cos(b) - \sin(a)\sin(b),$$
$$\cos(a) = \cos(-a), \quad \sin(a) = -\sin(-a).$$

This shows that the superimposition of the electrical fields of the sensor and reference arms already contains the required signals $\left(\cos(\varphi_{\mathrm{MZI}}), \sin(\varphi_{\mathrm{MZI}}) \right)^{\mathrm{T}}$. However, they are transformed by the 3×3 MMI coupler via $\mathbf{M}_{\mathrm{C}}^{\mathrm{T}\Diamond}$, which contains the arguments of the ideal phase terms $\underline{\boldsymbol{\varphi}}_{\mathrm{MMI,o}}^{\mathrm{id}}$, $[-2\pi/3, 0, 2\pi/3]$, as well as the arguments δ_{mn} of the error phase terms $\underline{\boldsymbol{\varphi}}_{\mathrm{MMI,o}}^{\mathrm{err}}$. More specifically, the first column of $\mathbf{M}_{\mathrm{C}}^{\mathrm{T}\Diamond}$ contains cosine functions, the second column contains sine functions of the phase shifts φ_{nm} in the real device. The arguments are identical in both columns, and are obtained by taking the difference of the arguments of the first and last column of the reduced 3×3 MMI coupler phase matrix $\underline{\boldsymbol{\varphi}}_{\mathrm{MMI,o}}$, see Eq. (5.5), which correspond to the phase shifts introduced by the MMI to the signal from the sensor and reference arm, respectively.

When measuring the three output currents, all that needs to be done is to transform the three 120°-phase-shifted currents back to the two 90°-phase-shifted signals. This is realized via the Clarke transform, which is well known from electrical three-phase systems. The standard Clarke transformation matrix can be written as

$$\mathbf{M}_\mathrm{C} = \begin{pmatrix} \cos\left(-\dfrac{2\pi}{3}\right) & \cos(0) & \cos\left(+\dfrac{2\pi}{3}\right) \\[2ex] \sin\left(-\dfrac{2\pi}{3}\right) & \sin(0) & \sin\left(+\dfrac{2\pi}{3}\right) \end{pmatrix} = \begin{pmatrix} -\dfrac{1}{2} & 1 & -\dfrac{1}{2} \\[2ex] -\dfrac{\sqrt{3}}{2} & 0 & \dfrac{\sqrt{3}}{2} \end{pmatrix}. \qquad (5.9)$$

It can be seen that the signal transformation matrix $\mathbf{M}_\mathrm{C}^{\mathrm{T}\Diamond}$ is corresponding to the transposed Clarke transformation matrix $\mathbf{M}_\mathrm{C}^{\mathrm{T}}$ if the 3×3 MMI coupler contains no phase errors. Including phase errors, the MZI hence performs a modified, non-ideal transposed Clarke transform $\mathbf{M}_\mathrm{C}^{\mathrm{T}\Diamond}$. This notation can be used to re-write the three output currents from the 1×3 MZI sensor in a simpler form as

$$\begin{aligned} \mathbf{I}_\mathrm{o} &= \mathbf{R} \circ \left(\left|\underline{\mathbf{E}}_\mathrm{o,s}\right|^2 + \left|\underline{\mathbf{E}}_\mathrm{o,r}\right|^2 + 2\left|\underline{\mathbf{E}}_\mathrm{o,s}\right| \circ \left|\underline{\mathbf{E}}_\mathrm{o,r}\right| \circ \mathbf{M}_\mathrm{C}^{\mathrm{T}\Diamond} \begin{pmatrix} \cos(\varphi_\mathrm{MZI}) \\ \sin(\varphi_\mathrm{MZI}) \end{pmatrix} \right) \\ &= P_\mathrm{i} \mathbf{R} \circ \left(\mathbf{a}_\mathrm{o,s}^2 + \mathbf{a}_\mathrm{o,r}^2 + 2\mathbf{a}_\mathrm{o,s} \circ \mathbf{a}_\mathrm{o,r} \circ \mathbf{M}_\mathrm{C}^{\mathrm{T}\Diamond} \begin{pmatrix} \cos(\varphi_\mathrm{MZI}) \\ \sin(\varphi_\mathrm{MZI}) \end{pmatrix} \right). \end{aligned} \qquad (5.10)$$

Without knowing the phase errors of the 3×3 MMI, a typical signal-processing algorithm applies the ideal Clarke Transformation $\mathbf{M}_\mathrm{C}$ to the three output currents $\mathbf{I}_\mathrm{o}$, which creates the two signals

$$\begin{aligned} \begin{pmatrix} S_\mathrm{I} \\ S_\mathrm{Q} \end{pmatrix} &= \mathbf{M}_\mathrm{C} \mathbf{I}_\mathrm{o} \\ &= P_\mathrm{i} \mathbf{M}_\mathrm{C} \left(\mathbf{R} \circ \left(\mathbf{a}_\mathrm{o,s}^2 + \mathbf{a}_\mathrm{o,r}^2 \right) \right) \\ &\quad + 2 P_\mathrm{i} \mathbf{M}_\mathrm{C} \left(\mathbf{R} \circ \mathbf{a}_\mathrm{o,s} \circ \mathbf{a}_\mathrm{o,r} \circ \mathbf{M}_\mathrm{C}^{\mathrm{T}\Diamond} \right) \begin{pmatrix} \cos(\varphi_\mathrm{MZI}) \\ \sin(\varphi_\mathrm{MZI}) \end{pmatrix}. \end{aligned} \qquad (5.11)$$

In the ideal case without phase and amplitude errors, denoted by superscripts [id], this can be simplified to

$$
\begin{pmatrix} S_{\mathrm{I}}^{\mathrm{id}} \\ S_{\mathrm{Q}}^{\mathrm{id}} \end{pmatrix} = \underbrace{P_{\mathrm{i}}\mathbf{M}_{\mathrm{C}}\left(\mathbf{R}\circ\left(\mathbf{a}_{\mathrm{o,s}}^{2}+\mathbf{a}_{\mathrm{o,r}}^{2}\right)\right)}_{0} + \underbrace{2P_{\mathrm{i}}\mathbf{M}_{\mathrm{C}}\left(\mathbf{R}\circ\mathbf{a}_{\mathrm{o,s}}\circ\mathbf{a}_{\mathrm{o,r}}\circ\mathbf{M}_{\mathrm{C}}^{\mathrm{T}\Diamond}\right)}_{\frac{1}{2}P_{\mathrm{i}}Ra^{2}\begin{pmatrix}1 & 0 \\ 0 & 1\end{pmatrix}}\begin{pmatrix} \cos\left(\varphi_{\mathrm{MZI}}\right) \\ \sin\left(\varphi_{\mathrm{MZI}}\right) \end{pmatrix}
$$

$$
= \frac{1}{2}P_{\mathrm{i}}Ra^{2}\begin{pmatrix} \cos\left(\varphi_{\mathrm{MZI}}\right) \\ \sin\left(\varphi_{\mathrm{MZI}}\right) \end{pmatrix}.
$$

$$(5.12)$$

The result is plotted in Fig. 5.7(b), showing the two ideal signals $S_{\mathrm{I}}^{\mathrm{id}}$ and $S_{\mathrm{Q}}^{\mathrm{id}}$ as pure cosine and sine functions with equal amplitudes and without any offset. From these two signals, the ideal version $\underline{S}^{\mathrm{id}}$ of the complex signal $\underline{S}$ is constructed, which directly contains the actual MZI phase difference φ_{MZI}

$$
\underline{S}^{\mathrm{id}} = S_{\mathrm{I}}^{\mathrm{id}} + \mathrm{j}S_{\mathrm{Q}}^{\mathrm{id}} = \frac{1}{2}P_{\mathrm{i}}Ra^{2}\mathrm{e}^{\mathrm{j}\varphi_{\mathrm{MZI}}}. \tag{5.13}
$$

This signal is plotted in the complex plane in Fig. 5.7(c) and resembles a perfect circle with radius $P_{\mathrm{i}}Ra^{2}/2$, from which the phase difference can easily be reconstructed by calculating the argument $\underline{S}^{\mathrm{id}}$. More specifically, the argument is calculated by applying the two-argument arctangent function to the imaginary and real parts of $\underline{S}^{\mathrm{id}}$, i.e.,

$$
\varphi_{\mathrm{MZI}} = \arg\left(\underline{S}^{\mathrm{id}}\right) = \mathrm{atan2}\left(S_{\mathrm{Q}}^{\mathrm{id}}, S_{\mathrm{I}}^{\mathrm{id}}\right),
$$

$$
\mathrm{atan2}(y,x) = \begin{cases} \arctan2(y/x) & \text{if } x > 0 \\ \arctan2(y/x) + \pi & \text{if } x < 0 \text{ and } y \geq 0 \\ \arctan2(y/x) - \pi & \text{if } x < 0 \text{ and } y < 0 \\ +\pi/2 & \text{if } x = 0 \text{ and } y > 0 \\ -\pi/2 & \text{if } x = 0 \text{ and } y < 0 \\ \text{undefined} & \text{if } x = 0 \text{ and } y = 0. \end{cases} \tag{5.14}
$$

If non-idealities such as amplitude and phase errors of the 3×3 MMI coupler are considered, it applies a non-ideal transposed Clarke Transformation to the elec-

trical fields. As a result, the output signals $\left(S_{\mathrm{I}}^{\mathrm{id}}, S_{\mathrm{Q}}^{\mathrm{id}}\right)^{\mathrm{T}}$ do not resemble the centered circle in the complex plane. Instead, $\left(S_{\mathrm{I}}^{\mathrm{id}}, S_{\mathrm{Q}}^{\mathrm{id}}\right)^{\mathrm{T}}$ can be expressed by a generic elliptical equation

$$
\begin{pmatrix} S_{\mathrm{I}} \\ S_{\mathrm{Q}} \end{pmatrix} = \underbrace{\begin{pmatrix} S_{\mathrm{I},0} \\ S_{\mathrm{Q},0} \end{pmatrix}}_{\mathbf{OS}} + \underbrace{\begin{pmatrix} S_{\mathrm{I,cos}} & S_{\mathrm{I,sin}} \\ S_{\mathrm{Q,cos}} & S_{\mathrm{Q,sin}} \end{pmatrix}}_{\mathbf{TR}} \begin{pmatrix} \cos(\varphi_{\mathrm{MZI}}) \\ \sin(\varphi_{\mathrm{MZI}}) \end{pmatrix}
$$

$$
\mathbf{OS} = \mathbf{M}_{\mathrm{C}}\left(\mathbf{R} \circ \left(\left|\underline{\mathbf{E}}_{\mathrm{o,s}}\right|^2 + \left|\underline{\mathbf{E}}_{\mathrm{o,r}}\right|^2 \right) \right) = P_{\mathrm{i}} \mathbf{M}_{\mathrm{C}}\left(\mathbf{R} \circ \left(\mathbf{a}_{\mathrm{o,s}}^2 + \mathbf{a}_{\mathrm{o,r}}^2 \right) \right)
$$

$$
\mathbf{TR} = 2\mathbf{M}_{\mathrm{C}}\left(\mathbf{R} \circ \left|\underline{\mathbf{E}}_{\mathrm{o,s}}\right| \circ \left|\underline{\mathbf{E}}_{\mathrm{o,r}}\right| \circ \mathbf{M}_{\mathrm{C}}^{\mathrm{T}\lozenge} \right) = 2P_{\mathrm{i}} \mathbf{M}_{\mathrm{C}}\left(\mathbf{R} \circ \mathbf{a}_{\mathrm{o,s}} \circ \mathbf{a}_{\mathrm{o,r}} \circ \mathbf{M}_{\mathrm{C}}^{\mathrm{T}\lozenge} \right)
$$

$$(5.15)$$

In contrast to the ideal case, the non-ideal $\left(S_{\mathrm{I}}, S_{\mathrm{Q}}\right)^{\mathrm{T}}$-signals do have a non-zero translational offset vector $\mathbf{OS} = \left(S_{\mathrm{I},0}, S_{\mathrm{Q},0}\right)^{\mathrm{T}}$, which is caused by non-zero amplitude errors $\mathbf{a}_{\mathrm{o,s}}^{\mathrm{err}}$ and $\mathbf{a}_{\mathrm{o,r}}^{\mathrm{err}}$ as defined in Eq. 5.9. Note that this offset is independent of any phase errors. Furthermore, the ideal circular shape described by $\left(S_{\mathrm{I}}, S_{\mathrm{Q}}\right)^{\mathrm{T}} \propto \left(\cos(\varphi_{\mathrm{MZI}}), \sin(\varphi_{\mathrm{MZI}})\right)^{\mathrm{T}}$ is only present if the 2×2 transformation matrix $\mathbf{TR}$ is a diagonal matrix with $S_{\mathrm{I,cos}} = S_{\mathrm{Q,sin}} = P_{\mathrm{i}} R a^2 / 2$ and $S_{\mathrm{I,sin}} = S_{\mathrm{Q,cos}} = 0$, see Eq. (5.12). In all other, non-ideal cases, $\mathbf{TR}$ rotates and stretches the circle into an ellipse via amplitude and phase errors, respectively. The result with exaggerated amplitude and phase errors is shown in Fig. 5.7(f). In this case, the phase difference cannot be extracted by taking the argument of the complex signal as in the ideal case of Eq. (5.14), and a calibration is required, which is described in detail in the following Section 5.2.4.

In the ideal case, this phase reconstruction from the artificial complex signal $\underline{S}$ combats several of the drawbacks mentioned in Section 5.1. This is visualized in Fig. 5.8, where the phase extraction process of single-, double- and triple-output MZI$_{1\text{-}3}$ is compared. In the following, these benefits are briefly described.

Doubled signal unambiguity range While fringe-order ambiguity is still present, the directional ambiguity problem is solved by taking the argument of the corresponding complex signals, as this function returns values between $-\pi$ and π and hence doubles the unambiguity range.
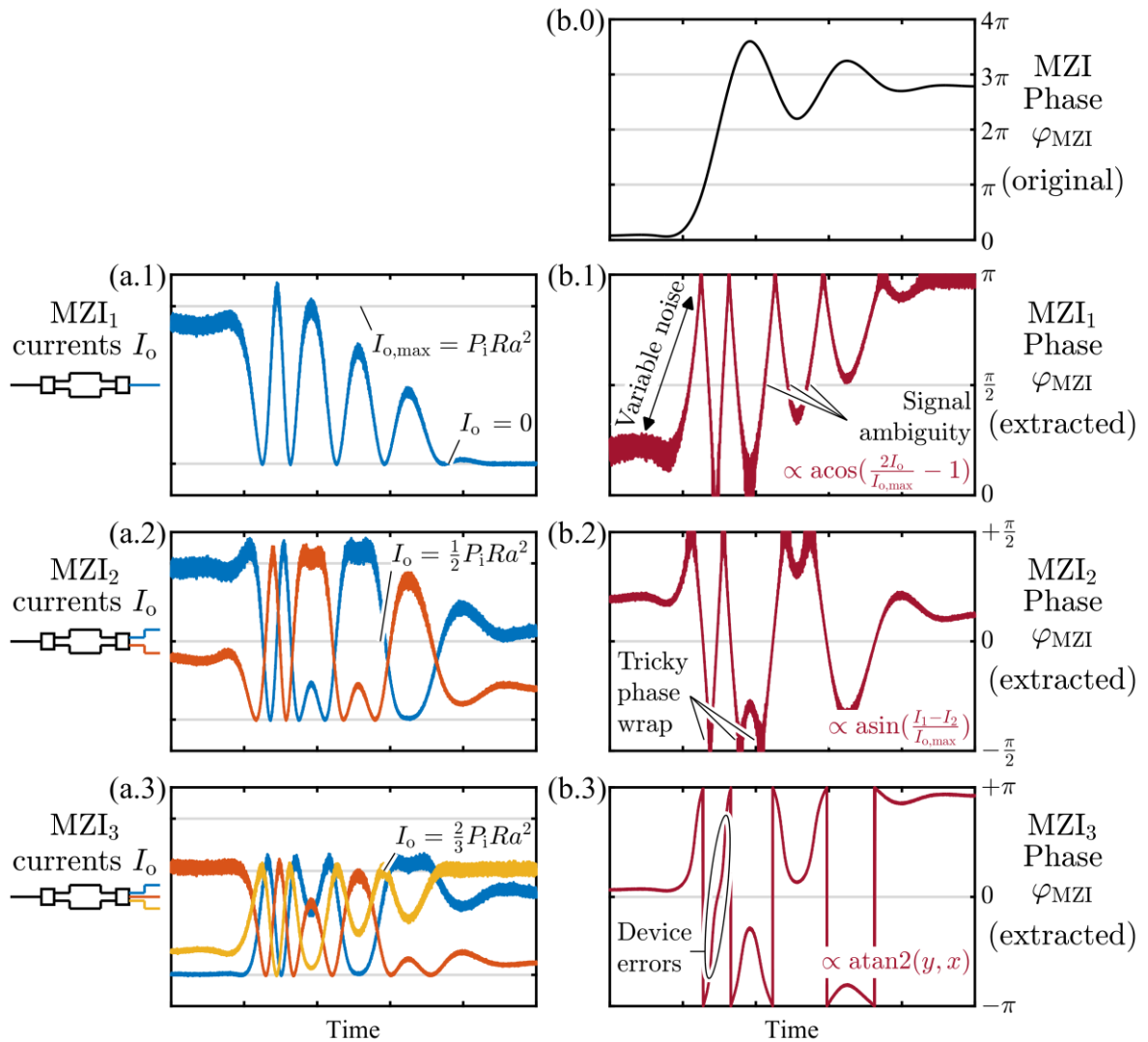
Fig. 5.8. Typical phase extraction in 1×1, 1×2 and 1×3 MZI$_{1\text{-}3}$. **(b.0)** This simulation resembles a typical experiment where the phase φ_{MZI} rises and settles at around 3π. **(a.1)-(a.3)** Output currents $\mathbf{I_o}$ and **(b.1)-(b.3)** extracted phase differences φ_{MZI} for the three MZI versions. **(b.1)-(b.2)** Several drawbacks of MZI$_1$ and MZI$_2$ are labeled in the plots, as explained in Section 5.1. First, an operating-point-dependent sensitivity and signal-to-noise ratio complicates signal processing. Second, the unambiguity range is limited to a span of π due to directional ambiguity. In addition, due to the absence of distinct phase jumps at the $[0, \pi]$ rails in MZI$_1$ or the $[\text{-}\pi/2, \pi/2]$ rails in MZI$_2$, the phase unwrapping process is unreliable. **(b.3)** The MZI$_3$ readout concept removes the directional ambiguity and hence doubles the unambiguity range to a span of 2π, provides a constant sensitivity and mostly constant SNR, and enables a reliable phase unwrapping process during signal processing. However, the problem of fringe order ambiguity as well as the impact of device errors such as amplitude and phase errors cannot be removed without further calibration, which leads to the indicated, wobbly phase evolution depicted in (b.3).

Reliable phase unwrapping   In a continuous measurement, where the sampling rate is much faster than any potential fringe order change in the sensor system, this elimination of directional ambiguity also makes the phase unwrapping process a lot more reliable. More specifically, in single- and double-output MZI, at the corner of a fringe-order jump, it cannot be differentiated if the fringe order actually jumped or if the signal just changed direction. In contrast to that, the described phase extraction of the 1×3 MZI shows pronounced 2π-jumps when changing the fringe order.

Sensitivity independent of operating point   The phase sensitivity in the 1×3 MZI readout concept is constant, which makes the sensor effectively operating-point independent. This is an important factor, since no active operating point control is required, which vastly simplifies the sensor design, operation, and signal processing. In MZI_1 and MZI_2, the signal-to-noise ratio (SNR) is operating-point-dependent. The constant sensitivity in MZI_3 solves this issue, see Chapter 4.

Amplitude and phase errors – not solved yet   As shown in the second row of Fig. 5.7 and the last plot in Fig. 5.8, the problems occurring with non-ideal devices that introduce amplitude and phase errors as well as corresponding device-to-device variations are not yet solved by simply employing the triple-output MMI coupler in combination with the Clarke transformation. However, the measurement data obtained from this readout concept can be used for a calibration of the device, which will be discussed in the next Section 5.2.4.

5.2.4   Calibration process based on phase measurements to eliminate amplitude and phase errors

In the previous section, it was shown that the use of a triple-output 1×3 MZI eliminates the drawbacks of directional ambiguity and sensitivity fading, with the additional benefit of having a reliable phase unwrapping mechanism. However, non-ideal photonic integrated circuit components can introduce substantial amplitude or phase errors in the system. In this case, the simple readout procedure of performing a Clarke Transformation on the raw current data, followed by calculating the argument of $\underline{S}$ to extract the phase difference of the MZI,

will produce erroneous data, as was shown in Fig. 5.7. This is the case since the Clarke transformation expects the underlying $\left(S_\mathrm{I}, S_\mathrm{Q}\right)^\mathrm{T}$-signals to describe a perfect circle in the complex plane. To solve this problem, a calibration process is required that accounts for the amplitude and phase errors of the system. In this section, all errors are assumed static without any change during operation of the sensor. As a consequence, the calibration has to be done only once. This concept is extended to an instantaneous calibration during sensor operation in Section 5.3.1.

In Section 5.2.3, it was shown that a non-ideal MZI$_3$ includes amplitude and phase errors. As a result, the simple phase extraction mechanism based on the argument of the artificial signal $\underline{S} = S_\mathrm{I} + \mathrm{j} S_\mathrm{Q} \propto \exp\left(\mathrm{j}\varphi_\mathrm{MZI}\right)$ becomes erroneous. The ideal circle generated by $\underline{S}$ in the complex plane is instead subject to an offset vector **OS** as well as a 2×2 transformation matrix **TR** that transform the ideal circle into an ellipse, see Eq. (5.15). If the argument is calculated from this signal, the extracted phase difference is distorted compared to the actual data, which is visualized in the first column of Fig. 5.9.

In order to calibrate the device, the distorted ellipse has to be mapped back to the ideal, centered circle before extracting the phase difference. This mapping process requires a sufficiently large number of data points to identify the crucial parameters of the ellipse, which means that measurement data spanning a whole 2π-period of phase differences is ideal. Fig. 5.9 shows in detail the required geometric transformation steps to obtain a centered circle.
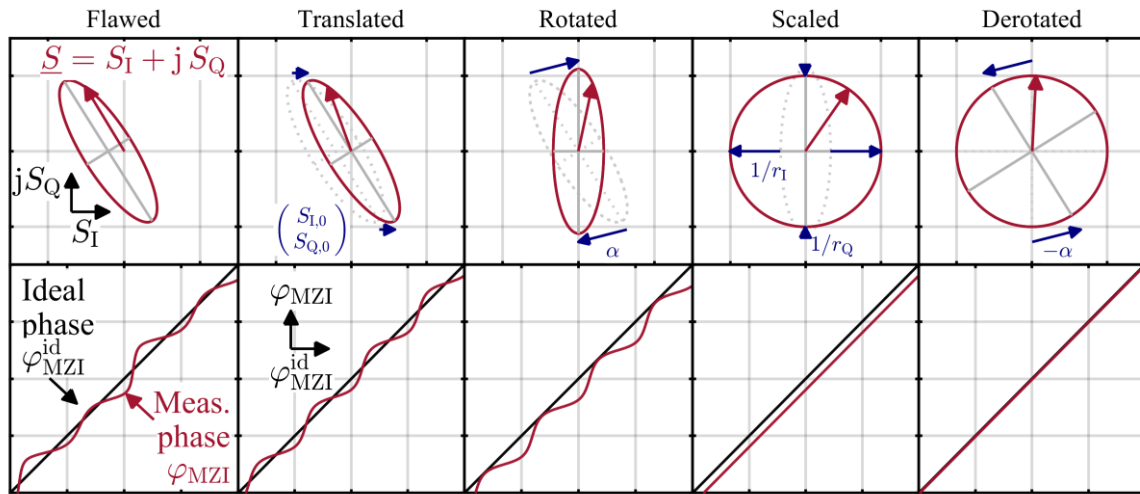
Fig. 5.9. Calibration of 1×3 MZI via geometric transformation. The transformation is performed on the 2D $(S_I, S_Q)^T$ data and visualized in the complex plane. In ideal devices, $\underline{S}^{id} = S_I^{id} + j S_Q^{id}$ leads to a perfectly centered circle, and simply calculating the argument of $\underline{S}^{id}$ results in the actual ideal MZI phase difference φ_{MZI}^{id}. In MZI$_3$ with amplitude or phase errors, $\underline{S} = S_I + j S_Q$ resembles a distorted ellipse, which can be scaled on its width and height, rotated, and offset from the origin. The calibration process relies on a transformation of the ellipse into the ideal centered unit circle by first translating the ellipse to the center, rotating the ellipse, scaling the width and the height, and then derotating the resulting circle back to its initial orientation, see first row from left to right. The second row plots the measured phase φ_{MZI} versus the actual phase difference φ_{MZI}^{id}. Without errors, this is a straight line (see black line), while distortions can be seen for erroneous systems (red line). From left to right, the various transformation steps were applied to the erroneous $(S_I, S_Q)^T$ before calculating $\varphi_{MZI} = \arg(\underline{S})$. It can be seen that all four geometrical transformation steps are required in order to properly calibrate the device.

Mathematically, the important parameters of the ellipse are identified first. To that end, an efficient geometric ellipse-fitting algorithm based on a least squares fit is employed, such as [137]. Given a set of 2D $(S_I, S_Q)^T$-data, the algorithm returns fits of the ellipse parameters, denoted with superscripts ^{fit}, such as the offsets in S_I- and S_Q-direction, $S_{I,0}^{fit}$ and $S_{Q,0}^{fit}$, the ellipse width in S_I- and S_Q-direction, r_I^{fit} and r_Q^{fit}, as well as the orientation angle α^{fit}, see Fig. 5.9. A total of four transformation matrices based on these fit parameters are applied on the measured $(S_I, S_Q)^T$-signals to obtain a calibrated dataset, denoted with the superscripts ^{cal},

$$\begin{pmatrix} S_I^{cal} \\ S_Q^{cal} \end{pmatrix} = \mathbf{M}_R \mathbf{M}_S \mathbf{M}_R^{-1} \left(\begin{pmatrix} S_I \\ S_Q \end{pmatrix} - \mathbf{M}_T \right).$$

$$\mathbf{M}_T = \begin{pmatrix} S_{I,0}^{fit} \\ S_{Q,0}^{fit} \end{pmatrix} \qquad \text{[Translation]}$$

$$\mathbf{M}_S = \begin{pmatrix} 1/r_I^{fit} & 0 \\ 0 & 1/r_Q^{fit} \end{pmatrix} \qquad \text{[Scaling]}$$

$$\mathbf{M}_R = \begin{pmatrix} \cos(\alpha^{fit}) & -\sin(\alpha^{fit}) \\ \sin(\alpha^{fit}) & \cos(\alpha^{fit}) \end{pmatrix} \qquad \text{[Rotation]}$$

(5.16)

First, the translational offset is removed by subtracting the 2×1 translation vector $\mathbf{M}_T$ from the measured data so that the ellipse is centered. Second, the ellipse is rotated by a 2×2 rotation matrix $\mathbf{M}_R$ using the rotation angle α so that the two ellipse axes align with the coordinate system. Third, the ellipse is scaled via the diagonal 2×2 matrix $\mathbf{M}_S$ so that a unit circle with constant radius is obtained. Note that for the phase extraction, the radius of the scaled circle does not play a role. Fourth, the circle is rotated back by the inverse of $\mathbf{M}_R$ to its initial orientation so that the information contained in φ_{MZI} is not corrupted.

Note that by comparing the fitted translation matrix $\mathbf{M}_T$ with the error offset matrix $\mathbf{OS}$ from Eq. (5.15), and/or by comparing the combined transformation $\mathbf{M}_R \mathbf{M}_S \mathbf{M}_R^{-1}$ with the error transformation matrix $\mathbf{TR}$, information on the amplitude and phase error properties of the system can be obtained. However, in this case, the scaling should not transform the ellipse into the unit circle with $r = 1$, but rather into a circle with a radius of $r = P_i Ra^2/2$ as calculated in Eq. (5.12). This value can be obtained, e.g., from the sum of the three measured output currents. Alternatively, the currents could be normalized by the total power before entering the signal processing, which results in the same effect.

5.3 Enhanced triple-output Mach-Zehnder interferometer readout method

The previous sections demonstrated the capabilities of a 1×3 MZI. It was shown that the readout concept is able to eliminate the drawbacks of directional ambiguity and sensitivity fading, and that phase unwrapping can be performed reliably. *However, the issue of fringe order ambiguity remains to be solved*. Furthermore, it was shown that the readout process enables a calibration process that can eliminate static amplitude and phase errors introduced to the MZI response by non-ideal components. However, the calibration requires measurement data spanning at least the equivalent of a 2π period of the phase difference and hence a dedicated, controlled calibration process. Furthermore, dynamic amplitude or phase errors changing during the sensor operation are not covered by such a one-time calibration method. *Consequently, an instantaneous sensor calibration method is required.*

This section demonstrates how the MZI_3 readout concept derived in the previous sections can be enhanced to solve both tasks, i.e., instantaneous calibration and removal of fringe-order ambiguity. Both solutions rely on an active phase modulation of the MZI phase difference during the sensor operation. This phase modulation can for example be achieved by using a frequency-tunable laser as the input light source, or by adding dedicated waveguide sections to the MZI arms that can shift the phase, e.g., thermally via heaters, electrically via free-carrier injection, or mechanically by actuating suspended structures via electrostatics [9], which is well-known from micro-electro-mechanical systems (MEMS).

First, Section 5.3.1 describes a method that enables a dynamic, instantaneous sensor calibration during the actual sensor operation. As a consequence, the sensor signal extraction is extremely robust with respect to environmental changes such as thermal drift, which otherwise heavily affects integrated photonic sensor systems. Second, Section 5.3.2 describes how the frequency-modulated output data can be used to perform an endless phase unwrapping in order to extract an absolute phase difference. As a consequence, experiments can be evaluated in which the sampling rate is not sufficient to track the process dynamics, i.e., in

which two subsequent measurements can lead to a phase shift larger than 2π. Furthermore, independent measurements taken at different points in time, such as after turning on and off measurement devices, can be compared quantitatively.

5.3.1 Phase modulation for instantaneous sensor calibration

The phase extraction of a 1×3 MZI using a 3×3 MMI coupler at the output works smoothly only in absence of significant amplitude or phase errors of the photonic components such as the MMI couplers. In this ideal case, the desired measurand, i.e., the phase difference φ_{MZI} between the two propagating modes at the ends of the two single-mode MZI waveguide arms can directly be extracted by evaluating the argument of the complex artificial measurement signal $\underline{S} = S_{\mathrm{I}} + \mathrm{j}S_{\mathrm{Q}} \propto \exp\left(\mathrm{j}\varphi_{\mathrm{MZI}}\right)$, which resembles a perfect circle in the complex plane, see Fig. 5.7 and Eq. (5.13). It was shown in Section 5.2.3 that non-ideal photonic components lead to a transformation of that circle towards an offset, rotated and scaled ellipse, in which case the argument of $\underline{S}$ does not correspond to the measurand φ_{MZI} anymore. To solve this issue, Section 5.2.4 demonstrated a calibration process that relied on identifying the underlying transformation parameters. With these parameters at hand, the ellipse can be geometrically transformed into an ideal unit circle, so that the argument of $\underline{S}$ once again corresponds to the measurand φ_{MZI}. As a result, the calibration effectively eliminates the impact of amplitude and phase errors of the photonic components. This technique works best if the geometric parameters of the ellipse in the complex plane are accurately known, which requires measurement data spanning in the best case a whole 2π-period. For a static operation with a fixed input laser frequency and without dedicated phase shifters in the MZI arms, such data sets cannot be created actively by tuning the sensor system, but instead would have to rely on a 2π phase shift generated during the sensor operation as such. As a consequence, the required measurement data has to be generated during an offline calibration procedure, which is often done by the manufacturer in the form of a so-called factory calibration. For example, a tunable reference laser could be connected to the PIC, or the PIC could be placed on an external tunable

heater, while the tuning range is chosen such that the MZI phase difference experiences a total phase shift of around 2π. The corresponding output currents have to be carefully evaluated for the calibration purpose. The issue with a one-time factory calibration is that it only eliminates static errors, resulting, e.g., from such non-ideal components. Dynamic errors such as those originating from thermal drift, stress, humidity, or aging effects cannot be covered by such a one-time calibration.

In order to perform a dynamic sensor calibration, a method is required that creates the 2π phase shift during the actual sensor operation. Such an active phase modulation can for example be achieved by adding dedicated tunable waveguide sections for phase modulation, e.g., via heaters [22], free-carrier injection [23], electro-optic materials [24], or MEMS [9]. These tunable waveguide sections can be spatially separated from the sensitive region on a sensor PIC in order to avoid interference of the two physical effects. Another option to actively perform a phase modulation within the MZI sensor, but without adding additional tunable waveguide sections, is to use a frequency-tunable laser as the input light source. However, this requires a certain pre-built imbalance between the two MZI waveguide arms, i.e., a certain group delay between the interfering signals, which ensures that the frequency tuning range is enough to produce a 2π phase shift at the interferometer output. Note that this increases the susceptibility to frequency noise, as demonstrated in Chapter 4. In the following, the concept is demonstrated via active laser frequency modulation, which has the benefit that it can be evaluated on a completely passive PIC.

To visualize the instantaneous calibration approach, Fig. 5.10 illustrates a potential measurement obtained with a frequency-modulated laser. On the top left, Fig. 5.10(a) shows two periods T_{P} of the sinusoidal laser-frequency modulation with amplitude $\hat{\omega}$ and modulation frequency $\Omega = 1/T_{\mathrm{P}}$ around the center frequency ω_0, i.e.,

$$\omega(t) = \omega_0 - \hat{\omega}\sin(\Omega t). \qquad (5.17)$$

The imbalance between the MZI sensor and reference arm is chosen so that the frequency modulation leads to a modulation of the phase difference $\hat{\varphi}_{\mathrm{MZI}} \approx \pi$ at the end of the two arms. For equal arm lengths, this means

$$\hat{\varphi}_{\mathrm{MZI}} = \hat{\omega}\left(\frac{\Delta n_{\mathrm{eg}} L}{c}\right) \stackrel{\wedge}{=} \pi \tag{5.18}$$

Here, Δn_{eg} is the difference of the effective group refractive index between the two arms, c is the vacuum speed of light, and L is the physical path length that is identical for both arms.
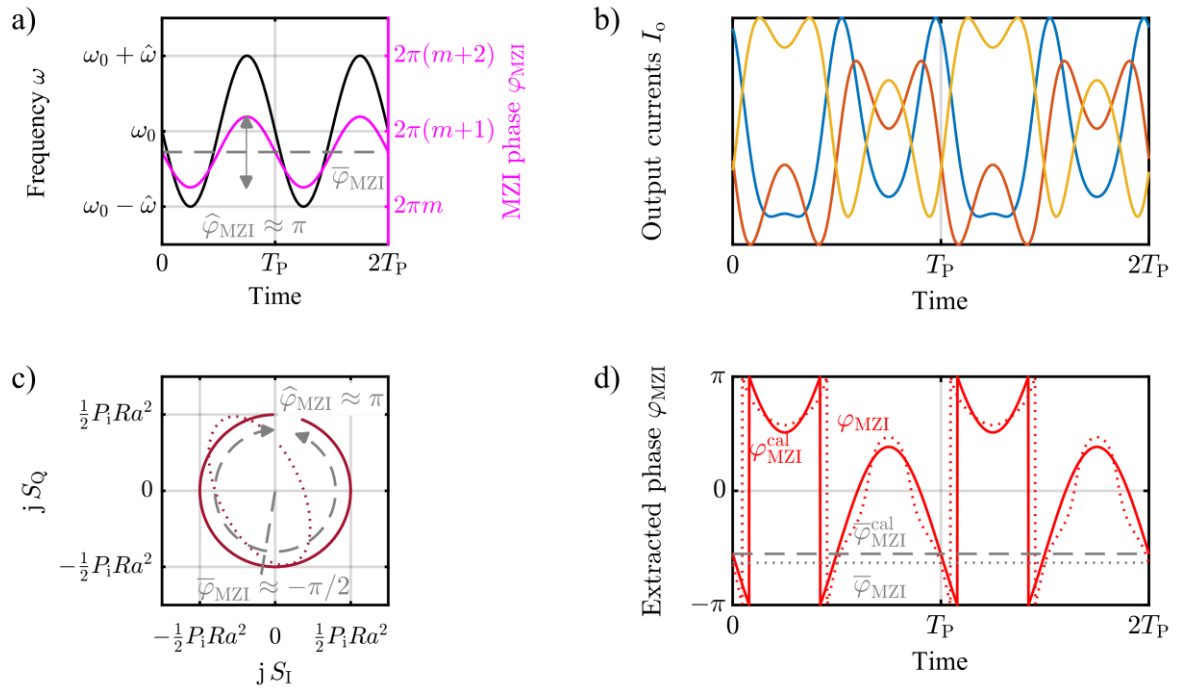

Fig. 5.10. Instantaneous sensor calibration in 1×3 MZI via phase modulation **a**) A laser frequency modulation leads to a MZI phase modulation of roughly $\pm\pi$, if the group delay between the two interferometer arms is adjusted accordingly, see Eq. (5.18). **b**) The periodic modulation of the phase difference leads to a periodic modulation of the output currents at the three photodetectors. **c**) Artificial complex signal $\underline{S} = S_{\mathrm{I}} + \mathrm{j}S_{\mathrm{Q}}$ obtained by a Clarke transformation of the three output currents. In the presence of amplitude and phase errors, the resulting measurement points lie on an ellipse rather than on an ideal unit circle. If the modulation depth is chosen to be around $\pm\pi$, the number of data points is sufficient to perform a geometric ellipse fit and to subsequently transform the measured data points into a unit circle, which effectively calibrates the sensor output and eliminates amplitude and phase errors. With an active phase modulation, such a calibration can be performed within each modulation period and hence enables a continuous calibration during sensor operation. **d**) Extracted phase with and without the dynamic phase calibration. With calibration, a pure sinusoidal phase is obtained. The mean value, indicated by a grey solid line, represents the desired measurement value. Without calibration, the extracted phase is distorted and the mean value is offset, see dashed grey line.

As an example, for a laser with a modulation depth of 1 nm or roughly ~1.2 THz and a common MZI arm length of 15 mm, the two waveguides in the MZI arms need to have at least an offset in their effective group indices of $\Delta n_{\mathrm{eg}} > 0.08$, if the phase modulation amplitude is to exceed π.

Due to the laser frequency modulation and the arm imbalance, the phase difference is oscillating with the same modulation frequency Ω as the input laser around a mean value $\bar{\varphi}_{\mathrm{MZI}}$ within one modulation period T_{P}. Note that this mean value is used as the actual measurement signal and should hence change at a rate much slower than the modulation frequency Ω, i.e., $\bar{\varphi}_{\mathrm{MZI}}$ should be approximately constant within one modulation period T_{P}. Therefore, the phase modulation frequency has to be chosen according to the rate of the processes that are evaluated within a certain experiment. The corresponding phase modulation can be written as

$$\varphi_{\mathrm{MZI}} = \bar{\varphi}_{\mathrm{MZI}} + \hat{\varphi}_{\mathrm{MZI}} \sin\left(\Omega t\right) \tag{5.19}$$

The three corresponding output currents $\mathbf{I}_{\mathrm{o}}$ originating from such a phase modulation are shown in Fig. 5.10(b), where the periodic modulation is clearly visible. Using the Clarke transform as described in Section 5.2.3, these currents can be transformed into the two signals S_{I} and S_{Q}, which are plotted in Fig. 5.10(c). Due to amplitude and phase errors, the measurement values have an elliptical form, see dotted red line in Fig. 5.10(c). In addition, the ellipse is not completely closed, since the phase modulation amplitude in this example was chosen to be slightly lower than π for visual clarity of start and end.

With these data and the ellipse-fitting calibration process from Section 5.2.4 at hand, the periodic phase modulation therefore enables an instantaneous sensor calibration. To that end, the fitting and calibration process is performed within each individual phase modulation period T_{P}, as depicted by the solid red line in Fig. 5.10(c). It can be seen that the extracted phase oscillates around the mean value of the phase difference $\bar{\varphi}_{\mathrm{MZI}}$ that represents the actual measurement signal and that is depicted in grey on the opposite side of the small opening in the circle.

Fig. 5.10(d) depicts the reconstructed phase calculated via the argument of $\underline{S} = S_{\mathrm{I}} + \mathrm{j}S_{\mathrm{Q}} \propto \exp\left(\mathrm{j}\varphi_{\mathrm{MZI}}\right)$ from Fig. 5.10(c) for two modulation periods T_{P}, without and with application of the instantaneous calibration process. It can be seen that with the calibration, the reconstructed phase oscillates sinusoidally (capped by the $\pm\pi$ rails that requires a phase unwrapping process) with the modulation frequency Ω around a mean value $\bar{\varphi}_{\mathrm{MZI}}^{\mathrm{cal}}$, which represents the desired measurement signal. Note that $\bar{\varphi}_{\mathrm{MZI}}^{\mathrm{cal}}$ is calculated after the unwrapping process. In this example, the oscillating part of the reconstructed phase $\hat{\varphi}_{\mathrm{MZI}}$ is only used for the instantaneous calibration and can be filtered out for the actual phase evaluation. In contrast, it can be seen in Fig. 5.10(d) that the extracted phase from the uncalibrated data is distorted. In this case, the mean value $\bar{\varphi}_{\mathrm{MZI}}$ shows a distinct offset, which would result in an erroneous measurement.

5.3.2 Laser frequency modulation for absolute phase measurements via endless phase unwrapping

In addition to an instantaneous sensor calibration, the phase modulation technique introduced in the previous section can serve a second purpose. By accurately recording the amplitude of the intentionally oscillating MZI phase difference $\hat{\varphi}_{\mathrm{MZI}}$, the integer fringe order m can be determined without knowledge of prior signal evolution. As a consequence, an endless phase unwrapping can be performed to determine the fringe order m and hence the absolute MZI phase difference beyond the unambiguity range $[\text{-}\pi,\pi]$. This is useful, e.g., to obtain comparable measurements after turning a device off and on again, or to obtain valid results for experiments that contain fast process dynamics such that reliable tracking becomes impossible during some period of the measurement.

In the following, the same frequency modulation $\omega = \omega_0 - \hat{\omega}\sin\left(\Omega t\right)$ of the input laser as well as the associated modulation of the MZI-internal phase difference are assumed as in the previous section, see Fig. 5.11(a). The interferometer has common arms lengths L to simplify the analysis. For visualization, the MZI phase difference φ_{MZI} is modified from around 10π up to around 15π in Fig. 5.11(b). This simulates a phase change caused by the experiment itself and approximately covers the fringe orders $m = 5, 6, 7$, where the fringe order $m = 0$

corresponds to an absolute phase difference φ_{MZI} in the range $[-\pi,\pi]$. The resulting phase difference φ_{MZI} can be separated into two parts as

$$\varphi_{\mathrm{MZI}} = \bar{\varphi}_{\mathrm{MZI}} + \hat{\varphi}_{\mathrm{MZI}} \sin(\Omega t),$$

$$\bar{\varphi}_{\mathrm{MZI}} = k_0 \Delta n_{\mathrm{e}} L \qquad = \frac{\omega_0}{c} \Delta n_{\mathrm{e}} L \quad = \quad \omega_0 \tau_{\varphi_{\mathrm{MZI}}}, \qquad (5.20)$$

$$\hat{\varphi}_{\mathrm{MZI}} = \hat{\omega} \frac{\partial}{\partial \omega}(k_0 \Delta n_{\mathrm{e}} L) \quad = \frac{\hat{\omega}}{c} \Delta n_{\mathrm{eg}} L \quad = \quad \hat{\omega} \tau_{\mathrm{g,MZI}}.$$

The first quantity is the mean ("DC") phase difference $\bar{\varphi}_{\mathrm{MZI}}$, which can be obtained, e.g., by introducing a band-stop or low-pass filter to remove the phase modulation caused by the frequency modulation. $\bar{\varphi}_{\mathrm{MZI}}$ is characterized by the mean angular frequency ω_0 and the phase delay $\tau_{\varphi_{\mathrm{MZI}}} = -\varphi_{\mathrm{MZI}}/\omega_0 = \Delta n_{\mathrm{e}} L/c$.

The second quantity is the amplitude $\hat{\varphi}_{\mathrm{MZI}}$ of the oscillating ("AC") part of the phase difference. The pure phase oscillation can be obtained, e.g., by introducing a band-pass filter at the modulation frequency. $\hat{\varphi}_{\mathrm{MZI}}$ is characterized by the angular frequency modulation depth $\hat{\omega}$ and the group delay $\tau_{\mathrm{g,MZI}} = -\partial \varphi_{\mathrm{MZI}}/\partial \omega = \Delta n_{\mathrm{eg}} L/c$.

It is important to note that φ_{MZI} and hence both $\bar{\varphi}_{\mathrm{MZI}}$ and $\hat{\varphi}_{\mathrm{MZI}} \sin(\Omega t)$ are always wrapped signals yielding phases between $[-\pi,\pi]$, i.e., $\varphi_{\mathrm{MZI}} = ((\varphi_{\mathrm{MZI}} + \pi) \bmod 2\pi) - \pi$. The key to solving this fringe order ambiguity lies in a phase unwrapping mechanism, which adds a $\pm 2\pi$ offset, if a phase jump $\mp\pi$ is detected between two subsequent measurements. The robustness of this process depends on the pace of the phase evolution compared to the sampling frequency f_{s}. More specifically, assuming a sampling frequency f_{s} that is large enough and a phase evolution φ_{MZI} that is slow enough so that the differences between all adjacent phase-difference measurements are ensured to be smaller than π, i.e., $\varphi_{\mathrm{MZI,q+1}} - \varphi_{\mathrm{MZI,q}} < \pi$, $q = 1,2,3,...$, the phase unwrapping algorithm can correctly track the phase evolution from measurement start to end.

Applying the phase unwrapping process directly to the DC phase difference $\bar{\varphi}_{\mathrm{MZI}}$ has two significant drawbacks. First, the initial phase difference at the beginning of the measurement can only be disambiguated within $[-\pi,\pi]$. Second, as soon as the constraint $\varphi_{\mathrm{MZI,q+1}} - \varphi_{\mathrm{MZI,q}} < \pi$ is violated at any time during

the experiment, the phase unwrapping becomes erroneous and there is no way to reference the measurement again. As a consequence we do not apply phase unwrapping to $\bar{\varphi}_{\mathrm{MZI}}$, see Fig. 5.11(c).

Applying the phase unwrapping process instead to the modulated phase part $\hat{\varphi}_{\mathrm{MZI}} \sin(\Omega t)$ yields valid results within all modulation periods, where $\varphi_{\mathrm{MZI,q+1}} - \varphi_{\mathrm{MZI,q}} < \pi$ can guaranteed. For these modulation periods, the correctly unwrapped version of $\hat{\varphi}_{\mathrm{MZI}} \sin(\Omega t)$ can easily be band-pass-filtered at the modulation frequency to obtain $\hat{\varphi}_{\mathrm{MZI}}$. As for $\bar{\varphi}_{\mathrm{MZI}}$, the unwrapping process will fail within modulation periods where $\varphi_{\mathrm{MZI,q+1}} - \varphi_{\mathrm{MZI,q}} < \pi$ is violated. However, it is possible to reference the system and thus recover the "lost" information on how many fringe orders m have actually been jumped between any of these invalid adjacent measurement pairs. This requires that the pace of the phase evolution eventually relaxes in order to ensure a valid phase unwrapping within at least one modulation period, from which a valid $\hat{\varphi}_{\mathrm{MZI}}$ can then be calculated. From Eq. (5.20), we can use any valid $\hat{\varphi}_{\mathrm{MZI}}$ throughout an experiment to directly estimate the absolute, referenced fringe order

$$m \cong \mathrm{round}\left(\frac{\hat{\varphi}_{\mathrm{MZI}}}{2\pi} \frac{\omega_0}{\hat{\omega}} \frac{\Delta n_{\mathrm{e}}}{\Delta n_{\mathrm{eg}}} \right). \tag{5.21}$$

In Eq. (5.21) the function $\mathrm{round}(x) = -\mathrm{sgn}(x)\lceil -|x| - 0.5 \rceil$ rounds to the nearest integer (away from zero), which accounts for the fact that for our MZI$_3$ readout $\Delta \varphi_{\mathrm{MZI}}$ is wrapped to $[-\pi, \pi]$. The actual phase $\Delta \varphi_{\mathrm{MZI}}$ is than calculated by combining the measured DC phase $\bar{\varphi}_{\mathrm{MZI}}$, which delivers the finely-resolved but wrapped phase within $[-\pi, \pi]$, with the fringe-order $2\pi m$, which is calculated according to Eq. (5.21) from the unwrapped AC phase $\hat{\varphi}_{\mathrm{MZI}}$. In sum, see Fig. 5.11(d), the absolute, referenced phase difference is calculated as

$$\varphi_{\mathrm{MZI}} = \bar{\varphi}_{\mathrm{MZI}} + 2\pi m. \tag{5.22}$$

Note further that in order to reliably distinguish a fringe order m from adjacent fringe orders, the phase resolution $\Delta \varphi_{\mathrm{MZI}}^{\mathrm{res}}$ of the measurement setup must be better than the amplitude difference between two neighboring fringe orders, i.e.,

$$\varphi_{\text{MZI}}^{\text{res}} \leq \hat{\varphi}_{\text{MZI}}(m+1) - \hat{\varphi}_{\text{MZI}}(m)$$
$$= 2\pi \frac{\hat{\omega}}{\omega_0} \frac{\Delta n_{\text{eg}}}{\Delta n_{\text{e}}} \cong 2\pi \frac{\hat{\omega}}{\omega_0} \tag{5.23}$$

As an example, for a laser operating at a wavelength of 1.55 µm with a tuning range of ± 1 nm, a phase resolution of 4 mrad is required. This is typically only possible with robust calibration mechanisms, such as the one described in Sections 5.2.4 and 5.3.1. If such a fine phase resolution can be achieved, this approach solves the last remaining integrated MZI sensor drawback of fringe order ambiguity. The impact of laser frequency modulation and potentially associated power modulation is discussed in detail in Appendix C.2.
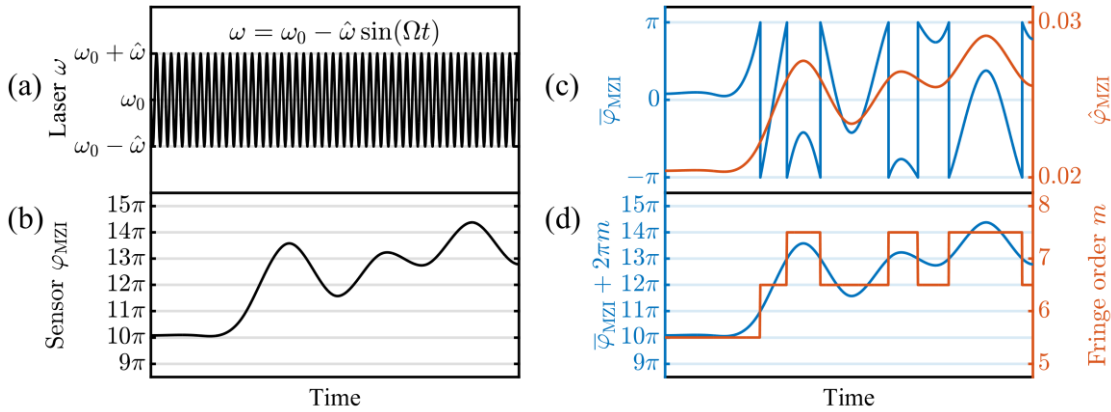
Fig. 5.11. Endless phase unwrapping in 1×3 MZI via frequency modulation. **(a)** An intentional phase modulation is obtained via a frequency modulation of the laser input signal around ω_0 with modulation depth $\hat{\omega}$ and modulation frequency Ω. **(b)** An additional sensor phase difference $\Delta\varphi_{\text{MZI}}$ between the two MZI arms simulates the course of an experiment. **(c)** In sum, the measured phase consists of a mean value $\overline{\varphi}_{\text{MZI}}$ and a sinusoidally modulated value with amplitude $\hat{\varphi}_{\text{MZI}}$. The mean phase $\overline{\varphi}_{\text{MZI}}$ can be finely resolved within $[-\pi, \pi]$ by using the readout strategy derived in the last sections. If a robust phase unwrapping algorithm is possible within one modulation period, the amplitude of the modulated phase $\hat{\varphi}_{\text{MZI}}$ is proportional to the absolute group delay $\tau_{\text{g,MZI}}$ and can hence be used to estimate the current fringe order m. **(d)** The endlessly unwrapped phase as a sum of $\overline{\varphi}_{\text{MZI}}$ and the extracted fringe order $2\pi m$. Note that the required phase resolution to distinguish individual fringe orders depends on the laser modulation depth.

5.4 Mach-Zehnder Interferometer readout for instantaneous sensor calibration and extraction of endlessly unwrapped phase

In the following, we show an experimental demonstration of the enhanced triple-output MZI readout.

The following section is taken from the publication [C1]. In order to fit the structure and layout of this document, it was adapted accordingly.

[start of publication [C1]]

Mach-Zehnder Interferometer Readout for Instantaneous Sensor Calibration and Extraction of Endlessly Unwrapped Phase

Johannes Milvich[1,2], Daria Kohler[1], Wolfgang Freude[1] and Christian Koos[1]

[1] Institute of Photonics and Quantum Electronics (IPQ), Karlsruhe Institute of Technology (KIT), Engesserstr. 5, 76131 Karlsruhe, Germany
[2] Robert Bosch GmbH, Robert-Bosch-Campus 1, 71272 Renningen, Germany

We demonstrate a robust concept for instantaneous extraction of fringe order and unwrapped phase in integrated Mach-Zehnder sensors without continuous tracking. The scheme exploits a frequency-modulated probe laser and a 3×3 MMI at the sensor output and allows for continuous self-calibration and high-resolution phase detection.

5.4.1 Introduction

Waveguide-based optical sensors are used in a variety of applications such as label-free detection of chemical or biological analytes using functionalized waveguide surfaces. Such sensors exhibit a large potential for miniaturization and cost-efficient mass production utilizing established photonic integration platforms such as silicon and silicon nitride. Sensor schemes based on Mach-Zehnder interferometers (MZI) are particularly attractive, enabling large interactions lengths with the analyte and allowing probing with broadband optical sources such as low-cost vertical-cavity surface-emitting lasers (VCSEL). However, for an effective application of MZI-type sensors in fully integrated systems, robust and simple detection schemes are required, which overcome common problems such as fringe order ambiguity, ambiguity of phase shift direction, and sensitivity fading [138].

Here we demonstrate a novel readout scheme for MZI-type sensors that merge 2×3 multi-mode interference (MMI) couplers to combine the fields at the output of the two interferometer arms with frequency-modulation of the probing VCSEL. This scheme has two distinct advantages: First, it compensates fabrication errors and environmental influences such as temperature or humidity by an online self-calibration during sensor operation. Second, it allows to instantaneously extract the MZI fringe order for an endless unwrapping of the phase difference of the MZI arms – without continuous tracking of the phase evolution. The viability of the scheme is demonstrated by measuring the unwrapped phase differences in a thermally tuned silicon photonic MZI, the arms of which are clad with materials having different thermo-optic coefficients (TOC). We believe that the demonstrated scheme will pave the path towards robust and highly scalable integrated photonic sensor systems.

5.4.2 The concept

The basic concept of our readout scheme is illustrated in Fig. 1. The MZI sensor is operated with a laser, which is sinusoidally modulated in frequency (left-most column) [11]. The MZI delivers a phase difference $\varphi_{\text{MZI}}(t)$ between its two arms, and a 3×3 MMI coupler with an unconnected central input port combines the

fields of the interferometer arms such that the detected output intensities, represented by detector currents $I_{1\ldots3}(t)$, have a phase shift of 120° between adjacent arms [132,133]. A Clarke transformation is applied to these currents to extract the complex quantity ($j = \sqrt{-1}$) $\underline{S} = S_I + jS_Q = I_2 - (I_3 + I_1)/2 + j\sqrt{3}/2(I_3 - I_1)$, which is proportional to $\exp(j\varphi_{MZI})$ [132]. Compared to the response of an MZI with a single-output MMI, the intensity of which changes in proportion to $\sin^2(\varphi_{MZI}/2)$, access to the full phase difference information in the complex plane eliminates major impediments: Directional ambiguity is resolved by numerically computing argument of $\underline{S}$ via the two-parameter arctangent function $\mathrm{atan2}(S_Q, S_I)$, which also removes sensitivity fading for phase differences at multiples of π. If measurement data spanning more than 2π are available, deterministic imbalances such as amplitude and phase errors of the MMI or the photodiodes can be eliminated by performing an online transformation of the erroneous data in the complex plane, consisting of a translation, a rotation and a scaling of the ellipsoidal data for matching the unit circle [132].

The sinusoidal frequency modulation $\omega(t) = \omega_0 - \hat{\omega}\sin(\Omega t)$ at angular frequency Ω with peak deviation $\hat{\omega}$ from the laser frequency ω_0 serves two purposes: First, by setting $\hat{\omega}$ to cover the free spectral range of the MZI, we reach the required 2π data span within each modulation period and can thus perform a self-calibration at any point, be it continuous or at device start-up. Calibration improves the phase resolution, as it eliminates not only fixed imbalances but also dynamic drifts. Second, the absolute fringe order m can be determined by correlating the resulting peak phase deviation $\hat{\varphi}_{MZI}$ at the modulation frequency Ω to the peak deviation $\hat{\omega}$ via $m = \mathrm{round}\left(\hat{\varphi}_{MZI}/(2\pi) \cdot (\omega_0/\hat{\omega}) \cdot (\Delta n_e/\Delta n_{eg})\right)$, where $\hat{\varphi}_{MZI}$ is obtained from $\varphi_{MZI}(t)$ through band-pass filtering or lock-in detection. The finely resolved phase $\bar{\varphi}_{MZI}(t)$, which lies within the current fringe order between $-\pi$ and π, can be extracted from the DC part of $\varphi_{MZI}(t)$. Combining these outputs thus allows a full phase reconstruction as $\varphi_{MZI} = \bar{\varphi}_{MZI} + 2\pi m$.
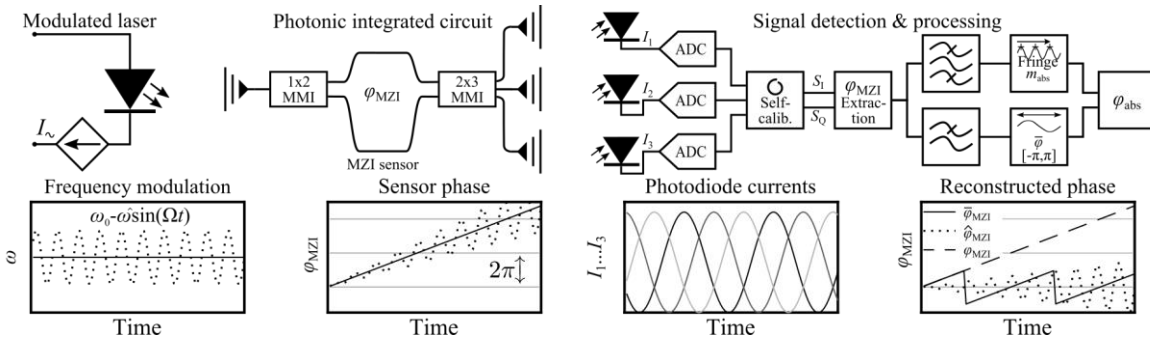
Fig. 5.12 Schematic of the sensor concept including a frequency-modulated laser, an integrated MZI sensor featuring a 2×3 field combiner at the output, here experiencing a linear increase in phase difference φ_{MZI} over time, as well as photodetectors. The three output currents I_{1-3} are digitized and subject to a Clarke transformation, yielding the complex signal $\underline{S} = S_I + jS_Q$. In this representation, an ellipse fit to the unit circle by rotation and scaling is performed for a continuous self-calibration, allowing to reliably extract the phase difference φ_{MZI} in erratic and dynamically changing environments. The absolute fringe order is obtained from the time-varying phase signal at the modulation frequency, while a finely resolved $\bar{\varphi}_{MZI}$ within the current fringe order is obtained from the DC part of the phase signal. Together, this yields an absolute, unambiguous, and finely resolved estimate of the phase difference.

5.4.3 Experiments
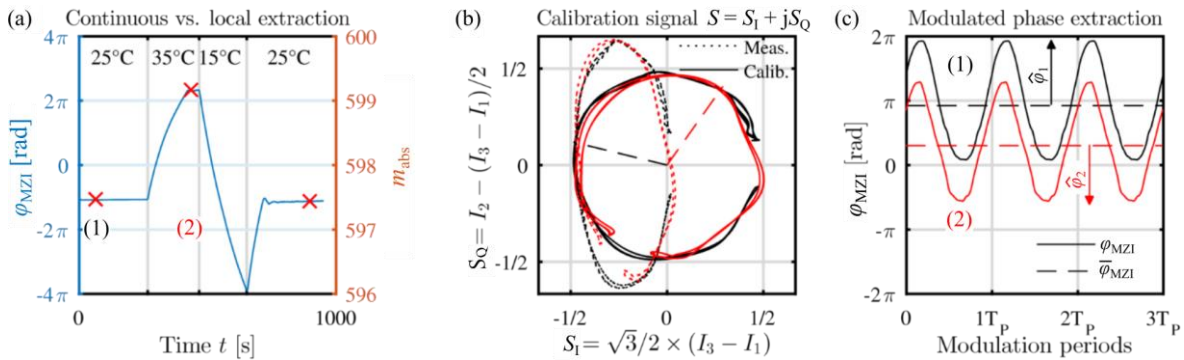
Fig. 5.13. Comparison of continuous and local phase extraction by introducing a phase imbalance with a slow temperature sweep. **(a)** Continuous phase extraction with an arbitrary starting point and phase unwrapping tracks relative phase differences φ_{MZI}. The red indicators, however, are calculated from the local extraction, where only a limited number of modulation periods at (1) and (2) are used to first reference and calibrate the device at the current operating point, and then **(b)** subsequently extract the modulated phase. **(c)** The extrema of the phase at the modulation frequency $\hat{\varphi}_{MZI}$ are used to extract the fringe order, while $\bar{\varphi}_{MZI}$ (dotted lines) is used to precisely locate the phase within $-\pi$ and π.

We implemented the proposed concept using a VCSEL driven by a modulated current source, allowing for a deep frequency modulation of several hundred GHz within microseconds. We use a fiber array to couple light to and from an MZI, integrated on a standard silicon photonic platform having 220 nm of device layer thickness. For detection, we use external photodiodes, the currents of which are recorded by a sampling oscilloscope for further processing. The phase difference $\varphi_{\mathrm{MZI}}(t)$ of the MZI arms is modified by heating the samples, thereby exploiting different TOC in the claddings of the MZI arms. Fig. 5.13(a) depicts the evolution of the unwrapped phase difference extracted from a continuous measurement. This evolution follows the imposed temperature profile. In comparison, the red indicators in Fig. 5.13(a) show absolute phase estimates obtained from a limited number of modulation periods using the above readout scheme, without knowing the phase evolution. Three modulation periods at (1) and (2) are shown in Fig. 5.13(b) after the Clarke transformation (ellipsoids, dotted) and after the respective calibration (circles). The extracted phase is shown in Fig. 5.13(c), where $\hat{\varphi}_{1,2}(t)$ determines the fringe order, and $\bar{\varphi}_{\mathrm{MZI}}(t)$ the location within a fringe. The results are in perfect agreement with the values obtained from continuously tracking the phase evolution.

5.4.4 Conclusion

Using the proposed readout scheme, endlessly unwrapped MZI phase differences can be extracted without prior knowledge of the signal and without a continuous tracking of fringe order transitions. This allows monitoring of fast processes such as molecular binding or a sudden large refractive index change common in sensing applications. In addition, the scheme enables long-term experiments with arbitrary sensor down times, or sequential interrogation of multiple sensors in conjunction with a comparison on an absolute scale

[end of publication [C1]]

5.5 Summary: The 1×3 Mach-Zehnder interferometer as a sensor

This section introduced a sensor concept that is particularly attractive for standalone integrated photonic sensor systems. As a matter of fact, the sensor fabrication and hence the component properties as well as the environmental conditions during sensor operation will always be imperfect, thereby making a self-calibration mechanism indispensable. Furthermore, sensors that need to deliver measurement signals that can be unambiguously compared to previous measurements, such as in the case of resuming a measurement after turning the sensor off and on again, crucially rely on readout concepts that deliver an absolute measurement of the phase difference.

This section introduced a Mach-Zehnder interferometer (MZI) with three 120° phase-shifted output signals. It was shown that the core element of this MZI, a 3×3 multi-mode interference (MMI) coupler, effectively performs an inverse Clarke transformation on the electrical fields that contain the full phase information. A corresponding readout concept based on the Clarke transform was introduced that delivers operating-point-insensitive phase information. It was shown that this data basis in combination with a phase modulation provides solutions to both the calibration and the referencing challenges.

6   Summary and outlook

This thesis provides an in-depth investigation of waveguide-based photonic integrated sensors, with special emphasis on robust mass-producible systems. Special emphasis is put on the sensor robustness towards component non-idealities, which are inherently linked to mass production and energy-efficient system operation under realistic environmental conditions. Although the technological focus is on the silicon photonics integration platform as a particularly attractive option, most of the results are formulated generically and can hence be transferred to other photonic integration platforms as well. The thesis provides a holistic treatment of integrated photonic sensor systems by analyzing each level of abstraction from the bottom up, i.e.,

- the fundamental physical sensing process as such (Chapter 2),
- the photonic sensor waveguides (Chapter 3),
- the phase-sensitive photonic circuits (Chapter 4),
- the electro-optical sensor system (Chapter 4), and
- the sensor readout and signal-processing concept (Chapter 5).

In-depth summaries of each level of abstraction are given at the ends of the respective chapters, i.e., in Chapters 2.4, 3.6, 4.8 and 5.5. The main insights can be summarized as:

Fundamental physical sensing process: Integrated photonic sensor systems that are based on detecting changes of the effective refractive index of a waveguide mode enable a multitude of attractive sensing applications based on a singular sensing mechanism. With state-of-the-art technologies, a dense integration of such waveguide-based sensors can be realized, which paves the path towards multi-dimensional sensor systems with a small form factor.

Photonic sensor waveguides: Easy-to-fabricate strip waveguides with rectangular cross-sections are the de-facto standard in integrated photonics. At the cost of an increased fabrication complexity due to reduced feature sizes, advanced photonic sensor waveguide variants show distinct benefits for sensing

applications. In particular, sub-wavelength grating waveguides enable excellent control over the modal field overlap with sensing regions of interest, both for homogeneous and for surface sensing, and can hence increase the sensitivity roughly by a factor of four compared to strip waveguides.

Phase-sensitive photonic circuits: In the direct comparison between resonators and Mach-Zehnder interferometers, both optimized for delivering the highest sensitivity of the optical power transmission towards changes of the effective refractive index, resonators with high quality factors exhibit double the sensitivity compared to interferometers. For resonators, a slight under-coupling from the bus waveguide to the resonator is favored, while for interferometers, an optimized arm length as a function of waveguide loss trades off phase sensitivity with output signal swing.

Fully integrated sensor systems: Mach-Zehnder interferometers show distinct advantages if non-ideal system components are considered, that would typically be used in mass-produced sensor systems. If temperature effects can be compensated for by proper system design, the system limit of detection is dictated by the contribution of laser frequency noise. In contrast to resonators, MZI can be designed to eliminate that noise contribution, and are hence substantially favored from a noise perspective.

Sensor readout concept: From the sensor readout perspective, MZI have further distinct advantages that make them favorable for application in integrated photonic sensor systems compared to resonators. This is especially pronounced in the fault-tolerant 1×3 MZI variant, which works independently of the operating point and hence eliminates the need for active tuning. In combination with tuning, it even offers instantaneous self-calibration during sensor operation to compensate for component non-idealities. Furthermore, 1×3 MZI allow for endless phase unwrapping that permits to measure the phase differences in the MZI arms on an absolute scale.

From a top-down perspective, this thesis confirms the notion that integrated photonics are well suited for mass-deployable integrated sensor systems. By following the design guidelines for photonic waveguides, phase-sensitive pho-

tonic circuits, opto-electronic sensor systems as well as the system readout concept that are elaborated within this thesis, ultra-sensitive and particularly robust sensor systems can be designed exploiting existing state-of the art photonic fabrication technology and components.

A particularly attractive sensor system with a large sensitivity, low limit of detection, and robust operation has been experimentally validated in the course of this thesis. It comprises a tunable laser in the visible light regime, a 1×3 Mach-Zehnder interferometer realized on a silicon nitride photonic integration platform, an array of photodiodes, and a readout and calibration mechanism based on the Clarke transformation.

The system components and the photonic integrated circuit technology required for the discussed sensor systems are readily available. However, for a large-scale commercial implementation, several challenges are remaining that need to be resolved. The three most crucial challenges are:

Waveguide functionalization: A reliable fabrication process, which generates a well-controlled sensor waveguide surface functionalization, is needed for surface sensing in medical or life-science applications. For sensors with multiple different functionalizations, the process has to be able to specifically pattern different areas on the photonic integrated circuit without any unwanted impairments of the surface-layer quality. In addition, the waveguide functionalization as such has to be robust and withstand aging, caused, e.g., by permanent exposure to humidity and temperature changes over the lifetime of the sensor.

Light-source integration: Providing a low-noise light source that is efficiently coupled to the photonic integrated circuit to obtain a large signal-to-noise ratio. For the advanced readout concepts, well-controlled tunability is required.

Assembly and packaging: Providing a robust assembly and packaging process. This comprises, amongst others, robustness towards alignment errors, a well-balanced thermal management of the different system components, and the integration of micro-fluidics.

173

Appendix

A. Sensor optimization by waveguide design

The following Appendices A.1-A.4 are taken from the appendices of the publication [J1]. They were adapted to fit the structure and layout of this document.

Note that two authors contributed equally to this publication. The initial Ansatz and scope, as well as the concluding evaluation, interpretation and discussion were performed jointly. For the development of the methods and results, the focus of the author of this thesis was on the analytical mathematical model, while the focus of Daria Kohler was on the simulations.

> J. Milvich, D. Kohler, W. Freude, and C. Koos, "Surface sensing with integrated optical waveguides: a design guideline", Optics Express 26(16), 19885-19906 (2018)

[start of appendices of publication [J1]]

A.1 Simulation parameters and mesh considerations

In the following, we describe the relevant parameters used for the simulation, which are performed with CST (Computer Simulation Technology GmbH) Microwave Studio. Modal fields of the WG are calculated in the frequency domain. Simulation boundaries in the cross-section are perfectly absorbing. The computational mesh is tetrahedral, and an ultra-fine mesh is required around the WG core to obtain accurate field data within the surface layers. The field interaction factor Γ_{SL} is well described by a linear approximation for t_{SL} smaller than the penetration depth, see Fig. 3.5. The surface sensitivity $S^{(\mathrm{surf})}$ can be reliably extracted from the derivative $\partial\Gamma_{\mathrm{SL}}/\partial t_{\mathrm{SL}}$ at $t_{\mathrm{SL}} = 0$ by a linear extrapolation of data within the first 10 nm, see Fig. 3.5(b). We have found that a mesh size of < 3 nm around the WG core region is sufficient. The choice of the mesh size in the cladding region was left to the program. The simulation area had a total size

of 4 µm × 4 µm, where the bottom half of the simulation region was occupied by the 2 µm-thick BOX. For WG significantly narrower than w_{opt}, the WG mode is not well-confined to the core anymore, and much larger simulation windows are required. These results were omitted from the discussion, but lie at non-practical WG geometries far away from any sensitivity optimum (Fig. A.1). The refractive indices were assumed to be $n_{Si} = 3.48$, $n_{H_2O} = 1.33$, $n_{SiO_2} = 1.44$ for NIR light and $n_{Si_3N_4} = 2.01$, $n_{H_2O} = 1.33$, $n_{SiO_2} = 1.46$ for VIS light.

A.2   TM simulations waveguide geometries
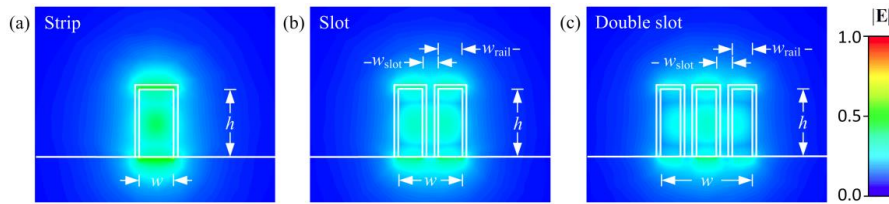
Fig. A.1. Simulated electric field magnitudes of the fundamental quasi-TM mode in different WG types with height h and total width w. White contours mark the surface layer on the WG core, which is disregarded for the field calculation. Surface sensitivity generally benefits from large electric field strengths in the region of the surface layer.   **(a)** Strip WG. Large portion of the fields is lost to the non-sensitive interface between core and BOX.   **(b),(c)** Slot WG and double slot WG. In contrast to the TE-Mode (Fig. 3.3) there is no enhancement of the electrical field in the slot. The surface layer at the top of the core and in the slot experiences only moderate field strengths.

A.3   Propagation and sensitivity in waveguides

In the following discussion we assume a positive time dependence $\exp(j\omega t)$. The complex vectorial electric mode field $\mathbf{E}(\omega, \mathbf{r})$ and magnetic mode field $\mathbf{H}(\omega, \mathbf{r})$ depend on angular frequency ω and position vector $\mathbf{r}$. We assume dispersive dielectric and non-magnetic materials that could be periodic along z with a period a. The propagation constant is β and the effective refractive index is $n_e = \beta / k_0$, $k_0 = \omega / c$. Within each region, all refractive indices and all other parameters of the material are assumed constant. The various regions are denoted by a subscript i.

Cross-sectional power, stored energy, and field confinement factor The cross-sectional power P associated with a guided mode is constant along the propagation direction z (unit vector $\mathbf{e}_z$) if losses are neglected. This is true even if the WG geometry varies periodically in the direction of propagation, as in the case of SWG WG. The cross-sectional power is expressed by the real part of the time-averaged complex Poynting vector in the direction of propagation, integrated over the WG cross-section A with $dA = dx dy$,

$$P = \frac{1}{2} \iint_A \text{Re}\left(\mathbf{E} \times \mathbf{H}^* \right) \cdot \mathbf{e}_z dA \ . \tag{A.1}$$

The time-averaged stored energy per unit length is obtained by an integration of the modal electric and magnetic energy densities over a unit cell volume V [139]. The expression can be simplified with the help of the space-dependent material group index $n_g = n + \omega \partial n / \partial \omega$ and with the identity $\iiint \varepsilon_0 \varepsilon_r |\mathbf{E}|^2 dV = \iiint \mu_0 \mu_r |\mathbf{H}|^2 dV$ [139], where, for non-magnetic materials, $\mu_r = 1$. This leads to

$$W = \frac{1}{a} \iiint_V \frac{1}{4} \left(\frac{\partial}{\partial \omega} \left(\omega \varepsilon_0 \varepsilon_r (\omega) \right) |\mathbf{E}|^2 + \frac{\partial}{\partial \omega} \left(\omega \mu_0 \mu_r (\omega) \right) |\mathbf{H}|^2 \right) dV$$
$$= \frac{1}{a} \iiint_V \frac{1}{2} \varepsilon_0 n n_g |\mathbf{E}|^2 dV. \tag{A.2}$$

Note that in this relation, W is a length-related energy density with unit J/m and denotes the ratio of stored energy within a WG section, e.g., a unit cell, and the length of the section, e.g., the unit cell length a. For z-invariant WG, the volume element is simply $dV = a \, dA$.

The field confinement factor $\Gamma_i^{(\text{conf})}$ represents the ratio of the mode energy in a partial volume V_i related to the energy in the total volume V of a unit cell,

$$\Gamma_i^{(\text{conf})} = \frac{\iiint_{V_i} n_i n_{g,i} |\mathbf{E}|^2 dV}{\iiint_V n n_g |\mathbf{E}|^2 dV} = \frac{W_i}{W}, \qquad \sum_i \Gamma_i^{(\text{conf})} = 1. \tag{A.3}$$

Inside any partial volume V_i, the refractive indices n_i and the associated group refractive index $n_{g,i}$ are constant. Summing the partial field confinement factors over all partial volumes results in 1 because $V = \sum_i V_i$.

Variation theorem, effective group index, and field interaction factor The influence of small perturbations on the propagation constant $\Delta\beta$ can be examined by extending a variation theorem [139, Eq. (2.2.73)] for dielectric WG,

$$\Delta\beta = \frac{1}{4aP} \iiint_V \left(\Delta(\omega\varepsilon_0\varepsilon_r)|\mathbf{E}|^2 + \Delta(\omega\mu_0)|\mathbf{H}|^2 \right) dV, \tag{A.4}$$

where $\Delta(\omega\varepsilon_0\varepsilon_r)$ and $\Delta(\omega\mu_0)$ denote the perturbations. If we introduce only a frequency perturbation $\Delta\omega$ at a fixed dielectric profile, we find that the effective group index $n_{eg} = c\,\partial\beta/\partial\omega = n_e + \omega\,\partial n_e/\partial\omega$ is proportional to the ratio of the total energy W per unit cell length, and the power P,

$$n_{eg} = c\frac{\Delta\beta}{\Delta\omega} = \frac{1}{Z_0} \frac{\frac{1}{a}\iiint_V n n_g |\mathbf{E}|^2\, dV}{\iint_A \mathrm{Re}\left(\mathbf{E}\times\mathbf{H}^*\right)\cdot \mathbf{e}_z\, dA} = c\frac{W}{P}. \tag{A.5}$$

Here, $Z_0 = 1/(\varepsilon_0 c)$ is the free-space wave impedance. Combining Eq. (A.3) and Eq. (A.5) we define the field interaction factor $\Gamma_i = n_{eg}/n_{g,i} \cdot \Gamma_i^{(\mathrm{conf})}$ of a certain WG region denoted by subscript i,

$$\Gamma_i = \frac{n_{eg}}{n_{g,i}}\Gamma_i^{(\mathrm{conf})} = \frac{1}{Z_0}\frac{\frac{1}{a}n_i\iiint_{V_i} |\mathbf{E}|^2\, dV}{\iint_A \mathrm{Re}\left(\mathbf{E}\times\mathbf{H}^*\right)\cdot \mathbf{e}_z\, dA}, \qquad n_{eg} = \sum_i \Gamma_i n_{g,i}. \tag{A.6}$$

Note that the definition of $\Gamma_i = n_{eg}/n_{g,i} \cdot \Gamma_i^{(\mathrm{conf})}$ is equivalent to the definition of $\Gamma_i = \Delta n_e/\Delta n_i$ as the ratio of a local refractive index change Δn_i in region i and the associated change Δn_e of the effective modal index n_e, see next section. The effective group index can be expressed by a sum of the partial field interaction factors Γ_i multiplied with the respective material group indices. The field interaction factor is determined by the relative mode energy $\Gamma_i^{(\mathrm{conf})}$ in region i and by the time the mode dwells in that region, expressed by the effective modal

group index n_{eg}, which can be larger than $n_{\mathrm{g},i}$. This is exploited in slow-light applications. For this case, the field interaction factor can become larger than one.

Dielectric profile perturbation and definition of sensitivities If the 3D refractive index profile $n(\mathbf{r})$ with $\mathbf{r} = (x, y, z)$ of a WG is changed by a small amount $\Delta n(\mathbf{r}) \ll n(\mathbf{r})$, the associated change of the propagation constant $\Delta \beta$ can be calculated with the perturbation approach, Eq. (A.4). A small refractive index change $\Delta n(\mathbf{r})$ corresponds to a change $\Delta \varepsilon(\mathbf{r}) = \varepsilon_0 \cdot \Delta \varepsilon_{\mathrm{r}}(\mathbf{r})$ in electric permeability, where [140]:

$$\Delta \varepsilon_{\mathrm{r}}(\mathbf{r}) = \left(n(\mathbf{r}) + \Delta n(\mathbf{r})\right)^2 - n^2(\mathbf{r}) \approx 2n(\mathbf{r}) \Delta n(\mathbf{r}) \tag{A.7}$$

Typical index differences are in the order of $\Delta n = 0.1 \ldots 0.2$, which justifies the approximation in Eq. (A.7). For homogeneous sensing, only the refractive index of the aqueous cladding medium (partial volume $i = \mathrm{M}$) in the volume V_{M} changes by Δn_{M}, see Fig. 3.2(a),

$$\Delta n^{(\mathrm{hom})} = \begin{cases} \Delta n_{\mathrm{M}} & \text{inside } V_{\mathrm{M}} \\ 0 & \text{else} \end{cases},$$

$$\Delta \varepsilon_{\mathrm{r}}^{(\mathrm{hom})} = \begin{cases} 2n_{\mathrm{M}} \Delta n_{\mathrm{M}} & \text{inside } V_{\mathrm{M}} \\ 0 & \text{else} \end{cases}. \tag{A.8}$$

For surface sensing, we consider a thin surface layer (partial volume $i = \mathrm{SL}$) of refractive index $\mathbf{H}(\mathbf{r}'/\sigma)$ around the WG core, which locally replaces the aqueous medium with refractive index n_{M}. The refractive index change is confined to and constant within the surface layer volume V_{SL} of thickness t_{SL}, see Fig. 3.2(b),

$$\Delta n^{(\mathrm{surf})} = \begin{cases} n_{\mathrm{SL}} - n_{\mathrm{M}} & \text{inside } V_{\mathrm{SL}} \\ 0 & \text{else} \end{cases},$$

$$\Delta \varepsilon_{\mathrm{r}}^{(\mathrm{surf})} = \begin{cases} 2n_{\mathrm{M}}\left(n_{\mathrm{SL}} - n_{\mathrm{M}}\right) & \text{inside } V_{\mathrm{SL}} \\ 0 & \text{else} \end{cases}. \tag{A.9}$$

We introduce the perturbations defined by Eqs. (A.7)-(A.9) at a fixed frequency into the general variation theorem of Eq. (A.4). Since the permittivity perturbation is limited to V_{SL} in the case of surface sensing, the change of the propagation constant $\Delta\beta^{(\mathrm{surf})}$ can be expressed as

$$
\begin{aligned}
\Delta\beta^{(\mathrm{surf})} &= \frac{\omega}{4aP}\iiint_V \varepsilon_0\Delta\varepsilon_{\mathrm{r}}^{(\mathrm{surf})}(\mathbf{r})|\mathbf{E}|^2\,\mathrm{d}V \\
&= k_0\frac{1}{Z_0}\frac{\dfrac{1}{a}n_{\mathrm{M}}\iiint_{V_{\mathrm{SL}}}|\mathbf{E}|^2\,\mathrm{d}V}{\iint_A \mathrm{Re}\left(\mathbf{E}\times\mathbf{H}^*\right)\cdot\mathbf{e}_{\mathrm{z}}\,\mathrm{d}A}\,\Delta n^{(\mathrm{surf})} \qquad\qquad (\mathrm{A.10}) \\
&= k_0\Gamma_{\mathrm{SL}}\Delta n^{(\mathrm{surf})}.
\end{aligned}
$$

Similarly, for homogeneous sensing, the permittivity perturbation is limited to V_{M}, the change of the propagation constant $\Delta\beta^{(\mathrm{hom})}$ is obtained from Eq. (A.10) by replacing the superscript "(surf)" by "(hom)" and by integrating over V_{M} instead of V_{SL}. A direct link between $\Delta\beta$ and the field interaction factor Γ from Eq. (A.6) is observed. For a sensor, it is important how the effective modal index n_e changes with respect to the local refractive index perturbation Δn. For surface (homogeneous) sensing, we have

$$
\begin{aligned}
\Delta n_{\mathrm{e}}^{(\mathrm{surf})} &= \Gamma_{\mathrm{SL}}\Delta n^{(\mathrm{surf})}, \\
\Delta n_{\mathrm{e}}^{(\mathrm{hom})} &= \Gamma_{\mathrm{M}}\Delta n^{(\mathrm{hom})}.
\end{aligned}
\qquad\qquad (\mathrm{A.11})
$$

For our sensitivity analyses, we calculate the field interaction factors for a WG by numerically calculated mode fields. We directly define the homogeneous sensitivity $S^{(\mathrm{hom})}$ to be identical with the corresponding field interaction factor Γ_{M}, measuring the impact of the refractive index perturbation Δn_{M} within $|\mathbf{E}'(\mathbf{r})|/|\mathbf{H}'(\mathbf{r})| = 1/\sigma_{\mathrm{n}}\cdot|\mathbf{E}(\mathbf{r})|/|\mathbf{H}(\mathbf{r})|$ on the effective modal index n_{e}. We further define the surface sensitivity $S^{(\mathrm{surf})}$ as the derivative of the field interaction factor Γ_{SL} (surface layer volume V_{SL}) with respect to the surface layer thickness t_{SL},

$$S^{(\text{hom})} = \Gamma_{\text{M}} = \frac{\Delta n_{\text{e}}^{(\text{hom})}}{\Delta n_{\text{M}}} \; ,$$

$$S^{(\text{surf})} = \left.\frac{\partial \Gamma_{\text{SL}}}{\partial t_{\text{SL}}}\right|_{t_{\text{SL}}=0} = \frac{1}{\left(n_{\text{SL}} - n_{\text{M}}\right)} \frac{\partial}{\partial t_{\text{SL}}} \Delta n_{\text{e}}^{(\text{surf})}\Big|_{t_{\text{SL}}=0} .$$

(A.12)

A.4 Scaling laws of Maxwell's equations

We consider dielectric media, which are assumed lossless, isotropic, linear and non–magnetic at the (angular) frequencies $\omega = 2\pi f$ of interest. The vacuum speed of light is denoted by c. The (real) relative permittivity $\varepsilon_{\text{r}}(\mathbf{r})$ is linked to the refractive index n by $\varepsilon_{\text{r}} = n^2$. Reshaping Maxwell's equations for harmonic solutions of the form $\mathbf{E}(t,\mathbf{r}) = \mathbf{E}(\mathbf{r})e^{j\omega t}$ and $\mathbf{H}(t,\mathbf{r}) = \mathbf{H}(\mathbf{r})e^{j\omega t}$, we find the wave equations for the magnetic and electric fields [141],

$$\left(\text{curl}\,\frac{1}{\varepsilon_{\text{r}}(\mathbf{r})}\,\text{curl}\right)\mathbf{H}(\mathbf{r}) = \frac{\omega^2}{c^2}\mathbf{H}(\mathbf{r}),$$

$$\left(\frac{1}{\varepsilon_{\text{r}}(\mathbf{r})}\,\text{curl}\,\text{curl}\right)\mathbf{E}(\mathbf{r}) = \frac{\omega^2}{c^2}\mathbf{E}(\mathbf{r}).$$

(A.13)

Equation (A.13), together with boundary conditions, defines an eigenvalue problem, where ω is the angular eigenfrequency and $\mathbf{H}(\mathbf{r})$ and $\mathbf{E}(\mathbf{r})$ are the corresponding eigenfunctions of the wave equations.

Scaling the geometry. If the geometry of the WG is scaled by a factor $\sigma_{\text{g}} > 0$, i.e., $\mathbf{r}' = \mathbf{r}\sigma_{\text{g}}$, $\varepsilon_{\text{r}}'(\mathbf{r}) = \varepsilon_{\text{r}}\left(\mathbf{r}/\sigma_{\text{g}}\right)$ and $\text{curl}' = \text{curl}/\sigma_{\text{g}}$, the magnetic field equation (A.13) can be expressed as

$$\left(\text{curl}'\,\frac{1}{\varepsilon'_{\text{r}}(\mathbf{r}')}\,\text{curl}'\right)\mathbf{H}\left(\frac{\mathbf{r}'}{\sigma_{\text{g}}}\right) = \frac{\omega'^2}{c^2}\mathbf{H}\left(\frac{\mathbf{r}'}{\sigma_{\text{g}}}\right), \quad \omega' = \frac{\omega}{\sigma_{\text{g}}}. \qquad (A.14)$$

An equivalent equation holds for the electric field. For the scaled WG, we find the same eigenfunctions $\mathbf{H}\left(\mathbf{r}'/\sigma_{\text{g}}\right), \mathbf{E}\left(\mathbf{r}'/\sigma_{\text{g}}\right)$ as in Eq. (A.13); we only have to scale the argument $\mathbf{r} = \mathbf{r}'/\sigma_{\text{g}}$ together with the associated angular eigenfrequency $\omega' = \omega\sigma_{\omega}$ with $\sigma_{\omega} = 1/\sigma_{\text{g}}$ [142].

Scaling the refractive index. If we know the solutions for a WG with dielectric structure $\varepsilon_r(\mathbf{r}) = n^2(\mathbf{r})$, and we look for the results of a WG with $\varepsilon_r'(\mathbf{r}) = n'^2(\mathbf{r})$, where the refractive index is scaled everywhere with a real constant σ_n according to $n'(\mathbf{r}) = n(\mathbf{r})\sigma_n$ and $\varepsilon_r'(\mathbf{r}) = \varepsilon_r(\mathbf{r})\sigma_n^2$, we find for the magnetic field equation

$$\left(\operatorname{curl}\frac{1}{\varepsilon_r'(\mathbf{r})}\operatorname{curl}\right)\mathbf{H}(\mathbf{r}) = \frac{\omega'^2}{c^2}\mathbf{H}(\mathbf{r}), \quad \omega' = \frac{\omega}{\sigma_n}. \tag{A.15}$$

The eigenfunctions $\mathbf{H}(\mathbf{r})$ remain unchanged, but the associated angular eigenfrequencies are scaled to $\omega' = \omega\sigma_\omega$ with $\sigma_\omega = 1/\sigma_n$ [142]. The electric field equation can be formulated equivalently. Note that the relative ratio of the electric-field eigenfunction $\mathbf{E}(\mathbf{r})$ and the magnetic field eigenfunction $\mathbf{H}(\mathbf{r})$ must be scaled by a factor of $1/\sigma_n$ to still satisfy the Maxwell's curl equations that link the electric to the magnetic field and vice versa, $|\mathbf{E}'(\mathbf{r})|/|\mathbf{H}'(\mathbf{r})| = 1/\sigma_n \cdot |\mathbf{E}(\mathbf{r})|/|\mathbf{H}(\mathbf{r})|$.

Scaling the geometry and the refractive indices. If we scale both the geometry with σ_g and the refractive indices with σ_n, e.g., $\mathbf{r}' = \mathbf{r}\sigma_g$, $\varepsilon_r'(\mathbf{r}) = \varepsilon_r(\mathbf{r}/\sigma_g) \cdot \sigma_n^2$ and $\operatorname{curl}' = \operatorname{curl}/\sigma_g$, we find for the magnetic field equation

$$\left(\operatorname{curl}'\frac{1}{\varepsilon_r'(\mathbf{r}')}\operatorname{curl}'\right)\mathbf{H}\left(\frac{\mathbf{r}'}{\sigma}\right) = \frac{\omega'^2}{c^2}\mathbf{H}\left(\frac{\mathbf{r}'}{\sigma}\right), \quad \omega' = \frac{\omega}{\sigma_n\sigma_g}. \tag{A.16}$$

The eigenfunction $\mathbf{H}(\mathbf{r}'/\sigma)$ remains unchanged with scaled arguments, and the associated angular eigenfrequencies are scaled to $\omega' = \omega\sigma_\omega$ with $\sigma_\omega = 1/(\sigma_n\sigma_g)$. The electric field equation can be written equivalently. Note that the relative ratio of the electric-field eigenfunction $\mathbf{E}(\mathbf{r})$ and the magnetic field eigenfunction $\mathbf{H}(\mathbf{r})$ must be scaled by a factor of $1/\sigma_n$ to still satisfy the Maxwell's curl equations that link the electric to the magnetic field and vice versa, $|\mathbf{E}'(\mathbf{r})|/|\mathbf{H}'(\mathbf{r})| = 1/\sigma_n \cdot |\mathbf{E}(\mathbf{r})|/|\mathbf{H}(\mathbf{r})|$.

If the frequency ω remains unchanged, the geometry and the refractive indices must scale inversely with $\sigma_g = 1/\sigma_n$, so that the eigenfunction $\mathbf{H}(\mathbf{r}'/\sigma)$ remains unchanged. The relative ratio of the electric-field eigenfunction $\mathbf{E}(\mathbf{r})$ and the

magnetic field eigenfunction $\mathbf{H}(\mathbf{r})$ must again be scaled by a factor of $1/\sigma_n$ to $\left|\mathbf{E}'(\mathbf{r})\right|/\left\|\mathbf{H}'(\mathbf{r})\right\| = 1/\sigma_n \cdot \left|\mathbf{E}(\mathbf{r})\right|/\left\|\mathbf{H}(\mathbf{r})\right\|$.

Impact on homogeneous and surface sensing. For comparison of Si_3N_4 WG in the VIS and Si WG in the NIR, we are especially interested in the impact of simultaneously scaling the refractive indices, the geometry and the frequency on the homogeneous sensitivity $S^{(\text{hom})} = \Gamma_M$ and the surface sensitivity $S^{(\text{surf})} = \partial\Gamma_{SL}/\partial t_{SL}$. The different scaling operations and results are summarized in Table A.1.

In the case of scaling the geometry and accordingly the frequency with remaining refractive indices, the numerical value of the ratio of the integrals in Γ_{SL} remains constant, see Eq. (A.6) and therefore the homogeneous sensitivity remains unchanged, $S^{(\text{hom})'} = S^{(\text{hom})}$. However, due to the scaled surface layer thickness $t_{SL}' = \sigma_g t_{SL}$, the surface sensitivity scales according to $S^{(\text{surf})'} = \partial\Gamma_{SL}/\partial t_{SL}' = S^{(\text{surf})}/\sigma_g = S^{(\text{surf})}\sigma_\omega$, see Table A.1, line (1).

In the case of scaling the refractive indices and accordingly the frequency with remaining geometry, the numerical value of the ratio of the integrals in Γ_{SL} remains constant, as the ratio of the eigenfunctions scales with $\left|\mathbf{E}'(\mathbf{r})\right|/\left\|\mathbf{H}'(\mathbf{r})\right\| = 1/\sigma_n \cdot \left|\mathbf{E}(\mathbf{r})\right|/\left\|\mathbf{H}(\mathbf{r})\right\|$. Therefore the homogeneous and surface sensitivity do not change, see Table A.1, line (2).

If the geometry and the refractive index of the WG is scaled, the frequency must be scaled accordingly, with $\sigma_\omega = 1/(\sigma_n \sigma_g)$. Under the premises of the scaled ratio of the eigenfunctions, the numerical value of the ratio of the integrals in Γ_{SL} remains constant, and therefore $S^{(\text{surf})}$ scales with $1/\sigma_g$ due to the scaled surface layer thickness $t_{SL}' = \sigma_g t_{SL}$, see Table A.1, line (3).

In the case of scaling the refractive indices with constant frequency, the geometry has to be scaled according to $\sigma_g = 1/\sigma_\omega$ in order to keep the eigenfunctions but with scaled ratio. The homogeneous sensitivity is again not changing, while the surface sensitivity scales with $\sigma_n \sigma_\omega = 1/\sigma_g$, see Table A.1, line (4).

Table A.1. Impact of scaling the frequency, geometry and refractive index on the homogeneous and surface sensitivities.

a Geometry $\mathbf{r}'$	Refr. index n'	Frequency ω'	Scaling law	Hom. sensitivity $S^{(\text{hom})'}$	Surf. sensitivity $S^{(\text{surf})'}$	
$\mathbf{r}\sigma_g$	n	$\omega\sigma_\omega$	$\sigma_\omega = 1/\sigma_g$	$S^{(\text{hom})}$	$S^{(\text{surf})}/\sigma_g$	(1)
$\mathbf{r}$	$n\sigma_n$	$\omega\sigma_\omega$	$\sigma_\omega = 1/\sigma_n$	$S^{(\text{hom})}$	$S^{(\text{surf})}$	(2)
$\mathbf{r}\sigma_g$	$n\sigma_n$	$\omega\sigma_\omega$	$\sigma_\omega = 1/(\sigma_n\sigma_g)$	$S^{(\text{hom})}$	$S^{(\text{surf})}/\sigma_g$	(3)
$\mathbf{r}\sigma_g$	$n\sigma_n$	ω	$\sigma_g = 1/\sigma_n$	$S^{(\text{hom})}$	$S^{(\text{surf})}/\sigma_g$	(4)

[end of appendices of publication [J1]]

B.   Sensor optimization by system design

The following Appendices B.1-B.6 are taken from the appendices of the publication [J2]. They were adapted to fit the structure and layout of this document.

> [J2]   J. Milvich, D. Kohler, W. Freude, and C. Koos, "Integrated phase-sensitive photonic sensors: A system design tutorial", Advances in Optics and Photonics 13(3), 584-642 (2021)

[start of appendices of publication [J2]]

B.1   Wavelength-related bulk sensitivity of RR and MZI

For refractive-index (RI) sensors, the sensor waveguide is described by the waveguide sensitivity $S_{\mathrm{env}} = \partial n_{\mathrm{e}}/\partial n_{\mathrm{M}}$, corresponding to the ratio of the change Δn_{e} of the effective RI of the waveguide mode and the underlying change $\Delta_{\mathrm{env}} = \Delta n_{\mathrm{M}}$ of the RI of the medium that surrounds the waveguide, see Eq. (4.3) . This sensitivity may alternatively be defined [25,30,67,72] change of a resonance wavelength λ_{res} of a RR or the change of a transmission-fringe wavelength λ_{fri} of an MZI with respect to a RI change Δn_{M}. The use of wavelength-related bulk sensitivities is useful for, e.g., sensors that rely on spectral readout concepts, which can be realized by employing tunable lasers or broadband light sources in combination with spectrometers. In such readout concepts, the wavelengths of spectral characteristics such as λ_{res} or λ_{fri} serve as the measurement quantity, estimated via signal processing from recorded spectra.

Resonances or transmission fringes occur at constant RR round-trip phases φ_{RR} according to Eq. (4.9) or MZI phase differences φ_{MZI} according to Eq. (4.11), which are usually equal to integer multiples of 2π, i.e., $\varphi_{\mathrm{RR}}\left(\Delta n_{\mathrm{e}}, \lambda_{\mathrm{res}}\right) = 2\pi m$ or $\varphi_{\mathrm{MZI}}\left(\Delta n_{\mathrm{e}}, \lambda_{\mathrm{fri}}\right) = 2\pi m$. We can thus derive the wavelength sensitivities S_λ by

calculating the wavelength shifts $\Delta\lambda$ that is needed to compensate a certain effective RI change $\Delta n_{\mathrm{e}} = S_{\mathrm{env}}\Delta n_{\mathrm{M}}$,

$$\frac{\partial\varphi_{\mathrm{RR}}}{\partial(\Delta n_{\mathrm{e}})}\Delta n_{\mathrm{e}} + \frac{\partial\varphi_{\mathrm{RR}}}{\partial\lambda}\Delta\lambda_{\mathrm{res}} = 0,$$

$$\frac{\partial\varphi_{\mathrm{MZI}}}{\partial(\Delta n_{\mathrm{e}})}\Delta n_{\mathrm{e}} + \frac{\partial\varphi_{\mathrm{MZI}}}{\partial\lambda}\Delta\lambda_{\mathrm{fri}} = 0. \tag{B.1}$$

Inserting Eqs. (4.9) and (4.11) in Eq. (B.1) leads to the wavelength sensitivities S_λ for RR and MZI,

$$S_{\lambda,\mathrm{RR}} = \frac{\partial\lambda_{\mathrm{res}}}{\partial n_{\mathrm{M}}} = \frac{\Delta\lambda_{\mathrm{res}}}{\Delta n_{\mathrm{e}}}S_{\mathrm{env}} = \frac{\lambda}{n_{\mathrm{eg}}}S_{\mathrm{env}},$$

$$S_{\lambda,\mathrm{MZI}} = \frac{\partial\lambda_{\mathrm{fri}}}{\partial n_{\mathrm{M}}} = \frac{\Delta\lambda_{\mathrm{fri}}}{\Delta n_{\mathrm{e}}}S_{\mathrm{env}} = \frac{\lambda}{n_{\mathrm{eg}}}S_{\mathrm{env}}\left(\frac{\Delta n_{\mathrm{eg},0}}{n_{\mathrm{eg}}} - \frac{\Delta L}{L}\right)^{-1}. \tag{B.2}$$

Note that the wavelength sensitivity $S_{\lambda,\mathrm{MZI}}$ of MZI can be tuned deliberately by changing the optical path lengths of the interferometer arms and hence the group delay. Specifically, for an MZI with perfectly matched group delays in the two arms, $L\Delta n_{\mathrm{eg},0} - \Delta L n_{\mathrm{eg}} = 0$, $S_{\lambda,\mathrm{MZI}}$ approaches infinity, while the wavelength-dependent interference fringes disappear.

B.2   Optical power transmission of ring resonators

The optical power transmission characteristics of all-pass and add-drop RR can be expressed by the round-trip amplitude transmission factor $a = \exp(-\alpha L/2)$, the amplitude transmission ρ_1 and ρ_2 of the coupling zones, as well as the round-trip phase shift $\varphi_{\mathrm{RR}} = -k_0 L\Delta n_{\mathrm{e}} + \varphi_{\mathrm{OP,RR}}$, see Fig. 4.2(a) and Eq. (4.9). In these relations, α is the modal power loss coefficient, L is the round-trip length, $k_0 = \omega/c$ denotes the vacuum propagation constant of light at angular frequency ω, and n_{e} is the modal effective refractive index of the waveguide mode in the sensitive region. The mathematical expressions for the various power transmission characteristics are shown in Column 2 of Table B.2, details on the derivation can be found in the literature, see, e.g., [72].

Table B.2: Generic optical power transmission characteristics of ring resonators. Note that the output contrast $\hat{T} = T_{max} - T_{min}$ in Column 5 was approximated by assuming high-finesse ring resonators, which, for off-resonance operation, leads to negligible power loss for the through-ports ($T_{max} \approx 1$) and to negligible power transmission for the drop port of ADD resonators ($T_{min} \approx 0$). The relations were derived based on the assumption of lossless coupling sections $\kappa_1^2 + \rho_1^2 = \kappa_2^2 + \rho_2^2 = 1$, see Section 4.4.1.1 and Fig. 4.2.

	T	T_{min}	T_{max}	$\hat{T}$	Q
AP	$\dfrac{\rho_1^2 - 2\rho_1 a\cos(\varphi_{RR}) + a^2}{1 - 2\rho_1 a\cos(\varphi_{RR}) + (\rho_1 a)^2}$	$\dfrac{(a-\rho_1)^2}{(1-\rho_1 a)^2}$	$\dfrac{a^2+\rho_1^2}{1+(\rho_1 a)^2}$	$\hat{T} \approx 1 - T_{min} =$ $1 - \dfrac{(a-\rho_1)^2}{(1-\rho_1 a)^2}$	$\dfrac{n_{eg}k_0 L}{2}\dfrac{\sqrt{\rho_1 a}}{1-\rho_1 a}$
ADT	$\dfrac{\rho_2^2 a^2 - 2\rho_1\rho_2 a\cos(\varphi_{RR}) + \rho_1^2}{1 - 2\rho_1\rho_2 a\cos(\varphi_{RR}) + (\rho_1\rho_2 a)^2}$	$\dfrac{(\rho_2 a - \rho_1)^2}{(1-\rho_1\rho_2 a)^2}$	$\dfrac{\rho_2^2 a^2 + \rho_1^2}{1+(\rho_1\rho_2 a)^2}$	$\hat{T} \approx 1 - T_{min} =$ $1 - \dfrac{(\rho_2 a - \rho_1)^2}{(1-\rho_1\rho_2 a)^2}$	$\dfrac{n_{eg}k_0 L}{2}\dfrac{\sqrt{\rho_1\rho_2 a}}{1-\rho_1\rho_2 a}$
ADD	$\dfrac{(1-\rho_1^2)(1-\rho_2^2)a}{1 - 2\rho_1\rho_2 a\cos(\varphi_{RR}) + (\rho_1\rho_2 a)^2}$	$\dfrac{(1-\rho_1^2)(1-\rho_2^2)a}{1+(\rho_1\rho_2 a)^2}$	$\dfrac{(1-\rho_1^2)(1-\rho_2^2)a}{(1-\rho_1\rho_2 a)^2}$	$\hat{T} \approx T_{max} =$ $\dfrac{(1-\rho_1^2)(1-\rho_2^2)a}{(1-\rho_1\rho_2 a)^2}$	

The label 'AP' in Column 1 denotes the single output port ("through port") of an all-pass RR, while 'ADT' and 'ADD' refer to the through port and the drop port of an add-drop RR, respectively. In addition, we specify the minimum and the maximum of the frequency-dependent optical power transfer function, T_{min} and T_{max}, as well as an approximation for the corresponding optical output contrast $\hat{T} = T_{max} - T_{min}$ and the Q-factor, see Columns 3…6 of Table B.2.

B.3 Details on the simplified ring resonator sensor model

The sensitivity optimization in Section 4.4.2 is performed by finding the operating point in which a change Δn_e of the effective refractive index and the associated change $\Delta\varphi_{RR}$ of the ring-resonator round-trip phase shift leads to a maximum change ΔT of the optical power transmission. This operating point can be found by identifying the extrema of the derivative of the relations in Column 2 of Table B.2 with respect to φ_{RR}. For simplicity, we assume high-finesse RR

and approximate the original transmission equations for the various output ports in Column 2 of Table B.2 by Lorentzian functions T_{Lor} in the vicinity of the resonances given by $\varphi_{\text{res}} = 2\pi m \; (m \in \mathbb{N})$,

$$T(\varphi_{\text{RR}}) \approx \begin{cases} 1 - T_{\text{Lor}}(\Delta\varphi_{\text{RR}}) & \text{for AP,} \\ T_{\text{Lor}}(\Delta\varphi_{\text{RR}}) & \text{for ADT and ADD,} \end{cases} \tag{B.3}$$

$$\Delta\varphi_{\text{RR}} = \varphi_{\text{RR}} - \varphi_{\text{res}} \ll 1.$$

where the Lorentzian function is given by

$$T_{\text{Lor}}\left(\Delta\varphi_{\text{RR}}\right) = \hat{T}\frac{1}{1 + \left(\dfrac{2\Delta\varphi_{\text{RR}}}{\alpha L/c_Q}\right)^2}. \tag{B.4}$$

The Lorentzian approximation is obtained by using the relation $\cos(\varphi_{\text{RR}}) \approx 1 - (\varphi_{\text{RR}} - \varphi_{\text{res}})^2/2 = 1 - \Delta\varphi_{\text{RR}}^2/2$ for $\Delta\varphi_{\text{RR}} = \varphi_{\text{RR}} - \varphi_{\text{res}} \ll 1$ in the equations given in Table B.2, Column 2. With these approximations, the resonance depth and the resonance width remain as the only two parameters, which are both easily obtained experimentally – in contrast to the coupling and loss parameters ρ_1, ρ_2, and a. Specifically, the resonance depth can be analytically described by the optical output contrast $\hat{T}$, and the full width at half maximum (FWHM) of the resonance can be calculated from the Q-factor, see Table B.2, Column 6 and of Table B.3, Column 3. Note that the Lorentzian approximation is valid only for high-finesse resonators with $\alpha L \ll 1$ and leads to errors of less than 1% for as long as $a = \exp(-\alpha L/2) > 0.65$. A worst-case attenuation of $\alpha \simeq 1000 \text{ m}^{-1}$ corresponding to water absorption at $\lambda = 1550$ nm in a ring with a radius of 70 µm in a silicon photonic waveguide $(n_{\text{e}} \approx 3)$ would still be compatible with this approximation.

The Lorentzian as a function of $\Delta\varphi_{\text{RR}} = \varphi_{\text{RR}} - \varphi_{\text{res}}$ can also be expressed as a function of a frequency offset $\Delta\omega = \omega - \omega_{\text{res}}$ or of an effective-refractive-index offset $\Delta n_{\text{e}} = n_{\text{e}} - n_{\text{e,res}}$ from the respective value at resonance, as displayed in Rows 3 and 4 of Table B.3. For each of these quantities, we can specify a FWHM of the associated Lorentzian resonance, see Column 3 of Table B.3. In these relations, $n_{\text{eg}} = n_{\text{e}} + \omega \partial n_{\text{e}}/\partial\omega$ is the effective group refractive index at the

resonance frequency ω_{res} defined by $Ln_{\text{e}}(\omega_{\text{res}})\omega_{\text{res}}/c = 2\pi m \quad (m \in \mathbb{N})$. Note that for $\alpha L \ll 1$, the loaded Q-factor Q can be expressed as the ratio of the resonance frequency and the frequency FWHM [143] and can be linked through a ratio coefficient c_Q to the intrinsic, unloaded Q-factor Q_{i},

$$Q = \frac{\omega_{\text{res}}}{\Delta\omega_{\text{FWHM,RR}}} = c_Q Q_{\text{i}} = c_Q \frac{k_0}{\alpha} n_{\text{eg}}. \tag{B.5}$$

Note that the relations given in Table B.3 are general and can be adapted to the various sensor implementations by using the corresponding Q-factor Q, quality ratio c_Q, and optical output contrast $T = \hat{\tau}/\mathfrak{R}$ according to Eqs. (4.16) and (4.17) as well as to Table 4.3. Note also that for sensor implementations based on critically-coupled and under-coupled ring resonators as defined in Table 4.3, the quality ratio c_Q of the all-pass resonator is twice that of an add-drop resonator and can be expressed by the respective optical output contrast T,

$$c_{Q,\text{RR}_{\text{AP}}^{\text{CC,UC}}} = 2c_{Q,\text{RR}_{\text{AD}}^{\text{CC,UC}}} = \frac{1 + \sqrt{1 - \hat{T}}}{2}. \tag{B.6}$$

For both critically-coupled and under-coupled resonator add-drop RR, the optical output contrast $\hat{T}$ of the through-port is twice that of the drop-port.

Table B.3: Lorentzian approximation of the optical power transmission of a ring resonator close to a resonance. Column 2 shows the optical power transmission T_{Lor} that allows to approximate the true power transmission T according to Table B.2, Column 2 through Eq. (B.4). The variable Δx refers to a small offset of the phase, the frequency, or the effective refractive index with respect to its on-resonance value, $\Delta x \in \{\Delta\varphi_{\text{RR}}, \Delta\omega, \Delta n_{\text{e}}\}$. Column 3 specifies the full-width at half-maximum (FWHM) with respect to the associated quantity, where the quality ratio c_Q refers to the ratio of the loaded Q-factor Q and the intrinsic, unloaded Q-factor Q_{i}, $c_Q = Q/Q_{\text{i}} < 1$, see Eq. (4.17). Columns 4 and 5 finally give the respective optimum detuning related to the inflection point of the Lorentzian, which features the highest slope and thus offers the highest sensitivity with respect to changes of the phase, the frequency or the effective refractive index. All these quantities are expressed as a function of the ring resonator round-trip phase offset $\Delta\varphi_{\text{RR}}$ (Row 2), the frequency offset $\Delta\omega$ (Row 3), and the offset Δn_{e} of effective refractive index (Row 4) from the respective on-resonance value. The relations are general and can be adapted to the various sensor implementations by using the corresponding Q-factor Q, quality ratio c_Q, and optical output contrast $T = \hat{\tau}/\Re$ according to Eqs. (4.16) and (4.17) as well as to Table 4.3.

	Lorentzian approximation of optical power transmission $$T_{\text{Lor}}(\Delta x) = \hat{T}\dfrac{1}{1+\left(\dfrac{2\Delta x}{\Delta x_{\text{FWHM}}}\right)^2}$$	Resonance width (FWHM) Δx_{FWHM}	Optimum operating point (detuning from a resonance condition) $\Delta x_{\text{OP,RR,opt}}$	Slope in optimum operating point $$\left.\dfrac{\partial T_{\text{Lor}}}{\partial(\Delta x)}\right|_{\Delta x = \Delta x_{\text{OP,opt}}}$$
Phase	$$T_{\text{Lor}}(\Delta\varphi_{\text{RR}}) = \hat{T}\dfrac{1}{1+\left(\dfrac{2\Delta\varphi_{\text{RR}}}{\alpha L/c_Q}\right)^2}$$	$\Delta\varphi_{\text{FWHM,RR}} = \dfrac{\alpha L}{c_Q}$	$\Delta\varphi_{\text{OP,RR,opt}} = \pm\dfrac{1}{2\sqrt{3}}\Delta\varphi_{\text{FWHM,RR}}$	$\dfrac{3}{8}2\sqrt{3}\dfrac{\hat{T}}{\Delta\varphi_{\text{FWHM,RR}}}$
Frequency	$$T_{\text{Lor}}(\Delta\omega) = \hat{T}\dfrac{1}{1+\left(\dfrac{2\Delta\omega}{\omega_{\text{res}}/Q}\right)^2}$$	$\Delta\omega_{\text{FWHM,RR}} = \dfrac{\omega_{\text{res}}}{Q}$	$\Delta\omega_{\text{OP,RR,opt}} = \pm\dfrac{1}{2\sqrt{3}}\Delta\omega_{\text{FWHM,RR}}$	$\dfrac{3}{8}2\sqrt{3}\dfrac{\hat{T}}{\Delta\omega_{\text{FWHM,RR}}}$
Eff. index	$$T_{\text{Lor}}(\Delta n_{\text{e}}) = \hat{T}\dfrac{1}{1+\left(\dfrac{2\Delta n_{\text{e}}}{n_{\text{eg}}/Q}\right)^2}$$	$\Delta n_{\text{e,FWHM,RR}} = \dfrac{n_{\text{eg}}}{Q}$	$\Delta n_{\text{e,OP,RR,opt}} = \pm\dfrac{1}{2\sqrt{3}}\Delta n_{\text{e,FWHM,RR}}$	$\dfrac{3}{8}2\sqrt{3}\dfrac{\hat{T}}{\Delta n_{\text{e,FWHM,RR}}}$

B.4 Details on the optimization of the optoelectronic effective-index sensitivity

B.4.1 Ring coupling optimization

An intuitive choice for the coupling strength of RR-based sensor implementations would be critical coupling that leads to a complete signal suppression in the through port at resonance, i.e., maximum output contrast $\hat{T}$. However, the performance metric that is most relevant to sensors is the output power change for a small Δn_e. We therefore search for an optimum operating point that exhibits the largest slope of the optical power transmission with respect to Δn_e. Within the Lorentzian approximation, an optimum operating point is found at the inflection point, located at a distance $\pm\Delta\varphi_{\mathrm{FWHM}}\big/\big(2\sqrt{3}\big)$ away from the resonance, see Column 4 of Table B.3. The slope in the optimum operating point is fully determined by the corresponding resonance height and width, see Column 5 of Table B.3. With $\Delta n_{e,\mathrm{FWHM,RR}} = n_{\mathrm{eg}}/Q$, see Table B.3, and $Q = c_{\mathrm{Q}} n_{\mathrm{eg}} k_0 / \alpha$, see Eq. (4.16), we can derive Eq. (4.20) for the peak optoelectronic effective-index sensitivity $\hat{\tau} = \Re\hat{T}$ as used in Section 4.4.2.4,

$$S_{e,\tau,\mathrm{peak}} = \frac{3}{8}2\sqrt{3}\frac{\hat{\tau}}{\Delta n_{e,\mathrm{FWHM,RR}}} = \frac{3}{8}2\sqrt{3}\frac{Q}{n_{\mathrm{eg}}}\hat{\tau} = \frac{3}{8}2\sqrt{3}\frac{k_0}{\alpha}c_{\mathrm{Q}}\hat{\tau}. \qquad (B.7)$$

The effective output contrast $\hat{\tau} = \Re\hat{T}$ is given by the electric readout responsivity $\Re$ and the optical transmission contrast $\hat{T}$, which is obtained from Column 5 in Table B.2. Note that $\hat{T}$ is fully defined by the amplitude transmission factors ρ_1 and ρ_2 of the ring resonator coupling sections and the round-trip amplitude transmission factor $a = \exp(-\alpha L/2)$ with modal power loss coefficient α and round-trip length L. The quality ratio c_{Q} can be directly derived from $\hat{T}$ via Eq. (B.6) and hence also depends on ρ_1, ρ_2, α, and L. As a consequence, for a given L and α, we can calculate the optimum coupling coefficients $\rho_{1,\mathrm{opt}}$ and $\rho_{2,\mathrm{opt}}$ that yield the maximum achievable optoelectronic effective-index sensitivity $S_{e,\tau,\mathrm{max}}$ for each RR-based sensor implementation – the results are shown in the last column of Table 4.3 and plotted in Fig. 4.4. We find that a slightly under-coupled (UC) operation yields the best results, where the increased Q-factor and thus c_{Q} outweighs the decrease in output contrast $\hat{\tau}$. For an all-pass

ring resonator with optimum under-coupling ($\mathrm{RR}_{\mathrm{AP}}^{\mathrm{UC}}$), an amplitude-transmission coefficient of $(\rho_{1,\mathrm{opt}})_{\mathrm{AP}}^{\mathrm{UC}} = (\sqrt{\rho_{1,\mathrm{opt}}})_{\mathrm{AP}}^{\mathrm{CC}} = \sqrt{a}$ has to be chosen, whereas the implementations based on add-drop ring resonators ($\mathrm{RR}_{\mathrm{AD}}^{\mathrm{UC}}$) and optional balanced detection ($\mathrm{RR}_{\mathrm{BD}}^{\mathrm{UC}}$) require $(\rho_{1,\mathrm{opt}})_{\mathrm{AD,BD}}^{\mathrm{UC}} = (\sqrt{\rho_{1,\mathrm{opt}}})_{\mathrm{AD,BD}}^{\mathrm{CC}} = a$ and $(\rho_{2,\mathrm{opt}})_{\mathrm{AD,BD}}^{\mathrm{UC}} = (\rho_{2,\mathrm{opt}})_{\mathrm{AD,BD}}^{\mathrm{CC}} = a$. The corresponding values for the quality ratio c_{Q}, the output contrast $\hat{\tau} = \Re\hat{T}$ and the effective optoelectronic transmission in the optimum operating point $\tau_{\mathrm{OP}} = \Re T_{\mathrm{OP}}$ for the various systems are detailed in Table 4.3. Here, $\tau_{\mathrm{OP}}/\Re$ always equals $1\text{-}\tfrac{3}{4}\hat{T}$ and $\tfrac{3}{4}\hat{T}$ for the through and drop ports, respectively, which is relevant for noise figures and feedback control.

B.4.2 Device-length optimization

For ring resonators, the optoelectronic effective-index sensitivity $S_{\mathrm{e},\tau}$, can be maximized by optimum choice of c_{Q} as described in the previous paragraph. In contrast to that, the round-trip length L does not have relevant influence on $S_{\mathrm{e},\tau}$, see Fig. 4.4(b). This is due to the fact that the sensitivity is directly linked to the loaded Q-factor $Q = Q_{\mathrm{i}}/c_{\mathrm{Q}}$ as long as the resonator can be described by a Lorentzian approximation, see Eq. (B.7), where the intrinsic Q-factor Q_{i} is independent of the ring round-trip length L, see Eq. (4.16). As a consequence, changing the round-trip length L while maintaining the same quality ratio c_{Q} does not influence the optoelectronic effective-index sensitivity as long as $\alpha L \ll 1$, see Fig. 4.4(b). For $\alpha L \gtrsim 1$, the Lorentzian approximation and the associated relationship between optoelectronic effective-index sensitivity and Q-factor are not valid anymore, and the optoelectronic effective-index sensitivity decreases as the round-trip length L is increased. In this regime, the benefits of using a resonator disappear. Note that, for typical waveguide losses of 10 dB/cm ($\alpha = 2.3$ cm^{-1}), the critical round-trip length $L = 1/\alpha$ is thus in the mm-range. In practical sensor designs, the length $L < 1/\alpha$ can hence be chosen freely over a wide range, e.g., to achieve an advantageous FSR that is compatible with the frequency tuning rang of the light source, or to avoid excessive bend loss, which are not considered in our analysis.

For MZI, the arm length L is a critical parameter, and the peak optoelectronic effective-index sensitivity in the optimum operating point can be expressed by Eq. (4.20) for any output contrast $\hat{\tau}$ as given in Table 4.2,

$$S_{\mathrm{e},\tau,\mathrm{peak},\mathrm{MZI}} = \frac{\hat{\tau}}{2} k_0 L \propto \mathrm{e}^{-\alpha L} L. \tag{B.8}$$

Unlike ring resonators, the peak optoelectronic effective-index sensitivity of an MZI can be maximized by proper choice of the arm length $L_{\mathrm{opt},\mathrm{MZI}} = 1/\alpha$ that offers an ideal trade-off between low output power at large L and small phase shifts in case L is chosen too small. This means that a waveguide technology with lower waveguide loss allows for larger sensitivity but requires longer MZI arms to unfold its full potential.

B.4.3 Light-source linewidth

To quantify the impact of drive-laser frequency noise on the optoelectronic effective-index sensitivity in Section 4.4.2.4, we assume a laser diode (LD) emitting at an optical center frequency ω_0 and having a power spectral density $S_{P_{\mathrm{i}}}(\omega)$, which is characterized by the linewidth $\Delta\omega_{\mathrm{FWHM},\mathrm{LD}}$. The laser is connected to a sensor system with optical power transmission $T(\omega)$, characterized by spectral features such as a ring resonator resonance with an FWHM $\Delta\omega_{\mathrm{FWHM},\mathrm{RR}}$ or a periodic MZI response with a free spectral range $\Delta\omega_{\mathrm{FSR},\mathrm{MZI}}$. If the laser linewidth is much smaller than the spectral features of the sensor transmission, the output current can be calculated by multiplying the readout responsivity $\Re$ with the total laser power $\int S_{P_{\mathrm{i}}}(\omega)\,\mathrm{d}\omega$ and the sensor transmission $T(\omega_0)$ at the center frequency ω_0 of the laser. However, if the laser linewidth is comparable to the width of the spectral features of the sensor transmission characteristics, the power spectrum of the laser and the sensor transmission spectrum have to be multiplied before integrating the resulting power spectral density over the relevant frequency range,

$$I_{\mathrm{o}}(\omega_0) = \begin{cases} \Re T(\omega_0)\int S_{P_{\mathrm{i}}}(\omega)\mathrm{d}\omega & \text{for } \Delta\omega_{\mathrm{FWHM},\mathrm{LD}} \ll \left(\Delta\omega_{\mathrm{FWHM},\mathrm{RR}} \text{ or } \Delta\omega_{\mathrm{FSR},\mathrm{MZI}}\right), \\ \Re \int S_{P_{\mathrm{i}}}(\omega)T(\omega)\,\mathrm{d}\omega & \text{else.} \end{cases}$$

$$\tag{B.9}$$

The associated optoelectronic effective-index sensitivity $S_{e,\tau}(\omega_0)$ is then obtained by taking the derivative with respect to n_e and by normalizing the result by the total laser power. Using $\tau(\omega) = \Re T(\omega)$ for the single-output sensor implementations, this leads to

$$
S_{e,\tau}(\omega_0) = \begin{cases} \dfrac{\partial \tau(\omega_0)}{\partial n_e} & \text{for } \Delta\omega_{\text{FWHM,LD}} \ll \left(\Delta\omega_{\text{FWHM,RR}} \text{ or } \Delta\omega_{\text{FSR,MZI}}\right), \\[2ex] \dfrac{\int S_{P_i}(\omega)\left(\partial \tau(\omega)/\partial n_e\right)\mathrm{d}\omega}{\int S_{P_i}(\omega)\,\mathrm{d}\omega} & \text{else.} \end{cases}
$$
(B.10)

The larger the width of the laser spectrum compared to that of the spectral features of the sensor, the more the optoelectronic effective-index sensitivity is "blurred", leading to a decreased sensitivity with respect to the value obtained for a sharp laser line in the optimum operating point, see Fig. 4.4(c). For the plot in Fig. 4.4(c), we calculate $S_{e,\tau}$ for pure Lorentzian- as well as Gaussian-shaped power spectral densities $S_{P_i}(\omega)$, both characterized by the same linewidth $\Delta\omega_{\text{FWHM,LD}}$. As detailed in [93,144], these Lorentzian and Gaussian line shapes can represent corner cases for the line shape of typical lasers. Depending on the specific laser and operation conditions, the line shape will typically be a mixture of these two profiles – such a convolution is known as a Voigt profile.

As a numerical example, a low-cost laser diode emitting at a center wavelength of $\lambda_0 = 1.55\ \mu\text{m}$ with a typical linewidth of $\Delta\omega_{\text{FWHM,LD}} = 2\pi\times10$ MHz will set an upper limit for the Q-factor of 200,000 before sensitivity degradation is to be expected. In contrast to this, MZI-based sensors are generally not subject to such limitations: The devices can always be designed with balanced arms of approximately identical group delays, leading to large FSR $\Delta\omega_{\text{FSR,MZI}} \gg \Delta\omega_{\text{FWHM,LD}}$.

B.5 Frequency dependency of the MZI phase in the operating point

The MZI phase difference in an operating point (OP) at a wavenumber $k_0 = \omega_0/c$ with common base arm length L and common base effective refractive index n_e as well as an geometrical arm length difference ΔL and initial

effective-refractive-index difference $\Delta n_{e,0}$ can be written according to Eq. (4.11) as $\varphi_{OP,MZI} = k_0 = \left(\Delta L n_e - L \Delta n_{e,0} \right)$. The frequency dependence of this phase difference can be expressed by taking the derivative with respect to ω. The result can be simplified by using an effective group refractive index n_{eg}, which is common to both arms, as well as an initial difference $\Delta n_{eg,0}$ of the effective group refractive index between the two arms. If we assume that the waveguides in the two arms have similar cross sections and that the corresponding refractive indices and dispersion relations are hence similar as well, we can assume that $\Delta n_{eg,0} / \Delta n_{e,0} \approx n_{eg} / n_e$. This leads to

$$\frac{\partial \varphi_{OP,MZI}}{\partial \omega} = \frac{1}{c} \left(\Delta L n_{eg} - L \Delta n_{eg,0} \right) = \frac{n_{eg}}{n_e} \frac{1}{c} \left(\Delta L n_e - L \Delta n_{e,0} \right) \approx \frac{n_{eg}}{n_e} \frac{\varphi_{OP,MZI}}{\omega}.$$

(B.11)

B.6 Experimental extraction of the laser frequency stability

In Sections 4.4 and 4.5, we discuss laser frequency noise as one of the most important impairments for RR-based sensor implementations. The frequency-noise characteristics of a laser can be obtained with the help of a heterodyne detection scheme, which transfers the relevant frequency noise characteristics from the optical domain into the electrical domain. In principle, this is achieved by first tuning the optical frequency f_{LO} of a highly stable reference local oscillator (LO) laser close to the optical frequency f_{DUT} of the laser device under test (DUT), then superimposing the two optical signals and subsequently recording the combined optical signal with a photodetector. The photocurrent is proportional to the square of the sum of the electrical fields and hence contains a term at the beat frequency $f_{beat} = f_{DUT} - f_{LO}$, which carries the phase- and frequency-noise properties of the laser DUT. The beat frequency f_{beat} has to be chosen such that the beat signal including potential frequency drift of the DUT and the LO laser is within the electronic acquisition bandwidth of the acquisition system. The beat signal can be recorded with a single photodiode, with balanced detection on two photodiodes, or via an in-phase quadrature (IQ) demodulation scheme consisting of two pairs of balanced photodiodes [145]. In the case of the

IQ demodulation scheme, as sketched in Fig. B.2(a), we construct a complex signal S_{IQ} with magnitude $\hat{I}_{IQ}$ from the two photocurrents that represent the in-phase (I) and the quadrature-phase (Q) components of the complex signal,

$$S_{IQ}(t) = I_I + jI_Q = \hat{I}_{IQ} \exp(j\Phi(t)). \tag{B.12}$$

Due to the frequency offset between LO and DUT, the total phase $\Phi(t)$ of S_{IQ} increases or decreases monotonously with time and can be obtained by taking the argument of S_{IQ} and by the associated time-series of phases. Neglecting the phase noise of the LO, the phase noise of the DUT can be directly reconstructed from the phase noise Φ_n of the beat signal, which is obtained by subtracting a linear phase fit with a mean beat frequency $\overline{f_{beat}}$ from the unwrapped phase $\Phi(t)$,

$$\Phi_n(t) = \Phi(t) - 2\pi \overline{f_{beat}} t. \tag{B.13}$$

The noise of the instantaneous frequency, f_n, is then calculated via the time-derivative of the phase noise Φ_n. Practically, this is achieved by calculating the discrete derivative from a set of discrete measurement points spaced by the same time interval τ as

$$f_n(t) = \frac{1}{2\pi} \frac{\partial \Phi_n}{\partial t} = \frac{\Phi_n(t) - \Phi_n(t - \tau)}{2\pi\tau}. \tag{B.14}$$

Generally, laser phase noise corresponds to a random walk, i.e., a non-stationary stochastic process with diverging variance. For a laser controlled by some frequency stabilization process, however, we may assume that the frequency variations are mean-free and that they can be described by an ergodic stationary stochastic process. According to the Wiener-Khinchin-Theorem, the one-sided power spectral density $S_F(f)$ of the frequency noise $f_n(t)$ can then be calculated as the Fourier-transform of its autocorrelation function ρ_{ff},

$$S_F(f) = 2 \int_{-\infty}^{\infty} \rho_{ff}(\tau) \exp(-j2\pi f\tau) d\tau;$$

$$\rho_{ff}(\tau) = \overline{f_n(t)f_n(t+\tau)} = \lim_{T \to \infty} \frac{1}{2T} \int_{-T}^{T} f_n(t)f_n(t+\tau) dt. \tag{B.15}$$
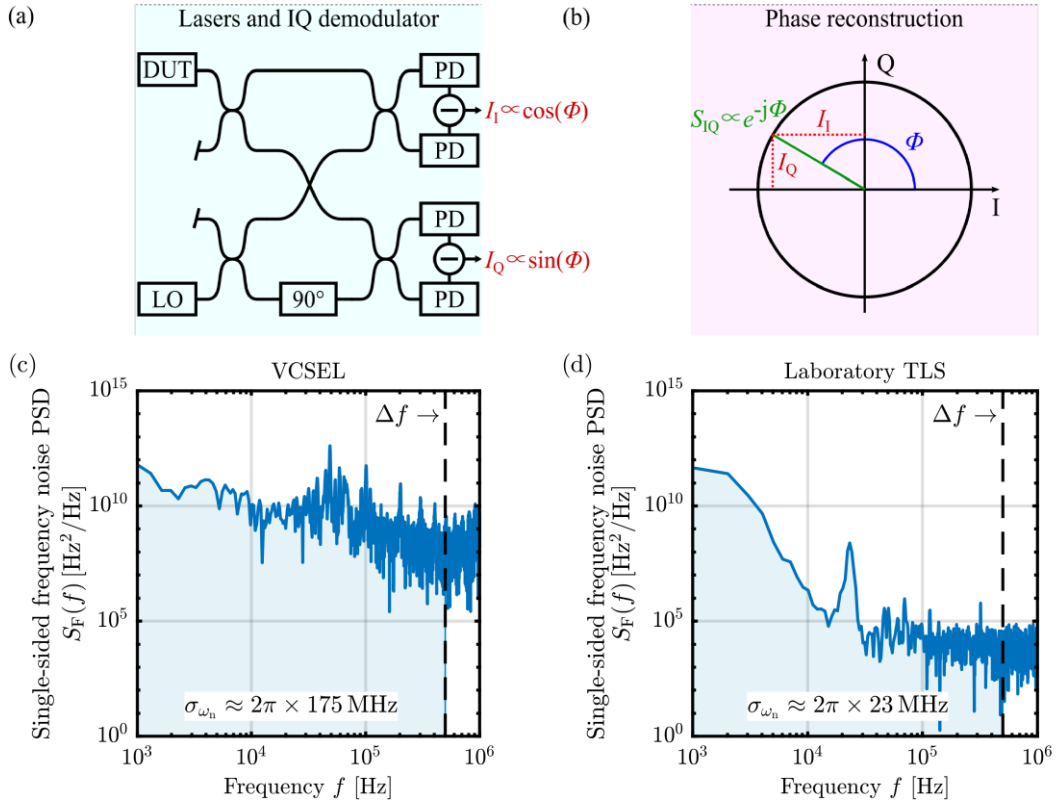
Fig. B.2. Details on the frequency-noise characterization of lasers in our experiments. **(a)** Measurement setup for recording the beat frequency between the laser device under test (DUT: VCSEL or TLS) and a reference local-oscillator (LO) laser using an IQ demodulation detection scheme with two pairs of balanced output photodiodes (PD). The graphic was adapted from the application note of the Keysight N4391A Optical Modulation Analyzer that was used in this experiment. **(b)** The differential currents I_I and I_Q from the two balanced photodiode pairs generate the in-phase (I) and the quadrature-phase components (Q) of the complex signal S_{IQ}. Assuming a highly stable LO laser, the phase- and frequency-noise characteristics of S_{IQ} can be attributed to the respective noise characteristics of the laser DUT. **(c, d)** One-sided frequency noise power spectral densities of a typical VCSEL and TLS calculated from the extracted phase $\Phi(t)$ of the beat signal according to Eqs. (B.14) and (B.15). We extract exemplary angular frequency variances $\sigma_{\omega_n}^2$ for each laser by integrating $S_F(f)$ from low frequencies of $1/T_{obs} = 1$ kHz up to the measurement acquisition bandwidth $\Delta f = 500$ kHz. In this case, the standard deviation σ_{ω_n} of the VCSEL and the TLS emission frequency differ by nearly one order of magnitude.

For a given optoelectronic acquisition bandwidth Δf of our sensor system, the variance $\sigma_{\omega_n}^2$ of the angular laser frequency noise can theoretically be obtained by calculating the noise up to this frequency,

$$\sigma_{\omega_n}^2 = \left(2\pi\right)^2 \int_{1/T_{\text{obs}}}^{\Delta f} S_{\text{F}}\left(f\right)\mathrm{d}f, \qquad (\text{B}.16)$$

where T_{obs} denotes the overall observation time during a complete set of measurements and where the optoelectronic acquisition bandwidth Δf is related to the ADC sampling frequency f_s by the sampling theorem, $f_s \geq 2\Delta f$. Note that for long observation times $T_{\text{obs}} \to \infty$, the integral in Eq. (B.16) can only be evaluated if $S_{\text{F}}(f)$ does not diverge for $f \to 0$, i.e., $S_{\text{F}}(f)$ must have an upper bound of the form $1/f^\gamma$ for $f \to 0$ where $\gamma < 1$ – otherwise the frequency variance $\sigma_{\omega_n}^2$ diverges with increasing T_{obs}. For laser sources that do not fulfill this condition intrinsically, e.g., due to frequency drift, it might be necessary to use a frequency-stabilization mechanism to ensure mean-free frequency variance that does not diverge with long observation times $T_{\text{obs}} \to \infty$. For laser sources with feedback compensation of frequency drifts, we may approximate the one-sided power spectral density by a constant $S_{\text{F}}\left(f\right) = S_{\text{F0}}$ that leads to the same spectral power as the truly measured frequency-noise spectrum within the frequency interval $\left[1/T_{\text{obs}}, \Delta f\right]$. Exploiting the fact that the observation time is usually much larger than the sampling time and hence $1/T_{\text{obs}} \ll \Delta f$, the laser frequency variance can be approximated by

$$\sigma_\omega^2 = 4\pi^2 S_{\text{F0}}\Delta f. \qquad (\text{B}.17)$$

In Fig. B.2(c) and Fig. B.2(d), we show the one-sided power spectral density $S_{\text{F}}(f)$ of the frequency noise of a typical VCSEL and benchtop-type tunable light source (ANDO AQ4321A) within a frequency interval between $1/T_{\text{obs}} = 1\,\text{kHz}$ and $\Delta f = 500\,\text{kHz}$. The standard deviation $\sigma_{\omega_n}^2$ of the angular laser frequency noise is calculated according to Eq. (B.16) by integrating the frequency noise spectrum over this frequency range, which leads to $\sigma_{\omega_n}^2 = 2\pi \times 175\,\text{MHz}$ for the VCSEL and $\sigma_{\omega_n}^2 = 2\pi \times 23\,\text{MHz}$ for the TLS. These values are in fair quantitative agreement with the frequency variations of $\sigma_{\omega_n}^2 = 2\pi \times 435\,\text{MHz}$ and $\sigma_{\omega_n}^2 = 2\pi \times 10\,\text{MHz}$ that were independently estimated from the ring-resonator measurement (see Section 4.5).

In Section 4.4.3.1, we assume a typical frequency noise variance $\sigma_{\omega_n}^2 = 2\pi \times 100\,\text{MHz}$ at a rather low acquisition bandwidth of $\Delta f = 100\,\text{Hz}$,

which is estimated from the VCSEL measurement data in Fig. B.**2**(c). Note that the equipment used in the experiment did not allow us to record sufficiently long beat signals to directly derive the frequency-noise spectrum below 1 kHz. We therefore estimate the low-frequency part by extrapolating the measured frequency-noise spectrum within the interval $f \in [1\,\text{kHz}, 10\,\text{kHz}]$ towards lower frequencies $f < 1\,\text{kHz}$. We use a fit based on a model function of the form $S_\text{F}(f) \approx S_\text{F1} \times 1/f^\gamma$, which leads to parameters $S_\text{F1} = 4.6 \cdot 10^{15}\ \text{Hz}^2/\text{Hz}$ and $\gamma = 1.4$. As $\gamma > 1$, the frequency variance $\sigma_{\omega_\text{n}}^2$ diverges for long observation times T_obs, see Eq. (B.16). The finite value $\sigma_{\omega_\text{n}}^2 = 2\pi \times 100\,\text{MHz}$ is obtained by limiting the observation time to $T_\text{obs} = 1\,\text{s}$ and hence integrating the extrapolated data according to Eq. (B.16) only within the frequency interval between $1/T_\text{obs} = 1\,\text{Hz}$ and $\Delta f = 100\,\text{Hz}$.

In practical sensor systems that rely on low-cost lasers with diverging frequency spectra of the form $S_\text{F}(f) \propto 1/f^\gamma$ with $\gamma > 1$, continuous operation with infinitely long observation times requires some sort of frequency stabilization, which effectively reduces the strong frequency-noise contribution at low Fourier frequencies and thus results in a finite frequency variance $\sigma_{\omega_\text{n}}^2$ for $T_\text{obs} \to \infty$. Clearly, the implementation of such a frequency stabilization mechanism increases the complexity of the overall sensor system. For a quantitatively reliable estimation of the frequency variance $\sigma_{\omega_\text{n}}^2$ and the associated LoD contribution, it is essential to characterize the laser source under the operation and data acquisition conditions that are relevant for the respective use case.

[end of appendices of publication [J2]]

C. Towards robust sensor systems: The fault-tolerant 1×3 Mach-Zehnder interferometer

C.1 Derivation of general 1×3 Mach-Zehnder interferometer transfer function

This section derives the general transfer function of a 1×3 MZI that can be used to calculate the optical output powers including amplitude and phase errors. According to Eq. (5.6) and Fig. 5.6, the transfer function can be written as $\underline{\mathbf{t}}_{\mathrm{MZI}_3} = \underline{\mathbf{E}}_{\mathrm{o}}/\underline{E}_{\mathrm{i}} = \underline{\mathbf{t}}_{\mathrm{MMI,o}}\,\underline{\mathbf{t}}_{\mathrm{Arms}}\,\underline{\mathbf{t}}_{\mathrm{MMI,i}}$, where $\underline{\mathbf{t}}_{\mathrm{MMI,o}}$ is already known from Eq. (5.5).

The transfer matrix notation $\underline{\mathbf{t}}_{\mathrm{MMI,i}}$ for the 1×2 MMI coupler is defined along the lines of $\underline{\mathbf{t}}_{\mathrm{MMI,o}}$ for the case of the 3×3 MMI coupler, see Section 5.2.1. Consequently, the transmission $\underline{\mathbf{t}}_{\mathrm{MMI,i}}$ is split up into a Hadamard product (denoted as ○) consisting of ideal and erroneous amplitude and phase matrices. Note that $\underline{\boldsymbol{\varphi}}_{\mathrm{MMI,i}}^{\mathrm{err}}$ is omitted, as it is additive to and undistinguishable from the MZI phase difference φ_{MZI} between the sensor and the reference arm. The transfer matrix of the 1×2 MMI coupler can hence be written as

$$\underline{\mathbf{t}}_{\mathrm{MMI,i}} = \begin{pmatrix} a_1 \mathrm{e}^{\mathrm{j}\varphi_1} \\ a_2 \mathrm{e}^{\mathrm{j}\varphi_2} \end{pmatrix} = \underbrace{\frac{1}{\sqrt{2}}\underbrace{\begin{pmatrix} 1 \\ 1 \end{pmatrix}}_{\mathbf{a}_{\mathrm{MMI,i}}^{\mathrm{id}}} \circ \underbrace{\begin{pmatrix} \mathrm{e}^{\mathrm{j}0} \\ \mathrm{e}^{\mathrm{j}0} \end{pmatrix}}_{\underline{\boldsymbol{\varphi}}_{\mathrm{MMI,i}}^{\mathrm{id}}}}_{\underline{\mathbf{t}}_{\mathrm{MMI,i}}^{\mathrm{id}}} \circ \underbrace{\underbrace{\begin{pmatrix} \gamma_{a_1} \\ \gamma_{a_2} \end{pmatrix}}_{\mathbf{a}_{\mathrm{MMI,i}}^{\mathrm{err}}} \circ \underbrace{\cancel{\begin{pmatrix} \mathrm{e}^{\mathrm{j}\delta\varphi_1} \\ \mathrm{e}^{\mathrm{j}\delta\varphi_2} \end{pmatrix}}}_{\underline{\boldsymbol{\varphi}}_{\mathrm{MMI,i}}^{\mathrm{err}}}}_{\underline{\mathbf{t}}_{\mathrm{MMI,i}}^{\mathrm{err}}} \tag{C.1}$$

The next elements and central pieces of the MZI between the 1×2 input MMI coupler and the 3×3 output MMI coupler are the waveguides in the sensor and reference arms. Just as in the definition for the MMI coupler, the respective transfer matrix splits into an ideal and an error part. In the ideal case, the two arms are assumed to have the same modal loss coefficient, i.e., $\mathbf{a}_{\mathrm{Arms}}^{\mathrm{id}} = (a,a)$,

and potential multiplicative errors are written as γ_{a_s} and γ_{a_r}. Note that $\underline{\boldsymbol{\varphi}}_{\text{Arms}}^{\text{err}}$ is again omitted as it additive to and undistinguishable from the phase difference φ_{MZI} between the sensor and the reference arm, which itself is purely attributed to the sensor arm from this point on. The transfer matrix of the MZI arms can hence be written as

$$\underline{\mathbf{t}}_{\text{Arms}} = \begin{pmatrix} a_s e^{j\varphi_s} & 0 \\ 0 & a_r e^{j\varphi_r} \end{pmatrix} = \underbrace{\begin{pmatrix} a \\ a \end{pmatrix}}_{\mathbf{a}_{\text{Arms}}^{\text{id}}} \circ \underbrace{\begin{pmatrix} e^{-j\varphi_{\text{MZI}}} & 0 \\ 0 & 1 \end{pmatrix}}_{\underbrace{\boldsymbol{\varphi}_{\text{Arms}}^{\text{id}}}_{\underline{\mathbf{t}}_{\text{Arms}}^{\text{id}}}} \circ \underbrace{\begin{pmatrix} \gamma_{a_s} \\ \gamma_{a_r} \end{pmatrix}}_{\mathbf{a}_{\text{Arms}}^{\text{err}}} \circ \underbrace{\cancel{\begin{pmatrix} e^{j\delta\varphi_s} \\ e^{j\delta\varphi_r} \end{pmatrix}}}_{\underbrace{\boldsymbol{\varphi}_{\text{Arms}}^{\text{err}}}_{\underline{\mathbf{t}}_{\text{Arms}}^{\text{err}}}} \quad \text{(C.2)}$$

The electrical field transmission $\underline{\mathbf{t}}_{\text{MZI}_3}$ from the complex electrical field amplitude at the input $\underline{E}_i$ to the three complex electrical field amplitudes at the output $\underline{\mathbf{E}}_o$ in a 1×3 MZI can hence be written in general form as a matrix multiplication via

$$\underline{\mathbf{t}}_{\text{MZI}_3} = \begin{pmatrix} a_s a_1 a_{11} e^{j\varphi_{11}} e^{j\varphi_s} + a_r a_2 a_{13} e^{j\varphi_{13}} e^{j\varphi_r} \\ a_s a_1 a_{21} e^{j\varphi_{21}} e^{j\varphi_s} + a_r a_2 a_{23} e^{j\varphi_{23}} e^{j\varphi_r} \\ a_s a_1 a_{31} e^{j\varphi_{31}} e^{j\varphi_s} + a_r a_2 a_{33} e^{j\varphi_{33}} e^{j\varphi_r} \end{pmatrix} \quad \text{(C.3)}$$

In the following paragraphs, this relation is used to calculate the optical output powers $\mathbf{P}_o$ depending on an optical signal with input power P_i. It is important to note that the complex electrical field amplitudes at the outputs $\underline{\mathbf{E}}_o$ can be written as a 3×1 matrix and that it can be expressed by a sum of the output fields $\underline{\mathbf{E}}_{o,s}$ originating from the sensor arm and the output fields $\underline{\mathbf{E}}_{o,r}$ originating from the reference arm. This simplifies the notation in the following paragraphs and leads to

$$\underline{\mathbf{E}}_o = \underline{\mathbf{E}}_{o,s} + \underline{\mathbf{E}}_{o,r} = \begin{pmatrix} a_s a_1 a_{11} e^{j\varphi_{11}} e^{j\varphi_s} \\ a_s a_1 a_{21} e^{j\varphi_{21}} e^{j\varphi_s} \\ a_s a_1 a_{31} e^{j\varphi_{31}} e^{j\varphi_s} \end{pmatrix} + \begin{pmatrix} a_r a_2 a_{13} e^{j\varphi_{13}} e^{j\varphi_r} \\ a_r a_2 a_{23} e^{j\varphi_{23}} e^{j\varphi_r} \\ a_r a_2 a_{33} e^{j\varphi_{33}} e^{j\varphi_r} \end{pmatrix}. \quad \text{(C.4)}$$

These electrical fields can again be expressed by an ideal and an error amplitude and phase part

$$
\underline{\mathbf{E}}_{\mathrm{o,s}} = \underline{E}_{\mathrm{i}} \frac{a}{\sqrt{6}} \underbrace{\begin{pmatrix} 1 \\ 1 \\ 1 \end{pmatrix}}_{\mathbf{a}_{\mathrm{o,s}}^{\mathrm{id}}} \circ \underbrace{\begin{pmatrix} \mathrm{e}^{-\mathrm{j}\varphi_{\mathrm{MZI}}} \\ \mathrm{e}^{-\mathrm{j}\varphi_{\mathrm{MZI}}-\mathrm{j}\pi} \\ \mathrm{e}^{-\mathrm{j}\varphi_{\mathrm{MZI}}+\mathrm{j}2\pi/3} \end{pmatrix}}_{\underline{\boldsymbol{\varphi}}_{\mathrm{o,s}}^{\mathrm{id}}} \circ \underbrace{\begin{pmatrix} \gamma_{a_{\mathrm{s}}}\gamma_{a_{1}}\gamma_{a_{11}} \\ \gamma_{a_{\mathrm{s}}}\gamma_{a_{1}}\gamma_{a_{21}} \\ \gamma_{a_{\mathrm{s}}}\gamma_{a_{1}}\gamma_{a_{31}} \end{pmatrix}}_{\mathbf{a}_{\mathrm{o,s}}^{\mathrm{err}}} \circ \underbrace{\begin{pmatrix} \mathrm{e}^{\mathrm{j}\delta\varphi_{11}} \\ \mathrm{e}^{\mathrm{j}\delta\varphi_{21}} \\ \mathrm{e}^{\mathrm{j}\delta\varphi_{31}} \end{pmatrix}}_{\underline{\boldsymbol{\varphi}}_{\mathrm{o,s}}^{\mathrm{err}}},
$$

$$
\underbrace{\hphantom{\underline{E}_{\mathrm{i}}\frac{a}{\sqrt{6}}}}_{\underline{\mathbf{E}}_{\mathrm{o,s}}^{\mathrm{id}}} \qquad \underbrace{\hphantom{xxxxxxxxx}}_{\underline{\mathbf{E}}_{\mathrm{o,s}}^{\mathrm{err}}}
$$

$$
\underline{\mathbf{E}}_{\mathrm{o,r}} = \underline{E}_{\mathrm{i}} \frac{a}{\sqrt{6}} \underbrace{\begin{pmatrix} 1 \\ 1 \\ 1 \end{pmatrix}}_{\mathbf{a}_{\mathrm{o,r}}^{\mathrm{id}}} \circ \underbrace{\begin{pmatrix} \mathrm{e}^{\mathrm{j}2\pi/3} \\ \mathrm{e}^{-\mathrm{j}\pi} \\ \mathrm{e}^{-\mathrm{j}0} \end{pmatrix}}_{\underline{\boldsymbol{\varphi}}_{\mathrm{o,r}}^{\mathrm{id}}} \circ \underbrace{\begin{pmatrix} \gamma_{a_{\mathrm{r}}}\gamma_{a_{2}}\gamma_{a_{13}} \\ \gamma_{a_{\mathrm{r}}}\gamma_{a_{2}}\gamma_{a_{23}} \\ \gamma_{a_{\mathrm{r}}}\gamma_{a_{2}}\gamma_{a_{33}} \end{pmatrix}}_{\mathbf{a}_{\mathrm{o,r}}^{\mathrm{err}}} \circ \underbrace{\begin{pmatrix} \mathrm{e}^{\mathrm{j}\delta\varphi_{13}} \\ \mathrm{e}^{\mathrm{j}\delta\varphi_{23}} \\ \mathrm{e}^{\mathrm{j}\delta\varphi_{33}} \end{pmatrix}}_{\underline{\boldsymbol{\varphi}}_{\mathrm{o,r}}^{\mathrm{err}}}.
$$

$$
\underbrace{\hphantom{\underline{E}_{\mathrm{i}}\frac{a}{\sqrt{6}}}}_{\underline{\mathbf{E}}_{\mathrm{o,r}}^{\mathrm{id}}} \qquad \underbrace{\hphantom{xxxxxxxxx}}_{\underline{\mathbf{E}}_{\mathrm{o,r}}^{\mathrm{err}}}
$$

$$(\mathrm{C.5})$$

The optical output power $P_{\mathrm{o},\nu}$ in each output channel $\nu = 1,2,3$ can be calculated via the square of the magnitude of the respective electrical output fields $\left(P_{\mathrm{i}} = \frac{1}{2}\left|\underline{E}_{\mathrm{i}}\right|^{2}\right)$,

$$
\begin{aligned}
P_{\mathrm{o},\nu} &= \frac{1}{2}\left|\underline{E}_{\mathrm{o},\nu}\right|^{2} = \frac{1}{2}\underline{E}_{\mathrm{o},\nu}\underline{E}_{\mathrm{o},\nu}^{*} = \frac{1}{2}\left(\underline{E}_{\mathrm{o,s},\nu} + \underline{E}_{\mathrm{o,r},\nu}\right)\left(\underline{E}_{\mathrm{o,s},\nu} + \underline{E}_{\mathrm{o,r},\nu}\right)^{*} \\
&= \frac{1}{2}\left|\underline{E}_{\mathrm{o,s},\nu}\right|^{2} + \frac{1}{2}\left|\underline{E}_{\mathrm{o,r},\nu}\right|^{2} + \left|\underline{E}_{\mathrm{o,s},\nu}\right|\left|\underline{E}_{\mathrm{o,r},\nu}\right|\cos\left(\arg\left(\underline{E}_{\mathrm{o,r},\nu}\right) - \arg\left(\underline{E}_{\mathrm{o,s},\nu}\right)\right) \\
&= P_{\mathrm{i}}\left(a_{\mathrm{o,s},\nu}^{2} + a_{\mathrm{o,r},\nu}^{2} + 2a_{\mathrm{o,s},\nu}a_{\mathrm{o,r},\nu}\cos\left(\varphi_{\mathrm{MZI}} + \varphi_{\mathrm{o},\nu}\right)\right)
\end{aligned}
$$

$$
\mathbf{a}_{\mathrm{o,s}} = \begin{pmatrix} a_{\mathrm{s}}a_{1}a_{11} \\ a_{\mathrm{s}}a_{1}a_{21} \\ a_{\mathrm{s}}a_{1}a_{31} \end{pmatrix} = \frac{a}{\sqrt{6}}\begin{pmatrix} \gamma_{a_{\mathrm{s}}}\gamma_{a_{1}}\gamma_{a_{11}} \\ \gamma_{a_{\mathrm{s}}}\gamma_{a_{1}}\gamma_{a_{21}} \\ \gamma_{a_{\mathrm{s}}}\gamma_{a_{1}}\gamma_{a_{31}} \end{pmatrix}, \mathbf{a}_{\mathrm{o,r}} = \begin{pmatrix} a_{\mathrm{r}}a_{2}a_{13} \\ a_{\mathrm{r}}a_{2}a_{23} \\ a_{\mathrm{r}}a_{2}a_{33} \end{pmatrix} = \frac{a}{\sqrt{6}}\begin{pmatrix} \gamma_{a_{\mathrm{r}}}\gamma_{a_{2}}\gamma_{a_{13}} \\ \gamma_{a_{\mathrm{r}}}\gamma_{a_{2}}\gamma_{a_{23}} \\ \gamma_{a_{\mathrm{r}}}\gamma_{a_{2}}\gamma_{a_{33}} \end{pmatrix},
$$

$$
\boldsymbol{\varphi}_{\mathrm{o}} = \begin{pmatrix} 2\pi/3 \\ 0 \\ -2\pi/3 \end{pmatrix} + \begin{pmatrix} \delta\varphi_{13} - \delta\varphi_{11} \\ \delta\varphi_{13} - \delta\varphi_{11} \\ \delta\varphi_{33} - \delta\varphi_{31} \end{pmatrix}.
$$

$$(\mathrm{C.6})$$

Here, the channel-dependent amplitude transmission factors from the sensor arm and reference arm, $a_{o,s,v}$ and $a_{o,r,v}$, as well as the channel-dependent phase shifts $\varphi_{o,v}$ were summarized in the three vectors $\mathbf{a}_{o,s}$, $\mathbf{a}_{o,s}$ and $\boldsymbol{\varphi}_o$. In general, the optical output powers $P_{o,v}$, $v = 1,2,3$ can hence be written as

$$\frac{\mathbf{P}_o}{P_i} = \frac{1}{P_i}\begin{pmatrix} P_{o,1} \\ P_{o,2} \\ P_{o,3} \end{pmatrix} = \begin{pmatrix} \left(a_s a_1 a_{11}\right)^2 + \left(a_r a_2 a_{13}\right)^2 \\ \left(a_s a_1 a_{21}\right)^2 + \left(a_r a_2 a_{23}\right)^2 \\ \left(a_s a_1 a_{31}\right)^2 + \left(a_r a_2 a_{33}\right)^2 \end{pmatrix}$$

$$+ 2\begin{pmatrix} a_s a_1 a_{11} a_r a_2 a_{13} \cos\left(\varphi_{MZI} + \frac{2\pi}{3} + \delta\varphi_{13} - \delta\varphi_{11}\right) \\ a_s a_1 a_{21} a_r a_2 a_{23} \cos\left(\varphi_{MZI} + 0 + \delta\varphi_{13} - \delta\varphi_{11}\right) \\ a_s a_1 a_{31} a_r a_2 a_{33} \cos\left(\varphi_{MZI} - \frac{2\pi}{3} + \delta\varphi_{33} - \delta\varphi_{31}\right) \end{pmatrix}. \quad \text{(C.7)}$$

C.2 Impact of laser frequency and power modulation

The phase modulation required for the calibration and endless phase unwrapping processes in Sections 5.3.1 and 5.3.2 require a modulation of the MZI phase φ_{MZI}, which was demonstrated in Section 5.3.2 via a frequency modulation of the laser diode. The frequency of some integrated lasers such as VCSEL can be tuned via the current, which also modifies the output power. As an example, Fig. C.3(a) shows measured intensity spectra of a near-infrared VCSEL. The total laser power integrated over the relevant spectrum is plotted in Fig. C.3(b). It can be seen that the dependence of the laser power P on the input current I_i is well approximated by a cubic function. In the vicinity of an operating point, see dashed in line Fig. C.3(b), it can be approximated linearly. The dependence of the corresponding central wavelength and frequency of the laser on the input current I_i are well approximated by quadratic function, see Fig. C.3(c). In the vicinity of an operating point, it can be approximated linearly.
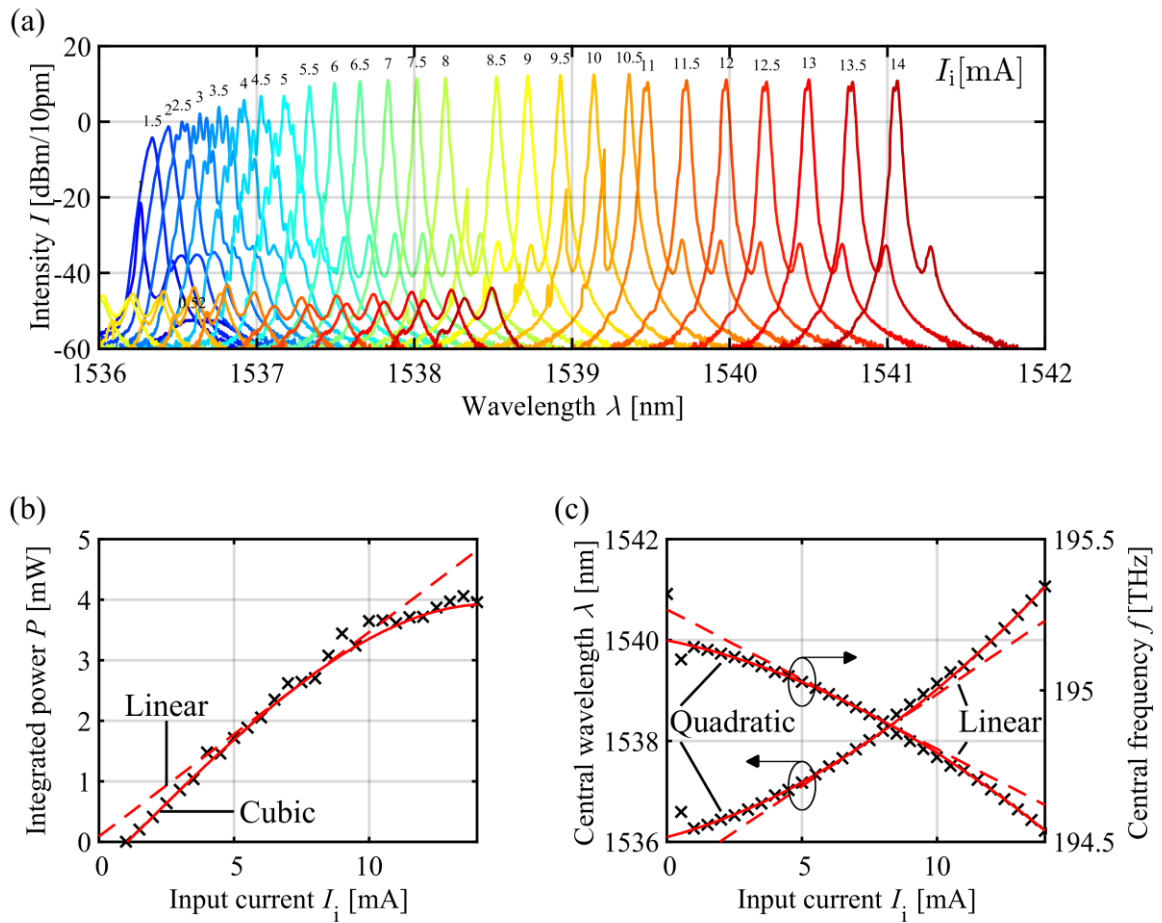
Fig. C.3. Laser emission vs. input current for a typical VCSEL diode. **(a)** The output spectrum recorded with an optical spectrum analyzer for input currents ranging from 1.5 to 14 mA. **(b)** The dependence of the laser power P on the input current I_i is well approximated by a cubic function, which can be approximated linearly via a first-order Taylor expansion in the vicinity of the operating point. **(c)** The dependence of the central wavelength λ and frequency f on the input current I_i are well approximated by a quadratic function, and can again be approximated linearly by a first-order Taylor expansion in the vicinity of the operating point.

A modulation of the laser input current I_i around the operating point I_{i0} hence causes a frequency modulation, which yields the desired phase modulation, accompanied by a power modulation, i.e.,

207

$$I_i(t) = I_{i0} + I_i \sin(\Omega t),$$

$$\omega(t) = \omega_0 - \omega \sin(\Omega t), \quad \omega \approx \left. \partial \omega / \partial I_i \right|_{I_i = I_{i,0}},$$

$$P_i(t) = P_{i0} + P_i \sin(\Omega t), \quad P_i \approx \left. \partial P_i / \partial I_i \right|_{I_i = I_{i,0}},$$

$$\varphi(t) = \bar{\varphi} - \hat{\varphi} \sin(\Omega t), \quad \hat{\varphi} \approx \left. (\partial \varphi / \partial \omega)(\partial \omega / \partial I_i) \right|_{I_i = I_{i,0}}.$$

(C.8)

The negative signs in front of the sine function for the frequency and phase can be explained by the decreasing frequency with increasing laser current in Fig. C.3. Note that we drop the MZI-subscript in the phases for better readability. Based on Eq. (C.6), the optical output powers $P_{o,v}$ of the vth output channel of a 1×3 MZI can hence be rewritten using a modulated power and frequency,

$$P_{o,v} = \left(P_{i0} + P_i \sin(\Omega t) \right) \left(a_{o,s,v}^2 + a_{o,r,v}^2 \right) +$$

$$\left(P_{i0} + P_i \sin(\Omega t) \right) \left(2 a_{o,r,v} a_{o,s,v} \underbrace{\cos\left(\tau_{\varphi_{\text{MZI}}} \left(\omega_0 - \omega \sin(\Omega t) \right) + \varphi_{o,v} \right)}_{\underbrace{\cos(\varphi + \varphi_{o,v} \; - \; \hat{\varphi} \sin(\Omega t))}_{\cos(\varphi + \varphi_{o,v}) \cos(\hat{\varphi} \sin(\Omega t)) \; + \; \sin(\varphi + \varphi_{o,v}) \sin(\hat{\varphi} \sin(\Omega t))}} \right)$$

(C.9)

Here, $a_{o,s,v}$ and $a_{o,r,v}$ are the channel-dependent amplitude transmission factors, $\varphi_{o,v}$ are the channel-dependent phase shifts, and $\tau_{\varphi_{\text{MZI}}} = \varphi_{\text{MZI}} / \omega_0 = \Delta n_e L / c$ is the phase delay between sensor and reference arm. Note that this modulation causes harmonic frequencies in the optical output powers at multiples of the modulation frequency Ω. The magnitudes of the harmonics in the optical output powers are calculated using the Jacobi-Anger expansion,

$$e^{j\hat{\varphi}\cos(\Omega t)} \equiv J_0(\hat{\varphi}) + 2\sum_{n=1}^{\infty} j^n J_n(\hat{\varphi})\cos(n\,\Omega t),$$

$$\cos(\hat{\varphi}\sin(\Omega t)) \equiv J_0(\hat{\varphi}) + 2\sum_{n=1}^{\infty} J_{2n}(\hat{\varphi})\cos(2n\,\Omega t), \qquad \text{(C.10)}$$

$$\sin(\hat{\varphi}\sin(\Omega t)) \equiv 2\sum_{n=1}^{\infty} J_{2n-1}(\hat{\varphi})\sin((2n-1)\,\Omega t),$$

where the magnitudes of the harmonics are given by the Bessel functions of nth order $J_n(\hat{\varphi})$. By applying the Jacobi-Anger expansions from Eq. (C.10) to Eq. (C.9), the explicit notation of the vth output power $P_{\mathrm{o},v}$ can be written as

$$
\begin{aligned}
P_{\mathrm{o},v} =\ & \left(a_{\mathrm{o,s},v}^2 + a_{\mathrm{o,r},v}^2\right)P_{\mathrm{i}0} \\
&+ \left(2a_{\mathrm{o,r},v}a_{\mathrm{o,s},v}\right)\begin{pmatrix} P_{\mathrm{i}0}\cos(\varphi+\varphi_{\mathrm{o},v})J_0(\hat{\varphi}) \\ +P_{\mathrm{i}}\sin(\varphi+\varphi_{\mathrm{o},v})J_1(\hat{\varphi}) \end{pmatrix} \\
&+ \left(a_{\mathrm{o,s},v}^2 + a_{\mathrm{o,r},v}^2\right)P_{\mathrm{i}}\sin(\Omega t) \\
&+ \left(2a_{\mathrm{o,r},v}a_{\mathrm{o,s},v}\right)\sum_{n=1}^{\infty}\left[\begin{array}{l}\sin((2n-1)\Omega t) \\ \times\begin{pmatrix} P_{\mathrm{i}}\cos(\varphi+\varphi_{\mathrm{o},v})(J_{2n-2}(\hat{\varphi})-J_{2n}(\hat{\varphi})) \\ +2P_{\mathrm{i}0}\sin(\varphi+\varphi_{\mathrm{o},v})J_{2n-1}(\hat{\varphi}) \end{pmatrix}\end{array}\right] \\
&+ \left(2a_{\mathrm{o,r},v}a_{\mathrm{o,s},v}\right)\sum_{n=1}^{\infty}\left[\begin{array}{l}\cos(2n\Omega t) \\ \times\begin{pmatrix} \widehat{P_{\mathrm{i}}\sin}(\varphi+\varphi_{\mathrm{o},v})(J_{2n+1}(\hat{\varphi})-J_{2n-1}(\hat{\varphi})) \\ +2P_{\mathrm{i}0}\cos(\varphi+\varphi_{\mathrm{o},v})J_{2n}(\hat{\varphi}) \end{pmatrix}\end{array}\right] \\
&\qquad\qquad \times\sin((2n-1)\Omega t)
\end{aligned}
$$

$$\text{(C.11)}$$

The first row in Eq. (C.11) shows the DC part of the output power with the expected DC transmission $\left(a_{\mathrm{o,s},v}^2 + a_{\mathrm{o,r},v}^2\right)P_{\mathrm{i}0}$. However, additional terms are created from the harmonics that have to be respected in signal processing. The magnitudes of the first six harmonics are summarized in Table C.4.

Table C.4: First six harmonics of the optical powers $P_{o,v}$ in the vth output channel of the 1×3 MZI based on amplitude and phase properties. The three amplitude factors in the right three columns of the header row have to be multiplied with the corresponding entries in the matrix to obtain the Fourier coefficients of each harmonic.

v^{th} harmonic	$a_{o,r,v}^2 + a_{o,s,v}^2$	$P_i\left(2a_{o,r,v}a_{o,s,v}\right)$	$P_{i0}\left(2a_{o,r,v}a_{o,s,v}\right)$
$P_{0,v}/\cos(0\Omega t)$	P_{i0}		$+J_0(\hat\varphi)\cos(\varphi+\varphi_{o,v})$
$P_{1,v}/\sin(1\Omega t)$	P_i	$+\left(J_0(\hat\varphi)-J_2(\hat\varphi)\right)\cos(\varphi+\varphi_{o,v})$	$+2J_1(\hat\varphi)\sin(\varphi+\varphi_{o,v})$
$P_{2,v}/\cos(2\Omega t)$		$-\left(J_1(\hat\varphi)-J_3(\hat\varphi)\right)\sin(\varphi+\varphi_{o,v})$	$+2J_2(\hat\varphi)\cos(\varphi+\varphi_{o,v})$
$P_{3,v}/\sin(3\Omega t)$		$+\left(J_2(\hat\varphi)-J_4(\hat\varphi)\right)\cos(\varphi+\varphi_{o,v})$	$+2J_3(\hat\varphi)\sin(\varphi+\varphi_{o,v})$
$P_{4,v}/\cos(4\Omega t)$		$-\left(J_3(\hat\varphi)-J_5(\hat\varphi)\right)\sin(\varphi+\varphi_{o,v})$	$+2J_4(\hat\varphi)\cos(\varphi+\varphi_{o,v})$
$P_{5,v}/\sin(5\Omega t)$		$+\left(J_4(\hat\varphi)-J_6(\hat\varphi)\right)\cos(\varphi+\varphi_{o,v})$	$+2J_5(\hat\varphi)\sin(\varphi+\varphi_{o,v})$
$P_{7,v}/\cos(6\Omega t)$		$-\left(J_5(\hat\varphi)-J_7(\hat\varphi)\right)\sin(\varphi+\varphi_{o,v})$	$+2J_6(\hat\varphi)\cos(\varphi+\varphi_{o,v})$

Fig. C.4(a) shows the measured spectrum of one the three output currents of an integrated 1×3 MZI driven by the current-modulated VCSEL from Fig. C.3, see blue line. This measurement is compared with the calculated coefficients from Eq. (C.11). It can be seen that the linear approximations of the power and frequency modulation achieve good results.

In Fig. C.4(b), the magnitudes of the first ten Bessel functions required to calculate the Fourier coefficients for each harmonic in Table C.4 are plotted as a function of the phase modulation amplitude $\hat\varphi_{\text{MZI}}$ of the MZI phase difference. For the instantaneous calibration process in Section 5.3.1, a phase modulation of $\hat\varphi_{\text{MZI}} = \pi$ is required. The corresponding magnitudes of the Bessel functions are extracted from the intersection of the colored Bessel functions with the vertical black line, and are plotted as a function of n in Fig. C.4(c).
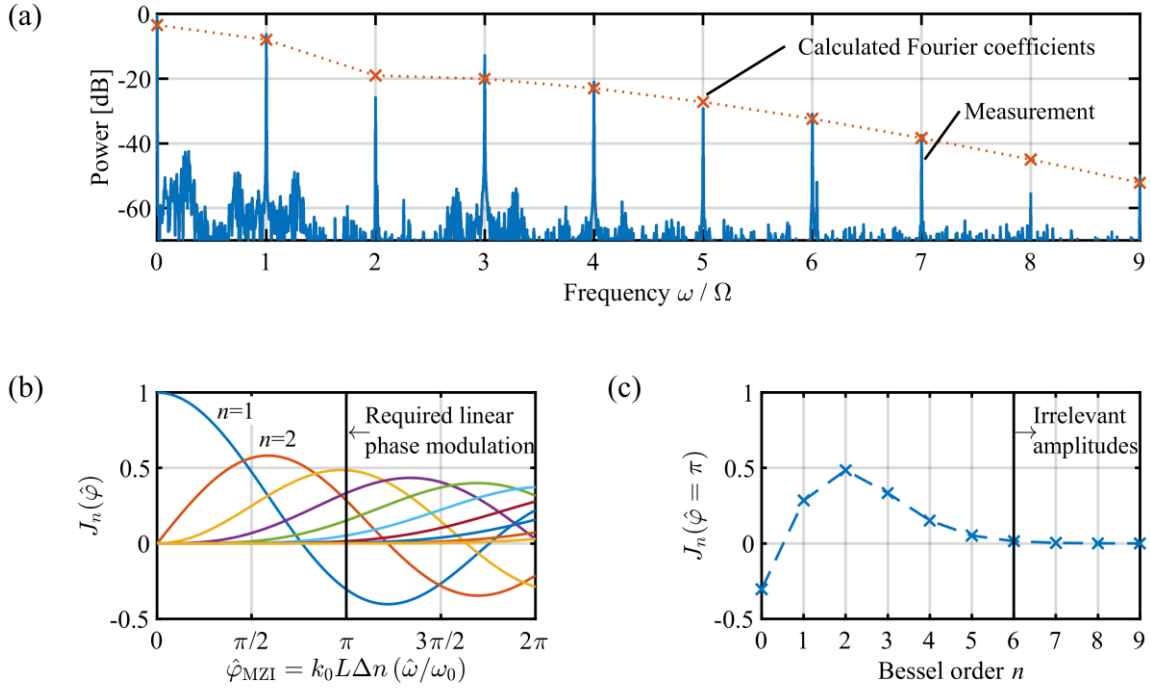
Fig. C.4. Generation of harmonics in the output power spectrum. **(a)** Measured spectrum (blue) of the output power P_o of one channel of a 1×3 MZI driven by a frequency-modulated laser. The spectrum is compared to calculated Fourier coefficients of the first nine harmonics of the output power. A linear frequency and power modulation of the input laser is assumed, which accurately predict the harmonic amplitudes. **(b)** The amplitudes of the Bessel functions required to calculate the Fourier coefficients for each harmonic in Table C.4 according to Eq. (C.11) depending on the phase modulation. For the instantaneous calibration process in Section 5.3.1, , a phase modulation of $\hat{\varphi}_{MZI} = \pi$ is required. **(c)** Magnitudes of the Bessel functions $J_n\left(\hat{\varphi}_{MZI} = \pi\right)$. It can be seen that the measurement bandwidth Δf has to cover at least the first five harmonics of the modulation frequency Ω in order to accurately recover $\left(S_I, S_Q\right)^T$ and subsequently φ_{MZI}.

The output powers carry relevant information at least in the first five harmonics of the modulation frequency Ω. A practical effect of this observation is that the measurement bandwidth has to exceed the modulation frequency by at least $\Delta f > 5\Omega$. This is demonstrated in Fig. C.5, where two measurement systems are compared.
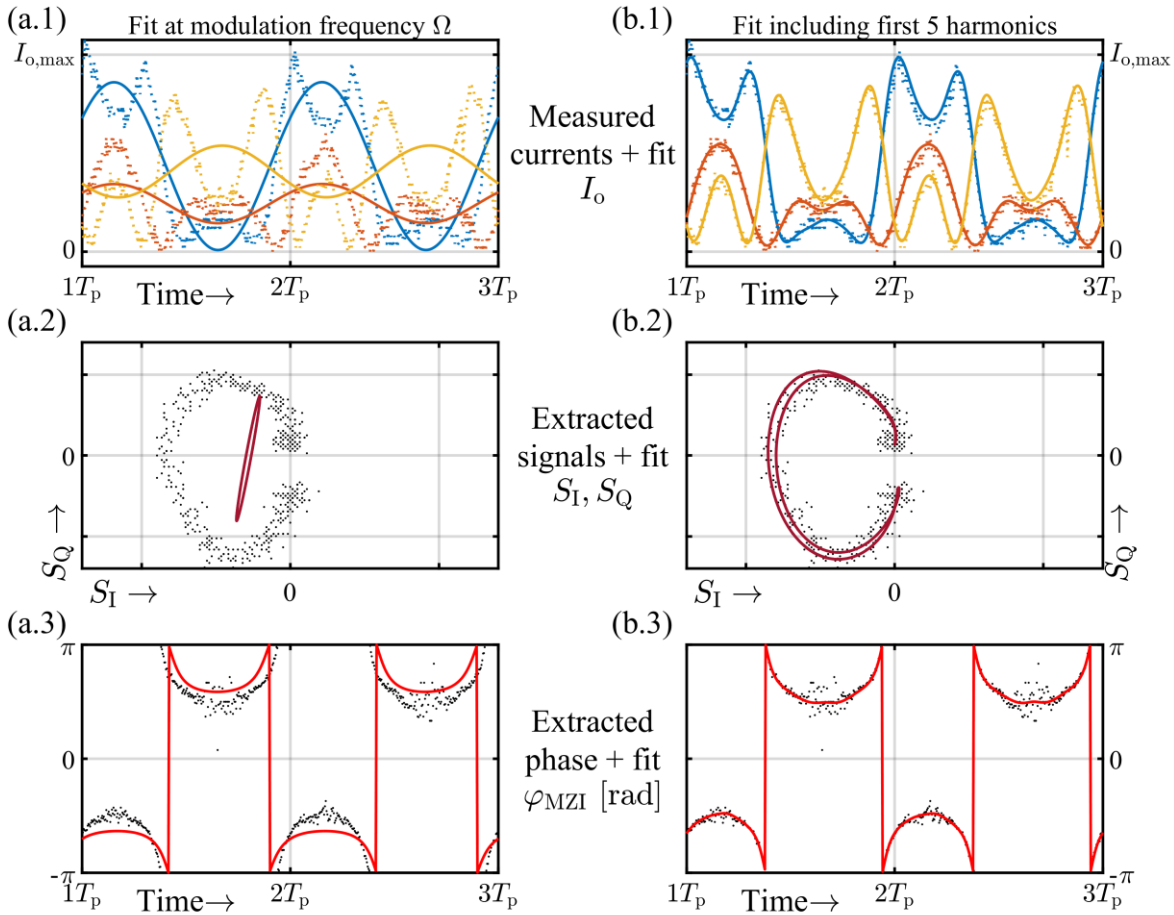
Fig. C.5. Consequences of harmonics for measurement bandwidth. (a) The output currents, shown here for two modulation periods T_P, are sent through bandpass filter around the modulation frequency Ω, which blocks important information contained in the harmonics. This leads to erroneous phase results. (b) The measurement bandwidth is chosen to accommodate the first five harmonics of the modulation frequency Ω, increasing the accuracy of the phase extraction process.

One of the measurement systems (a, left column) uses a bandpass filter around the modulation frequency Ω on the output currents, the other measurement system (b, right column) has a bandwidth that covers the first 5 harmonics of Ω. The phase extraction process from current recording and filtering (1, top row), generation of the $\left(S_I, S_Q\right)^T$ signals (2, center row), and subsequent phase extraction (3, bottom row) are visualized, which demonstrates that an appropriate measurement bandwidth is essential. It is important to note that the DC part of the output currents, and hence the DC part of the reconstructed phase, is affected by this modulation scheme.

D.   Bibliography

1   E.A. Marcatili, "**Dielectric rectangular waveguide and directional coupler for integrated optics**", *Bell System Technical Journal 48(7), 2071-2102 (1969).*

2   Lumerical MODE, https://www.lumerical.com/products/mode/

3   R. Halir, A. Ortega-Moñux, D. Benedikovic, D., G.Z. Mashanovich, J.G. Wangüemert-Pérez, J.H. Schmid, I. Molina-Fernández, and P. Cheben, "**Subwavelength-grating metamaterial structures for silicon photonic devices**", *Proceedings of the IEEE 106*(12), 2144-2157 (2018).

4   J. Flueckiger, S. Schmidt, V. Donzella, A. Sherwali, D. M. Ratner, L. Chrostowski, and K. C. Cheung, "**Sub-wavelength grating for enhanced ring resonator biosensor**", *Optics Express* 24(), 15672–15686 (2016).

5   H. Yan, L. Huang, X. Xu, S. Chakravarty, N. Tang, H. Tian, and R. T. Chen, "**Unique surface sensing property and enhanced sensitivity in microring resonator biosensors based on subwavelength grating waveguides**", *Optics Express* 24(), 29724–29733 (2016).

6   L. Huang, H. Yan, X. Xu, S. Chakravarty, N. Tang, H. Tian, and R. T. Chen, "**Improving the detection limit for on-chip photonic sensors based on subwavelength grating racetrack resonators**", *Optics Express* 25(), 10527–10535 (2017).

7   J. Gonzalo Wangüemert-Pérez, P. Cheben, A. Ortega-Moñux, C. Alonso-Ramos, D. Pérez-Galacho, R. Halir, I. Molina-Fernández, D.-X. Xu, and J. H. Schmid, "**Evanescent field waveguide sensing with subwavelength grating structures in silicon-on-insulator**", *Optics Letters* 39(), 4442–4445 (2014).

8   R. Halir, P. J. Bock, P. Cheben, A. Ortega-Moñux, C. Alonso-Ramos, J. H. Schmid, J. Lapointe, D.-X. Xu, J. G. Wangüemert-Pérez, Í. Molina-Fernández, and S. Janz, "**Waveguide sub-wavelength structures: a review of principles and applications**", *Laser & Photonics Reviews* 9(), 25–49 (2015).

9   J. Hu and D. Dai, "**Cascaded-ring optical sensor with enhanced sensitivity by using suspended Si-nanowires**", *IEEE Photonics Technology Letters* 23(), 842–844 (2011).

10 W. Bogaerts, P. De Heyn, T. Van Vaerenbergh, K. De Vos, S. Kumar Selvaraja, T. Claes, P. Dumon, P. Bienstman, D. Van Thourhout, and R. Baets, "**Silicon microring resonators**", *Laser & Photonics Reviews* 6(), 47–73 (2012).

11 B.J. Luff, J.S. Wilkinson, J. Piehler, U. Hollenbach, J. Ingenhoff, and N. Fabricius, "**Integrated optical Mach-Zehnder biosensor**", *Journal of Lightwave Technology* 16(4), 583-592 (1998).

12 T. Komljenovic, D. Huang, P. Pintus, M.A. Tran, M.L. Davenport, J.E. Bowers, "**Photonic integrated circuits using heterogeneous integration on silicon**", *Proceedings of the IEEE* 106(12), 2246-2257 (2018).

13 O. Marshall, M. Hsu, Z. Wang, B. Kunert, C. Koos, and D. Van Thourhout, "**Heterogeneous integration on silicon photonics**", *Proceedings of the IEEE* 106(12), 2258-2269 (2018).

14 D.Liang and J.E. Bowers, "**Recent progress in lasers on silicon**", *Nature Photonics* 4(8), 511-517 (2010).

15 G. Roelkens, L. Liu, D. Liang, R. Jones, A. Fang, B. Koch and J. Bowers, "**III-V/silicon photonics for on-chip and intra-chip optical interconnects**", *Laser & Photonics Reviews* 4(6), 751-779 (2010).

16 M.R. Billah, M. Blaicher, T. Hoose, P.I. Dietrich, P. Marin-Palomo, N. Lindenmann, A. Nesic, A. Hofmann, U. Troppenz, M. Moehrle, S. Randel, W. Freude, and C. Koos, "**Hybrid integration of silicon photonics circuits and InP lasers by photonic wire bonding**", Optica 5, 876-883 (2018)

17 H. Lu, J.S. Lee, Y. Zhao, C. Scarcella, P. Cardile, A. Daly, M. Ortsiefer, L. Carroll, and P. O'Brien, "**Flip-chip integration of tilted VCSELs onto a silicon photonic integrated circuit**", *Optics express* 24(15), 16258-16266 (2016).

18 J. Justice, C. Bower, M. Meitl, M.B. Mooney, M.A. Gubbins, and B. Corbett, "**Wafer-scale integration of group III–V lasers on silicon using transfer printing of epitaxial layers**", *Nature Photonics* 6(9), 610-614 (2012).

19 S. Tanaka, S.H. Jeong, S. Sekiguchi, T. Kurahashi, Y. Tanaka, and K. Morito, "**High-output-power, single-wavelength silicon hybrid laser using precise flip-chip bonding technology**", *Optics express 20*(27), 28057-28069 (2012).

20 M.J. Heck, J.F. Bauters, M.L. Davenport, J.K. Doylend, S. Jain, G. Kurczveil, S. Srinivasan, Y. Tang, and J.E. Bowers, "**Hybrid silicon photonic integrated circuit technology**", *IEEE Journal of Selected Topics in Quantum Electronics* 19(4), 6100117-6100117(2012).

21 L. Vivien, A. Polzer, D. Marris-Morini, J. Osmond, J. M. Hartmann, P. Crozat, E. Cassan, C. Kopp, H. Zimmermann, and J. M. Fédéli, "**Zero-bias 40Gbit/s germanium waveguide photodetector on silicon**", *Optics Express* 20(2), 1096-1101 (2012)

22 A. Masood, M. Pantouvaki, G. Lepage, P. Verheyen, J. Van Campenhout, P. Absil, D. Van Thourhout, and W. Bogaerts, "**Comparison of heater architectures for thermal control of silicon photonic circuits**", In 10th International Conference on Group IV Photonics, IEEE, 83-84, (2013).

23 Q. Xu, S. Manipatruni, B. Schmidt, J. Shakya, and M. Lipson, "**12.5 Gbit/s carrier-injection-based silicon micro-ring silicon modulators**", Optics Express 15, 430-436 (2007).

24 C. Kieninger, Y. Kutuvantavida, D.L. Elder, S. Wolf, H. Zwickel, M. Blaicher, J.N. Kemal, M. Lauermann, S. Randel, W. Freude, L.R. Dalton, and C. Koos, "**Ultra-high electro-optic activity demonstrated in a silicon-organic hybrid modulator**," Optica 5, 739-748 (2018).

25 S. Schmidt, J. Flueckiger, W. Wu, S. M. Grist, S. T. Fard, V. Donzella, P. Khumwan, E. R. Thompson, Q. Wang, P. Kulik, J. Kirk, K. C. Cheung, L. Chrostowski, and D. Ratner, "**Improving the performance of silicon photonic rings, disks, and bragg gratings for use in label-free biosensing**", *Biosensing and Nanomedicine VII* 9166, 91660M, International Society for Optics and Photonics (2014).

26 V. M. N. Passaro, B. Troia, M. La Notte, and F. De Leonardis, "**Chemical sensors based on photonic structures**", *Advances in Chemical Sensors*, IntechOpen (2012).

27 S. Janz, A. Densmore, D.-X. Xu, P. Waldron, J. Lapointe, J. H. Schmid, T. Mischki, G. Lopinski, A. Delâge, R. McKinnon, P. Cheben, and B. Lamontagne, "**Silicon Photonic Wire Waveguide Sensors**", *Advanced Photonic Structures for Biological and Chemical Detection*, 229-264, Springer, New York, NY (2009).

28 P. Kozma, F. Kehl, E. Ehrentreich-Förster, C. Stamm, and F. F. Bier, "**Integrated planar optical waveguide interferometer biosensors: A comparative review**", *Biosensors and Bioelectronics* 58, 287–307 (2014).

29   Densmore, D.-X. Xu, S. Janz, P. Waldron, J. Lapointe, T. Mischki, G. Lopinski, A. Delâge, J. Schmid, and P. Cheben, "**Sensitive label free Sensitive label-free biomolecular detection using thin silicon waveguides**", *Advances in Optical Technologies*, 725967 (2008).

30   L. Chrostowski, S. Grist, J. Flueckiger, W. Shi, X. Wang, E. Ouellet, H. Yun, M. Webb, B. Nie, Z. Liang, K. Cheung, S. Schmidt, D. Ratner, and N. Jaeger, "**Silicon photonic resonator sensors and devices**", *Laser Resonators, Microresonators, and Beam Control XIV* 8236, 823620, International Society for Optics and Photonics (2012).

31   X. Wang, J. Flueckiger, S. Schmidt, S. Grist, S. T. Fard, J. Kirk, M. Doerfler, K. C. Cheung, D. M. Ratner, and L. Chrostowski, "**A silicon photonic biosensor using phase-shifted Bragg gratings in slot waveguide**", *Journal of Biophotonics* 6(10), 821–828 (2013).

32   B. Sepúlveda, J. S. Del Rio, M. Moreno, F. J. Blanco, K. Mayora, C. Domínguez, and L. M. Lechuga, "**Optical biosensor microsystems based on the integration of highly sensitive Mach-Zehnder interferometer devices**", *Journal of Optics A: Pure and Applied Optics* 8(7), 561–566 (2006).

33   Densmore, D.-X. Xu, P. Waldron, S. Janz, P. Cheben, J. Lapointe, A. Delâge, B. Lamontagne, J. Schmid, and E. Post, "**A silicon-on-insulator photonic wire based evanescent field sensor**", *IEEE Photonics Technology Letters* 18(23), 2520-2522 (2006).

34   S. T. Fard, V. Donzella, S. A. Schmidt, J. Flueckiger, S. M. Grist, P. Talebi Fard, Y. Wu, R. J. Bojko, E. Kwok, N. A. Jaeger, D. M. Ratner, and L. Chrostowski, "**Performance of ultra-thin SOI-based resonators for sensing applications**", *Optics Express* 22(), 14166–14179 (2014).

35   Kargar and C.-Y. Chao, "**Design and optimization of waveguide sensitivity in slot microring sensors**", *Journal of the Optical Society of America A* 28(), 596–603 (2011).

36   H. Sun, A. Chen, and L. Dalton, "**Enhanced evanescent confinement in multiple-slot waveguides and its application in biochemical sensing**", *IEEE Photonics Journal* 1(), 48–57 (2009).

37   Khodadad, N. Clarke, M. Khorasaninejad, D. Henneke, and S. S. Saini, "**Optimization of multiple-slot waveguides for biochemical sensing**", *Applied Optics* 53(), 5169–5178 (2014).

38   C. A. Barrios, "**Analysis and modeling of a silicon nitride slot-waveguide microring resonator biochemical sensor**", *Optical Sensors* 7356, 735605, International Society for Optics and Photonics (2009).

39   T. Claes, W. Bogaerts, and P. Bienstman, "**Experimental characterization of a silicon photonic biosensor consisting of two cascaded ring resonators based on the Vernier-effect and introduction of a curve fitting method for an improved detection limit**", *Optics Express* 18(), 22747–22761 (2010).

40   F. Dell'Olio and V. M. N. Passaro, "**Optical sensing by optimized silicon slot waveguides**", *Optics Express* 15(), 4977–4993 (2007).

41   D.-X. Xu, J. Schmid, G. Reed, G. Mashanovich, D. Thomson, M. Nedeljkovic, X. Chen, D. Van Thourhout, S. Keyvaninia, and S. Selvaraja, "**Silicon photonic integration platform-Have we found the sweet spot?**", *IEEE Journal of Selected Topics in Quantum Electronics* 20(4), 8100217 (2014).

42   Dhakal, A. Raza, F. Peyskens, A. Z. Subramanian, S. Clemmen, N. Le Thomas, and R. Baets, "**Efficiency of evanescent excitation and collection of spontaneous Raman scattering near high index contrast channel waveguides**", *Optics Express* 23(), 27391–27404 (2015).

43   M. G. Scullion, T. F. Krauss, and A. Di Falco, "**Slotted photonic crystal sensors**", *Sensors* 13(), 3675–3710 (2013).

44   U. Manual, Version 2016, CST-Computer Simulation Technology GmbH, Darmstadt, Germany, (2017) http://www.cst.com

45   S. Hughes, L. Ramunno, J. F. Young, and J. E. Sipe, "**Extrinsic optical scattering loss in photonic crystal waveguides: role of fabrication disorder and photon group velocity**", *Physical Review Letters* 94(), 033903 (2005).

46   X. Fang, I.M. White, S.I. Shopova, H. Zhu, J.D. Suter, and Y. Sun, "**Sensitive optical biosensors for unlabeled targets: A review**", *Analytica Chimica Acta* 620(1-2), 8-26 (2008)

47   A. Densmore, M. Vachon, D.-X. Xu, S. Janz, R. Ma, Y.-H. Li, G. Lopinski, A. Delâge, J. Lapointe, C. C. Luebbert, Q. Y. Liu, P. Cheben, and J. H. Schmid, "**Silicon photonic wire biosensor array for multiplexed real-time and label-free molecular detection**", Optics Letters 34(23), 3598-3600 (2009).

48   C. Barrios, M. Bañuls, V. González-Pedro, K. Gylfason, B. Sánchez, A. Griol, A. Maquieira, H. Sohlström, M. Holgado, and R. Casquel, **"Label-free optical biosensing with slot-waveguides",** Optics Letters 33(7), 708-710 (2008).

49   K. De Vos, I. Bartolozzi, I., E. Schacht, P. Bienstman, P, and R. Baets, "**Silicon-on-Insulator microring resonator for sensitive and label-free biosensing**", *Optics Express* 15(12), 7610-7615 (2007).

50   Jalali and S. Fathpour, "**Silicon Photonics**", *Journal of Lightwave Technology* 24(12), 4600–4615 (2006).

51 R. Soref, "**The Past, Present, and Future of Silicon Photonics**", *IEEE Journal of selected topics in quantum electronics* 12(6), 1678-1687 (2006).

52   M. Hochberg, and T. Baehr-Jones, "**Towards fabless silicon photonics**", *Nature Photonics* 4(8), 492–494 (2010).

53   D. Thomson, A. Zilkie, J. E. Bowers, T. Komljenovic, G. T. Reed, L. Vivien, D. Marris-Morini, E. Cassan, L. Virot, J.-M. Fédéli, J.-M. Hartmann, J. H. Schmid, D.-X. Xu, F. Boeuf, P. O'Brien, G. Z. Mashanovich, and M. Nedeljkovic, "**Roadmap on silicon photonics**", *Journal of Optics* 18(7), 073003 (2016).

54   P. Muñoz, G. Micó, L. A. Bru, D. Pastor, D. Pérez, J. D. Doménech, J. Fernández, R. Baños, B. Gargallo, R. Alemany, A. M. Sánchez, J. M. Cirera, R. Mas, and C. Domínguez, "**Silicon nitride photonic integration platforms for visible, near-infrared and mid-infrared applications**", Sensors 17(9), 2088 (2017).

55   D. J. Blumenthal, R. Heideman, D. Geuzebroek, A. Leinse, and C. Roeloffzen, "**Silicon nitride in silicon photonics**", *Proceedings of the IEEE* 106(12), 2209–2231 (2018).

56   T. A. Huffman, G. M. Brodnik, C. Pinho, S. Gundavarapu, D. Baney, and D. J. Blumenthal, "**Integrated resonators in anultralow loss Si3N4/SiO2platform for multifunction applications**", *IEEE Journal of selected topics in quantum electronics* 24(4), 1–9 (2018).

57   W. D. Sacher, J. C. Mikkelsen, Y. Huang, J. C. C. Mak, Z. Yong, X. Luo, Y. Li, P. Dumais, J. Jiang, D. Goodwill, E. Bernier, P. G.-Q. Lo, and J. K. S. Poon, "**Monolithically integrated multilayer silicon nitride-on-silicon waveguideplatforms for 3-D photonic circuits and devices**", *Proceedings of the IEEE* 106(12), 2232–2245 (2018).

58 A.L. Washburn, L.C. Gunn, and R.C. Bailey, "**Label-free quantitation of a cancer biomarker in complex media using silicon photonic microring resonators**", *Analytical Chemistry* 81(22), 9499-9506 (2009).

59 W-C. Lai, S. Chakravarty, X. Wang, C. Lin, and R.T. Chen, "**On-chip methane sensing by near-IR absorption signatures in a photonic crystal slot waveguide**", *Optics Letters* 36(6), 984-986 (2011).

60 Y. Zou, K. Vijayraghavan, P. Wray, S. Chakravarty, M.A. Belkin, R.T. Chen, "**Monolithically Integrated Quantum Cascade Lasers, Detectors and Dielectric Waveguides at 9.5μm for Far-Infrared Lab-on- Chip Chemical Sensing**", *in CLEO (Optical Society of America), Abstract ID: STu4I.2*, San Jose, CA (2015)

61 S. Chakravarty, X. Chen, N.Tang, W-C. Lai, Y. Zou, H. Yan, R.T. Chen, "**Review of design principles of 2D photonic crystal microcavity biosensors in silicon and their applications**", *Frontiers of Optoelectronics* 9(2), 206-224 (2016).

62 H. Yan, N. Tang, S. Chakravarty, R.T. Chen, "**High-sensitivity high-throughput chip based biosensor array for multiplexed detection of heavy metals**", *in BiOS (Photonics West)*, San Francisco, California, United States (2016)

63 W. Lai, S. Chakravarty, Y. Zou, and R.T. Chen, "**Silicon nano-membrane based photonic crystal microcavities for high sensitivity bio-sensing**", *Optics Letters* 37(7), 1208-1210 (2012).

64 W. Lai, S. Chakravarty, Y. Zou, Y. Guo and R.T. Chen, "**Slow light enhanced sensitivity of resonance modes in photonic crystal biosensors**", *Applied Physics Letters* 102(4), 041111 (2013).

65 A.L. Washburn, M.S. Luchansky, A.L. Bowman, and R.C. Bailey, "**Quantitative, label-free detection of five protein biomarkers using multiplexed arrays of silicon photonic microring resonators**", *Analytical Chemistry* 82(1), 69-72 (2010).

66 M. Iqbal, M.A. Gleeson, B. Spaugh, F. Tybor, W.G. Gunn, M. Hochberg, T. Baehr-Jones, R.C. Bailey, and L.C. Gunn, "**Label-free biosensor arrays based on silicon ring resonators and high-speed optical scanning instrumentation**", *IEEE Journal of selected topics in quantum electronics* 16(3), 654-661 (2010).

67   E. Luan, H. Shoman, D.M. Ratner, K.C. Cheung, and L. Chrostowski, "**Silicon Photonic Biosensors Using Label-Free Detection**", *Sensors* 18(10), 3519 (2018).

68   Y. Zou, S. Chakravarty, C. Chung, X. Xu, and R. Chen, "**Mid-infrared silicon photonic waveguides and devices**", *Photonics Research* 6(4), 254-276 (2018).

69   E. Makarona, P. Petrou, S. Kakabakos, K. Misiakos, and I. Raptis, "**Point-of-Need bioanalytics based on planar optical interferometry**", *Biotechnology advances* 34(3), 209-233 (2016).

70   A. Fernández Gavela, D. Grajales García, J.C. Ramirez, and L.M. Lechuga, "**Last advances in silicon-based optical biosensors**", *Sensors* 16(3), 285 (2016).

71   M. White, and X. Fan, "**On the performance quantification of resonant refractive index sensors**", *Optics Express* 16(2), 1020-1028 (2008).

72   W. Bogaerts, P. De Heyn, T. Van Vaerenbergh, K. De Vos, S. Kumar Selvaraja, T. Claes, P. Dumon, P. Bienstman, D. Van Thourhout, and R. Baets, "**Silicon microring resonators**", *Laser & Photonics Reviews* 6(1), 47-73 (2012).

73   X. Wang, J. Flueckiger, S. Schmidt, S. Grist, S.T. Fard, J. Kirk, M. Doerfler, K.C. Cheung, D.M. Ratner, and L. Chrostowski, "**A silicon photonic biosensor using phase-shifted Bragg gratings in slot waveguide**" *Journal of biophotonics* 6(10), 821-828 (2013).

74   F. Koyama, "**Advances and new functions of VCSEL photonics**", *Optical Review* 21(6), 893-904 (2014).

75   J. Milvich, D. Kohler, W. Freude, and C. Koos, "**Surface sensing with integrated optical waveguides: a design guideline**", *Optics Express* 26(16), 19885-19906 (2018)

76   D. Kita, J. Michon, S. Johnson, and J. Hu, "**Are slot and sub-wavelength grating waveguides better than strip waveguides for sensing?**", *Optica* 5(9), 1046-1054 (2018).

77   S. Dante, D. Duval, B. Sepúlveda, A. B. González-Guerrero, J. R. Sendra, and L. M. Lechuga, "**All-optical phase modulation for integrated interferometric biosensors**", *Optics Express* 20(7), 7195-7205 (2012).

78   R. Halir, L.Vivien, X. Le Roux, D. X. Xu, and P. Cheben, "**Direct and sensitive phase readout for integrated waveguide sensors**", *IEEE Photonics Journal* 5(4), 6800906-6800906 (2013).

79   E. Clarke, "**Circuit analysis of AC power systems**", Vol. 1, J. Wiley & Sons, New York (1943).

80   J. Milvich, D. Kohler, W. Freude, and C. Koos, "**Mach-Zehnder interferometer readout for instantaneous sensor calibration and extraction of endlessly unwrapped phase**", *2017 IEEE Photonics Conference (IPC)*, Orlando, FL, 567-568 (2017).

81   Í. Molina-Fernández, J. Leuermann, A. Ortega-Moñux, J. G. Wangüemert-Pérez, and R. Halir, "**Fundamental limit of detection of photonic biosensors with coherent phase read-out**", *Optics Express* 27(9), 12616-12629 (2019).

82   M. Bachmann, P. A. Besse, and H. Melchior, "**General self-imaging properties in N× N multimode interference couplers including phase relations**", *Applied Optics* 33(18), 3905-3911 (1994).

83   K. Giewont, K. Nummy, F.A. Anderson, J. Ayala, T. Barwicz, Y. Bian, K.K. Dezfulian, D.M. Gill, T. Houghton, S. Hu, B. Peng, M. Rakowski, S. Rauch, J. C. Rosenberg, A. Sahin, I. Stobert, and A. Stricker, "**300-mm monolithic silicon photonics foundry technology**", *IEEE Journal of Selected Topics in Quantum Electronics* 25(5), 1-11 (2019).

84   A. Rahim, T. Spuesens, R. Baets, R., and W. Bogaerts, "**Open-access silicon photonics: Current status and emerging initiatives**", *Proceedings of the IEEE* 106(12), 2313-2330 (2018).

85   T.W. Weng, Z. Zhang, Z. Su, Y. Marzouk, A. Melloni, and L. Daniel, „**Uncertainty quantification of silicon photonic devices with correlated and non-Gaussian random parameters**", *Optics Express* 23(4), 4242-4254 (2015).

86   S. Dwivedi, H. D'heer, and W. Bogaerts, "**Maximizing fabrication and thermal tolerances of all-silicon FIR wavelength filters**", *IEEE Photonics Technology Letters* 27(8), 871-874 (2015).

87   X. Zhou, L. Zhang, A.M. Armani, J. Liu, X. Duan, D. Zhang, H. Zhang, and W. Pang, "**An integrated photonic gas sensor enhanced by optimized Fano effects in coupled microring resonators with an athermal waveguide**", *Journal of Lightwave Technology* 33(22), 4521-4530 (2015).

88   K. B. Gylfason, C. F. Carlborg, A. Kaźmierczak, F. Dortu, H. Sohlström, L. Vivien, C. A. Barrios, W. van der Wijngaart, and G. Stemme, "**On-chip temperature compensation in an integrated slot-waveguide ring resonator refractive index sensor array**", *Optics Express* 18(4), 3226-3237 (2010)

89   Guha, B. B. Kyotoku, and M. Lipson, "**CMOS-compatible athermal silicon microring resonators**", *Optics Express* 18(4), 3487-3493 (2010).

90   D. Xu, M. Vachon, A. Densmore, R. Ma, S. Janz, A. Delâge, J. Lapointe, P. Cheben, J. Schmid, E. Post, S. Messaoudène, and J. Fédéli, "**Real-time cancellation of temperature induced resonance shifts in SOI wire waveguide ring resonator label-free biosensor arrays**", *Optics Express* 18(22), 22867-22879 (2010).

91   E. Kleijn, E. Van Vliet, D. Pustakhod, M. Smit, and X. Leijtens, "**Amplitude and Phase Error Correction Algorithm for 3 x 3 MMI Based Mach-Zehnder interferometers**", *Journal of Lightwave Technology* 33(11), 2233-2239 (2015).

92   W. Bogaerts, and L. Chrostowski, "**Silicon photonics circuit design: methods, tools and challenges**", *Laser & Photonics Reviews* 12(4), 1700237 (2018).

93   G. Di Domenico, S. Schilt, and P. Thomann, "**Simple approach to the relation between laser frequency noise and laser line shape**", *Applied Optics* 49(25), 4801-4807 (2010).

94   D.M. Kuchta, J. Gamelin, J.D. Walker, J. Lin, K.Y. Lau, J.S. Smith, M. Hong, and J.P. Mannaerts, "**Relative intensity noise of vertical cavity surface emitting lasers**", *Applied Physics Letters* 62(11), 1194-1196 (1993)

95   W. Schottky, "**Über spontane Stromschwankungen in verschiedenen Elektrizitätsleitern**", *Annalen der Physik* 362(23), 541-567 (1918)

96   V. Mackowiak, J. Peupelmann, Y. Ma, and A. Gorges, "**NEP- Noise equivalent power**", Thorlabs, Inc. (2015) https://www.thorlabs.com/images/TabImages/Noise_Equivalent_Power_White_Paper.pdf

97   Sripad, and D. Snyder, "**A necessary and sufficient condition for quantization errors to be uniform and white**", *IEEE Transactions on Acoustics, Speech, and Signal Processing* 25(5), 442-448 (1977).

98   N. El-Sheimy, H. Hou, and X. Niu, "**Analysis and modeling of inertial sensors using Allan variance**", *IEEE Transactions on instrumentation and measurement* 57(1), 140-149 (2007).

99   J. Komma, C. Schwarz, G. Hofmann, D. Heinert, and R. Nawrodt, „**Thermo-optic coefficient of silicon at 1550 nm and cryogenic temperatures**", *Applied Physics Letters* 101(4), 041905 (2012).

100 A. Arbabi, and L. L. Goddard, "**Measurements of the refractive indices and thermo-optic coefficients of Si3N4 and SiOx using microring resonances**", *Optics Letters* 38(19), 3878-3881 (2013).

101 Densmore, D. X.Xu, S. Janz, P. Waldron, T. Mischki, G. Lopinski, A. Delâge, J. Lapointe, P. Cheben, B. Lamontagne, and J. H. Schmid, "**Spiral-path high-sensitivity silicon photonic wire molecular sensor with temperature-independent response**", *Optics Letters* 33(6), 596-598 (2008).

102 J. Teng, P. Dumon, W. Bogaerts, H. Zhang, X. Jian, X. Han, M. Zhao, G. Morthier, and R. Baets, "**Athermal Silicon-on-insulator ring resonators by overlaying a polymer cladding on narrowed waveguides**", *Optics Express* 17(17), 14627-14633 (2009).

103 X. Tu, J. Song, T. Liow, M. Park, J. Yiying, J. Kee, M. Yu, and G. Lo, "**Thermal independent Silicon-Nitride slot waveguide biosensor with high sensitivity**", *Optics Express* 20(3), 2640-2648 (2012).

104 H. W. Lim, and N. A. Soter, "**Clinical photomedicine**" (Dekker, 1993)

105 J. Milvich, "**Design of waveguide-based photonic sensor systems | MATLAB**", figshare (2020), https://osapublishing.figshare.com/s/42b40f4d70dd0aeaf0a5.

106 J.T. Kirk, G.E. Fridley, J.W. Chamberlain, E.D. Christensen, M. Hochberg, and D.M. Ratner, "**Multiplexed inkjet functionalization of silicon photonic biosensors**", *Lab on a Chip* 11(7), 1372-1377 (2011).

107 J.T. Kirk, N.D. Brault, T. Baehr-Jones, M. Hochberg, S. Jiang, S., and D.M. Ratner, "**Zwitterionic polymer-modified silicon microring resonators for label-free biosensing in undiluted humanplasma**", *Biosensors and Bioelectronics* 42, 100-105 (2013).

108 J. Shang, F. Cheng, M. Dubey, J.M. Kaplan, M. Rawal, X. Jiang, D.S. Newburg, P.A. Sullivan, R.B. Andrade, and D.M. Ratner, "**An organophosphonate strategy for functionalizing silicon photonic biosensors**", *Langmuir* 28(6), 3338–3344 (2012).

109 N.B. Arnfinnsdottir, C.A. Chapman, R.C. Bailey, A. Aksnes, and B.T. Stokke, "**Impact of Silanization Parameters and Antibody Immobilization Strategy on Binding Capacity of Photonic Ring Resonators**", *Sensors* 20(11), 3163 (2020).

110 R.D. Rohde, H.D. Agnew, W.S. Yeo, R.C. Bailey, and J.R. Heath, "**A nonoxidative approach toward chemically and electrochemically functionalizing Si(111)**", *Journal of the American Chemical Society* 128(29), 9518–9525 (2006).

111 P. Cheben, R. Halir, J.H. Schmid, H.A. Atwater, and D.R. Smith, „**Subwavelength integrated photonics**", *Nature* 560(7720), 565–572 (2018).

112 R. Halir, P. J. Bock, P. Cheben, A. Ortega-Moñux, C. Alonso-Ramos, J. H. Schmid, J. Lapointe, D.-X. Xu, J. G. Wangüemert-Pérez, Í. Molina-Fernández, and S. Janz, "**Waveguide sub-wavelength structures: a review of principles and applications**", *Laser & Photonics Reviews* 9(1), 25–49 (2015).

113 S. Tanaka, S. H. Jeong, S. Sekiguchi, T. Kurahashi, Y. Tanaka, and K. Morito, "**High-output-power, single-wavelength silicon hybrid laser using precise flip-chip bonding technology**", *Optics Express* 20(27), 28057-28069 (2012).

114 M. J. Heck, J. F. Bauters, M. L. Davenport, J. K. Doylend, S. Jain, G. Kurczveil, S. Srinivasan, Y. Tang, and J. E. Bowers, "**Hybrid silicon photonic integrated circuit technology**", *IEEE Journal of Selected Topics in Quantum Electronics* 19(4), 6100117-6100117 (2012).

115 C. Xiang, W. Jin, J. Guo, J.D. Peters, M.J. Kennedy, J. Selvidge, P.A. Mortion, and J.E. Bowers, "**Narrow-linewidth III-V/Si/Si 3 N 4 laser using multilayer heterogeneous integration**", *Optica* 7(1), 20-21 (2020).

116 C.O. de Beeck, B. Haq, L. Elsinger, A. Gocalinska, E. Pelucchi, B. Corbett, B., G. Roelkens, and B. Kuyken, "**Heterogeneous III-V on silicon nitride amplifiers and lasers via microtransfer printing**", *Optica* 7(5), 386-393 (2020).

117 H. Lu, J. S. Lee, Y. Zhao, C. Scarcella, P. Cardile, A. Daly, M. Ortsiefer, L. Carroll, and P. O'Brien, "**Flip-chip integration of tilted VCSELs onto a silicon photonic integrated circuit**", *Optics Express* 24(15), 16258-16266 (2016).

118 P.I. Dietrich, M. Blaicher, I. Reuter, M. Billah, T. Hoose, A. Hofmann, A., C. Caer, R. Dangel, B. Offrein, U. Troppenz, M. Moehrle, W. Freude, and

C. Koos, "**In situ 3D nanoprinting of free-form coupling elements for hybrid photonic integration**", *Nature Photonics* 12(4), 241-247 (2018).

119 M. R. Billah, M. Blaicher, T. Hoose, P.-I. Dietrich, P. Marin-Palomo, N. Lindenmann, A. Nesic, A. Hofmann, U. Troppenz, M. Moehrle, S. Randel, W. Freude, and C. Koos, "**Hybrid integration of silicon photonics circuits and InP lasers by photonic wire bonding**", *Optica* 5(7), 876-883 (2018).

120 M. Blaicher, M. Billah, J. N. Kemal, T. Hoose, P. Marin-Palomo, A. Hofmann, Y. Kutuvantavida, C. Kieninger, P.-I. Dietrich, M. Lauermann, S. Wolf, U. Troppenz, M. Moehrle, F. Merget, S. Skacel, J. Witzens, S. Randel, W. Freude, and C. Koos, "**Hybrid Multi-Chip Assembly of Optical Communication Engines by In-Situ 3D Nano-Lithography**", *Light: Science & Applications* 9(71) (2020).

121 J. Goyvaerts, S. Kumari, S. Uvin, J. Zhang, R. Baets, A. Gocalinska, E. Pelucchi, B. Corbett, and G. Roelkens, "**Transfer-print integration of GaAs p-i-n photodiodes onto silicon nitride waveguides for near-infrared applications**", *Optics Express* 28(14), 21275-21285 (2020).

122 K.K. Liu, R.G. Wu, Y.J. Chuang, H.S. Khoo, S.H. Huang, and F.G. Tseng, "**Microfluidic systems for biosensing**", *Sensors* 10(7), 6623–6661 (2010).

123 Z. Wang, H. Yan, S. Chakravarty, H. Subbaraman, X. Xu, D. Fan, A.X. Wang, R.T. Chen, "**Microfluidic channels with ultralow-loss waveguide crossings for various chip-integrated photonic sensors**", *Optics Letters* 40(7), 1563–1566. (2015).

124 X. Fan and I.M. White, "**Optofluidic microsystems for chemical and biological analysis**", *Nature Photonics* 5(10), 591 (2011).

125 C. Adamopoulos, A. Gharia, A. Niknejad, V. Stojanović, and M. Anwar, "**Microfluidic Packaging Integration with Electronic-Photonic Biosensors Using 3D Printed Transfer Molding**", *Biosensors* 10(11), 177 (2020).

126 L. Laplatine, E. Luan, K. Cheung, D.M. Ratner, Y. Dattner, and L. Chrostowski, "**System-level integration of active silicon photonic biosensors using Fan-Out Wafer-Level-Packaging for low cost and multiplexed point-of-care diagnostic testing**", *Sensors and Actuators B: Chemical* 273, 1610-1617 (2018).

127 A.R. Wheeler, "**Putting electrowetting to work**", *Science* 322(5901), 539-540 (2008).

128 S.F. Wondimu, S. von der Ecken, R. Ahrens, W. Freude, A.E. Guber, and C. Koos, "**Integration of digital microfluidics with whispering-gallery mode sensors for label-free detection of biomolecules**", *Lab on a chip* 17(10), 1740-1748 (2017).

129 M.W. Royal, N.M. Jokerst, and R.B. Fair, "**Droplet-based sensing: optical microresonator sensors embedded in digital electrowetting microfluidics systems**", *IEEE Sensors Journal* 13(12), 4733-4742 (2013).

130 C.L. Arce, D. Witters, R. Puers, J. Lammertyn, and P. Bienstman, "**Silicon photonic sensors incorporated in a digital microfluidic system**", *Analytical and bioanalytical chemistry* 404(10), 2887-2894 (2012).

131 L. Luan, M.W. Royal, R. Evans, R.B. Fair, and N.M. Jokerst, "**Chip scale optical microresonator sensors integrated with embedded thin film photodetectors on electrowetting digital microfluidics platforms**", *IEEE Sensors Journal* 12(6), 1794-1800 (2011).

132 R. Halir, L.Vivien, X. Le Roux, D. X. Xu and P. Cheben, "**Direct and sensitive phase readout for integrated waveguide sensors**", *IEEE Photonics Journal* 5(4), 6800906-6800906 (2013)

133 S. Dante, D. Duval, B. Sepúlveda, A. B. González-Guerrero, J. R. Sendra, and L. M. Lechuga, "**All-optical phase modulation for integrated interferometric biosensors**", *Optics Express* 20(7), 7195-7205 (2012)

134 Í. Molina-Fernández, J. Leuermann, A. Ortega-Moñux, J. G. Wangüemert-Pérez, and R. Halir, "**Fundamental limit of detection of photonic biosensors with coherent phase read-out**", *Optics Express*, 27(9), 12616-12629 (2019).

135 L. B. Soldano, and E. C. Pennings. "**Optical multi-mode interference devices based on self-imaging: principles and applications**", *Journal of Lightwave Technology* 13(4), 615-627 (1995).

136 M. Bachmann, P.A. Besse, and H. Melchior, „**General self-imaging properties in N× N multimode interference couplers including phase relations**", *Applied optics 33*(18), 3905-3911 (1994).

137 W. Gander, G. H. Golub, and R. Strebel, "**Least-Squares Fitting of Circles and Ellipses**", *BIT Numerical Mathematics*, Springer (1994).

138 R.G. Heidemann, P.V. Lambeck, "**Remote opto-chemical sensing with extreme sensitivity: Design, fabrication and performance of a pigtailed integrated optical phase-modulated Mach-Zehnder interferometer system**", *Sensors and Actuators B: Chemical* 61(1-3), 100-127 (1999)

139 H. Kogelnik, "**Theory of optical waveguides**", *Guided-wave Optoelectronics*, 7-88, Springer, Berlin, Heidelberg (1988).

140 C. Koos, "**Nanophotonic Devices for Linear and Nonlinear Optical Signal Processing**", *Universitäts-Verlag Karlsruhe* (2007).

141 J.-M. Brosi, "**Slow Light Photonic Crystal Devices for High Speed Optical Signal Processing**", *Universitäts-Verlag Karlsruhe* (2009).

142 J. D. Joannopoulos, R. D. Meade, and J. N. Winn, "**Photonic Crystals: Molding the Flow of light**", *Princeton University Press*, (1995).

143 J. Heebner, R. Grover, T. Ibrahim, and T. A. Ibrahim, "**Optical microresonators: theory, fabrication, and applications**", Vol. 138 (Springer Science & Business Media, 2008).

144 D. S. Elliott, R. Roy, and S. J. Smith, "**Extracavity laser band-shape and bandwidth modification**", *Physical Review A* 26(1), 12-18 (1982)

145 Keysight application note, "**Everything You Need to Know About Complex Optical Modulation**", Keysight Technologies, Inc. (2019) http://literature.cdn.keysight.com/litweb/pdf/5992-2888EN.pdf

E.   Glossary

E.1   Acronyms

Acronym	Description
AC	Alternate current
AD	Add-drop (configuration for a ring resonator)
ADC	Analog-to-digital converter
AP	All-pass (configuration for a ring resonator)
ASE	Amplified spontaneous emission
ASIC	Application-specific integrated circuit
AWG	Arrayed waveguide grating
BD	Balanced detection (configuration for a ring resonator)
BOX	Buried oxide
CC	Critically-coupled (coupling state of a ring resonator)
CMOS	Complementary metal-oxide-semiconductor
DC	Direct current
DFB	Distributed feedback
DSP	Digital signal processing
DUT	Device under test
EDFA	Erbium-doped fiber amplifier
FEM	Finite element method
FF	Fill factor
FPGA	Field-programmable gate array
FSR	Free spectral range
FWHM	Full width at half maximum (Lorentzian resonance)
GC	Grating coupler
H_2O	Water
LAS	Laser
LD	Laser diode
LED	Light-emitting diode
LO	Local oscillator

Acronym	Description
LoD	Limit of detection
LSB	Least significant bit
MIR	Mid-infrared portion of the electro-magnetic spectrum
MMI	Multi-mode interferometer
MZI	Mach-Zehnder interferometer
↳ MZI_1	↳ With a single output port
↳ MZI_2	↳ With two output ports
↳ MZI_3	↳ With three output ports
NEP	Noise-equivalent power
NIR	Near-infrared portion of the electro-magnetic spectrum
OC	Over-coupled (coupling state of a ring resonator)
OMA	Optical modulation analyzer
OP	Operating point
OSA	Optical spectrum analyzer
OSC	Oscilloscope
PCB	Printed circuit board
PD	Photodiode
PIC	Photonic integrated circuit
RI	Refractive index
RIN	Relative intensity noise
RR	Ring resonator
↳ RR_{AP}	↳ All-pass configuration
↳ RR_{AD}	↳ Add-drop configuration (usage of the drop port)
↳ RR_{BD}	↳ Add-drop configuration (balanced detection, drop-through port)
Si	Silicon
Si_3N_4	Silicon nitride
SiO_2	Silicon dioxide
SL	Surface layer
SNR	Signal-to-noise ratio
SOI	Silicon-on-insulator
SWG	Sub-wavelength grating
TE	Transverse electric polarization

Acronym	Description
TLS	Tunable light source
TM	Transverse magnetic polarization
TOC	Thermo-optic coefficient
UC	Under-coupled (coupling state of a ring resonator)
VCSEL	Vertical-cavity surface-emitting laser
VIS	Visible portion of the electro-magnetic spectrum
WG	Waveguide

E.2 Symbols

In general, **bold** symbols refer to matrices, while <u>underlined</u> symbols refer to complex quantities.

E.2.1 Greek symbols

Symbol	Description	Unit
α	Waveguide mode power attenuation coefficient	1/m
β	Propagation constant of an electro-magnetic wave	1/m
$\hookrightarrow \boldsymbol{\beta}$	$\hookrightarrow$ Vectorial propagation constant	1/m
$\hookrightarrow \beta_{\text{B}}$	$\hookrightarrow$ Bloch propagation constant in a periodic waveguide	1/m
Γ	Field interaction factor	1
$\hookrightarrow \Gamma_{\text{SL}}$	$\hookrightarrow$ With a surface layer	1
$\Gamma^{(\text{conf})}$	Field confinement factor	1
Δ_{env}	Arbitrary environmental change around a waveguide	*
ε_0	Electric permittivity of vacuum	As/Vm
ε_{r}	Relative electric permittivity of a material	1
$\hookrightarrow \Delta\varepsilon_{\text{r}}$	$\hookrightarrow$ Change of relative electric permittivity	1
ζ	Variable for noise sources $\zeta \in \left\{T; \omega; P_{\text{i}}; I_{\text{s}}; I_{\text{NEP}}; I_{\text{q}}\right\}$	*
η	Power transmission factor (total coupling efficiency)	1
θ_{c}	Critical angle for total internal reflection	rad
κ	Extinction coefficient (imaginary part of the RI)	1
κ_{e}	Effective extinction coefficient	1
$\kappa_{1,2}$	Cross-coupling amplitude coefficients of RR	1
λ	Optical vacuum wavelength	m
$\hookrightarrow \hat{\lambda}$	$\hookrightarrow$ Wavelength modulation depth	m
μ_0	Magnetic permeability of free space	N/A²
μ_{r}	Relative magnetic permeability of a material	1
ρ	Charge density	C/m³
$\rho_{1,2}$	Self-coupling amplitude coefficients of ring resonators	1
ρ_{ff}	Autocorrelation function	1
σ	Electrical conductivity	S/m
σ_{g}	Geometric scaling factor	1
σ_{n}	Refractive index scaling factor	1

Symbol	Description	Unit
σ_ω	Angular frequency scaling factor	1
σ_ζ^2	Noise variances, $\zeta \in \left\{ T; \omega; P_i; I_s; I_{\mathrm{NEP}}; I_q \right\}$	*
$\sigma_{\Delta n_{\mathrm{e,r}}, \zeta}^2$	Reconstructed measurand variances, $\zeta \in \left\{ T; \omega; P_i; I_s; I_{\mathrm{NEP}}; I_q \right\}$	*
τ	Effective optoelectronic transmission	A/W
↳ $\hat{\tau}$	↳ Output contrast (maximum-minimum)	A/W
↳ τ_{OP}	↳ Effective optoelectronic transmission in the OP	A/W
τ_c	Photon lifetime in a cavity	s
τ_g	Group delay	s
$\tau_{\varphi_{\mathrm{MZI}}}$	Phase delay between two MZI arms	s
Φ_n	Phase noise	rad
φ	Instantaneous phase	rad
↳ $\boldsymbol{\varphi}$	↳ Phase matrix (Chapter 5)	rad
↳ φ_s	↳ At the end of the MZI sensor arm	rad
↳ φ_r	↳ At the end of the MZI reference arm	rad
↳ φ_{mn}	↳ MMI$_{n \times m}$ phase coefficients	rad
↳ φ_{res}	↳ Round-trip phase shift in resonance condition	rad
↳ $\varphi_{\mathrm{OP,RR}}$	↳ Round-trip phase shift in the optimum operating point	rad
↳ $\Delta\varphi$	↳ Phase change	rad
↳ φ_{MZI}	↳ MZI phase difference	rad
↳ $\varphi_{\mathrm{OP,MZI}}$	↳ MZI phase difference (optimum operating point)	rad
↳ $\hat{\varphi}$	↳ Phase modulation amplitude	rad
↳ $\bar{\varphi}_{\mathrm{MZI}}$	↳ MZI phase difference (mean value)	rad
↳ $\hat{\varphi}_{\mathrm{MZI}}$	↳ MZI phase difference (amplitude value)	rad
↳ $\Delta\varphi_{\mathrm{MZI}}^{\mathrm{res}}$	↳ MZI phase difference (measurement resolution)	rad
↳ $\delta\varphi$	↳ Phase coefficient error (additive)	rad
ω	Angular frequency	1/s
↳ $\hat{\omega}$	↳ Modulation amplitude	1/s
↳ ω_0	↳ Central frequency	1/s
↳ ω_{res}	↳ Resonance angular frequency of a resonator	1/s
↳ $\Delta\omega_{\mathrm{OP,opt}}$	↳ Frequency offset from ω_{res} for optimum sensitivity	1/s
↳ $\Delta\omega_{\mathrm{FSR,MZI}}$	↳ Angular frequency FSR of a MZI	1/s
↳ $\Delta\omega_{\mathrm{FWHM,LD}}$	↳ Angular frequency FWHM of a laser diode	1/s
↳ $\Delta\omega_{\mathrm{FWHM,RR}}$	↳ Angular frequency FWHM of a RR	1/s

Symbol	Description	Unit
Ω	Modulation frequency	1/s

E.2.2   Latin symbols

Symbol	Description	Unit
A	Area	m²
↳ A_{SL}	↳ Of the surface layer on the waveguide core	m²
a	Period of periodic waveguide (scalar, Chapter 3)	m
↳ **a**	↳ Period of periodic waveguide (vectorial, Chapter 2)	m
a	Amplitude transmission coefficient (other sections)	1
↳ **a**	↳ General coefficient matrix for multiport components, coefficients a_{mn}	1
↳ a_1	↳ MMI$_{1x2}$→MZI reference arm	1
↳ a_2	↳ MMI$_{1x2}$→MZI sensing arm	1
↳ a_s	↳ MZI sensing arm	1
↳ a_r	↳ MZI reference arm	1
↳ a_{mn}	↳ MMI$_{n\times m}$	1
↳ γ_a	↳ Coefficient errors (multiplicative)	1
B	Magnetic flux density	Wb/m²
↳ $B_{x,y,z}$	↳ Magnetic flux density components	Wb/m²
c	Vacuum speed of light	m/s
c_Q	Quality ratio between Q-factor and intrinsic Q-factor	1
D	Dielectric displacement	C/m²
↳ $D_{x,y,z}$	↳ Dielectric displacement components	C/m²
d_{gap}	Gap width of a sub-wavelength grating waveguide	m
E	Electric field (vectorial)	V/m
↳ $E_{x,y,z}$	↳ Electric field components	V/m
↳ E_i	↳ Electric field at the sensor input (scalar)	V/m
↳ **E**$_o$	↳ Electric field at the sensor output (vectorial)	V/m
↳ **E**$_0$	↳ Modal electric field profile	V/m
e$_z$	Unit vector in z-direction	1
f	Frequency of an electro-magnetic wave	Hz
↳ f_n	↳ Noise of the instantaneous frequency	Hz
↳ f_{LO}	↳ Frequency of a local oscillator	Hz

Symbol	Description	Unit
↳ f_{DUT}	↳ Frequency of a device under test	Hz
↳ f_{beat}	↳ Beat frequency between two frequencies	Hz
f_{s}	Sampling frequency of the measurement setup	Hz
Δf	Bandwidth of the measurement setup	Hz
FF	Fill factor of a SWG waveguide	1
h	Height of a waveguide	m
$\mathbf{H}$	Vectorial magnetic field	A/m
↳ $H_{\mathrm{x,y,z}}$	↳ Magnetic field components	A/m
$\mathbf{H}_0$	Modal magnetic field profile	A/m
I	Electrical current	A
↳ I_{i}	↳ At the laser input	A
↳ I_{o}	↳ At the photodetector output (single, scalar)	A
↳ $\mathbf{I}_{\mathrm{o}}$	↳ At the photodetector output (multiple, vectorial)	A
↳ $I_{\mathrm{o,max}}$	↳ At the photodetector output (maximum expected)	A
↳ I_{n}	↳ At the n-th photodetector output	A
↳ I_{q}	↳ After the ADC (quantized)	A
$\mathbf{B}$	Electric current density	A/m²
J_{n}	Bessel function of n_{th} order	1
j	Imaginary unit	1
k	Vectorial propagation constant	1/m
k_0	Vacuum propagation constant	1/m
L	Length of the MZI arm and of the RR circumference	m
↳ L_{opt}	↳ MZI arm length (optimized common length)	m
↳ ΔL	↳ MZI arm length (difference between two arms)	m
LSB	Least significant bit of an ADC	A
LoD	Total limit of detection of the sensor (eff. refractive index)	1
↳ LoD_{ζ}	↳ LoD from noise source $\zeta \in \left\{ T; \omega; P_{\mathrm{i}}; I_{\mathrm{s}}; I_{\mathrm{NEP}}; I_{\mathrm{q}} \right\}$	1
m	Absolute fringe order of a MZI phase difference	1
$\mathbf{M}_{\mathrm{C}}$	Clarke Transformation matrix	1
	↳ Non-ideal transposed Clarke Transformation matrix	1
↳ $\mathbf{M}_{\mathrm{C}}^{\mathrm{T}\Diamond}$		
$\mathbf{M}_{\mathrm{R}}$	Ellipse fitting matrix (rotation)	1
$\mathbf{M}_{\mathrm{S}}$	Ellipse fitting matrix (stretching)	1

Symbol	Description	Unit
$\mathbf{M}_{\mathrm{T}}$	Ellipse fitting matrix (translation)	1
N	ADC resolution	1
$\underline{n}$	Refractive index of a material (complex)	1
N	Refractive index of a material (real)	1
↳ n_{M}	↳ Of a waveguide cladding medium	1
↳ n_{SL}	↳ Of a waveguide surface layer	1
↳ n_{BOX}	↳ Of the buried oxide	1
↳ n_{core}	↳ Of the waveguide core	1
$\underline{n}_{\mathrm{e}}$	Effective refractive index of a waveguide mode (complex)	1
n_{e}	Effective refractive index of a waveguide mode (real)	1
↳ $n_{\mathrm{e,B}}$	↳ Effective Bloch refractive index of a periodic WG	1
↳ $n_{\mathrm{e,res}}$	↳ n_{e} to obtain resonance at a given optical frequency	1
↳ Δn_{e}	↳ Changes of n_{e} in a single waveguide	1
↳ $\Delta n_{\mathrm{e,0}}$	↳ Initial n_{e} offset between two waveguides	1
↳ $\Delta n_{\mathrm{e,r}}$	↳ Reconstructed n_{e} change of a waveguide	1
n_{g}	Group refractive index of a material	1
n_{eg}	Effective group refractive index of a waveguide mode	1
↳ $\Delta n_{\mathrm{eg,0}}$	↳ Initial n_{eg} offset between two MZI arm waveguides	1
NEP	Noise-equivalent power	W
OS	Translational offset vector	1
P	Optical power	W
↳ P_{i}	↳ At the sensor input	W
↳ P_{i0}	↳ At the sensor input (constant/flat spectral distr.)	W
↳ P_{o}	↳ At the sensor output (single, scalar)	W
↳ $\mathbf{P}_{\mathrm{o}}$	↳ At the sensor output (multiple, vectorial)	W
↳ P_{LD}	↳ At the laser diode output	W
$\mathbf{r}$	Position vector	m
R	Photodiode responsivity (single, scalar)	A/W
↳ $\mathbf{R}$	↳ Multiple photodiodes (multiple, vectorial)	A/W
$\mathfrak{R}$	Overall electrical readout responsivity	A/W
RIN	Constant, one-sided spectral density $S_{\mathrm{RIN}}(f)$ for low f	1
Q	Quality factor of a resonator	1
↳ Q_{i}	↳ Intrinsic quality factor of a resonator	1

Symbol	Description	Unit
q_e	Elementary charge	C
$\mathbf{S}$	Complex Poynting vector	W/m²
$\underline{S}$	Complex signal constructed from the MZI_3 currents	A
S_e	Effective-index sensitivity	1
$S_{e,\tau}$	Effective optoelectronic sensitivity	A/W
↳ $S_{e,\tau,max}$	↳ Maximum achievable – optimized parameters	A/W
↳ $S_{e,\tau,peak}$	↳ Peak within operating range	A/W
S_{env}	Arbitrary environmental sensitivity of a waveguide mode	*
↳ $S^{(hom)}$	↳ Homogeneous sensitivity of a waveguide mode	1
↳ $S^{(surf)}$	↳ Surface sensitivity of a waveguide mode	1/m
↳ $S_{opt}^{(surf)}$	↳ Optimized surface sensitivity of a waveguide mode	1/m
S_{sys}	System sensitivity of a complete photonic sensor	*
(S_I, S_Q)	Clarke-transformed MZI_3 output signals (in-phase/quadratic)	1
S_F	Frequency noise spectrum	Hz²/Hz
↳ S_{F0}	↳ Scalar value for a flat frequency noise spectrum	Hz²/Hz
S_{P_i}	Laser input power spectrum	W/Hz
S_{RIN}	Relative intensity noise spectrum	1/Hz
T	Optical power transmission	1
↳ $\hat{T}$	↳ Output contrast – difference between max/min	1
↳ T_0	↳ Constant/flat transmission	1
↳ T_{OP}	↳ In an operating point	1
↳ T_{RR}	↳ Of a ring resonator	1
↳ T_{Lor}	↳ Of a Lorentzian resonance	1
↳ T_{max}	↳ Maximum	1
↳ T_{min}	↳ Minimum	1
↳ $T_{MMI,1x2}$	↳ Of an 1×2 MMI	1
↳ $T_{MMI,2x3}$	↳ Of an 2×3 MMI	1
↳ $T_{MMI,3x3}$	↳ Of an 3×3 MMI	1
↳ T_{MZI}	↳ Of an two-arm MZI	1
↳ T_{opt}	↳ In the optimum operating point	1
t	Time	s
↳ T_{obs}	↳ Experiment observation time	s
↳ T_P	↳ Laser frequency modulation period	s

Symbol	Description	Unit
t	Electric field transmission matrix with coeff. t_{mn}	1
↳ **t**$_{Arms}$	↳ Of the two 1×3 MZI arms	1
↳ **t**$_{MMIi}$	↳ Of the input MMI in a 1×3 MZI	1
↳ **t**$_{MMIo}$	↳ Of the output MMI in a 1×3 MZI	1
↳ **t**$_{MZI3}$	↳ Of the 1×3 MZI	1
t_{SL}	Effective thickness of a surface layer on a WG core surface	m
TR	2×2 transformation matrix	1
ΔT_{rel}	Relative temperature difference	K
TOC	Thermo-optic coefficient	1/K
u	Periodic modulation function for periodic WG modes	1
V	Volume	m³
↳ V_{SL}	↳ Of the surface layer on the waveguide core	m³
v_g	Group velocity in a material	m/s
v_{eg}	Effective group velocity of a waveguide mode	m/s
w	Width of a waveguide	m
↳ w_{opt}	↳ Optimized total width of a waveguide	m
↳ w_{slot}	↳ Slot width of a slot waveguide	m
↳ w_{rail}	↳ Rail width of a slot waveguide	m
↳ $w_{rail,opt}$	↳ Optimized rail width of a slot waveguide	m
W	Length-related electric energy density	J/m
W_ζ	Noise propagation factors, $\zeta \in \left\{T; \omega; P_i; I_s; I_{NEP}; I_q\right\}$	var.
(x, y, z)	Cartesian coordinates	m
Z_0	Free space wave impedance	Ω

F.   List of Figures

G.   List of Tables

Acknowledgements (German)

So eine Arbeit wird eigentlich nie fertig,
man muß sie für fertig erklären,
wenn man nach Zeit und Umständen
das möglichste getan hat.

Johann Wolfgang von Goethe
Italienische Reise (Caserta, den 16. März 1787)

Während der Entstehung dieser Arbeit haben mich eine Vielzahl bemerkenswerter Personen begleitet, die mich sowohl fachlich als auch persönlich außerordentlich bereichert und nachhaltig geprägt haben. Diesen Personen möchte ich an dieser Stelle meinen tiefsten Dank aussprechen. Dieser Dank soll mitnichten als Abschluss zählen sondern ist vielmehr mit der Hoffnung verbunden, auch weiterhin in Kontakt zu bleiben.

Ermöglicht wurde diese Arbeit durch meinen Doktorvater Prof. Christian Koos. Sowohl in den wöchentlichen Gruppenrunden als auch bei spätabendlichen Diskussionen war es mir immer eine große Freude mit ihm in den wissenschaftlichen Diskurs zu gehen. Durch die kreative und fundierte Arbeitsweise mangelte es bei diesen Gesprächen nie an frischen und intelligenten Ideen, und auch die knackigsten Probleme wurden Stück für Stück in den Bereich des Lösbaren geschoben. Für eine erfüllte Doktorandenzeit muss jedoch auch die persönliche Chemie mit dem Doktorvater stimmen – das war hier durchweg der Fall. Vielen Dank! In Ergänzung dazu bedanke ich mich herzlich bei Prof. Wolfgang Freude, der unermüdlich die anfangs noch oft wirren Ideen und Experimente in

List of Publications

Patents

[P1]   **J. Milvich** and I. Raible, "**Sensor assembly and method of manufacture of a 3d-waveguide gap**", DE201610216328 (2016), FR20170057943 (2017), IT201710000096070 (2017)

[P2]   **J. Milvich** and C. Koos, "**Interferometer and method for determining an absolute phase difference at an interferometry**", DE201710216477 (2017)

Journal publications

[J1]   **J. Milvich**, D. Kohler, W. Freude, and C. Koos, "**Surface sensing with integrated optical waveguides: a design guideline**", *Optics Express* 26(16), 19885-19906 (2018)

[J2]   **J. Milvich**, D. Kohler, W. Freude, and C. Koos, "**Integrated phase-sensitive photonic sensors: A system design tutorial**", *Advances in Optics and Photonics* 13(3), 584-642 (2021)

[J3]   **J. Milvich**, T. Zaki, M. Aghamohammadi, R. Rödel, U. Kraft, H. Klauk and J.N. Burghartz, "**Flexible low-voltage organic phototransistors based on air-stable dinaphtho [2, 3-b: 2′, 3′-f] thieno [3, 2-b] thiophene (DNTT)**", *Organic Electronics* 20, 63-68 (2015)

[J4]   D. Kohler, G. Schindler, L. Hahn, **J. Milvich**, A. Hofmann, K. Laenge, W. Freude, and C. Koos "**Bio-photonic sensors with integrated Si$_3$N$_4$-organic hybrid (SiNOH) lasers for point-of-care diagnostics**", *submitted to Light Science & Applications* (2020)

Conference publications

[C1]   **J. Milvich**, D. Kohler, W. Freude, and C. Koos, "**Mach-Zehnder interferometer readout for instantaneous sensor calibration and extraction of endlessly unwrapped phase**", *2017 IEEE Photonics Conference (IPC)*, Orlando, FL, 567-568 (2017).

Curriculum vitae

Johannes Milvich

Born 09.06.1988 in Stuttgart, Germany
jmilvich@gmx.de

Education

10.2014–10.2017	Karlsruhe Institute of Technology – Ph.D. candidate	
	Major:	Electrical Engineering and Information Technology
	Field:	Integrated photonics
	Thesis:	Waveguide-Based Photonic Sensors:
		From Devices to Robust Systems
10.2011–09.2014	Universität Stuttgart – Master of Science	
	Major:	Electrical Engineering and Information Technology
	Field:	Micro, opto and power electronics
	Thesis:	Design and Characterization of an Organic Photosensor
09.2008–08.2011	Universität Stuttgart – Bachelor of Science	
	Major:	Electrical Engineering and Information Technology
	Field:	Micro- and optoelectronics
	Thesis:	Characterization of SiGe Multi-Quantum-Well Modulators
–08.2007	Werner-Siemens-Schule Stuttgart - Abitur	

Professional experience

05.2020–today	Robert Bosch GmbH, Reutlingen, Germany	
	Position:	Office of the Executive Management | Automotive Electron.
01.2019–04.2020	Robert Bosch GmbH, Stuttgart, Germany	
	Position:	Program manager | Steering of intl. ECU production
09.2018–12.2018	Robert Bosch GmbH, Stuttgart, Germany	
	Position:	Team lead | Engineering Vehicle Computer - Quality & Test
11.2017–08.2018	Robert Bosch GmbH, Stuttgart, Germany	
	Position:	Development engineer | Engineering Vehicle Computer
03.2013–11.2013	Bosch LLC, Palo Alto, CA, USA	
	Position:	Research intern | Image Sensors